UNLV | UNIVERSITY LIBRARIES

UNLV Theses, Dissertations, Professional Papers, and Capstones

12-2010

Characterization of unsaturated flow in dual-porosity granular media

Jeevan A. Jayakodilage
University of Nevada, Las Vegas

Follow this and additional works at: https://digitalscholarship.unlv.edu/thesesdissertations

 Part of the Hydrology Commons

Repository Citation

Jayakodilage, Jeevan A., "Characterization of unsaturated flow in dual-porosity granular media" (2010). *UNLV Theses, Dissertations, Professional Papers, and Capstones*. 770.
http://dx.doi.org/10.34917/2044107

This Thesis is protected by copyright and/or related rights. It has been brought to you by Digital Scholarship@UNLV with permission from the rights-holder(s). You are free to use this Thesis in any way that is permitted by the copyright and related rights legislation that applies to your use. For other uses you need to obtain permission from the rights-holder(s) directly, unless additional rights are indicated by a Creative Commons license in the record and/or on the work itself.

This Thesis has been accepted for inclusion in UNLV Theses, Dissertations, Professional Papers, and Capstones by an authorized administrator of Digital Scholarship@UNLV. For more information, please contact digitalscholarship@unlv.edu.

CHARACTERIZATION OF UNSATURATED FLOW IN DUAL-POROSITY GRANULAR MEDIA

by

Jeevan Anuradha Jayakody Rathmalsinghe Rajakaruna Jayakodilage

Bachelor of Science
University of Peradeniya, Sri Lanka
2005

A thesis submitted in partial fulfillment
of the requirements for the

Master of Science in Geoscience
Department of Geoscience
College of Sciences

Graduate College
University of Nevada, Las Vegas
December 2010

Copyright by Jeevan Anuradha Jayakody Rathmalsinghe Rajakaruna Jayakodilage
2011
All Rights Reserved

THE GRADUATE COLLEGE

We recommend the thesis prepared under our supervision by

Jeevan Anurandha Jayakody Rathmalsinghe Rajakaruna Jayakodilage

entitled

Characterization of Unsaturated Flow in Dual-porosity Granular Media

be accepted in partial fulfillment of the requirements for the degree of

Master of Science in Geoscience

Michael Nicholl, Committee Chair

Adam Simon, Committee Member

Michael Young, Committee Member

Dale Devitt, Graduate Faculty Representative

Ronald Smith, Ph. D., Vice President for Research and Graduate Studies
and Dean of the Graduate College

December 2010

ABSTRACT

Characterization of Unsaturated Flow in Dual-porosity Granular Media

by

Jeevan Anuradha Jayakody Rathmalsinghe Rajakaruna Jayakodilage

Dr. Michael Nicholl, Examination Committee Chair
Associate Professor of Geoscience
University of Nevada, Las Vegas

A geological medium made up of uncemented coarse porous rock fragments may be described as a "dual-porosity granular medium" due to the presence of two types of pores; small pores within individual fragments and large pores between the fragments. Crushed stone found in heap leach piles, mine waste, backfills, rock drains, and engineered capillary barrier systems fit this description. Unsaturated flow in a dual-porosity granular medium will occur both through the fragments (matrix flow), and on the fragment surfaces (film flow). The relative influence of gravity and capillary forces on these two flow regimes will be largely different. Therefore, unsaturated flow in this type of media is expected to differ from the conventional concepts developed for application to single porosity systems.

A test column (30 cm diameter, 100 cm tall) was filled with crushed sandstone (~1.5 - 3 cm diameter) as a dual-porosity granular media. Water entered the column from the top through a point source at a steady rate (8.0 ml/minute) and exited through nine equal-area sections at the bottom of the column. Inflow, outflow from each of the nine sections, weight of the column, temperature (ambient and inside the column), humidity (ambient and inside the column) and barometric pressure were measured at 2 minute intervals in four trials (2-40 days long) under variable conditions.

It was found that unsaturated flow in dual-porosity granular media is spatially non-uniform, and likely occurs in the form of narrowly focused discrete pathways. The resulting flow structure limits the matrix saturation of the rock fragments to well below 100%. The distribution of flow was observed to change spontaneously, without any apparent external perturbation. Furthermore, the flow distribution was observed to change in response to external perturbations (inflow interruption, relocation of the inlet, and reducing evaporative loss); however, the occurrence and magnitude of redistribution were not predictable.

ACKNOWLEDGEMENTS

First and foremost, I thank my advisor Dr. Michael Nicholl for providing me the motivation to explore the field of unsaturated zone hydrology, which was an entirely new discipline for me. His enormous support and encouragement always raised my enthusiasm on this research. I would also like to thank the other members of my committee, Dr. Adam Simon, Dr. Michael Young, and Dr. Dale Devitt for their helpful discussions and constructive critiques.

A special thanks goes to Seth Page for his invaluable help in fabrication of the experimental set-up. I would also like to acknowledge the support that I received from the faculty and my colleagues in the UNLV Geoscience Department. The education that I received from my undergraduate advisor Dr. Jagath Gunatilake and the other faculty at the Department of Geology, University of Peradeniya in Sri Lanka will always be remembered. Most of all, I am always thankful to my wife, Prabha, for her continuous support and patience.

This research was made possible from the funding received from NSF EPSCoR as a part of the project entitled “Scaling Environmental Processes in Heterogeneous Arid Soils”, and all of the facilities provided by UNLV.

TABLE OF CONTENTS

LIST OF FIGURES

CHAPTER 1

INTRODUCTION

This thesis presents experiments designed to investigate the spatial and temporal structure of unsaturated flow in dual-porosity granular media. The term dual-porosity refers to media in which the pore space exhibits two distinctly different geometries; while the term granular media refers to a collection of stone fragments that are not cemented to one another. Thus, a dual-porosity granular media consists of porous rock fragments, where the intra-granular pores within individual fragments are much smaller than the inter-granular pores between the fragments. From a practical perspective, dual-porosity granular media may occur in natural gravel deposits, but are most likely anthropogenic in origin; i.e., heap leach piles, backfills, rock drains, engineered capillary barriers, and mine tailings. Because of the size difference between intra-granular and inter-granular pores, unsaturated flow through such systems may not conform to existing conceptual models, and therefore must be considered through experiment. The work presented here focuses on spatial and temporal variability in unsaturated flow through dual-porosity granular media.

1.1 Overview of Unsaturated Flow in Dual-porosity Granular Media

Present day concepts regarding unsaturated flow have been primarily developed in the context of typical agricultural soils, where the pore size distribution is relatively narrow, with a single peak (i.e., single porosity or unimodal) at the sub-millimeter to millimeter scale. In the absence of thermal, osmotic, and barometric pressure gradients, unsaturated flow through such soils will be controlled by capillarity and gravity. The

magnitude of the gravitational force remains constant in space and time, while the capillary force varies with pore size, saturation, and wettability of the medium. In media where the pore size distribution is narrow and unimodal, the balance between capillarity and gravity is expected to vary smoothly across the domain, even under changing flow conditions. In contrast, the balance between the capillary and gravitational forces may show substantial and abrupt changes in a dual-porosity media. Flow behavior in the small intra-granular pores is likely to be controlled by capillary forces, while that in large inter-granular pores will be gravity dominated. As a result, unsaturated flow processes in dual-porosity granular media are likely to differ significantly from what would be expected in a typical unimodal soil.

Conceptual models developed for unsaturated flow in other types of dual-porosity media (e.g., fractured rocks, macroporous soils) may have limited applications in granular media because the pore geometry is fundamentally different. In general, the length scale of individual rock fractures is several orders of magnitude larger than the width of their apertures. Similarly, the lengths of soil macropores and cracks can be much larger (up to several orders of magnitude) than their diameter/width. All of these features tend to have a preferential orientation; cracks and macropores tend to be oriented vertically, while rock fractures typically occur in one or more parallel sets. In contrast, the length scale of an individual inter-granular pore in dual-porosity granular media will be similar in all dimensions and considerably shorter than that expected for the aforementioned features. This difference in geometry is expected to have a major effect on unsaturated flow.

It is expected that unsaturated flow in dual-porosity granular media will exhibit two primary flow elements: (a) flow through the matrices of fragments (matrix flow) that passes through contacts between fragments; and (b) flow along surfaces of fragments (film flow). In addition, fluid transfer between these two elements is also expected. Unlike the other forms of dual porosity media mentioned above, both flow elements are likely to connect in three-dimensions at the relatively short length scale imposed by particle size,

Capillary forces will control flow through the fragments, while gravity will control flow along the fragment surfaces. The magnitude of each flow element is expected to vary with the saturation of the media. At low saturation, flow is likely to be constrained to the matrix element, and behave in many ways similar to what we would expect for a typical unimodal soil, noting that fragment shape effects and flow across contacts will be unique to media of this type.

At higher saturations, we expect an abrupt transition to film flow as water flows along the surfaces of the fragments. Film flow is likely to be several orders of magnitude more rapid than matrix flow, and exhibit more complex behavior. Unlike the fluids in the matrix, fluid films moving on fragment surfaces are not tightly constrained to narrow channels. Therefore, such films may be unstable and sensitive to external perturbations (e.g., temperature and humidity changes). The films themselves may be highly non-uniform in thickness (e.g., Dragila and Weisbrod, 2003), with consequent effects on the uniformity of flow within the system. For these reasons, plus the interaction between the matrix and film flow elements, I anticipate the formation of complex flow structures that vary in both space and time. Therefore, the objective of the research presented here is to

characterize the spatial and temporal structure of unsaturated fluid flow in dual-porosity granular media.

1.2 Importance of Unsaturated Flow in Dual-porosity Granular Media

Understanding the characteristics of unsaturated flow in dual-porosity granular media will be directly applicable to a number of important problems associated with flow, solute transport, and weathering.

Gold and other precious metals are often extracted through the process of heap leaching. The ore is crushed to a nominal size of gravel to boulder (~1 - 20 cm), and then stacked in piles. The horizontal dimensions of a typical heap leach piles may extend several hundreds of meters, while the height may be on the order of 100 meters. The metal is extracted by sprinkling a leaching solution onto the top of the pile, then collecting it at the bottom. As the leaching solution passes downward through the unsaturated pile, it moves through both intra- and inter-granular pores, extracting the target metal along the way. The efficiency of metal extraction in a heap leach pile depends highly on the flow structure of the leaching solution. For the most effective operation, the leaching solution should move uniformly from the top to the bottom of the pile, contacting the intra-granular pore space of all crushed ore fragments for a uniform amount of time. Occurrences of non-uniform and unsteady flow (e.g., preferential flow paths) will lead to uneven extraction; metal will not be extracted from portions of the crushed ore that do not sufficiently contact the solution.

Mining operations tend to produce large volumes of crushed rock in the form of overburden and processed ore that are typically disposed or stored on the surface,

producing a dual-porosity granular media. Such materials potentially expose reactive minerals to weathering processes that may release hazardous or undesirable contaminants into both surface and underground water resources. The amount of contaminant released, the rate of release, and location of the releases will depend on unsaturated flow through the mine waste. If the flow processes that occur in mine waste piles are variable in space and time, then conceptual models that assume uniform flow will be inadequate for use in risk assessment and predictive modeling of remediation schemes. For example, the occurrence of preferential flow paths will transport solutes away from the site much faster than would be expected for a uniform flow field.

Engineered capillary barrier systems are important structures in waste isolation. A capillary barrier is composed of two layers of materials; a medium that contains large pores is used to separate the waste from a medium that contains small pores and overlies or surrounds the coarse-grained medium. If the coarse media is porous, it will act as a dual-porosity granular media. Under partially-saturated conditions, water in the fine-grained medium is restricted from entering the coarse-grained medium unless the water entry pressure is attained. As a result, the interface between the two media acts as a capillary barrier. This type of configuration is capable of diverting unsaturated flow through the fine-grained medium without reaching the waste. Several authors have investigated the performance of such capillary barrier systems (e.g., Conca et al., 1998; Tidwell et al., 2003) and found that they may fail under some conditions (e.g., fingering; Tidwell, 2003) and potentially expose the waste to water. Therefore, to optimize the efficiency of a capillary barrier system, flow through the coarse media (rock fragments,

natural gravel or coarse sand) should be understood. Conventional conceptual models that assume "uniform flow" may lead to inaccurate predictions in this type of system.

Another example where understanding of unsaturated flow in dual-porosity granular media becomes important is the long-term performance of backfills and rock drains constructed from crushed stone. Weathering of the rock fragments will be largely influenced by the distribution of water under unsaturated conditions, where oxygen is readily available. At the scale of an individual fragment, weathering is likely to be most intense at water-filled contacts between adjacent fragments, especially if that water is replaced regularly. In turn, weathering of contacts may lead to a reduction in structural strength, volume, or permeability. The products of chemical weathering (e.g., clay minerals) may also impede drainage. At the macroscopic scale, weathering may be concentrated along flow paths, rather than uniform throughout. For these reasons, understanding unsaturated flow structure in such media is important for design and construction of durable backfills and rock drains.

1.3 Formulating the Research Hypotheses

Previous research on unsaturated flow in dual-porosity granular media has mostly focused on the either the micro-scale or field-scale. Field investigations in natural gravels (e.g., Mali et al., 2007) and heap leach piles (e.g., Webb et al., 2008) have observed the existence of non-uniform flow fields (vertically and horizontally) that exhibit time-variant behavior. However, these systems were heterogeneous in nature and subject to variable boundary conditions (inflow, temperature, humidity, etc.). There was also the potential that water flow modified the media through chemical processes.

Conversely, small-scale experiments conducted under controlled laboratory conditions (e.g., Hu et al., 2004; Carminati et al., 2008) have focused on flow at the scale of an individual rock fragment, and thus tell us little about macroscopic behavior. The implied knowledge gap leads to this thesis, which poses the following hypotheses to be addressed at the intermediate scale:

(a) the distribution of unsaturated flow paths in dual-porosity granular media will be spatially non-uniform; and,

(b) the spatial structure of unsaturated flow paths, and thus the structure of flow fields, will be unsteady over time, and sensitive to changes in ambient temperature and/or humidity.

1.4 Investigative Approach

In order to test the above hypotheses, spatial distribution and temporal variability of water flow in a dual-porosity granular medium were monitored under controlled conditions. A test column of 30 cm inside diameter and 100 cm tall was used for this purpose. The column was filled with crushed and screened sandstone (1-3 cm in size) to form a substantially uniform dual-porosity granular medium. Water was supplied to the top of the column at a steady rate (8.0 ml/min) from a single-point source to establish unsaturated flow through the column. The bottom of the column was divided into nine equal-area sections to monitor the spatial distribution of flow exiting the column over time.

In a series of four experiments, inflow, outflow from each of the nine sections, temperature and humidity inside the column, as well as outside the column, atmospheric

pressure, and total weight of the test column were measured at two-minute intervals using an automated data acquisition system. During this series of experiments, the temperature, thus the dynamic viscosity of inflow water (~30%), as well as inflow boundary conditions were changed. The inflow boundary condition was changed by: (a) relocating the single-point source; (b) pausing the inflow (for 10-90 minutes); and, (c) changing the evaporation from the top of the column. Each change was made in isolation; i.e., one at a time. Distribution of outflow between the nine sections at the bottom of the column was analyzed graphically and statistically to determine the spatial and temporal flow structure in the test column. Changes in the ambient environment, inflow boundary conditions and the dynamic viscosity of water were then integrated into the analysis to understand their influences on the flow structure.

1.5 Organization of the Thesis

Background information for this research including principles of unsaturated fluid flow, the concept of dual-porosity granular media, as well as current understanding and knowledge gaps on unsaturated fluid flow in dual-porosity media are presented in chapter 2. Chapter 3 describes the conceptual design, physical set-up, instrumentation and operation of the experiment. Results of four experimental runs are presented in chapter 4 and discussed in chapter 5. Chapter 6 concludes the thesis with a summary of findings, conclusions and suggestions for further investigations.

CHAPTER 2

BACKGROUND

This chapter provides background information on unsaturated flow, dual-porosity media, and our current understanding of unsaturated fluid flow in dual-porosity media. The background review is then used to identify the knowledge gaps to be addressed in this thesis. The first section of the chapter (2.1) summarizes the fundamental concepts of unsaturated flow in geologic media. The concept of dual-porosity media and the basic unsaturated flow mechanisms that are expected to operate in such media are discussed in sections 2.2 and 2.3, respectively. A summary of the literature on unsaturated flow in macro- and field-scale dual-porosity granular systems is presented in section 2.4. The final section of the chapter (2.5) identifies several gaps in current knowledge on the topic.

2.1 Overview of Unsaturated Porous Media

An unsaturated porous medium is one in which the pore space is occupied by two fluid phases, liquid water and air (e.g., Gray and Hassanizadeh, 1991). The two fluid phases are generally treated as immiscible, and separated at the micro-scale by sharp interfaces known as menisci (e.g., Crist el al., 2004). The fraction of the pore volume that is occupied by liquid water is referred to as the saturation (S), which varies between 0 (for completely dry media) and 100% (pore space is completely water filled). Assuming that the total pore volume is static, the percentages of pore space occupied by water and the air must sum to 100%. It is important to note that S provides information on the amount of water present in a medium, but does not describe how the water is distributed.

Liquid water in unsaturated media is not randomly distributed within the pore space (figure 2.1). The most common minerals found in rock and soil, silicates, as well as

calcite and dolomites, which are the most common carbonate minerals, all tend to be strongly hydrophilic (e.g., Tschapek, 1984; Giese et al., 1996). Therefore, the solid surfaces of most porous media are expected to have a stronger affinity to water than to air. This affinity causes the water to spread on the solid surfaces and preferentially occupy small pores between surfaces. Because of this spreading mechanism, the water phase normally controls the spatial distribution of the air phase, driving it into large pores. Assuming that the system is at thermodynamic equilibrium, the exact distribution of the water (and hence air) is determined by: the geometry of the pore space, capillary properties (contact angle, surface tension), and the pressure history of the system (e.g., Phillip, 1970).

The spreading mechanism of the water also causes it to remain fully connected in three dimensions through water-filled pores, pendular rings and/or free-surface films, even at small saturations (figure 2.1). Conversely, the air phase is more likely to become fragmented as saturation approaches 100%. This difference in behavior is important because the connectivity of each phase greatly influences both flow (e.g., van Genuchten, 1980; Wildenschild et al., 2001) and changes in saturation through pore filling/emptying (e.g., Celia and Binning, 1992). From a traditional soil physics approach (e.g., Hillel, 1998), the pore-filling water has a larger impact on saturation and flow than water that is in the films and pendular rings; hence it is discussed in detail below (sections 2.1.1 and 2.1.2). Recently, a number of authors have proposed the importance of water films and pendular rings, particularly with respect to flow in rock fractures and large pores (e.g., Conca and Wright, 1992; Tokunaga and Wan, 1997; Tokunaga et al., 2000; Hu et al.,

2004). The significance of such water elements on unsaturated flow is discussed in Section 2.3.

2.1.1 Pore Size and Saturation

The three-dimensional geometry of pores in granular media is likely to be complicated beyond exact description, with individual pores exhibiting length scales that can range from micrometers to centimeters (e.g., Tuller et al., 1999). Following Luxemoore (1981), individual pores may be categorized into micropores, mesopores, and macropores on the basis of length scale. Micropores are several micrometers in diameter and are commonly present between layers of crystal lattices of minerals (e.g., clays, gypsum). Mesopores have diameters ranging from several micrometers to a few millimeters, and make up the bulk of pore space in typical, medium-textured soils. Macropores are from several millimeters to centimeters across and form through a variety of processes in both rock (e.g., fractures, vugs) and soil (e.g., cracks, worm burrows, particle bridging).

Considering the extremely complex geometry of pore space in natural media, it is common to conceptualize the media as a bundle of cylindrical capillary tubes with different radii (e.g., Bartley and Ruth, 1999; Dong et al., 2005). With this simplification, one can then relate pore size and saturation to fluid pressure through simple capillary theory. The capillary rise (h) of water in a vertical tube of radius, r, is given by:

$$h = \frac{2\gamma\cos\alpha}{\rho g r} \qquad \text{Eq. (2.1)}$$

where γ is the interfacial tension, α is the contact angle between water and the solid surface, ρ is the density of water, and g is the gravitational acceleration (e.g., Wang and Narasimhan, 1985; Or, 2008).

Equation 2.1 implies that, in a hydrophilic media, the fluid pressure at the entry to the tube will be negative (lower than the atmospheric pressure), thus water is drawn into the pore space under suction. The magnitude of the negative pressure (i.e., suction) is inversely proportional to pore radius, causing water to be preferentially attracted to small pores. In this conceptual model, as saturation increases, water enters into progressively larger pores and fluid pressure becomes less negative, with the reverse happening during drainage (e.g., Wang and Narasimhan, 1985). Continuing with the assumption of cylindrical pores, the water volume associated with filling a pore is proportional to r^2, while fluid pressure is proportional to r^{-1} (equation 2.1), leading to a highly nonlinear relationship between fluid pressure and saturation as illustrated in figure 2.2. Although the relationship between fluid pressure and saturation is typically considered as a single valued function, it often exhibits history dependent hysteresis (e.g., Richards, 1931; van Genuchten, 1980; Jerauld and Salter, 1990). Hysteresis is commonly attributed to poor reversibility in the pore-filling mechanisms.

The capillary bundle theory introduced above suggests that water will only enter into a pore when the water pressure exceeds a threshold defined by pore size (water-entry pressure). The water-entry pressure for macropores will be very close to zero, suggesting that they are likely to remain dry except when the medium is close to 100% saturation. At lower saturations, water cannot enter the large pores, causing them to act as barriers to capillarity-driven flow (e.g., Wang and Narasimhan, 1985; Jarvis, 2007). The capillary barrier formed by an individual spherical macropore (e.g., vug) will have relatively little impact on unsaturated flow because the surrounding mesopores are connected in three dimensions, and will thus allow flow to bypass the local barrier. Conversely, macropores

that have an extended length (e.g., fractures, cracks, worm burrows) may form significant diversionary barriers to unsaturated flow (e.g., Glass et al., 1995).

2.1.2 Pore Size and Flow

As described above, the ability of hydrophilic porous media to attract and retain water is inversely proportional to pore size. The smallest pores are filled first when the medium wets, and emptied last when the medium dries. Water that occupies micropores is tightly bound to the solid surfaces; hence mobility of that water under normal conditions is extremely low (e.g., Dubinin, 1980). We therefore restrict our discussion to fluid flow in mesopores and macropores. Also, the discussion in this section is limited to granular media (e.g., soil) that exhibit a unimodal pore size distribution.

Hydraulic conductivity of a partially saturated medium depends on the pore geometry (pore size distribution, interconnectedness of pores, tortuosity, etc.) and the degree of saturation (e.g., Mualem, 1976; van Genuchten, 1980; Schaap and Leij, 2000;Moldrup et al., 2001; Kutilek 2004). Volumetric water flow rate (volume per unit time) through a narrow tube (Q) can be given by the Poiseuille's equation:

$$Q = \frac{\pi r^{x} \rho g}{S\eta} \frac{dh}{dl} \qquad \text{Eq (2.2)}$$

where r is the pore radius, ρ is the density of water, g is the gravitational acceleration, η is the viscosity of water, dh/dl is the total pressure gradient, x and S are dimensionless constants (e.g., Sutera and Skalak, 1993; Arya, 1999). Assuming a circular cross section, flow rate per unit area (flux; q) can be derived from the equation 2.2 and given by:

$$q = \frac{Q}{\pi r^{2}} = \frac{r^{x-2} \rho g}{S\eta} \frac{dh}{dl} \qquad \text{Eq (2.3)}$$

For a cylindrical tube with a uniform diameter, x and S are equal to 4 and 8 respectively, however, for different soil types x can vary between ~2.6 and ~4.7 (Arya, 1999). Equation 2.3 implies that the hydraulic conductivity of an unsaturated medium increases exponentially as water starts to flow through large pores with increasing saturation (figure 2.3).

Based solely on pore size, it is therefore expected that small changes in saturation will produce significant changes in hydraulic conductivity of the unsaturated medium. As saturation increases, the area available for flow also increases and flow tortuosity decreases; both of these factors are expected to increase hydraulic conductivity to a lesser degree than the pore filling mechanism described above.

As shown in figure 2.3, hydraulic conductivity can increase by several orders of magnitude in response to a small increase in saturation of a porous medium (e.g., van Genuchten, 1980; Vogel and Cislerova, 1988; Schaap and Leij, 2000). Similarly, fluid pressure also can increase by several orders of magnitude (becomes less negative) in response to a small increase in saturation (described in section 2.1.1). Therefore, the relationship between the fluid pressure and hydraulic conductivity is highly non-linear (figure 2.4). Note that the hydraulic conductivity vs. fluid pressure graph is drawn in log-log scale because both parameters can vary over several orders of magnitude under normal conditions.

The above discussion makes the common assumption that the air phase has no effect on unsaturated flow (e.g., Gray and Hassanizadeh, 1991). The dynamic viscosity of air is orders of magnitude smaller than that of water; therefore, it flows easily in response to small changes in pressure. If air can freely escape the porous media, then pressure within

the air phase remains essentially constant in space and it has a negligible impact on the water phase. However, compression of trapped air due to lack of escaping pathways can substantially cause a build of pressure in the gas phase that impacts water flow (e.g., Touma and Vauclin, 1985).

2.1.3 Energy Considerations for Unsaturated Flow

At any point within a fluid, flow occurs in response to the gradient of the total energy at that point. For unsaturated flow of liquid water under isothermal conditions, the total energy in water, also known as the total water potential (Φ_t) is given by:

$$\Phi_t = \Phi_g + \Phi_m + \Phi_a + \Phi_o \qquad \text{Eq. (2.4)}$$

where Φ_g is gravitational potential, Φ_m is matric potential, Φ_a is pneumatic potential and Φ_o is osmotic potential (Bolt, 1976).

The gravitational potential (Φ_g) describes the body force applied to water molecules by the earth's gravitational field. The gravitational potential of a body at a given point is equal to the amount of energy required to move that body from a reference level to its present position against the earth's gravitational field. For this case, the gravitational potential (Φ_g) is a function of its mass (m), gravitational acceleration constant (g), which is ~ 9.8 ms^{-2} towards the earth's center, and the elevation of the mass above the arbitrary reference level (h). The gravitational potential can be expressed by;

$$\Phi_g = mgh \qquad \text{Eq. (2.5)}$$

When a unit mass of water is considered, gravitational potential becomes only a function of the vertical distance between the reference level and the point of interest. Since the gravitational potential is calculated with respect to an arbitrary reference level,

numerical values of gravitational potential are not important, just the gradient, which for water of constant density takes on a value of unity, oriented in the downwards direction.

The matric potential (Φ_m) represents the sum of capillary forces that operate at the air-water- solid interface, and the adsorptive forces that operate at the water-solid interface (e.g., Philip, 1977; Nitao and Bear, 1996; Tuller et al., 1999). At the scale of an individual pore, the capillary component of the matric potential is equal to the pressure difference across the meniscus (ΔP) at the water-air interface. It can be given by the Laplace-Young equation, which is the general form of equation 2.1;

$$P_0 - P_h = \Delta P = \gamma \left(\frac{1}{R_1} + \frac{1}{R_2} \right) \qquad \text{Eq. (2.6)}$$

where P_0 is the atmospheric pressure, P_h is the fluid pressure across the meniscus, γ is the interfacial tension, R_1 and R_2 are the principal radii of curvature of the meniscus (e.g., King et al., 1999; Huang et al., 2006). For a partially-saturated hydrophilic medium, the meniscus is concave with respect to the water phase; i.e., pressure decreases when crossing the meniscus from air to water ($P_0 > P_h$). Equation 2.6 suggests that as saturation increases the radii of curvature in all water filled pores become larger, approaching infinity as S goes to 100%. Because the capillary force is dependent on pore size and saturation, it can act in any direction, and vary in size from near zero to several orders of magnitude larger than the gravitational force.

The adsorptive component of the matric potential attributes to surface forces (e.g., electrostatic forces, hydration forces, van der Waals forces) between water and the solid surface (e.g., Philip, 1977; Tuller et al., 1999). Philip (1977) suggested the following empirical formula to express the magnitude of adsorptive forces (F_h);

$$F_h = \frac{-\lambda R' T}{h} \qquad \text{Eq. (2.7)}$$

where λ is a positive constant (10^{-10} m), R' is the gas constant per unit mass of water vapor ($JK^{-1}kg^{-1}$), T is absolute temperature (K), and h is the thickness of the adsorbed liquid film. It implies that water in very thin layers is subjected to high adsorptive forces.

A pneumatic potential (Φ_a) is present when the air pressure in a porous medium (P_a) differs from the atmospheric pressure (P_0), and is given by;

$$\Phi_a = P_a - P_0 \qquad \text{Eq. (2.8)}$$

The pneumatic potential becomes negligible for shallow, highly porous media because air pressure in such media can rapidly equilibrate with the changing atmospheric pressure. However, in deep, layered soil profiles, where interaction between the atmosphere and soil gas is limited, as well as in soils with potential gas generation, pneumatic potential can significantly affect fluid flow (e.g., Elberling et al., 1998; Kellner et al., 2004).

The osmotic potential is the difference in free energy between pure water and water that contains solutes. It describes the ability of water molecules to move from a solution of low solute concentration to a solution of high solute concentration across a semi-permeable membrane. The osmotic potential (Φ_o) can be given by the van't Hoff equation;

$$\Phi_o = - RTC \qquad \text{Eq. (2.9)}$$

where R is the universal gas constant (8.314×10^{-3} $kPam^3/mol\ K$), T is absolute temperature, and C is solute concentration. Osmotic potential of water becomes significant only when solute concentration in water is substantially high and the flow

occurs across a selectively permeable membrane. Typically, this condition is only found in the active root zone.

If we assume that the pneumatic (Φ_a) and osmotic (Φ_o) potentials are negligible, then the total potential (Φ_t) is given by:

$$\Phi_t = \Phi_g + \Phi_m \qquad \text{Eq. (2.10)}$$

The total water potential is most commonly expressed in terms of the height of a water column (cm, m, inches etc.) which is equivalent to the total potential (pressure) per unit area. For unsaturated conditions, the height of the equivalent water column will be negative because water is under negative pressure. Also, the total water potential can be expressed as energy per unit mass of water (e.g., J/kg) and as energy per unit volume, which yields the dimension of pressure (e.g., Nm-2, Pa).

2.2 Dual-porosity Media

As discussed above, flow in an unsaturated porous medium is largely influenced by pore size and geometry. Most of our current knowledge regarding unsaturated flow was developed based on soils where the pore size distribution is unimodal with a mean in the sub-millimeter to millimeter range (i.e., mesopores). Considerably less is known about flow in dual-porosity media that exhibit bimodal pore size distributions. Examples of dual porosity media include: macroporous soil (e.g., Bouma and Dekker, 1978), fractured porous rocks (e.g., Gvirtzman et al., 1988; Price et al., 2000; Brouyere et al., 2004), gravel deposits (e.g., Mali et al., 2007), karstic rocks (e.g., Palmer, 1991), and heap leach piles (e.g., Nichol et al., 2005; Webb et al., 2008; Wu et al., 2007).

2.2.1 Well-studied Types of Dual-porosity Media

Any porous medium that exhibits a bimodal pore size distribution can be described as a dual-porosity medium. Macroporous soil contains micropores and mesopores of sub-millimeter to millimeter scale, as well as macropores of millimeter to centimeter scale. Soil can contain structural macropores (e.g., cracks) and macropores created by plant roots and soil organisms (Bouma and Dekker, 1978; Tippkotter, 1983). Water flow and solute transport in macroporous soil are substantially different from that in typical soil (e.g., Boumaand Dekker, 1978). In general, macropores facilitate preferential water flow at high saturation, and hence potentially create rapid flow paths in comparison to the diffusive flow in the surrounding soil. Macropores will also drain rapidly following an infiltration event, and may exhibit film flow along the pore walls at intermediate saturations. Orientation of macropores and the connectivity between macropores are critical in determining the unsaturated flow in macroporous soil (e.g., Boumaand Dekker, 1978). Isolated individual macropores, as well as well-connected networks of macropores exist in soil and their inclination can commonly vary between 0^o and ~50^o from vertical (Tipkotter, 1983; Perret, 1999). Thus, an isolated inclined macropore will potentially create a capillary barrier to vertical flow, while a vertical macropore will create a preferential pathway.

All common rocks contain micropores in the matrix, and many rocks of hydrologic interest (e.g., sandstones) contain mesopores. However, the presence of macro-scale cavities in karstic rocks (e.g., limestone, gypsum), unfilled vugs in volcanic rocks, and open tectonic or cooling fractures can create rock with a bi-modal pore size distribution (e.g., Wang and Narasimhan, 1985; Gerke and van Genuchten, 1993). It is well known

that water flow occurs both through the matrix and fractures in partially saturated fractured rocks (e.g., Gvirtzman et al., 1988; Price et al., 2000). Matrix flow is thought to be dominant until the net infiltration rate exceeds the saturated hydraulic conductivity of the matrix; after which water starts to flow through the fractures (Brouyere et al., 2004). Furthermore, film flow along the surfaces of open fractures provides rapid and highly conductive pathways (e.g., Tokunaga and Wan, 1997; Zhang et al., 2006). In contrast to the concept of uniform flow, liquid flow in partially saturated fractured porous media can occur in narrowly focused pathways (Glass et al., 2002). Furthermore, conductivity of flow paths in such media substantially changes over time.

2.2.2 Dual-porosity Granular Media

The term "dual-porosity granular media" is used as a descriptor for media made up of uncemented coarse porous fragments. This type of media exhibit two distinctive pore sizes; mesopores within individual fragments (intra-granular pores) and macropores between fragments (inter-granular pores). The pore geometry of dual-porosity granular media is largely different from that of dual-porosity fractured rocks and macroporous soil described above. The length scale of three-dimensional macropores (i.e., inter-granular pores) in dual-porosity granular media will be of the same order (few millimeters to few centimeters) in all directions (figure 2.5). In contrast, macropores found in fractured rocks and macroporous soil exhibit extreme elongation along a preferred direction (e.g., Palmer, 1991; Tipkotter, 1983; Glass et al., 2002). Therefore, we can expect that flow processes in dual-porosity granular media will be substantially different from that in fractured rocks and macroporous soil.

Man-made systems such as heap leach piles (e.g., Webb et al., 2008), mine tailings (e.g., Azam et al., 2007), engineered capillary barriers (e.g., Conca et al., 1998), backfills (e.g., Yanful et al, 1993; Guebert and Gardner 2001), and rock drains (e.g., Chahar, 2004) composed of coarse porous stone fragments are the most common practical applications of dual-porosity granular media. Furthermore, natural gravel deposits (e.g., Mali et al., 2007) also belong to the category of dual-porosity granular media. Understanding unsaturated flow processes in dual-porosity granular media is essential for optimal performance of man-made systems, as well as for environmental protection associated with them. However, unsaturated flow in this type of media has received little attention in the past; thus, the flow processes are not well characterized.

2.3 Unsaturated Flow in Dual-porosity Granular Media

The pore geometry of dual-porosity granular media is expected to facilitate fluid flow through individual fragments (intra-granular pore space), as well as around fragments (inter-granular pore space; figure 2.6). Two main flow elements can be identified in unsaturated dual-porosity granular media; (a) flow through the porous matrices of fragments, i.e., matrix flow, and (b) flow on fragment surfaces, i.e., free surface flow or film flow (e.g., Conca and Wright, 1992). Matrix flow between adjacent fragments occurs across the solid contacts, as well as water-filled zones between them (e.g., Carminati et al., 2007). Water films on adjacent fragment surfaces are connected through pendular rings at the contacts between fragments (e.g., Hu et al., 2004).

Unsaturated flow in dual-porosity granular media is expected to differ largely from that in single porosity media. For fine-grained single porosity media such as typical agricultural soils and non-fractured porous rocks (e.g., sandstone) unsaturated flow is

expected to be dominated by capillary forces with relative smooth variations in velocity from point to point. In single porosity media with large pores (e.g., glass beads, quartz gravel) flow will be largely restricted to the surface of the grains because of the lack of intra-granular porosity and permeability (e.g., Tokunaga et al., 2003; Reinson et al., 2005).

The basic mechanism of water flow in dual-porosity granular media can be deduced from existing concepts of unsaturated flow. When water enters into a dry dual-porosity granular medium, the smallest pores, thus intra-granular pores, create the strongest capillary forces (e.g., Wang and Narasimhan, 1985; Gerke and van Genuchten, 1993). Therefore, provided that the net infiltration rate is lower than the saturated hydraulic conductivity of the matrix, water will preferentially occupy available intra-granular pores and flow through the matrices of interconnected fragments. Large inter-granular pores remain mostly air-filled and create barriers to capillary driven flow. When the saturation of the matrix is low, the matrix flow serves as the main flow element. Furthermore, transient flow is mostly dominated by capillary forces, but substantially influenced by gravity (e.g., Milczarek et al., 2008).

Unsaturated hydraulic conductivity of a single matrix element (in our case a porous stone fragment) largely depends on its saturation, shape and internal pore geometry (described in section 2.1.2). At larger scale, the number and the cross sectional area of water-filled contacts between fragments determine matrix flow through a network of interconnected fragments (Conca and Wright, 1992; Carminati et al., 2007; Carminati et al., 2008). As the cross-sectional area of the water-filled zone that connects two matrices at a contact between two grains increases, the conductivity of the contact is expected to

increase. Also, increasing the number of such contacts is likely to also increase the system-scale hydraulic conductivity.

As the saturation of the matrix increases, water films are expected to develop on the fragment surfaces, leading to free surface flow. The transition between the matrix-dominated flow and free surface (film) dominated flow is abrupt (e.g., Tokunaga and Wan, 1997). The magnitude of capillary forces on water in free-surface films largely decreases because water is not constrained into narrow channels. As a result, gravity becomes the dominant force that controls film flow. Water on free surfaces (water films) can flow across contacts between matrix blocks (i.e., individual fragments) through pendular rings, as well as drip under gravity.

Thickness of the surface water films increases as the saturation increases, and as a result, hydraulic conductivity and fluid flow velocity increase exponentially (e.g., Conca and Wright, 1992; Tokunaga and Wan, 1997; Tokunaga et al., 2000; Reinson et al., 2005). At steady state, the mean velocity (U) and the flow rate (Q) of a free surface film is proportional to the square and the cube of the film thickness (h), respectively. U and Q can be given by,

$$U = \left(\frac{\rho g}{3\mu}\right)^{1/3} \left(\frac{Q}{w \sin\alpha}\right)^{2/3} \qquad \text{Eq. (2.13)}$$

$$Q = \left(\frac{\rho g h^3}{3\mu}\right) \sin(\alpha) w \qquad \text{Eq. (2.14)}$$

where ρ is the density of the fluid, g is the gravitational acceleration, μ is the dynamic viscosity of the fluid, w is the wetted width of the film against the solid surface, and α is the surface dip (Dragila and Weisbrod, 2003). As a result, a very small increase in saturation can lead to a substantial increase in hydraulic conductivity of the system.

It has been observed that the natural flow mode (i.e., film, rivulet or capillary droplet) in a wide-aperture fracture is influenced by atmospheric pressure changes (Dragila and Weisbrod, 2003). Also, Glass et al. (2002) shows that the hydraulic conductivity in a fracture network is affected by changes in the ambient humidity. Therefore, we can expect that the spatial structure and the hydraulic properties of water films in dual-porosity granular media are sensitive to changes in the ambient environment.

2.4 Unsaturated Flow in Field-scale Dual-porosity Granular Systems

It is expected that most dual-porosity granular systems are man-made (i.e., made up of crushed rocks), with natural gravel deposits being the exception. Heap leach piles, backfills, rock drains, engineered capillary barriers and mine tailings are common examples of man-made dual-porosity granular systems. Field-scale flow processes determine the performance of such systems. Also, environmental protection (e.g., solute transport, groundwater contamination) associated with mine tailings and unsaturated gravel deposits highly depends on unsaturated flow processes in these media. While the number of field-scale investigations of unsaturated flow in heap leach piles, mine wastes and natural gravel deposits is small, they do provide important information to guide this research.

A “heap leach pile” is an important example of dual-porosity granular media. It is a large stack of crushed ore constructed on an impermeable surface in order to extract precious metals using a leaching solution. A leach pile can be several hundreds of meters long and wide, and about 100 m tall. Ore stacked in a heap leach pile is commonly crushed to a nominal size in the range of 10-100 mm (Kappes, 2002); however, a

substantial amount of fines may be generated during crushing, handling and construction. A leaching solution is applied from the top of the leach pile mostly using distributed point sources or sprinklers. The solution application rate depends on the characteristics of the ore and the target metal. For instance, it varies between 7 and 20 liter/hour/m^2 for crushed-ore type heaps in Nevada gold mining operations (Kappes, 2002). The leaching solution mobilizes target metals within the ore fragments, allowing them to migrate downwards to the bottom of the pile, where the pregnant solution is collected for processing to extract the metals.

It has been observed that fluid flow in heap leach piles is not spatially uniform (e.g., Nichol et al., 2005; Wu et al., 2007; Webb et al., 2008). One of the potential causes for a non-uniform distribution of flow is the presence of spatially non-uniform hydrological properties (e.g., porosity, permeability). Sources of this non-uniformity include material heterogeneity, segregation of particles, layering, differential compaction, and moisture content. The development of preferential flow paths through leach piles has been attributed to the solution application rate and the pore geometry (Wu et al., 2007). Under low fluid supply rates, flow is constrained to fine-grained regions (capillary dominated flow), with flow through the coarse-grained regions becoming dominant at high supply rates (gravity dominated flow). Interaction between capillarity-controlled and non-capillarity-controlled pathways creates transient infiltration in heap leach piles (Nichol et al., 2005). Therefore, point measurements (e.g., tracer concentrations) along a vertical profile provide poor indications of mass outflow from the bottom of the pile below the measuring points. Outflow from selected sections at the bottom of a leach pile can substantially vary over time (periods of hours to days). Nichol et al. (2005) and Webb et

al. (2008) mention that the abrupt changes of flow rates at different sections at the bottom of a pile do not necessarily indicate spatial changes in preferential flow paths. However, flow mechanisms that create outflow changes are not well understood.

Piles of mine tailings contain particles and rock fragments that range from fine (<1 mm) to boulder (> 100 mm) in size (Azam et al., 2007). Unlike in heap leach piles, weathering of rocks over time substantially alters the hydrological properties of mine tailings. Similar to heap leach piles, the spatial distribution of flow paths in mine wastes is also non-uniform. Eriksson et al. (1997) reports that approximately 55-70% of total fluid flow in mine waste can occur along preferential pathways. Furthermore, large temporal variations of outflow from different sections at the bottom of waste rock piles have been observed.

Natural gravel deposits fall into the category of dual-porosity granular media because they contain small intra-granular pores and large inter-granular pores. In water saturated gravel deposits, large inter-granular pores provide highly conductive flow paths and the importance of intra-granular pores as flow paths is very low. However interaction between intra-granular and inter-granular flow domains becomes important in partially saturated gravel deposits. Mali et al. (2007) reports an investigation on fluid flow and solute transport in a partially saturated gravel formation. The authors monitored the unsaturated flow in a coarse-gravel filled lysimeter (2 m wide, 2 m long and 5 m deep) using non-reactive tracers and natural isotopes. They observed that the distribution of tracer concentrations, hence the distribution of the fluid flow, is not uniform over the horizontal flow domain. Furthermore, point measurements of tracer concentrations

substantially varied along a vertical transect, which suggests changes in the temporal structure of flow paths along the vertical profile.

2.5 Gaps in Current Understanding on Unsaturated Flow in Dual-porosity Granular Media

Unsaturated flow within intra-granular fragments is expected to be consistent with existing conceptual models originally developed for flow in unimodal soils. The transfer of fluid across inter-granular contacts is fairly well understood (e.g., Carminati et al., 2008), as is the development of free surface flow on a porous matrix (e.g., Tokunaga and Wan, 1997). However, interaction between capillarity dominated and non-capillarity dominated flow domains, as well as spatial and temporal flow structure in partially saturated dual-porosity granular media has not been well studied. To characterize spatial structure of fluid flow in partially saturated dual-porosity granular media, future studies should explore:

(a) Spatial structure of pendular rings at contacts between individual fragments

Assuming that pendular rings at contact points between porous fragments facilitate both matrix and film flows, then understanding the processes that form the pendular rings and how they interact with the flow field is a necessary step to understand flow in dual porosity granular media. Influence of capillary and gravitational force on liquid exists in pendular rings should be explored.

(b) Influence of physical and hydrological properties of the porous medium on the flow structure

Properties such as surface roughness, fragment size distribution, intra-granular porosity, inter-granular porosity, and hydraulic conductivity of the matrix are expected to influence the flow structure. These properties will influence the magnitude of flow elements (matrix and film flow), as well as the hydraulic properties of the entire flow system.

(c) Influence of the ambient environment on the flow structure

Environmental factors such as temperature, humidity and atmospheric pressure may affect the development of flow structure by potentially changing physical properties of the fluid, vapor pressure and evaporation. For instance, ambient temperatures where heap leaching is operated vary over a large range from sub-zero (e.g., in Alaska) up to ~50 ^{o}C (e.g., in Hassai, Sudan; Kappes, 2002). Also, the mean daily temperature of a locality can vary substantially during the active lifetime of a heap leach pile (e.g., from sub-zero to ~38 ^{o}C in central Nevada). Increasing the temperature of water from 1 to 30 ^{o}C decreases its dynamic viscosity from 0.0017 to 0.0008 Ns/m^2 (~53%). Such a large change in the dynamic viscosity of the fluid may influence the flow structure. Because water films are more subject to evaporation than capillary water, changes in the relative humidity may affect the flow structure in a heap leach pile by locally altering film thickness.

(d) Influence of the physical and chemical properties of the liquid on the flow structure

Magnitudes of capillary, gravitational and viscous forces that operate on a liquid are proportional to interfacial tension, density and dynamic viscosity of the liquid

respectively. Therefore, changes in one or more of these properties can change the flow structure in dual-porosity granular media. For instance, dissolution of minerals in water substantially increases the density, thus increase the magnitude of gravitational force.

(e) How the inflow boundary influences the flow structure

Assuming that film flow is important and tends to be spatially non-uniform, then the initiation of film flow will also be important in determining flow structure. Thus, the manner in which water is applied to the media (e.g., point source vs. distributed) may have a substantial impact.

It has been observed that the spatial structure of flow paths, thus the flow fields change over time. However, the temporal variation of spatial flow structure is poorly understood, and hence cannot be accurately predicted. In order to characterize the temporal variability of spatial flow structure in unsaturated dual-porosity granular media, future studies should investigate:

(a) Magnitude of the temporal variability of spatial flow structure

The temporal variability of spatial flow structure is significant only if it is large enough to affect the flow processes in a given system. Therefore, such changes (spontaneous or in response to perturbations on the flow system) should be quantified in order to determine their significance.

(b) Patterns of temporal changes in spatial flow structure

It is unknown whether the temporal changes occur randomly or they follow a pattern. Spontaneous changes should be closely monitored for long periods to understand their patterns. Temporal changes that occur due to external perturbations should be studied

under controlled conditions. Such investigations will enable us to predict, as well as control, the temporal changes of spatial flow structure in a given flow system.

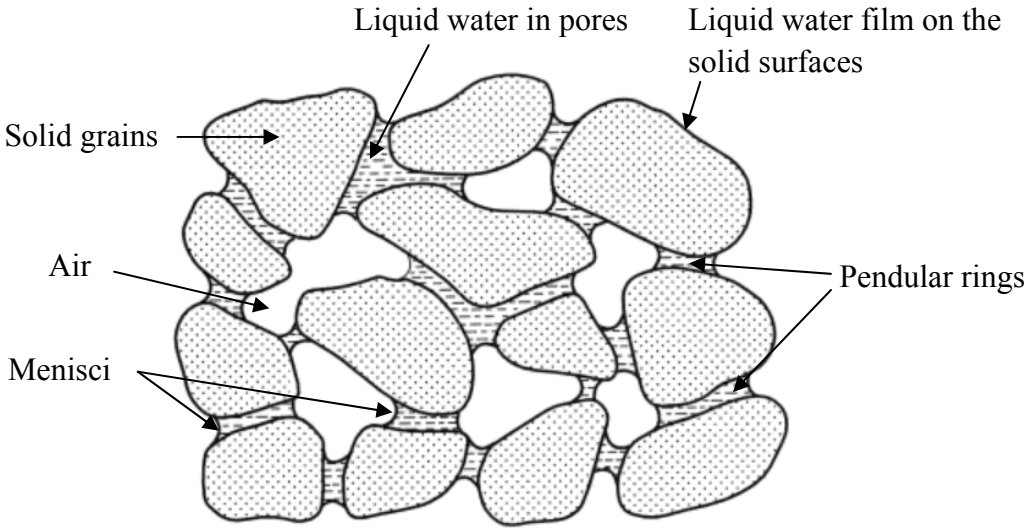

Figure 2.1 Schematic illustration of solid, water and air phases in an unsaturated coarse-textured soil (modified from Hillel, 1998)

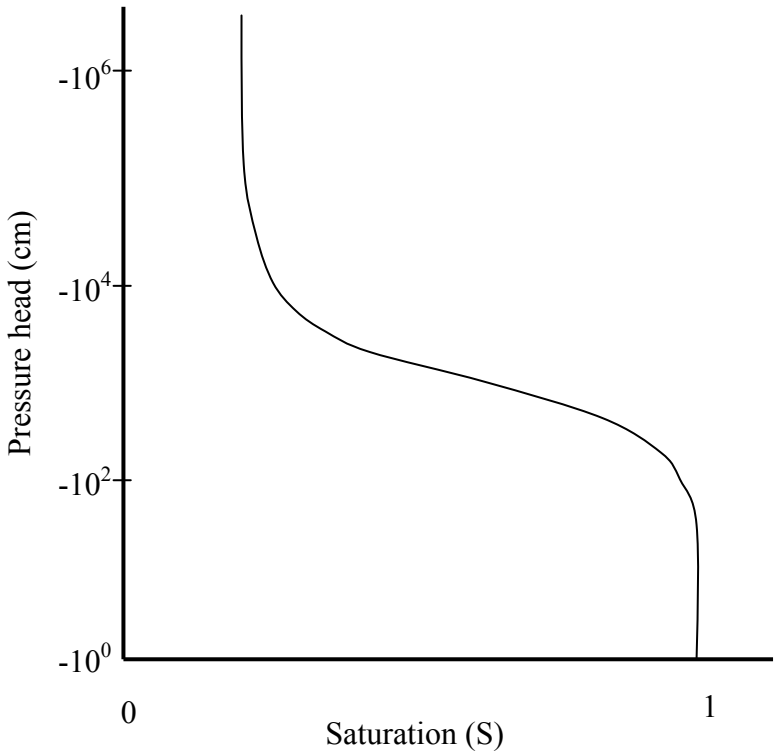

Figure 2.2 A typical curve illustrating the relationship between the saturation and fluid pressure.

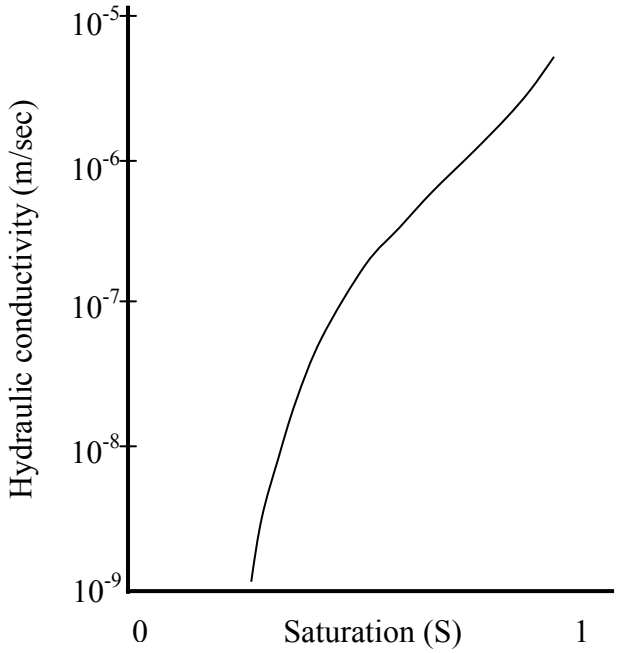

Figure 2.3 A typical curve showing the relationship between saturation and hydraulic conductivity.

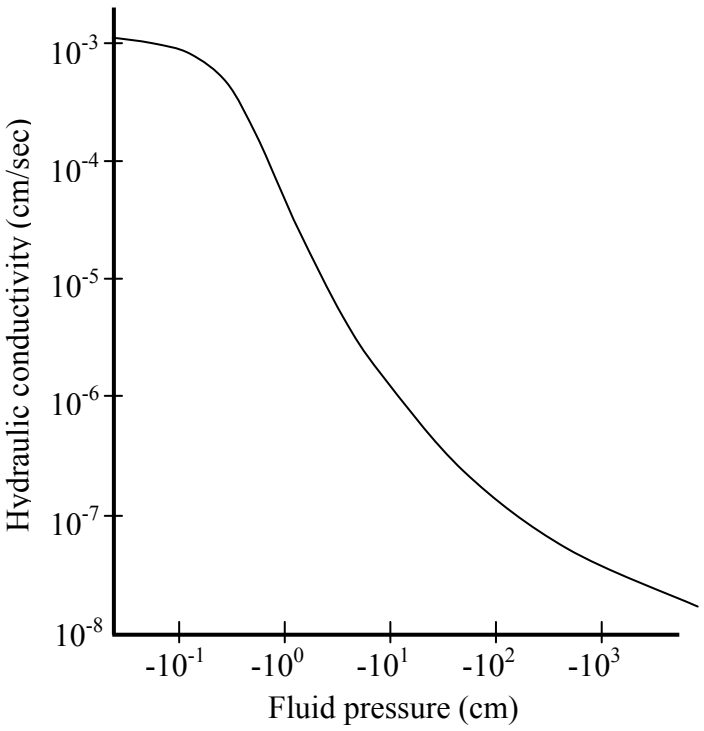

Figure 2.4 A typical graph of hydraulic conductivity vs. suction.

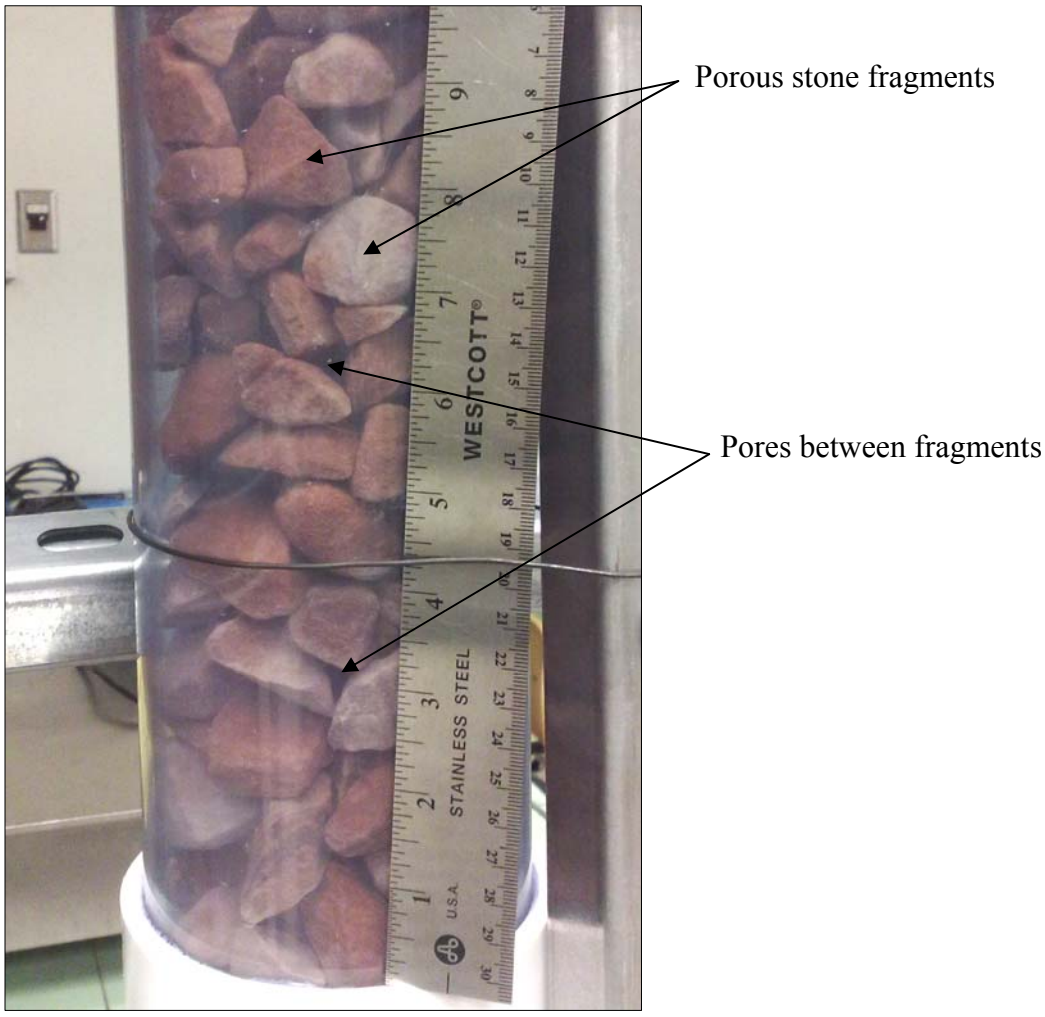

Figure 2.5 Porous stone fragments packed in a transparent test column to form a dual-porosity granular medium

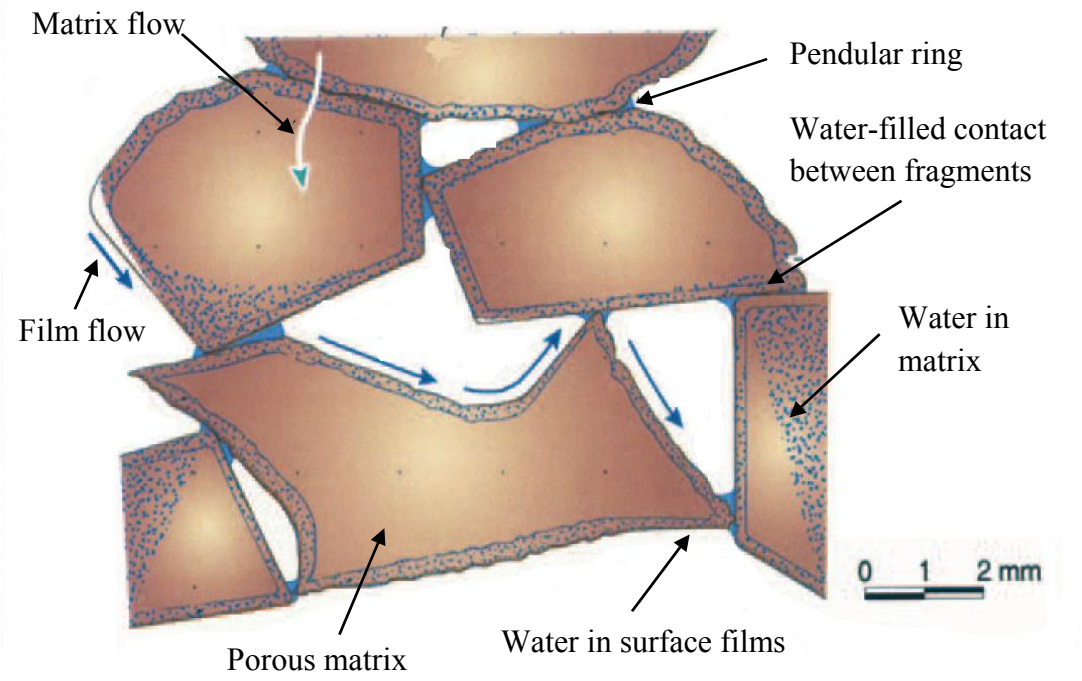

Figure 2.6 Schematic illustration of water flow elements in dual-porosity granular media (modified from Hu et al., 2004)

CHAPTER 3

EXPERIMENTAL METHODOLOGY

This chapter describes the conceptual design, physical set-up, instrumentation and operation of a meter-scale experiment for characterization of unsaturated flow structure in dual-porosity granular media. The first section of this chapter (3.1) introduces the conceptual design of the experiment. Physical properties of the geological medium (crushed porous rock) used in the experiment, as well as the preparation of those rocks are presented in section 3.2. Design and construction of the experimental apparatus are discussed in section 3.3, while instrumentation, data acquisition, and experimental control are presented in section 3.4. A description of the experimental procedure is given in section 3.5. The chapter concludes with a description of data processing and analysis in section 3.6.

3.1 Conceptual Design

The basic concept was to supply a steady influx of water to the top of a test column, and then measure the spatial and temporal structure of outflow from the bottom of the column (figure 3.1). The test column was filled with crushed porous sandstone to form a dual-porosity granular medium. The bottom of the column was divided into nine equal-area sections, thus allowing outflow from each section to be measured separately. Macroscopic changes in flow structure were identified by monitoring discharge from each section of the column as a function of time. Equal and constant outflows from all sections of the bottom would be evidence of a temporally-stable, uniform flow field.

Conversely, unequal outflow is taken as evidence of a non-uniform flow field and temporally-variant flows are evidence of an unstable flow field.

Based on preliminary experiments conducted in a 20 cm diameter and 19 cm tall test column filled with crushed sandstone, the following parameters were expected to impact the flow structure; inflow boundary (fluid supply rate, single-point source, multiple-point source, and horizontal location(s) of the inflow), physical properties of the fluid (viscosity and interfacial tension), temperature (ambient and inside the column), humidity (ambient and inside the column), and barometric pressure. Given their expected importance, these parameters were either monitored or controlled during each experiment.

3.2 Dual-porosity Granular Media

In order to meet the experimental objectives, the experimental medium must consist of hydrophilic, coarse rock fragments that are porous and permeable. It is also desirable that the media be chemically inert, durable (uniform over the course of the experiment series), and readily available. In such a medium, both matrix flow and the development of film flow on fragment surfaces can be expected. Based on these desired characteristics, we selected a silica-cemented sandstone (Aztec sandstone; Hewett, 1931) to produce the dual-porosity granular medium. The sandstone was obtained from a quarry located at Goodsprings, Nevada (N 35.91, W 115.46), about 35 km southwest of Las Vegas, and operated by Rainbow Quarries. Rocks were crushed and screened through ¾" (~2 cm) mesh at the quarry site. We also obtained several large samples (~15 x10 x 8 cm) from

the same formation for measurement of the saturated hydraulic conductivity and the preparation of thin sections for microscopic analysis of pore/particle sizes.

The selected rock was insoluble in water, chemically inert and physically durable in wet conditions. It did not react with hydrochloric acid, confirming the absence of calcite cement. Petrographic analysis of an individual rock fragment (figure 3.2) suggested that the intra-granular pores had an average diameter of ~20 μm. Porosity of the rock matrix (intra-granular porosity) was measured at ~21%, with a saturated hydraulic conductivity of ~0.003 cm/hour (see appendix A and B for calculations). Pores in the rock matrix were small enough to create strong capillary forces and sufficiently permeable to facilitate measurable water flow through the matrix. Crushed rock fragments were angular in shape and approximately 1-3 cm in size (figure 3.3a). This size is similar in size to crushed gold ore in heap leach piles (Kappes, 2002), mine tailings (Azam et al., 2007), and gravel used in capillary barriers (Conca et al., 1998). As seen in figure 3.3b, the inter-granular pore size varied approximately from 1 to 15 mm, which is much larger than the intra-granular pores (~20 μm). This difference in pore size was designed to create vastly different flow regimes between the two pore domains (capillary dominated and gravity dominated).

Before the experiment, the crushed rock fragments were processed to remove salts and fine particles. First, the rock fragments were thoroughly rinsed with local tap water to remove fine particles generated during crushing and transport, then they were submerged in deionized water (~30μS/cm) for 22 days to leach soluble salts; the water was changed every four days. Electrical conductivity (EC) of the wash water was measured daily; leaching was terminated after the EC equilibrated. The fragments were then oven-dried for 24 hours at ~105 ˚C and stored in plastic containers until packed in the test column.

The above procedure was repeated for several large pieces of the same rock (~15 x 10 x 8 cm) to prepare them for testing saturated hydraulic conductivity, as well as for analyzing pore/particle size.

3.3 Experimental Apparatus

Design of the experiment was based on a set of preliminary tests performed in a 20 cm diameter and 19 cm tall test column filled with the crushed sandstone described above. In those experiments we observed narrowly focused flow paths, spatial and temporal variability in the flow fields, and an apparent sensitivity to ambient humidity and temperature changes.

Based on the preliminary tests, it was concluded that the 20 cm diameter column was sufficiently larger than the particle size to prevent the side boundaries from interfering substantially with flow. It was also concluded that a longer column would be desirable to allow full development of the flow fields. Therefore, we decided to upscale the experiment to the maximum size feasible in our laboratory, emphasizing increased column height over diameter.

3.3.1 Test Column and Support Stand

The test column was fabricated from a 102 cm length of ~32 cm (12 inch) diameter schedule 40 PVC pipe that had a 30 cm inside diameter (Figure 3.3, 3.4a, and 3.4b). This was the biggest size that could be reasonably handled in the available laboratory space. The upscaled column was considerably larger than the preliminary column, where the desired behavior of spatial and temporal variability of flow was observed. Thus, we expected that the larger test column would be of sufficient size to observe macroscopic

flow fields larger than any local flow fields developed due to the specific arrangement of the crushed rock fragments.

The side boundaries of the column were impermeable. The top of the column was left open to the atmosphere to accommodate evaporation, as well as heat and air transfer between the column and the atmosphere. The bottom boundary of the column was fabricated from a 4 cm thick acrylic plate (figure 3.4, 3.5c, 3.6a and 3.6b). Nine equal-area basins were constructed in the acrylic plate, so that the outflow through each basin could be measured separately (see appendix C for construction details). The nine-basin design (figure 3.6a and 3.6b) was adequate to characterize the lateral distribution of flow fields, as well as convenient for construction. A thin hydrophobic surface coating on the bottom plate prevented pooling of water in basins. Vertical drains were smoothly mated to the bottom of each basin for efficient drainage. The acrylic plate was fastened to the test column with eight brass screws (~5 cm long) and 100% silicone rubber sealant (DAP®).

State variables (humidity, temperature, and atmospheric tension) were measured at depths of 10, 50 and 90 cm within the column. Measurements were made through two sets of three ports (1.9 cm diameter) drilled through the column wall along two vertical transects (figure 3.5b). The two vertical transects were separated from one another by ~90^{o}. After installing the sensors, the ports were sealed with silicone rubber sealant and rubber gasket sheet. The only other port in the column was a 5.1 cm diameter hole located slightly above the bottom (figure 3.5c) that was used to circulate air for drying the column between experiments. The three horizontal, curved brass rods (~2 mm diameter) seen in the figure form a grate that prevents rock fragments from falling out through the

drying port. This hole was kept closed during the experiment using a high density foam plug wrapped in a plastic sheet (figure 3.7, left bottom corner of the test column). During experiments, the test column was surrounded with an approximately 7.6 cm thick, vinyl backed fiberglass thermal insulation blanket (R=20, Frost King®) to minimize heat transfer through the column wall (figure 3.7).

The experiment rested on top of an 80 cm x 80 cm wide and 60 cm tall pedestal (figure 3.4 and 3.5a) that was constructed from cement and rebar filled concrete blocks. A 200 kg capacity (± 0.02 kg accuracy) electronic scale (Ohaus® Champ CD33) was placed on top of the pedestal to measure rock mass and changes in water content within the column. An approximately 35 cm tall fabricated steel stand was placed between the scale and the bottom of the column. The purpose of the stand was to enhance gravity drainage from the column to the vessels used to collect outflow from the column (figure 3.5d).

The experiment was surrounded by a ~250 cm tall steel frame that was fabricated using Unistrut® steel channel beams. The frame rested on the floor, and was bolted into the concrete pedestal, but did not touch the column or the scale. The primary purpose of the frame was for safety against collapse or tipping of the test column; however, it also provided attachment points for inflow plumbing, outflow plumbing, and ambient sensors.

3.3.2 Inflow to the Column

The fluid used in the experiment was ~60 µS/cm water sourced from a reverse osmosis (RO) system. We chose RO water because it was chemically less aggressive than distilled water, as well as cheaper, considering the amounts of water used (~11.5 liters/day). Before use, the RO water was allowed to equilibrate to ambient temperature

and pressure for a minimum of 24 hours. In the first experiment we noticed air bubbles forming in the water line on the suction side of the supply pump. This problem was resolved for the remaining experiments by degassing the RO water at ~25 kPa vacuum for ~5 hours. Liquid chlorine bleach (Clorox®) was added to the water (~0.6 ml/l) to inhibit biological growth in the test column.

Water was supplied to the top of the test column at a constant rate and temperature. A nominal inflow rate was arbitrarily selected at 8.0 ml/min. This rate was consistent with that applied to leach pads in Nevada gold mining operations (~18 ml/min/m^2; Kappes, 2002), and was sufficient to create flow in the inter-granular pore space, but was far less than the saturated hydraulic conductivity of the test column (~49 m/S, see appendix B for calculation). Water was supplied to the column by a computer controlled peristaltic pump (figure 3.8a, 3.8b and 3.8c). The source container (~20 liter bucket) was placed on a 32 kg capacity (± 0.1 g accuracy) electronic scale. The container was sealed to minimize evaporative loss, and opened once a day so that it could be refilled. The change in water mass over time was used to monitor the inflow rate to the column. Speed of the supply pump was software controlled to maintain constant flow (discussed in section 3.6.3).

Temperature of the water entering the column was maintained to ± 1 ^{o}C to minimize viscosity variations within the course of each trial. The inflow water was passed through a plate-type, liquid-to-liquid heat exchanger mounted on the steel framework close to the inlet (figure 3.8d). The other side of the heat exchanger was connected to a circulating water bath (Haake® K10) set to a constant temperature (figure 3.8a). The heat exchanger, inflow plumbing from the heat exchanger to the test column, and the plumbing connecting the heat exchanger to the water bath were all insulated to assist in maintaining

the inflow at a constant temperature. A 3-way valve was installed immediately upstream from the test column so that we could divert flow as needed (figure 3.8e). A single-point inlet (figure 3.8f) was used in all experimental trials reported here. The inlet was located above the center of the test column throughout the duration of the first three trials. At the beginning of the fourth trial the inlet was located above the center and subsequently it was relocated twice; first ~4 cm and next ~2.5 cm away from the center.

3.3.3 Outflow from the Column

Outflow from the nine sections at the bottom of the test column was collected into nine separate vessels for measurement. Height of the water column in each vessel was monitored in terms of hydrostatic pressure, and then was converted to the actual volume of water in the vessel.

Outflow from each of the nine outflow basins was routed to an individual collection vessel that was fabricated from 2" diameter schedule 40 PVC (figure 3.5d). Each collection vessel was 70 cm tall and had a 5.1 cm inside diameter. The bottom of each collection vessel was sealed with a PVC end cap, and was connected to a pressure transducer (see section 3.4.1) with a 3.2 mm inner diameter hard flexible tubing (Cole-Parmer® RZ 30526-16). The cap of each collection vessel was vented with a ~2 mm diameter hole to prevent pressure build-up during collection of water. Each collection vessel was emptied through a ~65 cm long, 1.3 cm inner diameter schedule 40 PVC pipe passing through the top cap of each vessel. The suction pipes of the nine collection vessels were individually connected to four computer-controlled peristaltic pumps through 0.95 cm inner diameter flexible vinyl tubing (figure 3.5d and 3.10). Evacuation of the collection vessels is described in section 3.4.3.3. Two extra vessels were installed

to assess background noise during the experiments. These vessels contained fixed amounts of water (~ 85% of capacity in a one and 15% in the other). All eleven collection vessels were attached to the steel framework alongside the concrete pedestal. They were shock mounted with 1.5 mm thick rubber gasket to minimize vibration.

3.4 Sensors, Experimental Control, and Data Acquisition

We created an array of sensors to monitor mass change in the column, inflow, outflows, temperature, humidity, atmospheric pressure and atmospheric tension. All of the sensors were monitored with an automated data acquisition system developed for this experiment. The data acquisition system also controlled the water pumps used in the experiment.

3.4.1 Sensor Array

State variables measured during the experiment were: inflow rate, outflow rate, temperature, humidity, atmospheric tension, barometric pressure and water content in the column (refer to figure 3.10 for sensor locations). Temperature was measured at nine locations using Omega® Type-T thermocouples. The tip of each thermocouple was coated with a thin layer of silicone rubber sealant (DAP®) to prevent corrosion. Three thermocouples were co-located with humidity sensors inside the column. Three others were placed outside the column at approximately 15, 130 and 225 cm above the floor. The elevations of the latter two were approximately 10 cm above the bottom of the column and level to the top of the column, respectively. To reduce the effects of air currents, the tips of these three external thermocouples were enclosed in 3.2 mm inner diameter and approximately 4 cm long flexible vinyl tubing. Two thermocouples were

co-located with the barometric sensors (described below). The last thermocouple was located at the water inlet to measure the temperature of the inflow water. All thermocouples were calibrated to 0 ˚C (see appendix D for calibration details).

Relative humidity (RH) was measured at seven locations using Humirel® HTM2500 sensors. The RH sensors were not individually calibrated, and humidity was calculated per manufacturer's specifications. Prior to this experiment I tested several brands and models of humidity sensors that were small enough to mount in the test column without perturbing the system. None of the sensors that we tested functioned well in the vicinity of 100% RH. The Humirel® HTM2500 sensor was selected because it responded to relative humidity changes over 90% better than the other sensors that were tested. Three RH sensors were located in the column at depths of 10, 50 and 90 cm from the top (figure 3.4b). Three ports of 1.9 cm diameter were drilled into the column, and then a humidity sensor and a thermocouple were inserted partway into each port. Neither humidity sensors nor thermocouples protruded into the column. Ports and sensor mountings were sealed with 1.5 mm thick rubber gasket, heavy duty construction adhesive (PL 400 ®) and silicone rubber sealant. Three other RH sensors were placed to measure the vertical humidity gradient above the column (figure 3.7d). They were mounted approximately 13 cm away from the center of the column, starting at 6 cm above the column, then at 13.5 cm intervals. Another RH sensor was mounted outside the column, approximately 190 cm above the floor to measure representative relative humidity in the room.

Atmospheric tensiometers were placed in the column at 10, 50 and 90 cm depths (at the same depths where the humidity sensors were located; figure 3.4b). To fabricate each sensor, an approximately 4 mm diameter hole was drilled longitudinally through a 5 cm

length of 1.9 cm diameter transparent acrylic rod (figure 3.11). A 3 mm diameter and 1.5 mm thick stainless steel frit (BECKMAN® part number 243067) was cemented into one end of the rod. The other end of the rod was connected to a 15 psi pressure transducer (Honeywell® ASCX15DN) through 3.2 mm inner diameter flexible tubing. The tensiometers were filled with deaired-distilled water. When relative humidity is below 100%, water evaporates through the frit, increasing tension on the pressure transducer. At saturation humidity, condensation of water vapor on the frit reduces tension. This method was not intended to provide an absolute measure of humidity, but rather to indicate changes in regime between evaporation and condensation. The three 15 psi pressure transducers were not calibrated as we were only interested in whether output voltage was increasing or decreasing. However, this approach to monitor the atmospheric tension inside the column was not successful, as all three tensiometers failed (i.e., air entered into the water column of the tensiometers) within ~4 hours from the beginning of each experiment.

Barometric pressure was measured with two Apogee® SB-100 sensors. Each sensor was placed in a 15 cm long piece of 5.1 cm inner diameter schedule 40 PVC pipe. One end of each pipe was capped with a PVC cap and the bottom end was covered with a layer of synthetic fabric intended to isolate the pressure sensors from air currents. Factory calibration was used to calculate barometric pressure. One sensor was leveled with the top of the column (figure 3.4a top right corner) and the other one was placed directly beneath the first sensor close to the floor at the same elevation as the pressure transducers used to measure outflow. Barometric data from McCarran International Airport were collected daily to support data from the barometric sensors. The airport measurement was

located about 3 km southwest of our laboratory and approximately 30 m above the ground level of the laboratory.

Water content in the test column was tracked by measuring the weight of the entire column (described in section 3.3.1). The electronic scale used to weigh the column had a resolution of 0.1 kg, which corresponded to approximately 100 ml of water.

As described in section 3.3.3, outflow from the nine sections at the bottom of the column was measured by tracking water heights in the nine active collection vessels. A 3.2 mm inner diameter hard flexible tubing (Cole-Parmer® RZ 30526-16) was routed from the bottom of each vessel to a 1 psi pressure transducer (HONEYWELL® part number 24PCAFA6D; figure 3.5d). Each pressure transducer was mounted in a ~2.5 mm (1 inch) diameter schedule 40 PVC end cap and encapsulated in epoxy resin (EasyCast®), then rigidly mounted to a steel framework (figure 3.9). Each collection vessel had a constant inside diameter over the collection length (not counting end caps). As a result, a linear relationship existed between volume of fluid added and fluid pressure at the measurement point within the vessel. Each vessel and the connected pressure transducer were calibrated individually to determine the change of volume of water per unit change of voltage (see appendix D for calibration details). Therefore, volume of water collected in each vessel during any given period could be calculated using output voltages from the pressure transducers.

3.4.2 Experimental Control

The primary experimental control functions were associated with inflow and outflow. A computer-controlled peristaltic pump (Masterflex® 7520-35) supplied water to the column from a ~20 liter container that sat on a 32 kg capacity (± 0.1 g accuracy)

electronic scale (Ohaus® Explorer Pro EP32001C; figure 3.8b and 3.8c). The inflow rate was determined by monitoring changes in the weight of the source water container as a function of time. The computer calculated the flow rate in real time, and then adjusted the speed of the supply pump as required to maintain a steady flow (see section 3.4.3.3 for flow rate calculation details).

Storage in the collection vessels was limited to approximately 1200 ml each, thus requiring that they be periodically emptied. For this purpose, the evacuation pipe from each of the nine active collection vessels was individually connected to four multi-channel, computer-controlled pumps (Masterflex® 7520-25 (2 pumps), 7549-50 and 900-654). These pumps were turned on when water in any of the nine vessels reached a predetermined maximum level, as determined by monitoring output voltage of the relevant pressure transducers (described in section 3.4.1). In 90 seconds, the evacuation pumps would draw water levels in all of the collection vessels down to the bottom of their suction pipes. The suction pipes were positioned such that water levels always remained within the central portion of the vessels, where the cross-sectional area was constant.

3.4.3 Data Acquisition and Automated Control Program

The automated data acquisition and control system is composed of a custom-built computer program and hardware. Assembly of hardware, wiring of sensors and hardware for communication and power supply, as well as functions of the computer program (i.e., software) are described below.

3.4.3.1 Hardware

All the sensors and scales were monitored using a PC-based multi-channel data acquisition system. The PC was a Dell™ Dimension™ XPS Gen 4 **(**Intel® Pentium® 4, 3.4 GHz processor and 2GB RAM) running the MS Windows® XP operating system.

Data Acquisition (DAQ) hardware manufactured by National Instruments™ was used to interface with the scales, pumps, and sensors. A model PCI-232/8 RS-232 interface mounted internal to the computer was used to communicate with the electronic scales. A second internal board (model PCI-6229) connected the computer to an external model SCXI-1000 DAQ system that contained three measurement/control modules (SCXI-1100, SCXI-1102, and SCXI-1124). All of the thermocouples were routed through a model SCXI-1303 terminal block connected to the model SCXI-1102 thermocouple and voltage input module. Output voltage of each thermocouple was converted to temperature in Celsius by referencing to an internal temperature sensor in the SCXI-1102 module. All of the voltage measurements (electronic barometers, humidity sensors, 1 and 15 psi pressure transducers and the output of the AC to 5V DC transformer) were routed into the SCXI-1100 voltage input module through a second model SCXI-1303 terminal block. Current signals used to control the pumps (the supply pump and four evacuation pumps) were generated in the model SCXI-1124 digital to analog converter module and output through a model SCXI-1325 terminal block.

3.4.3.2 Wire Connections and Routing

The barometers, humidity sensors and 15 psi pressure transducers were powered by a 5V DC supply (Acopian™ 5EB250 AC to DC transformer), while the 1 psi pressure transducers were powered by a 12V DC supply (OMEGA™ PSS-12 AC to DC

transformer). The two electronic scales, SCXI-1000 chassis and water pumps were powered with 110V AC supply.

Output signals from the barometers, humidity sensors and 15 psi pressure transducers were in the 0-5 V range and the 1 psi pressure transducers gave an output signal in the millivolt range. The balances communicated in both directions with a digital signal, and the pumps were controlled by 5-20 mA signals. The thermocouples, which did not require a power source, produced signals in the millivolt range. Wires that transmitted digital, millivolt, 5V, 12V and 110V current were routed separately, as well as away from water pumps and transformers to minimize interference from electromagnetic fields (figure 3.13). AWG-22, 4-conductor, 2-pair separately shielded wires were used to transmit power to, as well as signals between pressure transducers and the SCXI-1303 terminal blocks. AWG-22, 5-conductor, shielded wires were used to transmit power to the barometric and humidity sensors, as well as signals between these sensors and SCXI-1303 terminal block. Voltage output from the 5V power supply was recorded along with other data. The 12 V supply was not monitored because the 1 psi pressure transducers that it powers produce a negligible current drain.

3.4.3.3 Software

All data acquisition and control functions were performed using a purpose-built computer program developed with the National Instruments™ LabView 8 software package. The main functions of the computer program were; (a) reading data (signals) from sensors and electronic scales, (b) averaging multiple samples from the thermocouple and voltage input channels (c) writing time and data to a file, (d) controlling the water pumps, and (d) displaying data graphically on the computer screen. The program was

written so that the user could specify the data acquisition interval, number of samples per channel, and inflow rate to the experiment prior to starting the program.

After the program was started, the first operation was to create a tab-delimited text file with a user-defined name for data storage. Next, the sensors and electronic scales were interrogated at a user specified interval (2 minutes for all experiments reported here). Multiple samples were obtained from thermocouples, barometers, humidity sensors and pressure transducers (100 readings from each for all experiments reported here) and then averaged to obtain a single value for storage. The data were collected, processed and then stored in the specified file, along with the current time from the system clock. This process was repeated until each experiment was shut down. All sensor data were stored as raw values; adjustments for sensor calibration were carried out in post-processing.

The inflow pump was controlled by a 4-20 mA direct current signal. Our control program turned on the pump after the first two data acquisition intervals were completed. The initial current sent to the pump was estimated based on the user-defined flow rate and a calibration curve developed specifically for this apparatus (see appendix D for calibration details). Once the program was running, the pump could be turned on and off through software control without disturbing any of the other measurements. The control program began optimizing the inflow rate after seven data acquisition cycles had been completed. Basically, the program calculated a weighted average of the inflow rate for the preceding five intervals, and then adjusted the pump speed accordingly. The weighted inflow rate at the time after the T^{th} iteration (RW_T) was calculated as follows:

$$RW_T = 0.6R_T + 0.2R_{T-1} + 0.1R_{T-2} + 0.05R_{T-3} + 0.05R_{T-4} \qquad \text{Eq (3.1)}$$

where R_{T-i} is the flow rate i intervals before T. Weights for different intervals were arbitrarily selected in such a way that flow rates at more recent intervals made higher contributions to the weighted flow rate.

This optimization function given in equation 3.1 implicitly assumed that pumping water to the experiment was the only change of mass for the source water container. As a result refilling the container would cause equation 3.1 to calculate a negative flow rate and thus attempt to increase the pump speed. To avoid this issue, the automated pump adjustment function of the program was disabled when the source water container was refilled, and turned back on after six measuring intervals (i.e., 12 minutes) had passed. Pump speed was maintained at a constant rate during the time that the adjustment function was deactivated.

Evacuation of the collection vessels was considered during each measurement cycle. When water level in any of the nine active collection vessels reached a pre-defined maximum level, the program turned on the evacuation pumps for a period of 90 seconds. In order to avoid tubing failure, the evacuation pumps were first turned on at low speed (8 mA current), which was then increased gradually to near maximum speed (18 mA current). The maximum water level was identified by comparing the voltage output from each pressure transducer to an external data file that contained the maximum voltage for each individual collection vessel. If the water level in any of the collection vessels remained at or over the maximum level after evacuation (indicating an evacuation pump failure), the program would turn off the inflow pump to prevent flooding. A button in the program allowed the user to turn on the evacuation pumps and empty all collection vessels at any time.

The final program function was to provide a real-time display of data collected from thermocouples, pressure transducers, barometers, humidity sensors, 5V power supply, scales, as well as the average water level of collection vessels, inflow rate and direct current sent to the inflow pump (figure 3.14).

3.5 Experimental Procedure

Approximately 95.35 kg of dry crushed rock fragments were loaded into the column from the bottom to 100 cm height without artificial compaction. The column was loaded in a manner designed to minimize the generation of fine particles due to collisions between the rock fragments themselves, as well as to prevent damage to the acrylic bottom plate. Rock fragments were lowered into the bottom 40 cm of the column using a 0.5 m long piece of 15 cm inside diameter PVC pipe with a remote operated cover on the bottom. Crushed rocks were placed in the PVC pipe, which was then lowered to the bottom of the column, where the cover was slowly opened to release the rock fragments. Rock fragments were rearranged regularly using a steel rod to prevent bridging and the formation of large cavities during the loading process. The upper 60 cm of the column was filled by hand.

Inter-granular porosity, total porosity (due to intra- and inter-granular pores) and bulk density of the medium after it was packed in the test column were approximately 36%, 50% and 1.35 g/cm^3 respectively (see appendix A for calculations).

Running an individual experiment in the packed column followed a fairly simple procedure. The circulating water bath was set to the desired inflow temperature and run overnight to equilibrate. In the following morning, the data acquisition program was

started at about 7:30 am, with water from the inflow pump diverted away from the experiment at the same level of the single-point inlet. The system was run for several minutes in this condition so that the inflow would reach steady state, then the inflow was routed back into the column to start the experiment. Afterwards, the only maintenance required was refilling the source water container at about 5:15 pm daily and emptying the water bucket connected to the evacuation pumps. The experiment was also observed several times per day to make sure that it was running properly.

Four experimental trials were conducted under variable ambient environmental conditions and imposed perturbations. The first experiment was conducted for 10 days with a steady inflow rate. The second experiment was conducted for 40 days, and three inflow interruptions were made its course. The third experiment was started with low-temperature (~19 ^{o}C) inflow, but it was stopped after two days due to an equipment failure. The fourth experiment was run for 40 days and the system was perturbed with inflow interruptions, inflow temperature changes, relocation of the point source, and imposed evaporation changes. Each experiment started from a dry initial condition and water was supplied using a single-point source located at the top of the column at a nominal rate of 8.0 ml/minute. The following parameters were measured at 2 minute intervals during the course of each experiment: the inflow rate, outflow from nine equal-area sections at the bottom of the column, weight of the column, humidity and temperature inside the column (3 locations), inflow temperature, room temperature (5 locations), room humidity (4 locations) and atmospheric pressure (2 locations).

After each run of the experiment, dry warm air was blown through the test column using a desiccant dehumidifier (Munters® MG90) to dry the rock fragments in place. We

tested the effectiveness of this method and found that approximately 99% of water could be removed from 100% saturated rocks using this method.

3.6 Data Processing and Analysis

Processing of raw data retrieved from a tab-delimited file after each experiment included: (a) correction of temperature data for thermocouple offset, (b) conversion of raw voltages from the humidity sensors to relative humidity, (c) conversion of raw voltages from the barometric sensors to atmospheric pressure, (d) removal of inflow rate discontinuities that occurred after refilling the source water container to get mass inflow as a function of time, (e) removal of voltage change discontinuities in the 1 psi pressure transducers that occurred after evacuation of collection vessels, and (f) reduction of noise from the 1 psi pressure transducer voltages and conversion of that data to water mass changes.

The original data files were imported into MS Excel® for manipulation. Temperature measurements from each thermocouple were corrected by subtracting the offset of that thermocouple from the raw value. Voltage data from the humidity sensors were converted to relative humidity (RH) using the following equation (3.2) provided by the manufacturer.

$$RH = \frac{\left(-1.9206 \times 10^{-9}\right)V^3 + \left(1.437 \times 10^{-5}\right)V^2 + (3.421 \times 10^{-3})V - 12.4}{1 + (T-23) \times 2.4 \times 10^{-3}} \qquad \text{Eq. (3.2)}$$

where V is output voltage of the sensor (mV) and T is the atmospheric temperature at the measuring point (^{o}C). This equation compensates the RH for non-linearity of the sensor and temperature variation.

Manufacturer's specifications were used to convert voltage data from the barometric pressure sensors to actual atmospheric pressure. A linear relationship between the atmospheric pressure (P) and voltage output (V) was given by:

$$P = (V \times 0.0218 \text{ kPa/mV}) + C \qquad \text{Eq. (3.3)}$$

In this equation, units of the atmospheric pressure and output voltage are kPa and mV respectively. As per the manufacturer's specifications, the offset (C) should fall between 10.8 and 12.0 kPa. However, to match the atmospheric pressure in the laboratory with that at the McCarran International Airport, we assigned 19.4 and 19.8 kPa as the offsets for the upper and lower barometric pressure sensors, respectively.

Inflow rate to the column was calculated from the mass change of the source water container. Therefore, it showed a negative value for one measuring interval (2 minutes) immediately after refilling the source container. This data point was replaced with an average of the inflow rates immediately preceding and after refilling the source container.

The amount of water collected in each collection vessel during each measuring interval was calculated using the increase of output voltage from the 1 psi pressure transducer connected to it. However, when the amount of water received by each vessel during the time that it was being emptied could not be calculated using the change in output voltage of transducer. Therefore, the average of voltage changes at one interval before and one interval after emptying the vessels was assigned as the voltage change due to water received by each vessel during that period. The cumulative voltage increase of each pressure transducer was then calculated and converted to change in water mass.

Noise in the data collected from the thermocouples, 1 psi pressure transducers and humidity sensors was reduced by replacing each raw value with the 10-minute moving

average (i.e., five measuring intervals) around that time. After that, data at 20 minute intervals were extracted to create a small subset for analysis. The final step in processing was to convert data from the1 psi pressure transducers into flow rate using the calibration curves described in appendix D-2. Following this step, graphical and statistical functions in MS Excel® were then used to analyze processed data.

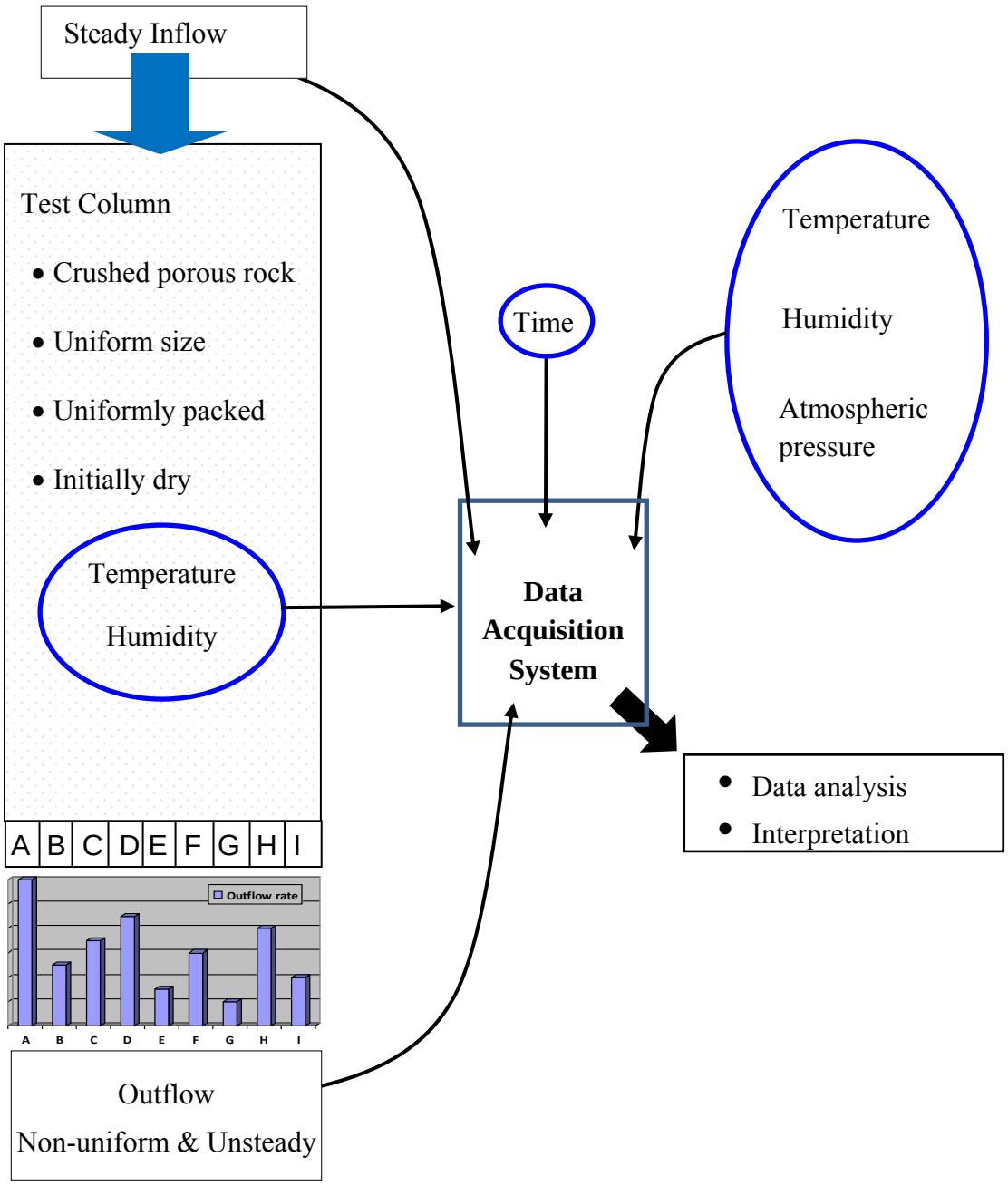

Figure 3.1 Conceptual design of the experiment. Inflow from the top, outflow from different sections at the bottom, temperature, humidity and atmospheric pressure is monitored over time.

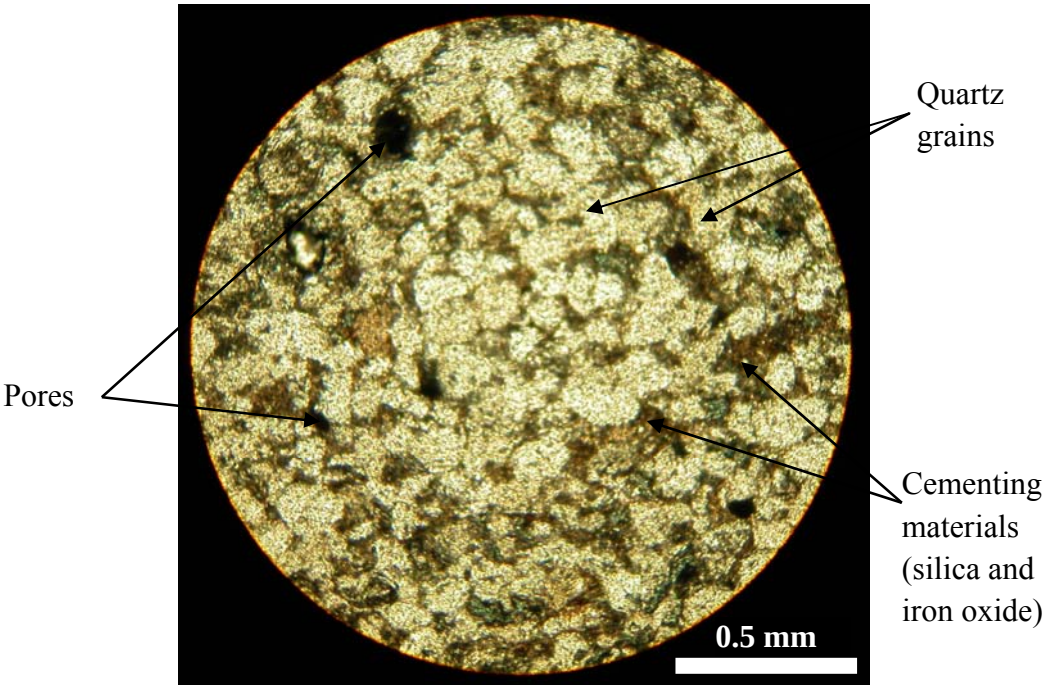

Figure 3.2 Photomicrograph of the sandstone used in the experiment

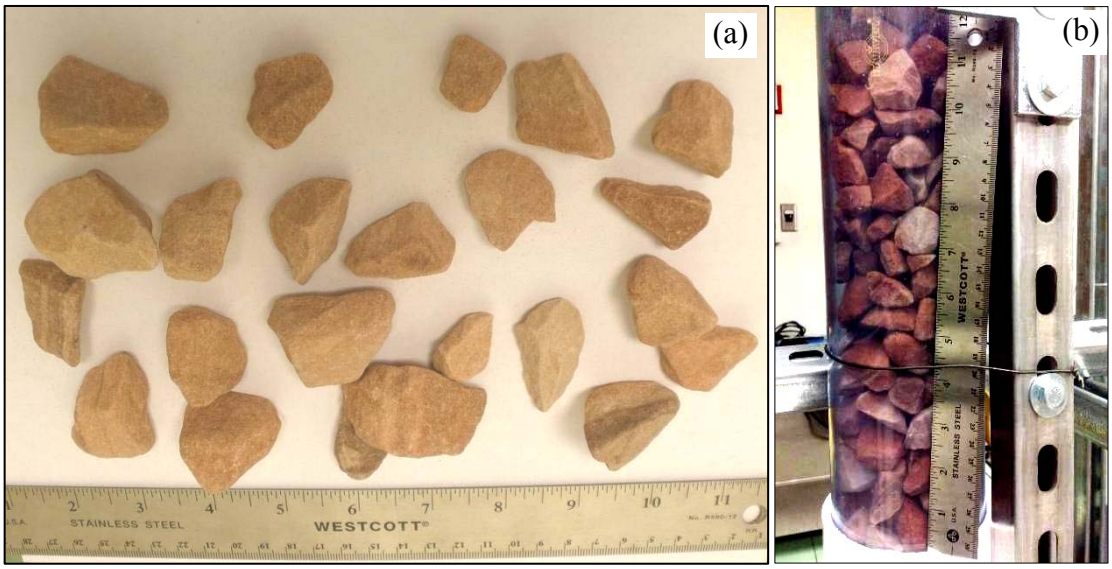

Figure 3.3 Experimental media. (a) Crushed sandstone fragments, (b) fragments packed into a transparent test column to illustrate the difference in size between intra- and inter-granular pores.

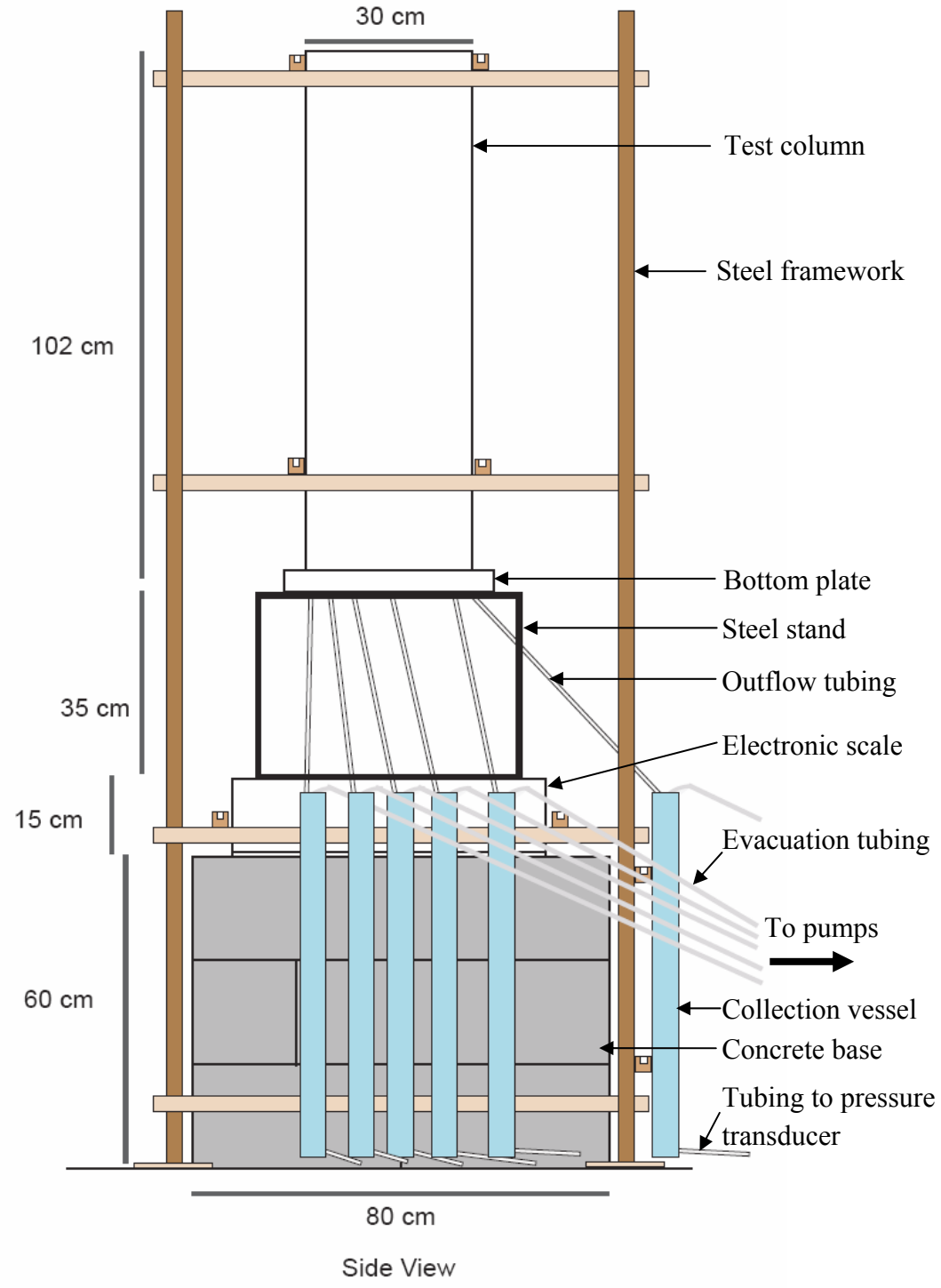

Figure 3.4 Schematic illustration of the test column (side view)

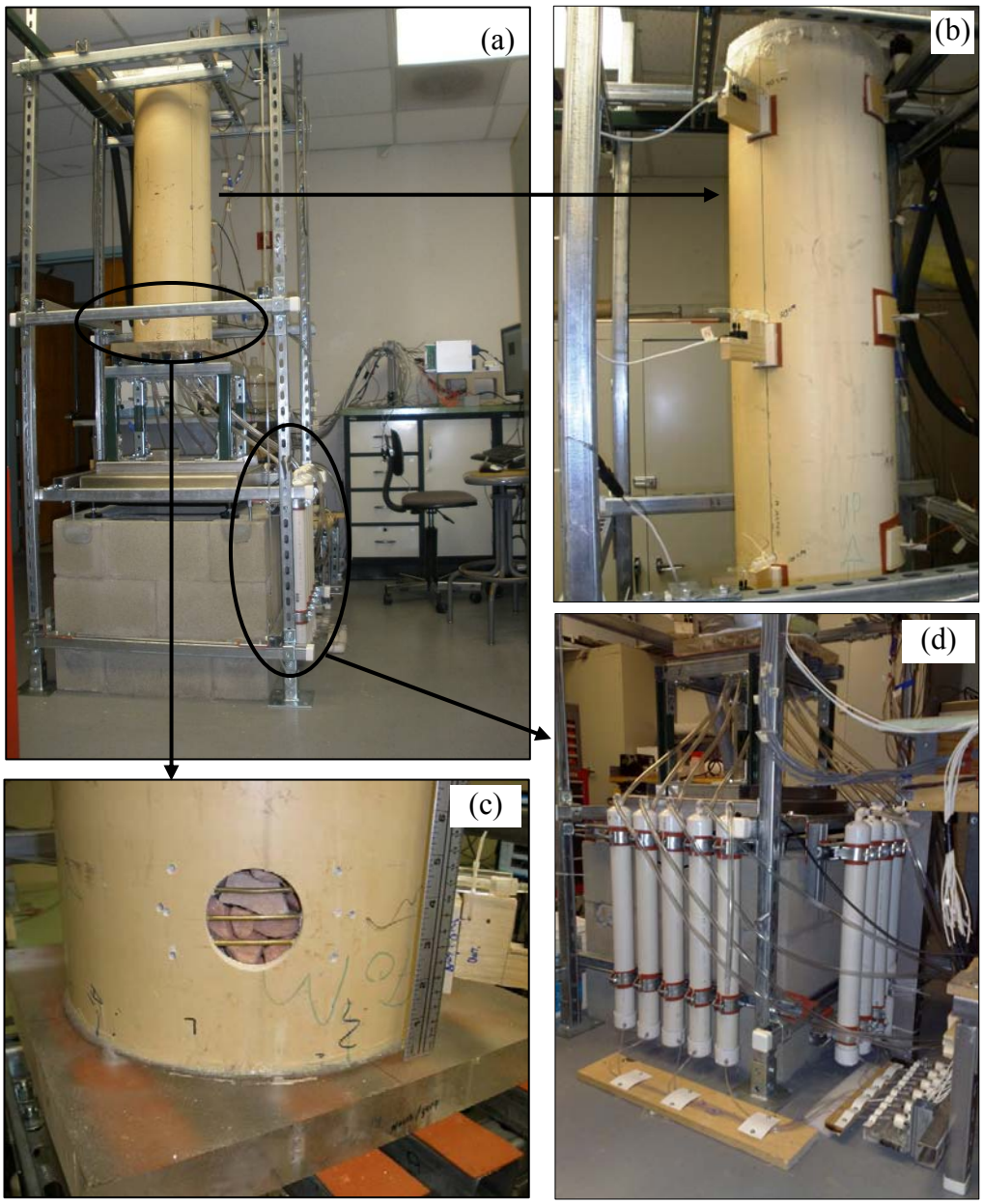

Figure 3.5 Set up of the test column. Photographs were taken before the column was surrounded with the insulation blanket. (a) An overview of the set-up, (b) tensiometers (on the left side), humidity sensors and thermocouples (on the right side) installed into the column at 10, 50 and 90 cm depths, (c) the port used to circulate warm air to dry the column, (d) collection vessels mounted on the steel frame, plumbing to collect the outflow from the column and to empty the vessels.

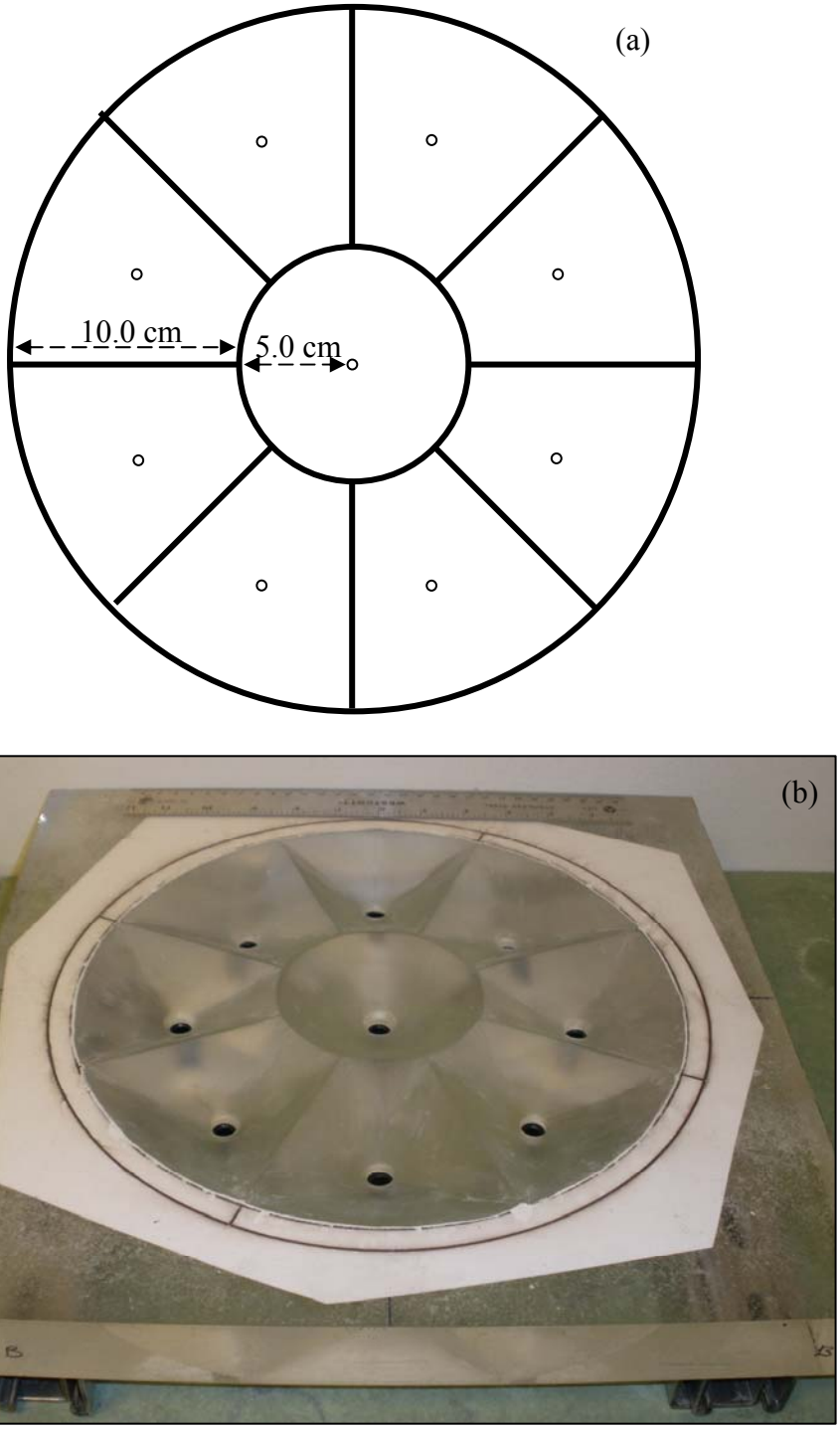

Figure 3.6 The bottom plate that divides the flow area into nine equal-area sections: conceptual design (a) and the finished bottom plate (b).

Figure 3.7 Test column covered with the insulation blanket. A high-density foam plug (left side bottom) is used to seal the port for circulating warm air to dry the column.

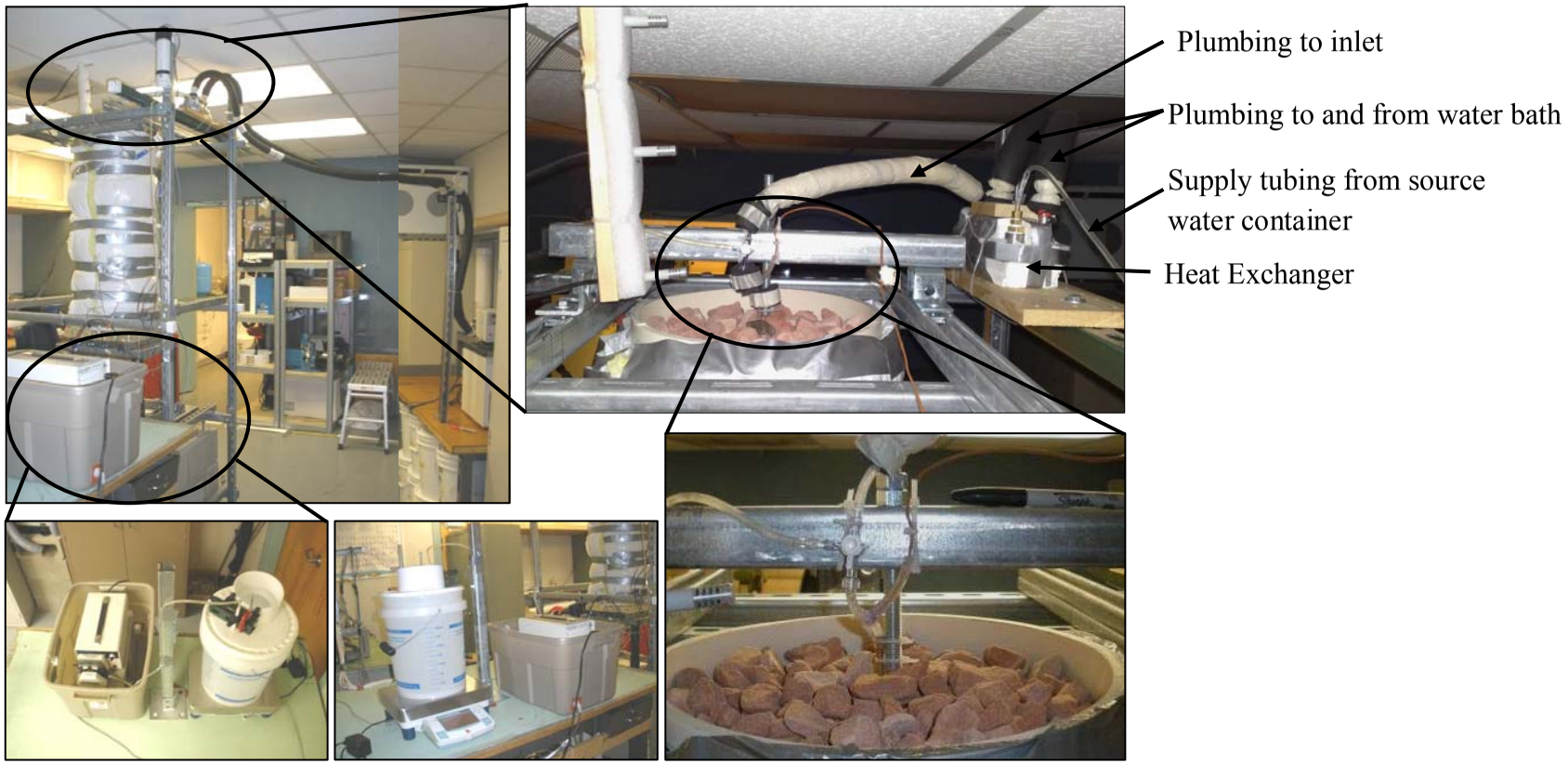

Figure 3.8 Set-up of the water inflow system. (a) An overview of the inflow set-up, (b) side view of the source water container, electronic scale and the supply pump, (c) top view of the source water container and the supply pump, the pump sits on a concrete block inside of a plastic storage bin to contain any spills in case the tubing breaks (d) heat exchanger, insulated inflow plumbing and three humidity sensors used to monitor the humidity gradient above the column, (e) single-point inlet, the thermocouple placed at the inlet and the 3-way valve used to divert the inflow away from the column

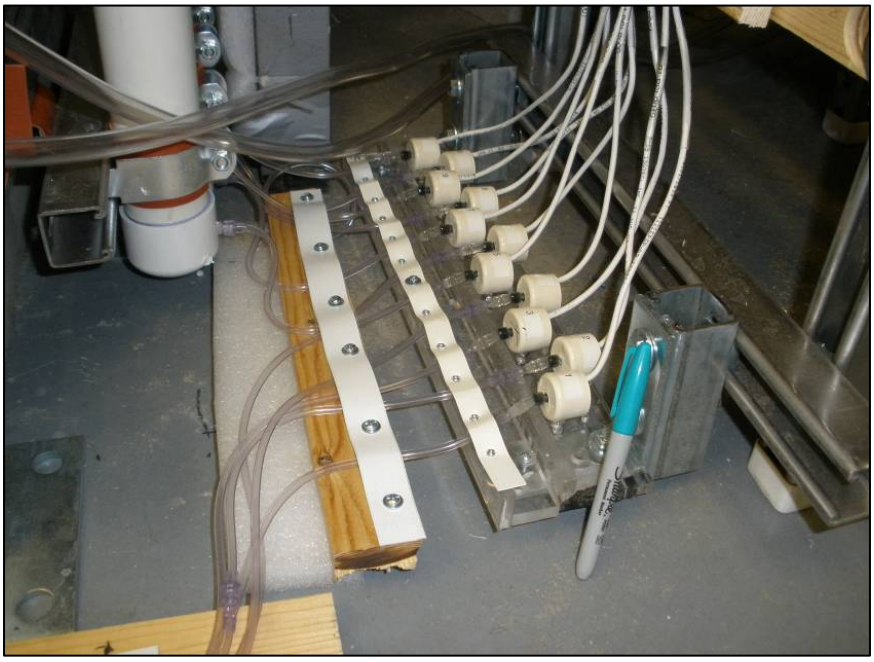

Figure 3.9 Pressure transducers connected to collection vessels and mounted on a steel framework

Figure 3.10 Pumps and plumbing of the evacuation system used to empty collection vessels

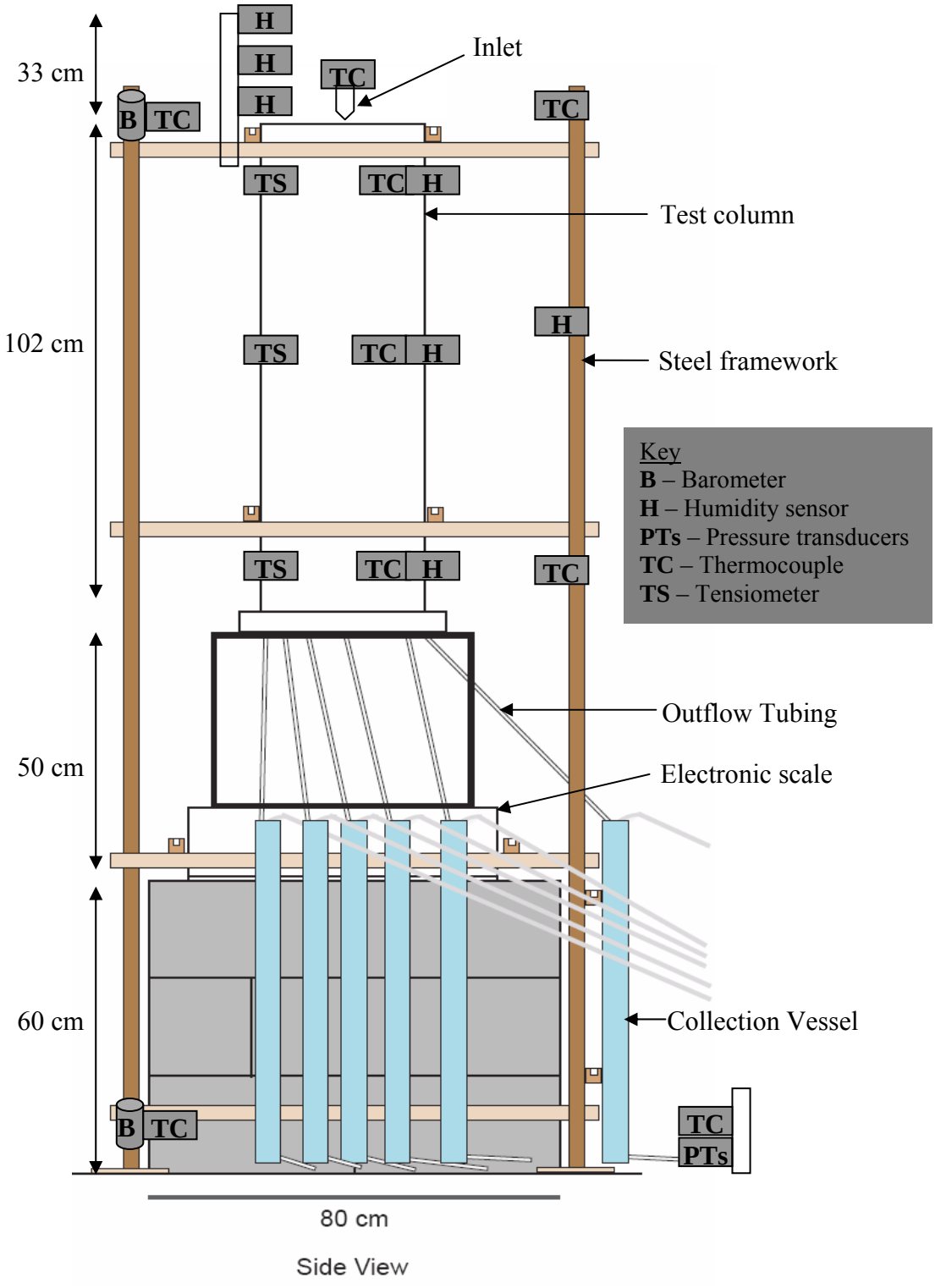

Figure 3.11 Schematic illustration of locations of the sensors in the experimental set-up (sensors are not drawn to scale)

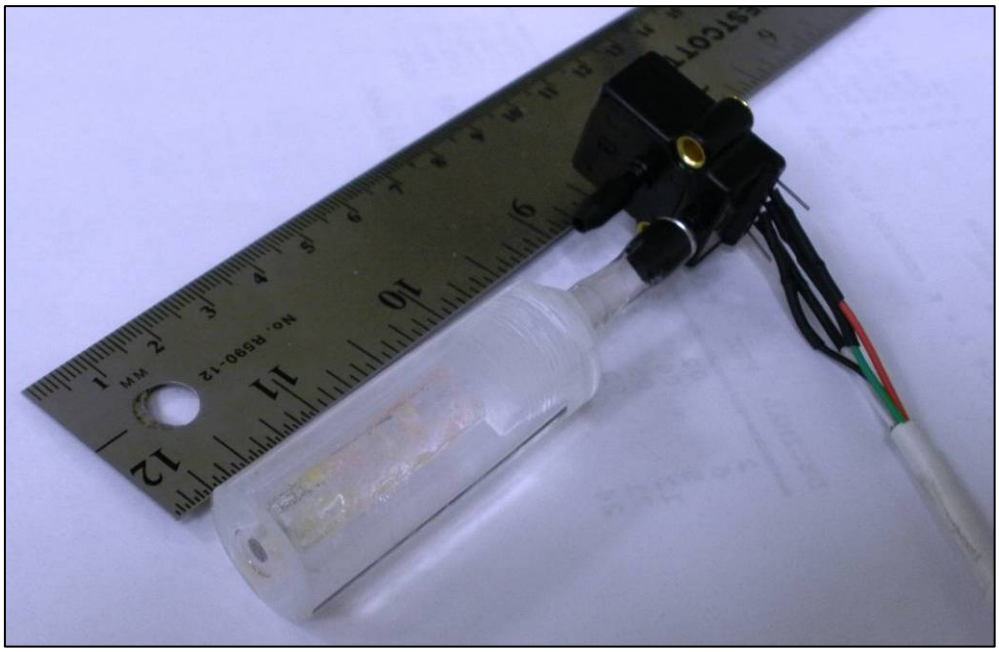

Figure 3.12 A tensiometer used to measure atmospheric tension inside the column. A porous metal plate is cemented to one end ofthe water-filled hole in the acrylic rod. The other end of the hole is connected to a 15 psi pressure transducer.

Figure 3.13 Routing of wires for power supply and data transmission

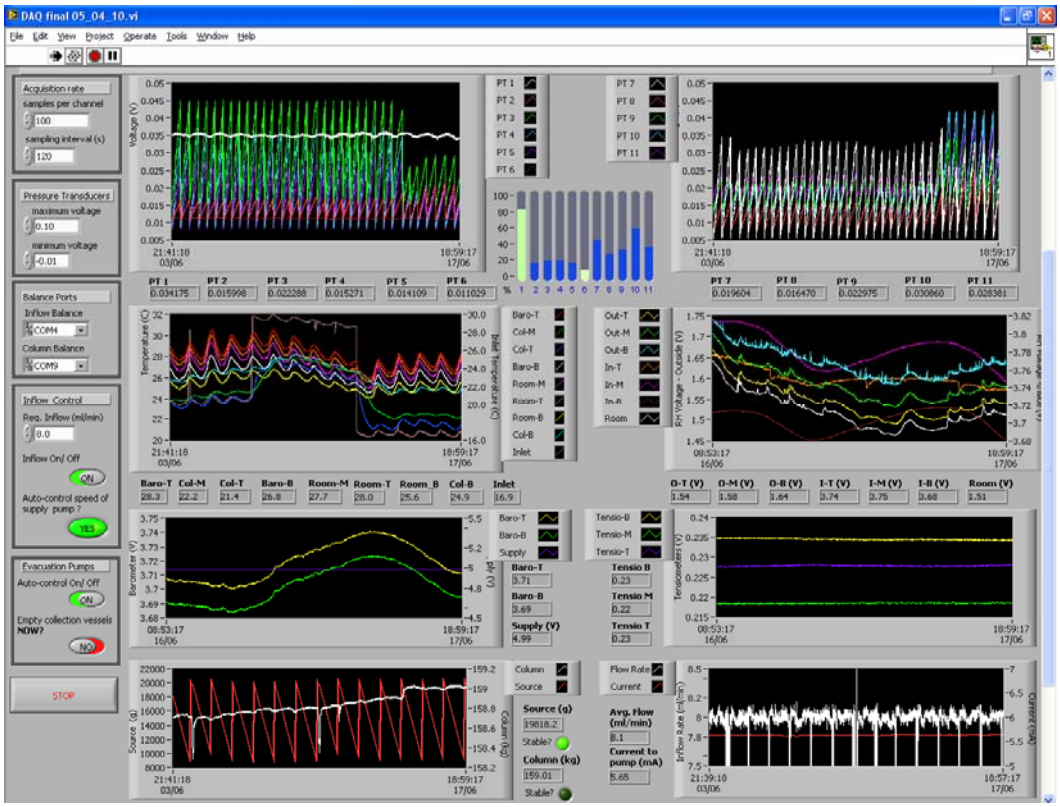

Figure 3.14 Graphical user interface of the software that controls the experiment and displays data.

CHAPTER 4

RESULTS

This chapter presents the results of four experiments conducted between 12/26/2009 and 6/29/2010 to investigate unsaturated flow structure in dual-porosity granular media. As described in Chapter 3, a 30 cm diameter and 100 cm tall column was filled with 95.35 kg of initially dry, crushed sandstone fragments (~1-3 cm) with an internal porosity of ~20%. Each experiment started from a dry initial condition and water was supplied using a single-point source located at the top of the column at a nominal rate of 8.0 ml/minute. The following parameters were measured at 2 minute intervals during the course of each experiment: the inflow rate, outflow from nine equal-area sections at the bottom of the column, weight of the column, humidity and temperature inside the column (3 locations), inflow temperature, room temperature (5 locations), room humidity (4 locations) and atmospheric pressure (2 locations).

The first experiment was run for 10 days with a continuous inflow. The second experiment was run for 40 days with three inflow pauses. The third experiment was started with a reduced inflow temperature, however the run was stopped after two days because of a failure in the inflow system. The fourth and final experiment was run for 40 days with multiple perturbations; inflow interruptions, changing the temperature of inflow, changing the location of the single-point inlet and reducing the evaporation from the column. Detailed results for each experiment are given in the following sections (4.1 through 4.4) of this chapter. A massive amount of data was collected that is presented here in its entirety. Analysis of the data is reserved for chapter 5.

4.1 Experiment #1

The first experiment was started on 12/26/09 and continued until 1/5/10; a duration of 10 days (240 hours). Water was supplied to the column at a nominal rate of 8.0 ml/min using a single-point inlet located at the top center of the column. The temperature of the circulating water-bath that regulates the inflow temperature was set to 25 ^{o}C (close to the mean room temperature). Immediately after the end of this run (within several minutes), the set-up was temporarily altered so that we could estimate the rate of evaporation from the column. This was done by rerouting all of the outflow into a single container; mass in the container was subsequently monitored at 2 minute intervals with an electronic balance (0.1 g accuracy). The inflow to the column, mass change in the column and the total outflow were measured for another 50 hours.

4.1.1 Ambient Environmental Conditions during Experiment #1

Temperature in the room was lowest at the bottom and highest at the top (figure 4.1). Temperature close to the floor (+15 cm above the floor) varied between 24 and 27.5 ^{o}C, with daily fluctuations of almost 2 ^{o}C. Temperatures at the middle (+130 cm) and near the top (+225 cm) of the room were similar to one another, and varied between 29 and 31 ^{o}C. Both showed daily fluctuations between 0.4 and 0.7 ^{o}C. Diurnal variations near the floor were considerably higher than at either of the two upper measurement points. In general, the overall difference between the top and bottom room temperatures stayed at ~4-5 ^{o}C throughout the experiment. The daily maximum temperatures were observed between 16:00 and 18:00 hours, while the minimum temperatures were observed between 05:00 and 07:00 hours. During the 10-day period of the experiment, temperature showed an increasing trend.

Relative humidity in the room varied between 13% and 16% (figure 4.2), with diurnal cycles apparent during the latter half of the experiment, but not during the first half. Atmospheric pressure in the room varied between 101.2 and 102.6 kPa , with a mild diurnal signal throughout the experiment (figure 4.3).

4.1.2 Inflow, Total Outflow and the Saturation of Rocks in Experiment #1

The inflow rate was maintained at 8.0 ± 0.1 ml/min most of the time during the experiment (figure 4.4). However, the inflow decreased to 7.0-7.8 ml/min for about 10 minutes immediately after each daily refilling of the source water container. The dips were attributed primarily to an error in the inflow control software. Air bubbles in the inflow plumbing tubing between the pump and the source container may have contributed to this problem. The software error was corrected prior to subsequent experiments. In order to minimize the possibility of air bubbles in the inflow line during subsequent experiments, we degassed all water for a minimum of five hours under ~25 kPa vacuum before adding it to the source container.

Outflow from the bottom of the column began ~3 hours after inflow was started (figure 4.4). The total outflow increased rapidly over the next ~13 hours, after which the rate of increase gradually decreased. After ~28 hours from the initiation of the inflow (i.e., ~25 hours after beginning of the outflow), the total outflow rate stabilized at slightly less than the inflow rate. The difference between the outflow and the inflow was attributed to both evaporation (~3 g/hour, described below) and increasing saturation within the column. After stabilizing, the total outflow remained steady, but showed small hourly scale fluctuations (± 0.2 ml/min) throughout the experiment. Changes in the spatial flow structure and associated flow processes could potentially create fluctuations

in the total outflow. However, changes of the total outflow that occurred simultaneously with substantial flow rate changes at individual sections were in the same order of spontaneous fluctuations and background noise, therefore they could not be exclusively related to changes in the flow structure. Furthermore, slight fluctuations of inflow rate resulted in short duration fluctuations of the total outflow (described below in section 4.1.6).

The weight of the test column (figure 4.5) rapidly increased (~300 g/hour) within the first ~14 hours of the experiment due to increased saturation. Afterwards, the rate of increase gradually decreased, eventually stabilizing at ~70 g/day, which was very small in comparison to the daily supply to the column (~11520 g/day). After 240 hours of inflow, the column contained ~4450 g of water. The gravimetric and volumetric water contents of the column were 0.05 kg/kg and 0.06 cm^3/cm^3, respectively. After the inflow was stopped, water drained from the column rapidly for about four hours, then much more slowly for the next 8 hours (figure 4.6a and b). Note that the transition between rapid and slow drainage was not abrupt and the 4-hour time frame was arbitrarily selected after analyzing the variation in the rate of change of the column weight in figure 4.6b. If we assume that rapid drainage can be attributed to film flow on the fragment surfaces, then we can apportion the total water as follows: ~3610 g of water in the intra-granular space (~38% saturation) ~840 g of water in the inter-granular pore space (3% saturation).

4.1.3 Outflow from Individual Sections at the Bottom of the Column in Experiment #1

Approximately 3 hours after inflow was initiated, outflow was first recorded from the section at the center (S1) of the column (refer to figure 4.7 for numbering of the sections at the bottom of the column). Outflow from this section rapidly increased to ~1.9 ml/min

over the next six hours (figure 4.8). As the outflow from other sections gradually increased, flow from S1 gradually decreased to ~1.2 ml/min at the ~24th hour of the experiment. The initial flow structure established, i.e., flow rates at all nine sections leveled off ~30 hours after initiation of inflow. All nine sections at the bottom of the column showed measurable outflows; however flow differed substantially between the sections. The relative contribution of each section to the total outflow varied between ~ 5% and ~16%. The lowest and the highest mean outflow rates were ~0.5 ml/min (at S2) and ~1.2 ml/min (at S1) respectively.

Outflow from each section varied over time, at hourly and daily scales. It was common for one or more sections to show increased outflow rates while others simultaneously showed decreased rates. After ~50 hours from the initiation of inflow, simultaneous changes of outflow were observed in several sections (A in figure 4.8). Flow from S3 increased from ~1.0 to 1.2 ml/min (20%) while that from both S4 and S5 increased from ~0.8 to 0.9 ml/min (over 12% each). These increases coincided with an outflow decrease at S7, from 1.0 to 0.9 ml/min (10%). The total outflow also slightly increased to ~8.2 ml/min simultaneously, but decreased below 8.0 ml/min after about an hour (A in figure 4.4). At the ~80th hour of the experiment, flow from S8 and S9 showed rapid increases from 0.6 to 0.7 ml/min (over ~15%), while S7 showed an increase from ~0.9 to 1.0 ml/min (~10%; B in figure 4.8). Simultaneously, S3, S4 and S5 showed rapid decreases from 1.2 to 1.1, 0.9 to 0.8 and 0.9 to 0.8 ml/min respectively (~10% in each section). After these rapid changes, S8 and S9 gradually decreased over next two days, while S1 gradually increased until the end of the experiment.

We observed sharp and short-duration changes in the calculated outflow rates due to background noise of pressure transducers (e.g., fluctuations at S4, S5, S8 and S9 in figure 4.8), and they could be identified using noise recorded at the two inactive collections vessels. Therefore, such short-lived spikes and dips were omitted and general trends of the flow rates were counted in analyzing data. Outflow from sections S4 and S5 showed substantial decreases for ~30-50 minutes following evacuation of the collection vessels. The cause for that change was not understood, and it could be related either to electrical noise in the data acquisition system or actual changes in water flow.

4.1.4 Temperature of the Inflow and Inside the Column in Experiment #1

Temperature of the inflow was ~27 ^{o}C during the first 36 hours of the experiment, then suddenly decreased to and remained at ~26.5 (± 0.2) ^{o}C (figure 4.1). It showed several abrupt changes, as well as fluctuations parallel to daily variations of the room temperature, but those changes were very small (± 0.2 ^{o}C). Sudden increases in the inflow temperature (0.5 to 0.2 ^{o}C) were recorded shortly (~6 minutes) after refilling the source container on a couple of occasions. It is believed that sudden changes in the inflow temperature resulted from air passing through the system, as bubbles formed on the upstream side of the pump would flush through when the source container was refilled.

Temperature inside the column was slightly lower than the temperatures at the middle and top of the room, however it was 2 – 4 ^{o}C higher than the temperature close to the bottom of the room (figure 4.1). Before the start of the inflow, temperature at the column top (measured at 10 cm depth) and the middle (measured at 50 cm depth) were ~28.5 ^{o}C while that at the column bottom (measured at 90 cm depth) was ~27.5 ^{o}C. Over the first four hours after the inflow started, temperature at the top of the column gradually

increased by ~0.7 ^{o}C, and then started to decrease. Temperature at 50 cm depth in the column increased over the first five hours by ~1 ^{o}C, and then started to decrease gradually. At the bottom of the column, the temperature increased by over 0.5 ^{o}C within the first 9 hours, but did not show a substantial decrease immediately afterwards. From the second day to until the end of the experiment, mean temperatures at the top, middle and bottom of the column were 27 (± 0.5), 28 (± 0.5) and 29 (± 0.5) ^{o}C respectively. The thermal insulation blanket placed around the column damped, but did not eliminate system response to fluctuations of the ambient temperature.

4.1.5 Relative Humidity Above and Inside the Column in Experiment #1

Relative humidity (RH) above the test column always remained slightly higher than the mean ambient RH measured at ~190 cm above the floor (figure 4.2). Relative humidity close to the top of the column (measured at ~6 cm above the top) was ~18% (i.e., ~4% higher than the ambient RH) it slightly decreased at higher elevations above the top of the column. Mean relative humidity measured ~19.5 and 33.0 cm above the top of the column were ~16% and 15%. Variation of RH (±2%) measured by all three sensors located above the column showed a strong correlation to the RH variations in the room. Despite the fluctuations, RH gradient above the column remained mostly unchanged.

Relative humidity inside the test column increased very rapidly during the first 18 hours after the inflow started (figure 4.9). The rate of increase in the middle of the column was more rapid than that observed in either the top or the bottom. Relative humidity at the top and the middle of the column reached 90% after ~35 hours from the start of the inflow, and thereafter slowly increased until the end of the experiment, but did not reach 100%. Relative humidity at the bottom was the lowest in the column. It rapidly

increased to 70% within the first 18 hours, then slowly increased up to 80% until the ~58th hour of the experiment. Thereafter, it varied between 80% and 85% until the end of the experiment. Variability of RH inside the column was highest at the bottom of the column and decreased towards the top. We noticed that a small decrease in measured RH inside the column for a short period (~10 minutes) after evacuation of collection vessels. The decrease was largest at the bottom (~3%) and the lowest at the top (~1%).

4.1.6 Evaporation from the Column

After running the experiment for 10 days, the experimental set-up was modified to estimate the evaporation from the test column. The total outflow from the bottom of the column was collected into a single container and measured using an electronic balance for ~50 hours. Inflow to the column and the change of weight of the test column were also measured during this period.

The total outflow rate measured using the electronic balance was slightly lower than the inflow rate (figure 4.10). The difference between the inflow and the outflow is attributed to increased saturation in the column and evaporation. Over a period of two days, the weight of the column increased by ~90 g. The difference between the cumulative inflow and the cumulative outflow was ~249.1 g during this period. Assuming mass balance (i.e., no other inputs or ouputs), evaporation was ~159.1 g in two days, thus ~80 g/day. As a reference, the measured evaporation from an open pan of ~800 cm^2 surface area that sat in the vicinity of the experiment was ~280 g/day. The maximum capacity of the electronic balance was ~4100 g, therefore the water collected on the balance had to be removed every ~5 hours. Most of the spikes in the total outflow data occurred due to the disturbances made during that operation. However, rapid decreases of

the total outflow at the 2nd and 26th hours (A and B in figure 4.10) were related to a decrease in inflow after refilling the source water container. The time lag between inflow and outflow spikes was ~20 min, which indicates a flow velocity of ~3.0 m/hour. This velocity is much larger than the velocity that would have been calculated assuming diffusive flow through the intra-granular pore space.

4.2 Experiment #2

Experiment #2 was started on 1/15/2010 and continued for 40 days. At the beginning it was intended to be a replication of the first experiment, and therefore started with the same settings (i.e., inflow of 8.0 ml/min using a single-point inlet located at the top center of the column and 25 ^{o}C set temperature of the circulating water-bath). The only significant change we made was degassing the water before adding it to the system. This eliminated some issues associated with bubbles forming on the upstream side of the pump. After running the experiment for 10 days, we realized that there was going to be a change in the weather (rain), which would increase humidity in the laboratory. Thus it was decided to continue the experiment. However, in the 15th day, a rupture in the tubing connecting the supply pump to the heat exchanger led to a ~90 minute interruption of the inflow. Immediately after restarting the inflow, we observed a substantial redistribution of outflow from the bottom of the column. To explore this unexpected effect, inflow was interrupted by turning off the supply pump in the 29th and 37th days for 90 and 10 minutes respectively.

4.2.1 Ambient Environmental Conditions during Experiment #2

Similar to the first experiment, the lowest and the highest temperatures were observed close to the bottom and the top of the room respectively (figure 4.11). Temperature at the bottom fluctuated between 24.0 and 26.5 ^{o}C, while that at the top fluctuated between 27.5 and 31.0 ^{o}C during the 40-day period of the experiment. The difference between the top and the bottom temperatures remained ~3 – 3.5 ^{o}C. Daily temperature fluctuations varied between 0.5 and 2 ^{o}C and were higher at the top than at the bottom, which is the opposite of what was observed during the first experiment.

Substantial changes in the ambient humidity were observed during the experiment (figure 4.12). RH was ~17% during the first three days, then it increased and varied between 23% and 28% over next four days (A1 in figure 4.12). After the first week, RH mostly remained between 20% and 24% until the 38th day, however 1-2 day long periods of slightly higher and lower RH values were observed (A2-A5 in figure 4.12). In the 12th day, RH increased and remained between 25% and 26% (I-2). After that, it again increased and varied between 25% and 28% from the 21st day to the 23rd day (I-3). Increase of RH upto 27% was again observed during the 26th day of the experiment (I-4). Ambient relative humidity decreased to 18% in the 35th day of the experiment (D-1). From the 38th to 40th day of the experiment (i.e., until the end of the experiment) RH dropped below 17%. Atmospheric pressure also substantially fluctuated during the course of the experiment (figure 4.13). At the beginning of the experiment, it was ~102.3 kPa, and then continuously decreased down to ~98.3 kPa over the first six days. Thereafter, the pressure increased until the 9th day, and reached ~101.8 kPa. After the first 10 days,

atmospheric pressure fluctuated between 100.2 and 101.7 kPa, but it increased up to ~102.2 kPa in the 39th day.

4.2.2 Inflow, Total Outflow and the Saturation of Rocks in Experiment #2

The inflow rate was maintained at 8.0 ± 0.1 ml/min most of the time during the experiment (figure 4.14). However, it decreased to 7.8 ml/min for less than 10 minutes immediately after refilling the source water container. In addition, the inflow exceeded 8.2 ml/min for a very short duration (less than 6 minutes) on three occasions due to software related problems.

Outflow from the bottom of the column started ~3 hours after the inflow started (figure 4.14). The total outflow increased rapidly over next ~10 hours and stabilized at slightly less than 8.0 ml/min. During the three inflow interruptions, the total outflow decreased rapidly, then quickly returned to its original level after the inflow was restarted (A1, A2 and A3 in figure 4.14). After each of the 90-minute interruptions, the total outflow decreased to ~2.5 ml/min, but increased back to ~7.8 ml/min within ~2 hours from the inflow resumption. The total outflow decreased to 6.8 ml/min after the 10-minute interruption, then increased back to 7.9 ml/min within ~1 hour after restarting the inflow.

The mass of water stored in the test column followed a pattern similar to that observed in experiment #1. The weight of the test column increased rapidly over the first ~11 hours at a rate of ~310 g/hour and then the rate of increase gradually decreased (figure 4.15). After the first two days (48 hours), weight of the column was increasing at a rate of ~70 g/day. This rate progressively decreased as the experiment continued. The rate of increase of the column weight was ~40 g/day during the third week and ~20 g/day

during the fourth week of the experiment. Weight of the column did not substantially increase after the 33rd day, however the weight did decrease ~80 g between the 34th and 37th days. The column regained the lost weight again in the 37th day, and remained steady until the end of the experiment. The three downward spikes in the data correspond to the three inflow interruptions and are described below.

The total amount water inside the column after 240, 480 and 960 hours from the beginning of the experiment were 4120, 4310 and 4490 g respectively. The corresponding gravimetric water contents were 0.04, 0.04 and 0.05 kg/kg. Assuming ~840 g of water existed as films on fragment surfaces (estimated in the first experiment), corresponding saturation of the intra-granular pores were 34%, 36% and 38% respectively. After 240 hours of wetting, the amount of water stored in the column in the first experiment (4450 g) was significantly higher than that observed in this experiment (4120 g). The final water storage between the two experiments was very similar, with a difference of ~40 g, which is on the order of measurement error.

After each of the two 90 minute inflow interruptions, the weight of the column decreased by ~420 g (A1, A2 on figure 4.15). After the inflow was restarted, the column rapidly gained ~380 g within an hour and ~420 g within two hours. After the 10 minute inflow interruption (A3 on figure 4.15), the weight of the column decreased by ~70 g, but the column recovered the lost weight within ~30 minutes. The total outflow started to rapidly decrease 10 minutes after the inflow was stopped at the end of the experiment. All nine sections at the bottom of the column responded to the inflow termination simultaneously.

4.2.3 Outflow from Individual Sections at the Bottom of the Column in Experiment #2

Outflow distribution between the nine sections at the bottom of the column showed large changes in response to inflow interruptions, along with some spontaneous events (figure 4.16). Approximately 3 hours after start of inflow to the column, measurable outflow was simultaneously observed from two sections; S1 (the section at the center) and S5. However, outflow from S1 was substantially higher than that from S5 (figure 4.17). The outflow from S1 rapidly increased up to ~1.4 ml/min within three hours (i.e., until the 6th hour of the experiment), followed by a slow increase over the next three hours, eventually leveling off at 1.5 ml/min at the 13th hour of the experiment. This behavior is different from that was observed in the first experiment (figure 4.8), where the flow rapidly increased for six hours up to 1.9 ml/min and then decreased in another 4 hours down to 1.2 ml/min.

After the beginning of outflow from each section, similar variations observed within the first ~12 hours; i.e., a rapid increase at the beginning and eventually leveling off thereafter. Outflow from the nine equal-area sections at the bottom of the column were significantly different from one another, and ranged from ~ 5% to ~18% of the total outflow. After 24 hours from the beginning of the inflow, S1, S3 and S4 showed the highest outflow rates (~1.5, 1.2 and 1.0 ml/min respectively), while S8 and S2 showed the lowest flow rates (~0.5 ml/min).

Substantial variations in outflow from different sections at hourly and daily scales were observed within the first 14 days of the experiment before the first accidental inflow interruption (figure 4.17). For instance, S3, S4, S7 and S8 showed long-term flow rate fluctuations within the first ~200 hours, with some rapid and simultaneous fluctuations

afterwards (figure 4.17). Between the 230th and 241st hours of the experiment, S3, S4 and S7 showed rapid and simultaneous flow changes (A in figure 4.17). At first, S7 showed an increase from ~0.9 to 1.1 ml/min, while both S3 and S4 showed decreases from 1.2 to 1.0 ml/min and 0.9 to 0.8 ml/min respectively. Then the flow rates remained steady for ~4 hours, thereafter S7 decreased to ~1.0 ml/min, while S3 and S4 increased back to 1.2 and 0.9 ml/min respectively. The other sections did not show any substantial changes during this period. However, similar to the first experiment, we observed spikes in the calculated outflows in S3, S4, S8 and S9 potentially due to electrical noise.

It was noted that the background noise indicated by the pressure transducer connected to the 80% water filled vessel (noise-1) was much higher than that indicated by the transducer connected to the 20% water filled vessel. Also, background noise in both inactive collection vessels were substantially higher than in the first experiment.

4.2.3.1 Changes in Outflow after the First Inflow Interruption

After a ~90 minute long break, inflow was restarted at the 340th hour of the experiment. The subsequent distribution of outflow was substantially different than that observed prior to the interruption (figure 4.18). Two adjacent sections; S6 and S7, both showed large increases in outflow. Mean outflow from S7 increased from 0.9 to 1.3 ml/min (~45%), while that from S6 increased from 0.8 to 1.1 ml/min (30%). Flow in S8 showed a ~15% increase from ~0.5 to 0.6 ml/min.

Sections S3 and S4 showed substantial decreases in outflow following the inflow interruption. Outflow from S4 showed the largest decrease from 0.9 to 0.6 ml/min (over 30%) soon after the interruption, but it gradually increased back to 1.0 ml/min over next 14 days (i.e., until the 660th hour). The decrease of S3 was from 1.0 to 0.8 ml/min

(~20%). Approximately 4 hours after the resumption of inflow the total outflow had returned to a level indistinguishable from that prior to the interruption.

Apart from the rapid flow changes soon after the inflow interruption, long-term changes (in the scale of days) were also observed. Flow from S7 continuously increased, and that from S1 continuously decreased over next ~90 hours (until the 430th hour of the experiment; figure 4.18). However, this trend reversed over next 50 hours (from ~430th to 480th hour); i.e., the flow from S7 slowly decreased while that of S1 slowly increased. Outflow from S9 started to gradually decrease ~28 hours after restarting the inflow. It decreased from 0.8 to 0.6 ml/min over a period of 14 days (from the 370th hour to the 660th hour of the experiment). Flow in S3, S5, and S6 also showed both short-term (for few hours) and long-term (for few days) fluctuations of smaller magnitudes between the first and the second inflow interruptions. However, fluctuations of outflows from S2 and S8 were very low in comparison to that of the other sections during this period. After ~6 days from the flow interruption (at the ~481st hour, A in figure 4.18), abrupt and simultaneous changes of outflows were observed. Outflow from several sections suddenly increased (e.g., S1 and S5), while that from some other sections rapidly decreased (e.g., S3 and S7).

4.2.3.2 Changes in Outflow after the Second Inflow Interruption

After the second 90 minute long inflow interruption in the 29th day of the experiment, large outflow changes were again observed (figure 4.19). Similar to the outflow changes after the first interruption, S6 and S7 showed large outflow increases. Mean outflow from S6 increased from 1.0 to 1.2 ml/min (~20%), while that from S7 increased from ~1.2 to 1.5 ml/min (25%). Section S3 and S4 showed substantial decreases in outflow. Outflow

from S4 again showed the largest decrease from 1.0 to 0.8 ml/min (~25%) immediately after the inflow interruption, but it gradually increased back to 1.0 ml/min over next 6 days. Flow in S3 decreased from 1.0 to 0.8 ml/min (over 15%). Section S2 and S8 showed a noticeable decrease and an increase, respectively; however, the magnitude of changes were very low. The other three sections (S1, S5 and S9) did not show any significant change in outflow rate. Approximately 29 hours from the resumption of inflow (713th hour of the experiment, A in figure 4.19), outflow from three sections (S1, S6 and S7) showed large abrupt changes within a period of ~2 hours. Flow in S7 increased from 1.5 to 1.7 ml/min (14%) while that in S1 showed a decrease from ~1.5 to 1.3 ml/min (11%). Section S6 showed a rapid decrease from 1.3 to 1.1 ml/min (~15%), followed by a progressive decrease down to 0.9 ml/min over a period of six days. After two days from the last rapid flow rate changes (i.e., at the ~768th hour, B in figure 4.19), S1 started to gradually increase, while S7 started to gradually decrease.

Abrupt changes were again observed ~6 days after the second inflow interruption (at ~826th hour of the experiment; C in figure 4.19). At this instance, simultaneous changes in several sections occurred twice within a period of 7 hours. The most substantial changes were observed in S1, S3, S6 and S7. The first change occurred at S3, where outflow increased from 0.9 to 1.6 ml/min (75%). Simultaneously, flow from S6 and S7 decreased from 0.9 to 0.7 ml/min (22%) and from 1.3 to 0.9 ml/min (~30%), respectively. About four hours after these changes, S1 and S3 showed substantial changes in their flow rates. Flow in S1 increased from 1.4 to 1.6 ml/min (~14%), while that in S3 rapidly decreased from 1.6 to 1.3 ml/min (~18%) within ~2 hours.

4.2.3.3 Changes of Outflow after the Third Inflow Interruption

Outflow changes observed after the 10 minute inflow interruption in the 37th day (at ~875th hour) were comparable with changes observed after the 90 minute interruptions. Three sections (S6, S7and S8) showed large increases in outflow (figure 4.20). Mean outflow from S7 showed the highest increase, from 0.8 to 1.1 ml/min (over 30%). Flow from S6 and S8 increased from 0.7 to 0.8 ml/min (~18%) and from 0.6 to 0.7 ml/min (~15%) respectively. Four sections (S1, S2, S3 and S4) showed decreases in outflow. Outflow from S4 showed the largest decrease, from ~1.0 to 0.8 ml/min (20%) immediately following the interruption. Decrease in S3 was ~10% (1.3 to 1.2 ml/min), but that in S1 was less than 10% (from 1.6 to 1.5 ml/min). S2 showed a very small decrease, but S5 and S9 did not show detectable flow rate changes.

4.2.3.4 Changes of Outflow after the Inflow was Terminated

Outflow from each section started to decrease rapidly ~20 minutes after the inflow termination at the end of the experiment, and became very close to zero after ~15 hours (A in figure 4.20).

4.2.4 Temperature of the Inflow and Inside the Column in Experiment #2

Temperature of the inflow showed daily and long-term variations parallel to room temperature, but it always remained between 25.7 ^{o}C and 27.7 ^{o}C during the 40 day duration of the experiment. The temperature gradient in the test column was similar to that in the ambient environment (room) before the beginning of the inflow. The top of the column was ~0.7 ^{o}C warmer than the bottom of the column (figure 4.11). During the first four hours after the inflow started, temperature at the top of the column gradually increased by over 0.7 ^{o}C, and then started to decrease. Temperature at the middle of the

column increased within the first five hours by ~1 ^{o}C, and then started to decrease gradually. Within the first eight hours of the experiment, temperature at the bottom of the column increased by over 1 ^{o}C. After the first 12 hours, the top of the column was the coldest and the bottom was the warmest, thus the temperature gradient within the column was reversed. Temperature gradient between the bottom and the middle of the column was higher than that between the middle and the top. After 24 hours from the beginning of the inflow, mean temperatures at the 10, 50 and 90 cm depths of the column were 24.3 (±0.5), 27.1 (±0.5) and 27.7 (±0.5) ^{o}C. Temperature inside the column showed daily and long-term fluctuations in response to the fluctuations of room temperature and the variability at the bottom and the top of the column was substantially higher than that at the middle.

4.2.5 Relative Humidity Above and Inside the Column in Experiment #2

Relative humidity above the test column fluctuated with the changes of RH in the ambient environment (figure 4.12). Relative humidity measured ~6 and 19.5 cm above the top of the column mostly remained ~3-4% and 1-2% higher than the ambient value. Relative humidity at ~33 cm above the top of the column was very close to the ambient value. Humidity gradient above the column slightly increased when the ambient humidity decreased, and it slightly decreased when the ambient humidity increased.

Over the first 10 hours of the experiment, RH inside the column increased very rapidly (figure 4.21). The rate of increase at the middle of the column was more rapid than that at the top and the bottom. Relative humidity at the top and the middle reached 90% after ~18 hours and 95% after 30 hours from the initiation of inflow, thereafter remained close to the saturation (100%). Relative humidity at the bottom was ~10-15%

lower than that either measured at the middle or the top of the column; it reached 75% after ~20 hours from the beginning, and then remained between 80% and 93%. Relative humidity slightly decreased for a short period (~10 minutes) immediately after evacuation of the collection vessels. The decrease was largest at the bottom (~3%) and the lowest at the top (~1%).

4.3 Experiment #3

Experiment #3 was started on 5/11/2010 and halted after ~56 hours due to equipment failure. After experiment #2, we found a black precipitate on several rock fragments located immediately adjacent to the inlet. The five contaminated fragments were removed and several other pieces were shifted to create a level surface before starting the third experiment. In the second day of the experiment #3, we observed formation of a black precipitate on some fragments close to the inlet; therefore the experiment was terminated in the third day, after running only for ~56 hours.

In experiment #3, the temperature of the circulating water-bath was set at 15 ^{o}C (10 ^{o}C lower than in experiment #1 and 2) in order to increase the dynamic viscosity of water in the column. Water was supplied to the column at 8.0 ml/min using a single-point inlet located at the top center of the column. Observations during experiment #3 are described here, and resolution of the precipitation issue is presented below with experiment #4.

4.3.1 Ambient Environmental Conditions during Experiment #3

Temperature at the top of the room was ~0.5 ^{o}C was warmer than that at the middle of the room, and both varied between ~23.5 and 25.5 ^{o}C (figure 4.22). Temperature close to the bottom of the room was ~2 ^{o}C lower than that at the top, and fluctuated between 21.5

and 23.0 ^{o}C. Relative humidity in the room and the barometric pressure showed increasing trends, and varied between 18% - 26% and 100.5 - 101.1 kPa respectively (figure 4.23 and 4.24).

4.3.2 Inflow, Total Outflow and the Saturation of Rocks in Experiment #3

Inflow was maintained at 8.0 ± 0.1 ml/min during the 56 hours of the experiment (figure 4.25). Outflow from the bottom of the column started ~4.5 hours after the inflow initiated. The total outflow increased rapidly during the first 11 hours and then stabilized at slightly less than the inflow rate. Weight of the test column rapidly increased (~375 g/hour) within the first ~9 hours, but the rate of increase gradually decreased thereafter (figure 4.26). After 48 hours from the beginning, the total increase of the weight of the column was 3950 g and the gravimetric water content was ~0.04 kg/kg. Assuming the amount of water existed in surface films to be ~840 g (estimated in experiment #1), the saturation of intra-granular pores was ~32%.

4.3.3 Outflow from Individual Sections at the Bottom of the Column in Experiment #3

A measurable outflow was first observed from S1 (the section at the center) ~4.5 hours after the start of inflow (figure 4.27). Shortly after that, flow from S3, S4 and S5 started simultaneously, but flow in S3 and S4 increased more rapidly than that in S5. Outflow from S3 became slightly higher than that from S1 approximately 10 hours after the start of the experiment. The nine basins could be divided in to two groups based on the outflow exhibited between the 10th and the 56th hours. The first group included three sections (S1, S3 and S4) that showed flow rates between 1.1 and 1.7 ml/min. The second group included the rest of the basins (S2, S5, S6, S7, S8 and S9) that showed outflows between 0.4 and 0.8 ml/min.

After ~25 hours from initiation of inflow, three sections of the first group showed some minor changes; i.e., flow from S3 and S4 slightly increased while that from S1 and S9 slightly decreased (A1 in figure 4.27). Outflow from the other sections remained mostly unchanged during this time.

4.3.4 Temperature of the Inflow and Inside the Column in Experiment #3

Temperature of the inflow was maintained between 18 and 19 ^{o}C during the run (figure 4.22). The heat exchanger dropped the inflow temperature several degrees from ambient, as evidenced by the steep gradients at the start and finish of the experiment; however, inflow temperature was still a little more than 3˚C warmer than the chiller setting of 15˚C. Temperature inside the column started to decrease after the inflow started, but the temperature at the top and the middle of the column slightly increased (by 0.1 – 0.3 ^{o}C) prior to the decrease. The temperature at the top, middle and bottom were 20.4, 21.8 and 23.3 ^{o}C, respectively 24 hours after the start of the inflow. The temperature inside the column was lower only by 2-4 ^{o}C than the ambient temperature with the chilled inflow water.

4.3.5 Relative Humidity Above and Inside the Column in Experiment #3

Relative humidity above the column remained ~1% to 4% higher than the ambient value (figure 4.23). Relative humidity measured at 33.0 cm above the column increased from 18% to 26%, while that at 6.0 cm above the column increased from 22% to 28% because of the increase in the ambient humidity from 18% to 26% over the period of 56 hours. The gradient in relative humidity above the column remained relatively constant throughout the experiment.

Relative humidity at the 10 cm depth inside the column started to increase at first, but that at 50 cm depth increased more rapidly (figure 4.28). At 10 cm and 50 cm depths, relative humidity reached 90% after ~13 and 9 hours respectively, then reached ~100% after 24 hours from the start of the inflow (calculated relative humidity at the 10 and 50 cm depths inside the column were over 100% at some instances, which were not physically realistic. Electronic humidity sensors were not properly functional at the vicinity of 100% RH, thus provide erroneous data. However, we could expect that when the calculated RH were over 100%, actual RH inside the column was close to 100%.). Relative humidity at the 90 cm depth of the column started to increase ~4 hours after the inflow initiated, and then rapidly increased to ~85% over next eight hours. The maximum RH measured at this depth was ~94%. In the first two experiments, humidity at the lowest internal sensor was observed to decrease when the collection vessels were periodically emptied; this behavior was not observed in the second half of experiment 3.

4.4 Experiment #4

After the third experiment, we noticed the presence of a black precipitate on many rock fragments that were located close to the center of the column, and down to a depth of ~10 cm. Therefore, ~930 g of contaminated rocks (40-50 fragments) were replaced with the same amount of fresh rocks before the fourth experiment. Furthermore, we found that the precipitate originated due to the corrosion of brass fittings on the heat exchanger located upstream of the inlet, and possibly the heat exchanger itself (brazed stainless steel). To avoid recurrence of this issue, the heat exchanger was thoroughly cleaned, brass fittings were replaced with stainless steel, the contaminated tubing was

replaced, and the amount of liquid chlorine bleach added to the inflow was reduced from 0.6 ml/l to 0.15 ml/l. These changes largely reduced formation of the precipitate on rock fragments, however a very thin (barely visible) layer of grey color precipitate was observed on the fragment that was located immediately below the inlet in the 14th day of the experiment.

Experiment #4 was started on 5/20/2010 and run for 40 days. We decided to test the influence of viscosity, inflow interruptions location of the inlet and reduced evaporation from the column. In addition, we planned to end the experiment by collecting all outflow into a single container, similar to what was done at the end of experiment #1. The experiment was started at a nominal inflow of 8.0 ml/min with the inlet located at the center of the column. The temperature of the circulating water-bath was set at 15 ^{o}C in order to reduce the temperature and increase the dynamic viscosity of the inflow water.

The system was perturbed several times during the first 37 days. The inflow to the column was paused for 90 minutes in the 11th and 16th days. After that, the temperature of the water-bath was increased to 30 ^{o}C in the 19th day to lower the viscosity of the inflow water. The inflow was temporarily stopped again for 90 minutes and 20 minutes in the 22nd and 23rd days, respectively. In the 24th day, the temperature of the water-bath was lowered to 10 ^{o}C. The inlet was laterally moved ~4 cm away from the center of the column in the 26th day, and three days later the inflow was again paused for 90 minutes. In the 30th day, the inlet was moved back to the center of the column and kept there for a day. After that it was again moved ~2.5 cm in the same direction as before. The top of the column was covered with a plastic sheet to minimize evaporation in the 34th day, and the cover was removed in the 36th day. In the 37th day, the setup was modified to collect the

total outflow into a single vessel that sat on a 6.1 kg capacity (0.1 g accuracy) electronic balance (Ohaus® Explorer Pro). Inflow, total outflow and the weight of the column were measured for three more days, and then the inflow was turned off in the 40th day.

4.4.1 Ambient Environmental Conditions during Experiment #4

The highest temperature was recorded at the top of the room, and a ~0.5 ^{o}C lower temperature was recorded at the middle (figure 4.29). The bottom of the room remained ~1 - 3.5 ^{o}C colder than the top throughout the experiment.

During the first four days, temperatures varied between 22.0 and 26.0 ^{o}C, then progressively increased until the 20th day. Temperature at the top and the middle of the room increased from ~23 to 29 ^{o}C, while that at the bottom increased from ~22 to 26 ^{o}C during that period. After that, temperatures gradually decreased by 2-3 ^{o}C until the 24th day, and then progressively increased by 2-3 ^{o}C until the end of the experiment. Diurnal temperature fluctuations that ranged from 1.0 to 2.5 ^{o}C were observed throughout the course of the experiment and the fluctuation was lowest at the bottom and the highest at the top of the room.

Relative humidity (RH) in the ambient environment varied between 16% and 34% during the course of the experiment (figure 4.30). At the beginning of the experiment it was ~28%, then gradually decreased over the next three days and reached 17%, which was the lowest value recorded during this experiment. Thereafter, RH increased until the 7th day of the experiment and reached to ~28%. After another day, it started to decrease rapidly and remained between 20% and 25% until the 12th day. After 16 days from the beginning, RH increased up to ~34%, then decreased again down to ~18% at the 22nd day. Between the 23rd and 27th day, RH remained between 25% and 30%, then between

18% and 23% until the end of the run. Atmospheric pressure varied between 99.6 and 101.3 kPa during the experiment (figure 4.31).

4.4.2 Inflow, Total Outflow and the Saturation of Rocks in Experiment #4

Inflow rate was maintained at 8.0 ± 0.1 ml/min most of the time during the course of the experiment, but sometimes it decreased down to 7.8 ml/min and increased to 8.2 ml/min for durations of less than 10 minutes (figure 4.32). Outflow from the bottom of the column started ~3 hours after inflow started and the total outflow increased rapidly up to 7 ml/min within the first 14 hours (figure 4.32). After that, the total outflow slowly increased over next 14 hours (i.e., until the 28th hour of the experiment) and stabilized at slightly less than the inflow rate. During the 90-minute inflow interruptions, the total outflow decreased to ~2.5 – 3.0 ml/min. After ~2 hours from restarting the inflow, the total outflow rapidly increased and leveled off slightly below 8.0 ml/min. During the 20-minute inflow interruption, the total outflow decreased to ~6.8 ml/min; afterwards, outflow rapidly increased and leveled off slightly below the inflow within about an hour. Redistribution of the outflow between the nine sections at the bottom of the column did not create any change of the total outflow that could be detected over the spontaneous fluctuations. Similarly, we could not detect changes in the total outflow associated with the temperature perturbations, nor when we covered the column to reduce evaporation.

The initial increase in the weight of the test column showed similar characteristics to the other runs. Weight of the test column rapidly increased over the first 10 hours of the experiment at a rate of ~310 g/hour (figure 4.33). After 48 hours, the weight was increasing at a rate of ~85 g/day. At the end of the second and third weeks, rates of increase for the column weight were ~50 g/day and ~35 g/day respectively. Thereafter,

weight continuously increased at a rate slightly above 20 g/day (during this period change of the weight of the column was in the same order of measurement error). The weight of the test column rapidly increased by ~60 g after the temperature of the inflow was lowered from ~28 to 16 ^{o}C at the 563rd hour (24th day) of the experiment. It is expected that this increase of the weight resulted from thickening of water films on fragment surfaces due to decreased dynamic viscosity of water. Weight of the test column rapidly decreased during inflow interruptions, and it progressively increased back to previous weight as the inflow restarted (A1 - A5 in figure 4.33). During the first two 90-minute interruptions (when inflow temperature was ~19 and 20 ^{o}C), weight of the column decreased by 390 and 430 g respectively (A1 and A2). After restarting the inflow after each interruption, the column gained 350 and 380 g respectively in ~150 minutes. During the third 90-minute inflow interruption (when inflow temperature was ~29 ^{o}C), weight of the column decreased by 430 g, and then it increased back to the previous weight within ~180 minutes after the inflow was restarted (A3). The weight of the column decreased by 160 g during the 20-minute inflow interruption (when inflow temperature was ~29 ^{o}C), but it gained that weight within ~100 minutes (A4). During the fourth 9-minute interruption (when inflow temperature was ~17 ^{o}C), the decrease of the column weight was 470 g, and that weight was gained by the column within ~120 minutes after resumption of inflow (A5).

Instantaneous weights of the total amount of water that existed inside the column after wetting for 10 and 20 days were 4500 and 4710 respectively. The corresponding gravimetric water contents were 0.04 and 0.05 kg/kg, respectively. The maximum amount of water in the column (~5000 g) was recorded 33 days from the beginning.

Based on the assumptions of that the increase of the water in films on fragment surfaces by 60 g after lowering the inflow temperature in the 24th day, plus 840 g of water existed in water films before that, saturation of the intra-granular pores after 10, 20 and 33 days of wetting were ~38%, 40% and 42%.

4.4.3 Outflow from Individual Sections at the Bottom of the Column in Experiment #4

The distribution of outflow between the nine sections at the bottom of the test column showed numerous substantial changes during the experiment (figure 4.34 and 4.35). Most of the rapid changes occurred after external perturbations, but some rapid spontaneous changes were also observed.

Detectable outflow started from sections S1 and S4 simultaneously, and then from S3 and S5 (figure 4.36). Within the first 8 hours, flow from S1, S3 and S4 increased rapidly in comparison to other sections. During the period between the 15th and 250th hours (until the first inflow interruption) flow rates from these three sections were close to each other and varied between ~1.3 and 1.6 ml/min. Outflow rate in S5 remained between 1.1 and 1.2 ml/min. Section S2 showed the lowest mean flow rate of ~0.3 ml/min, while outflow from the remaining sections varied between ~0.3 and 0.7 ml/min, while. Individual flow rate in each of S1, S3 and S4 was ~18% of the total outflow. The flow in S5 was ~14% of the total outflow, while each of other five sections (S2, S6, S7, S8 and S9) each contributed ~ 4% - 9% of the total flow.

Within the first 250 hours (~10 days) of the experiment, there were substantial variations in outflow from different sections at hourly and daily scales. For example, from the 48th hour to the 240th hour S4 showed an increasing trend while S1 and S8

showed decreasing trends. Section S4 showed a rapid increase at ~46th hour (A1 in figure 4.36) and S9 showed a rapid increase after the 72nd hour (A2 in figure 4.36).

Similar to the second experiment, the background noise indicated by the pressure transducer connected to the 80% water filled vessel (noise-1) was much higher than that indicated by the transducer connected to the 20% water filled vessel. Also, magnitude of noise-1 was substantially larger than that observed in the first and the second experiment. Note that the duration of the third experiment was not sufficient to adequately assess the background noise.

4.4.3.1 Changes of Outflow after the First Inflow Interruption

The first inflow interruption was made after ~250 hours of continuous supply to the column. Large and rapid changes of outflow at some sections were observed after this 90 minute long interruption (figure 4.37). Three sections (S3, S4 and S5) showed increased outflow. Mean outflow from S3 increased from ~1.5 to 1.9 ml/min (~25%) while that of S4 increased from 1.4 to 1.7 ml/min (~20%). The increase at S5 was about 10%, from ~1.1 to 1.2 ml/min. After the rapid increase, outflow from S3, S4 and S5 gradually decreased to 1.7, 1.5 and 0.9 ml/min over next five days (~119 hours) until the next interruption at the ~372nd hour of the experiment. Five sections (S1, S6, S7, S8 and S9) showed decreases in outflow after the interruption. Outflow from S7 showed the largest decrease, from 0.7 to 0.5 ml/min (34%). Decreases at S6 and S9 were from 0.7 to 0.5 ml/min and from 0.5 to 0.4 ml/min (~ 25%). Flow in S8 decreased from 0.4 to 0.3 ml/min (21%). Outflow from S1 showed a 9% decrease from 1.5 to 1.3 ml/min following the interruption, and then progressively increased to 1.5 ml/min after five days. Section S2 did not show a measurable change in the flow after the interruptions.

4.4.3.2 Changes of Outflow after the Second Inflow Interruption

The second 90 minute inflow interruption was done in the 16th day of the experiment at ~372 hours from the start (figure 4.38). Outflow from S3, S4 and S5 increased rapidly after the interruption, and the highest increase of 20%, from 0.9 to 1.1 ml/min was observed at S5. Flow in S4 increased from 1.5 to 1.6 ml/min (13% increase) while S3 increased from 1.7 to 1.8 ml/min (~6%). However, flow from S4 and S5 gradually decreased back to the rates exhibited before the interruption; 1.5 and 0.9 ml/min respectively within next three days (~72 hours), and thereafter showed only small variations for 3 more days until the third inflow interruption.

Section S1, S6, S7, S8 and S9 and showed large decreases in their outflows. Outflow from S1 and S6 decreased from 1.5 to 1.4 ml/min and from 0.6 to 0.5 ml/min respectively (slightly over 10%). Flow at S7 and S8 decreased from 0.6 to 0.5 ml/min (~15%) and from 0.4 to 0.5 ml/min (25%) respectively. Decrease of the outflow from S9 was from 0.5 to 0.4 ml/min (over 20%). However, S1 progressively increased back to 1.5 ml/min over next 72 hours (3 days), and thereafter showed only minor changes until the next flow interruption. Similar to the first inflow interruption, outflow from S2 did not show any detectable change after the second inflow interruption.

4.4.3.3 Changes in Outflow after the Third and the Fourth Inflow Interruptions

The third 90 minute long inflow perturbation was done in the 22nd day of the experiment (at the ~515th hour). This inflow interruption was made ~72 hours after the inflow temperature was raised to ~28 ^{o}C from 20 ^{o}C (outflow distribution at the bottom of the column did not substantially change after the inflow temperature increase). Very small changes (<7%) of outflow at some sections (e.g., S4, S5, S8 and S9) were observed

after the inflow interruption. However, the magnitude of these changes was similar to the natural flow rate changes observed throughout the experiment (figure 4.38). Thus it appears that this flow interruption did not immediately affect the outflow structure at the bottom of the column.

The fourth outflow interruption was made in the 22nd day (~539th hour) of the experiment, thus ~24 hours after the third interruption. This inflow break was done for 20 minutes in order to replicate the short interruption made in the second experiment. The magnitude of flow redistribution between the nine sections was slightly higher than that observed after the third interruption, however much smaller than that observed after all other 90-minute and 10-minute interruptions made in the second and the third experiments.

After the fourth inflow interruption, only S7 showed a change of ~10%; it decreased from 0.6 to 0.5 ml/min. Four other sections (S2, S6, S8 and S9) showed slight decreases (between 5% and 10%). Section S4 showed an increase of ~8% from 1.5 to 1.6 ml/min after the interruption. The observed increase of ~5% (from 1.7 to 1.8 ml/min) at S3 may not have resulted from the perturbation because it had been showing a progressively increasing trend for ~20 hours before the inflow pause.

4.4.3.4 Changes of Outflow after the Fifth Inflow Interruptions

The fifth inflow pause, which lasted for 90 minutes, was made in the 29th day (after ~683 hours from the start of the experiment). Temperature of the inflow was lowered to ~16 ^{o}C about 120 hours before the inflow interruption, but there was apparently no impact on outflow from the temperature change. The location of the inlet was changed (described below in section 4.4.3.5) 72 hours before this inflow interruption (figure 4.39).

Thereafter, the system was kept undisturbed until the outflow from all nine sections at the bottom of the column leveled off. Immediately after the inflow interruption, substantial changes in outflow from several sections were observed (figure 4.39). Section S1, S3, S4 and S9 showed increases in outflows. Flow in S3 increased from 0.8 to 1.0 ml/min (25%), while S4 increased from 0.6 to 0.8 ml/min (18%). Increase at S1 was from 1.3 ml/min to 1.5 ml/min (12%). S9 slightly increased from 0.9 to 1.0 ml/min (10%). Three sections (S6, S7 and S8) showed decreased outflows. Flow at S7 decreased from 1.3 to 1.0 ml/min (25%) and that at S6 decreased from 0.9 to 0.8 ml/min (17%). Section S8 showed a slight decrease, but that change was in of same order of its spontaneous changes. No discernable change in outflow was observed at S2 and S5.

4.4.3.5 Changes of Outflow after Relocation of the Inlet

The inlet was initially located at the center of the test column, thus at the center of S1 (point A in figure 4.40). It was moved to two other locations during the experiment. The last perturbation on the system before changing the inlet location was lowering the inflow temperature from ~28 to 16 ^{o}C, which was done ~48 hours prior to the first inlet relocation. Outflow structure did not show any substantial change after the temperature change, thus remained satisfactorily steady for more than 48 hours before the first inlet relocation.

In the 26th day of the experiment (~611 hours after the start) the inlet was moved ~4 cm towards the center of S7, so that it still remained within the central section (S1), but ~1 cm from the boundary with S7 (point B in figure 4.40).

Outflow at many sections at the bottom of the column started to change ~20 minutes after the inlet relocation. Outflow structure largely changed and the new structure

stabilized ~2 hours after the perturbation (figure 4.39). Outflow from S7 increased from 0.6 to 1.8 ml/min (over 200%), showing the highest outflow among the nine sections. During the same time, S6 increased from 0.5 to 1.3 ml/min (over 150%), while S8 increased from 0.3 to 0.6 ml/min (~100%). Flow from S9 also increased from 0.4 to 0.6 ml/min (~50%) over a period of two hours. Outflow from both S3 and S4 showed decreases of over 50%; from 1.7 to 0.8 ml/min and 1.5 to 0.6 ml/min respectively. Flow at S5 decreased from 1.1 to 0.6 ml/min (~40%), while that at S1 decreased from 1.4 to 1.3 ml/min (~10%). No measurable change was observed at S2 following the inlet relocation.

The major redistribution of flow was completed ~2 hours after the inlet was moved. Afterwards, only small fluctuations of (mostly <5% of the mean flow rate at each section) were observed over next 21 hours. Approximately ~23 hours after the inlet location change (i.e., ~634 hours from the start) outflow from many sections changed abruptly within a period of 2 hours. Flow at S8 and S9 showed large increases from 0.7 to 1.1 ml/min (60%) and 0.6 to 0.9 ml/min (50%) respectively. Outflow from S2 increased from 0.4 to 0.5 ml/min (over 25%), while that at S1 slightly increased by ~5% (from 1.2 to 1.3 ml/min). Section S6 showed the largest decrease from 1.3 to 0.9 ml/min (over 30%). Flow at S7 and S5 decreased from 1.8 to 1.3 ml/min (over 25%) and from 0.6 to 0.5 ml/min (20%) respectively. However, S3 and S4 did not show substantial changes.

The inlet was moved back to the center of S1, thus to the center of the column (point A in figure 4.40) in the 30th day of the experiment (after ~709 hours from the start). The last perturbation before this move was an inflow pause (described before in section 4.4.3.4) ~24 hours prior to it. The newly established outflow distribution appeared to be

stable during the period between the inflow interruption and relocation of the inlet (figure 4.39).

Outflow from all nine sections started to change ~20 minutes after the relocation, reaching a new "equilibrium" in ~5 hours. Section S3, S4 and S5 showed large increases. Flow at S4 showed an increase of over 100%, from 0.7 to 1.6 ml/min; both S3 and S5 increased by over 90%; from 1.0 to 1.9 ml/min and from 0.6 to 1.1 ml/min, respectively. Flow at all other sections (S1, S2, S6, S7, S8 and S9) substantially decreased after the inlet relocation. The highest decrease was observed at S8, from 1.1 to 0.4 ml/min (over 60%). Section S9 and S7 also showed large decreases, from 1.0 to 0.4 ml/min (60%) and from 1.0 to 0.5 ml/min (50%) respectively. The decreases at S2 and S6 were from 0.5 to 0.4 ml/min and 0.8 to 0.6 ml/min, respectively; both changes were over 20%. Flow at S1 decreased from 1.5 to 1.3 ml/min (over 10%). The outflow rates appeared to stabilize ~5 hours after the inlet was moved.

In the 31st day of the experiment (732 hours from the start), the inlet was relocated again. This time it was moved in the same direction as in the first relocation (i.e., towards the center of S7), but located only ~2.5 cm from the center of S1 (Point C in figure 4.40). Substantial changes in outflow rates at different sections were visible ~20 minutes after relocating the inlet, and the new outflow distribution stabilized after ~3 hours. Outflow from S1, S2, S6, S7, S8 and S9 increased, while that from S3, S4 and S5 decreased rapidly within the 3-hour period (figure 4.39).

Flow at S8 and S9 increased from ~0.4 to ~0.5 ml/min (over 30%), while that at S7 increased from ~0.4 to ~0.5 ml/min (25%). Flow at S1 increased from 1.2 to 1.4 (over 10%). The increases at S2 and S6 were less than 5% of their mean flow rates and the

actual increase was in the same order of the spontaneous changes. Flow from S3, S4 and S5 largely decreased over the period of three hours. The highest decrease was at S5, from 1.2 to 0.9 ml/min (25%). Section S3 and S4 decreased from 1.9 to 1.7 ml/min and 1.6 to 1.4 ml/min respectively; both over 10%.

At the 773rd hour of the experiment (i.e., ~41 hours after the third inlet relocation) flow at several sections showed large simultaneous changes (A in figure 4.39). Large and rapid changes occurred over a period of five hours, then small and progressive changes occurred over another ~10 hours. Flow at both S8 and S9 increased from 0.5 to 0.6 ml/min (~20%), while that at S7 increased from 0.6 to 0.7 ml/min (over 15%). Simultaneously, flow at S3, S4 and S5 showed rapid decreases. Change at S3 was from 1.8 to 1.5 ml/min (over 15%). Flows at S4 and S5 decreased from 1.5 to 1.3 ml/min and from 0.9 to 0.8 ml/min respectively (both over 10%). Section S1, S2 and S6 showed flow fluctuations of the order of their natural fluctuations during this period, but not any substantial changes.

4.4.3.6 Changes in Outflow after Reducing Evaporation from the Column

In the 34th day of the experiment (i.e., 803 hours after the initiation and 71 hours after the last inlet relocation) the top of the test column was covered with a plastic sheet. A small opening was left for the inflow tube. About 30 minutes after covering the top, outflow from several sections at the bottom of the column started to change (figure 4.41). Outflow from S1, S2, S6, S7, S8 and S9 started to increase, while S3, S4 and S5 decreased rapidly. Section S8 showed the highest increase from 0.5 to 1.0 ml/min (over 100%), while S9 showed an increase from 0.6 to 0.9 ml/min (~50%). Flow at S2 and S7

increased from 0.4 to 0.5 ml/min and from 0.7 to 0.8 ml/min and respectively (both were ~20%). Section S1 showed a slight increase of less than 10%, from 1.5 to 1.6 ml/min.

Decreases of flow at S3, S4 and S5 were over 20%. Section S3 decreased from 1.5 to 1.2 ml/min. Decreased at S4 and S5 were from 1.3 to 0.9 ml/min and from 0.8 to 0.7 ml/min respectively. The system appeared to reach equilibrium about five hours after covering the top of the column. The cover was removed after it had been in place for ~41 hours (i.e., in the 36th day; ~844 hours after the start of the experiment). Outflow at five sections (S3, S4, S5, S8 and S9) started to show changes ~1 hour later (figure 4.41). Flow at S8 increased from 0.9 to 1.1 ml/min (~20%), while that at S3 and S4 decreased from ~1.2 to 1.0 ml/min and 1.0 to 0.9 ml/min respectively (over 10%). Apparent changes at S5 (a decrease) and at S9 (an increase) were observed after uncovering the top of the column, but these changes were less than 10% of their mean flow rates and in the same range of natural fluctuations. The other four sections (S1, S2, S6 and S7) did not show any detectable change in their outflows.

4.4.4 Temperature of the Inflow and Inside the Column in Experiment #4

In the first 18 days (432 hours) of the experiment, inflow temperature varied between 18.0 and 20.5 ^{o}C (figure 4.29). The temperature inside the column remained below the mean room temperature. The bottom of the column was ~2 ^{o}C warmer than the top. The temperature at the top of the column varied between 20 and 23.9 ^{o}C, while that at the middle varied between 20.9 and 24.5 ^{o}C respectively. The temperature at the bottom fluctuated between 21.5 and 26.1 ^{o}C.

Temperature of the inflow was increased in the 19th day of the experiment (after 443 hours from the beginning) and maintained between 28.3 and 29.5 ^{o}C for five days (until

the 563rd hour). This change substantially increased the temperature inside the column (figure 4.29). The temperature at the top of the column started to increase first, followed by that at the middle. Temperature at its bottom started to increase after ~36 hours from the inflow temperature change. Therefore, within the first ~36 of the temperature increase of the inflow, temperature gradient in the column was very low. After the temperature at bottom of the column increased, it remained warmer than the top. The temperature at the top varied between 25.7 and 27.4 ^{o}C, while that at the middle and the bottom varied between 26 and 27.5 ^{o}C, but the bottom was slightly warmer than the middle. During the period between the 20th and 24th days, temperature at the middle and the bottom of the column, as well as middle of the room remained close to each other. In the 24th day of the run (~563 hours after the beginning) the inflow temperature was lowered and maintained between 16 and 16.7 ^{o}C until the end of the experiment (figure 4.29). After this change, the temperature inside the column substantially decreased. The top of the column was the coldest, and the temperature varied between 20.9 and 22.0 ^{o}C. Temperature increased towards the bottom, and the temperatures at the middle and at the bottom varied from 21.8 to 22.5 ^{o}C and from 24.1 to 25.1 respectively. The temperature at the top of the column decreased faster than that at the middle and the bottom. Daily and long-term fluctuations of the temperature inside the column were visible in response to changes in the room temperature.

4.4.5 Relative Humidity Above and Inside the Column in Experiment #4

Relative humidity (RH) measured at 6.0 and 33.0 cm above the top of the column always remained ~4% and 1% higher than that of the ambient environment (figure 4.30). In the first 10 hours of the experiment, RH inside the column increased rapidly (figure

4.42). The increase at the middle of the column (measured at 50 cm depth) was faster than the increases both at the top (measured at 10 cm depth) and the bottom (measured at 90 cm depth). At the top of the column, RH reached to 90% in 11 hours and then reached to ~100% within 24 hours. The lowest RH in the column was recorded at the bottom. At the bottom, RH reached to 90% after ~17 hours, but it took ~12 days to reach to ~100%.

Increased temperature of the inflow in the 19th day lowered the RH inside the column (A in figure 4.42). The decrease of RH at the top was very low, but the decreases were ~10% and 20% at the middle and the bottom respectively. After the temperature of the inflow was lowered again in the 24th day, RH inside the column increased back to ~100%. Immediately after covering the top of the test column to reduce the evaporation at the ~803rd hour, the RH at the top of the column increased by ~2%, but that at the middle and the bottom did not show any substantial change. Furthermore, any change in the RH above the column was not observed after covering the top of the column. Throughout the course of the experiment, RH inside the column slightly decreased for a short period (<10 minutes) during evacuation of the collection vessels. The decrease was highest at the bottom (~3%) and the lowest at the top (~1%).

4.4.6 Variation of the Inflow and the Total Outflow

The total outflow from the test column was measured for three days using an electronic balance. The mean total outflow always remained between 7.8 and 8.0 ml/min except several very short-term fluctuations (figure 4.43) and the cumulative outflow remained slightly less than the cumulative inflow (figure 4.44). The increase of the weight of the test column during this period was very low and in the range of the measurement error. Therefore, it appears that the difference between the inflow and the

outflow is mostly due to evaporation. The calculated evaporation over the three day period varied between ~87 and 98 g/day. Hourly scale fluctuations of the total outflow were strongly related to the fluctuations of the inflow. The lag between a particular inflow fluctuation and the corresponding outflow fluctuation was ~20 minutes, which is equal to that observed in the first experiment. It implied that the effective velocity of water flow in the column, which was dominated by film flow, ~ 3.0 m/hour.

The total outflow measured using the electronic balance did not show any instance that the total outflow rate exceeded the inflow rate. In contrast, the total outflow rate measured using 1 psi pressure transducers appeared to be higher than the inflow rate at some instances (figure 4.32). Furthermore, the outflow measured using pressure transducers showed a higher frequency of fluctuation in comparison to that measured using an electronic balance. It implies that the background noise, internal noise in the data acquisition system and/or calculation errors slightly affect the calculated outflow from the test column. However, that effect is very small in comparison to the total outflow from the column and does not have a substantial impact on overall results.

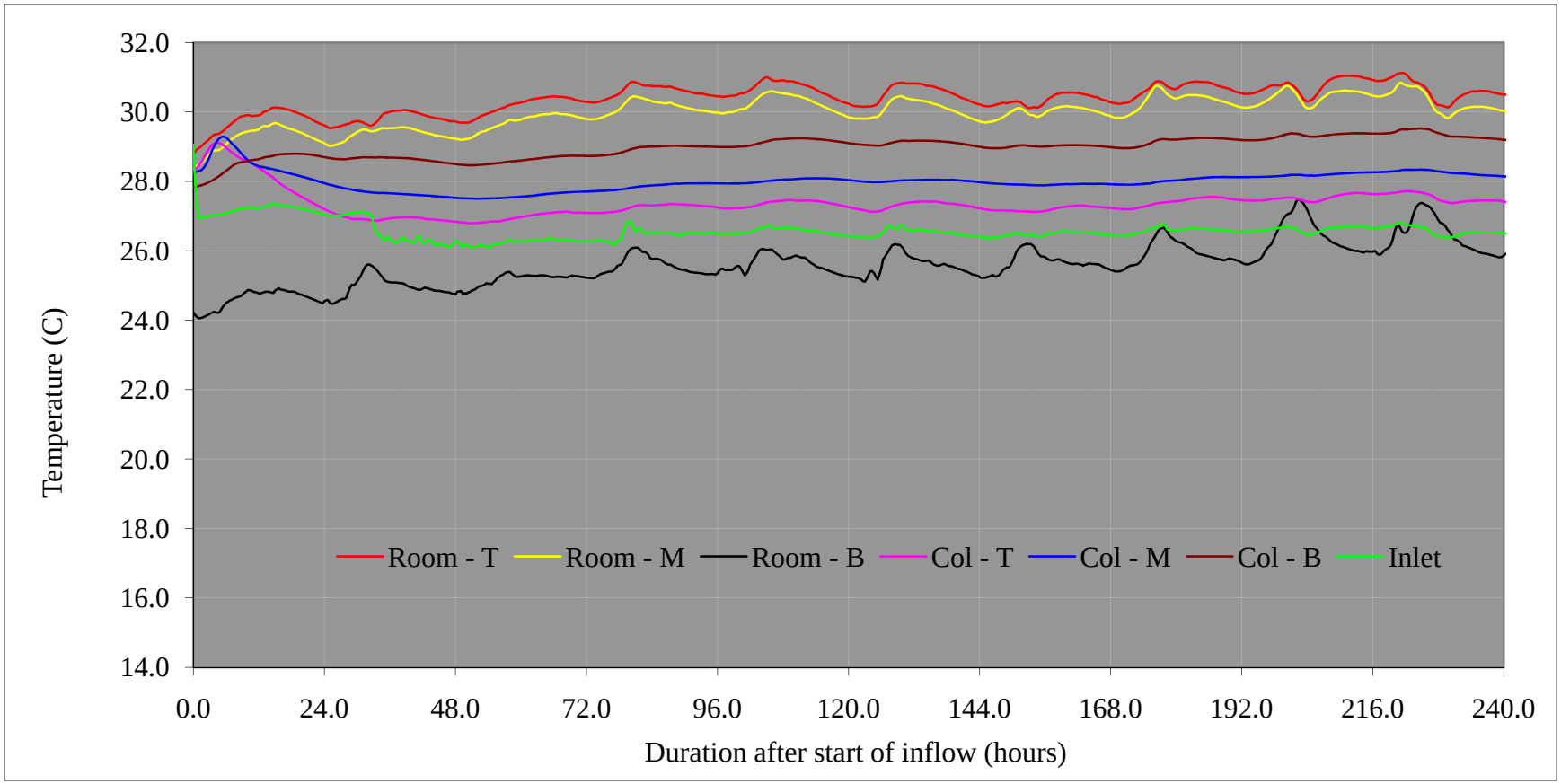

Figure 4.1 Variation of temperature in the room, inside the column and the inflow during experiment #1(T, M and B stand for top, middle and top. Refer to section 3.4.1 for locations of the sensors)

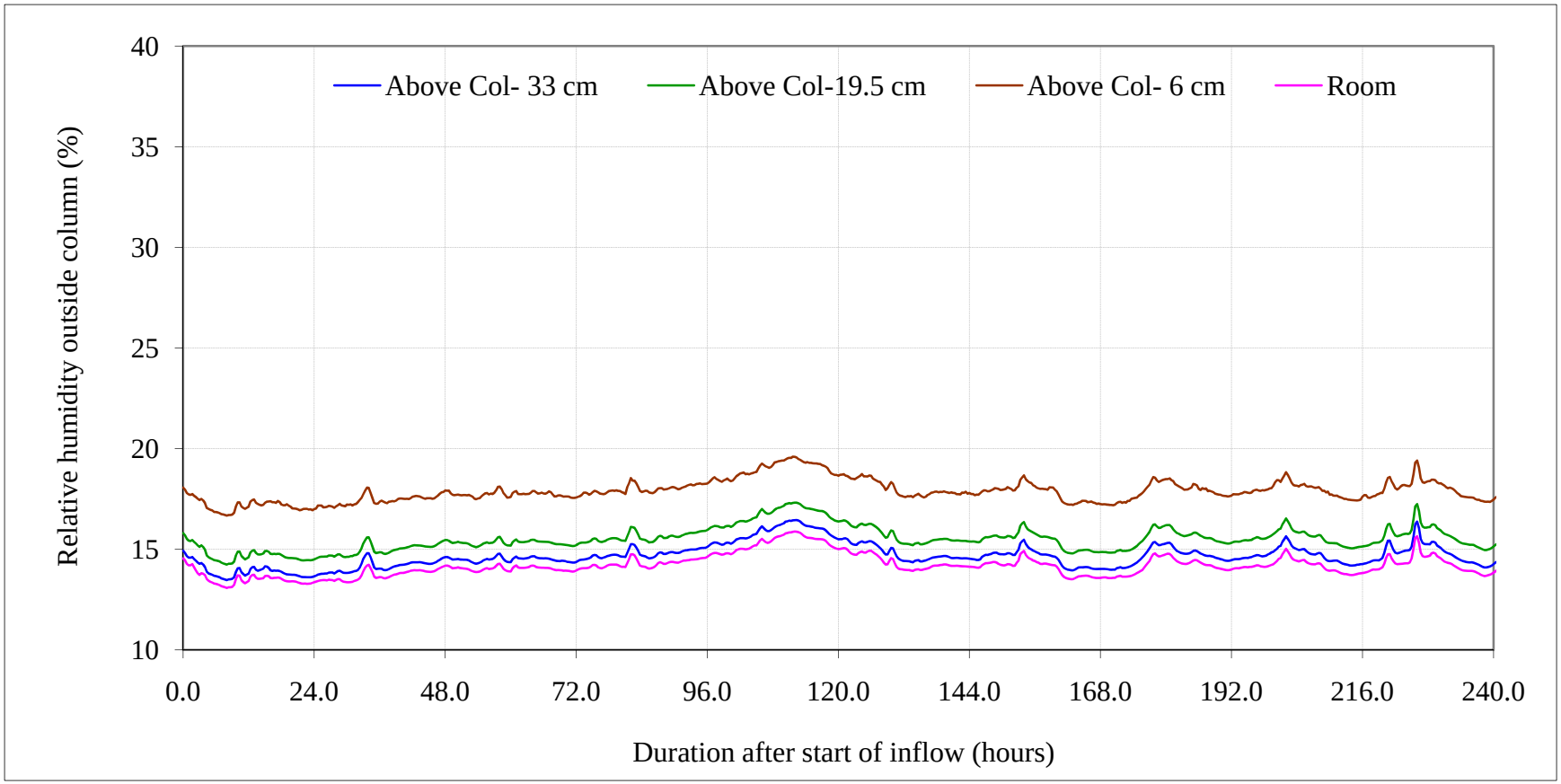

Figure 4.2 Variation of relative humidity in the ambient environment (room) and above the test column during experiment #1

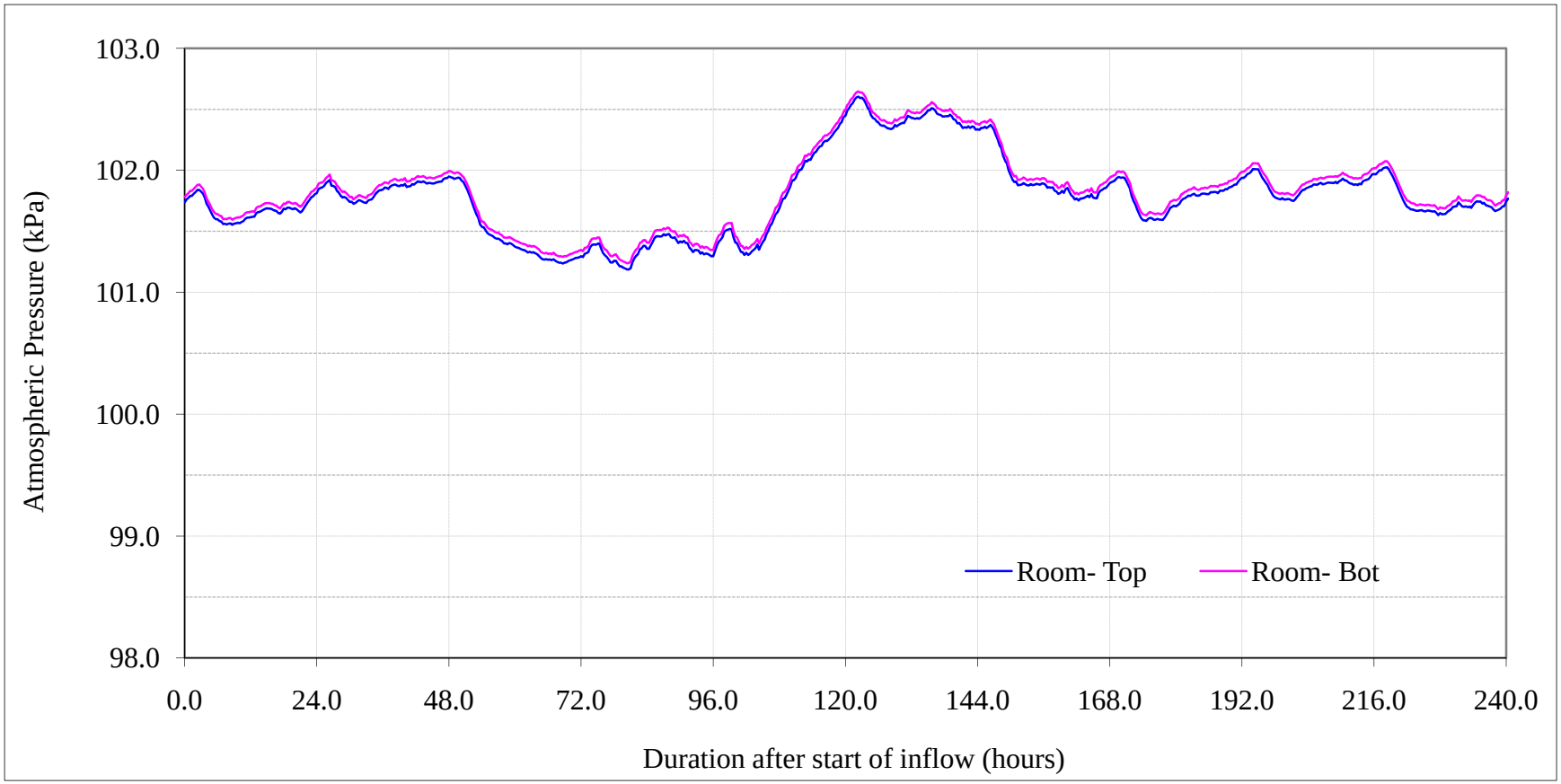

Figure 4.3 Variation of the atmospheric pressure during experiment #1

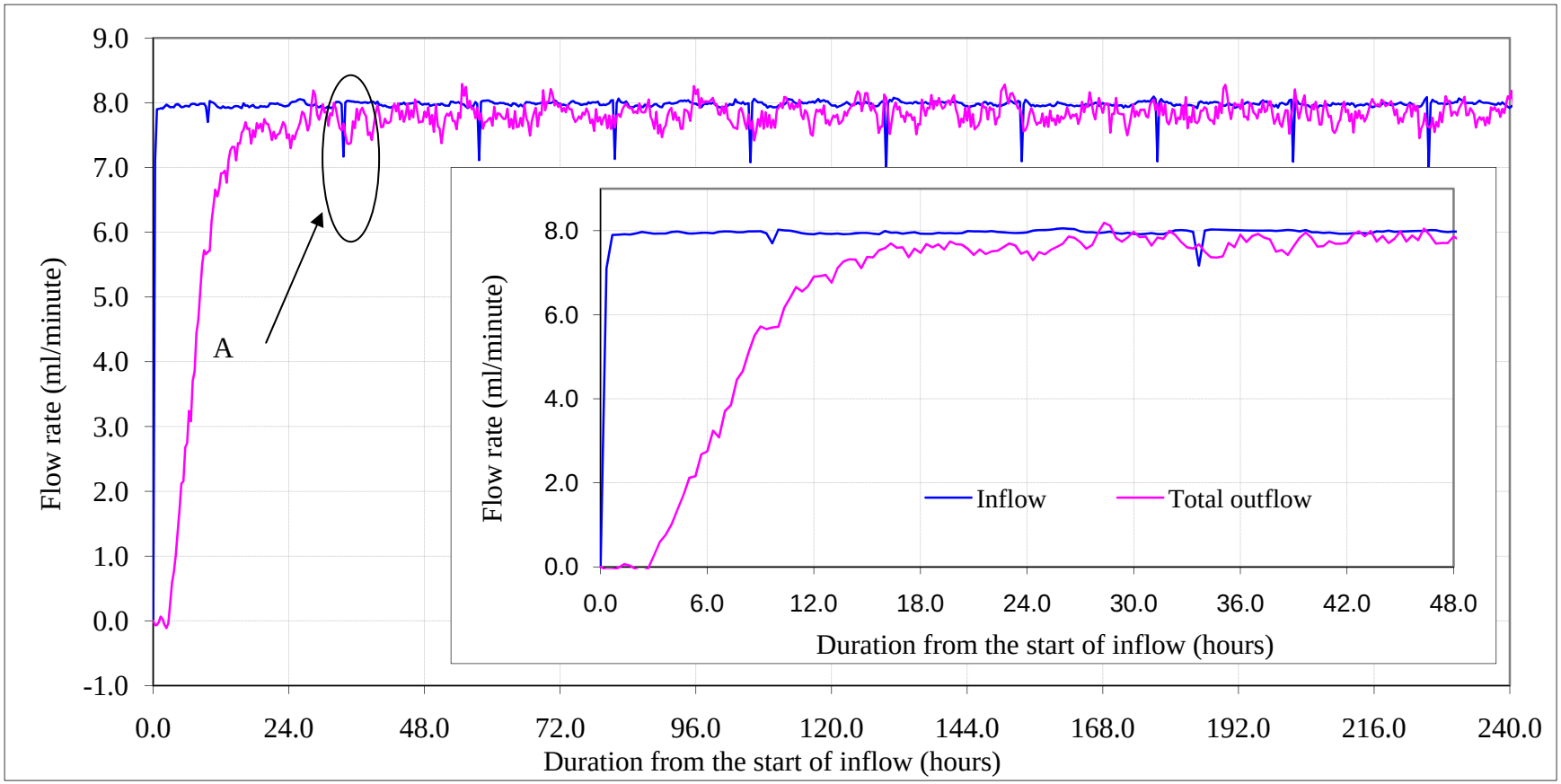

Figure 4.4 Variation of the inflow and total outflow during experiment #1. The inset graph shows the inflow and total outflow during the first 48 hours at a large scale.

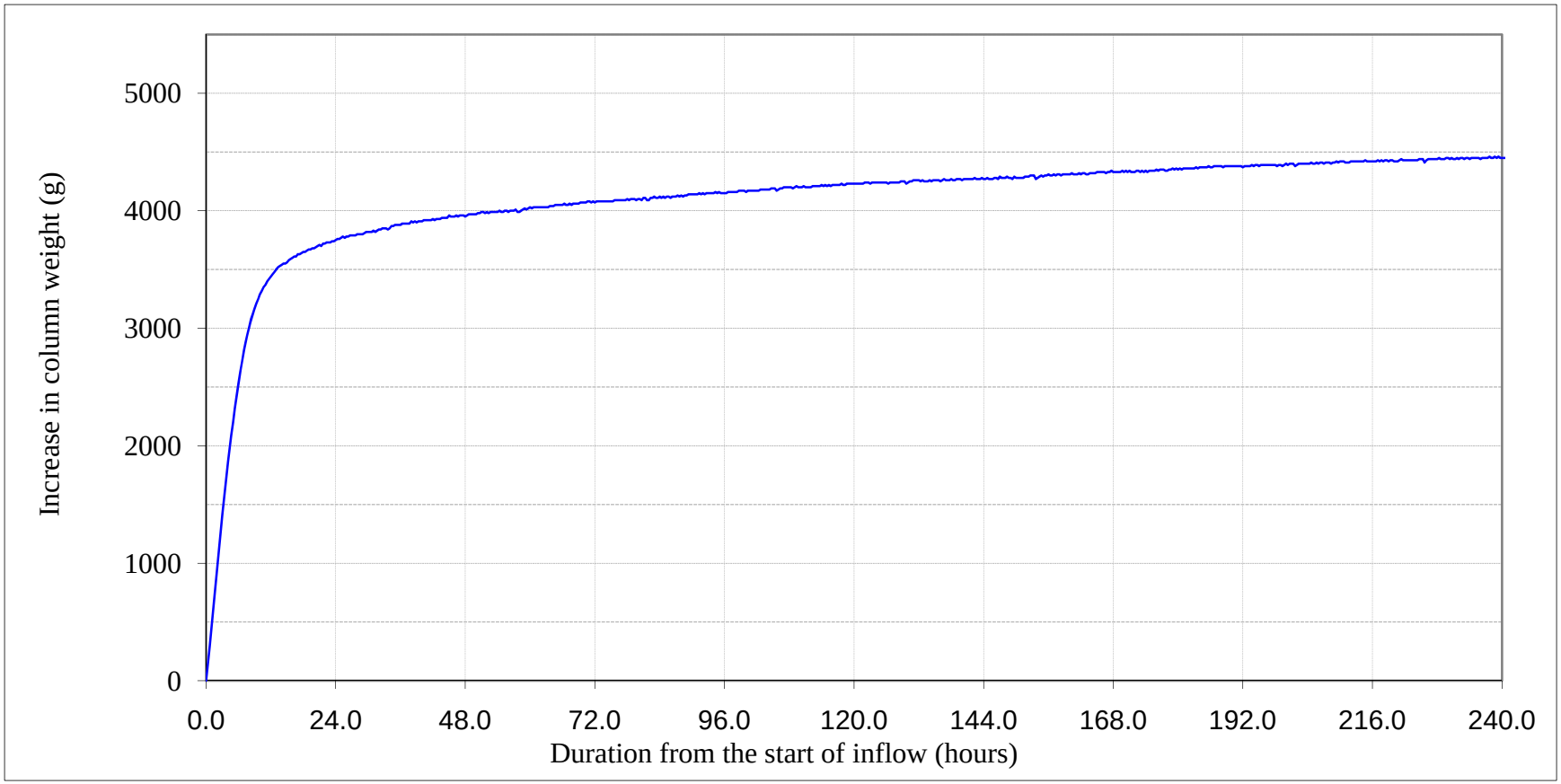

Figure 4.5 Increase of the weight of the test column due to the increase of saturation of the rocks during experiment #1

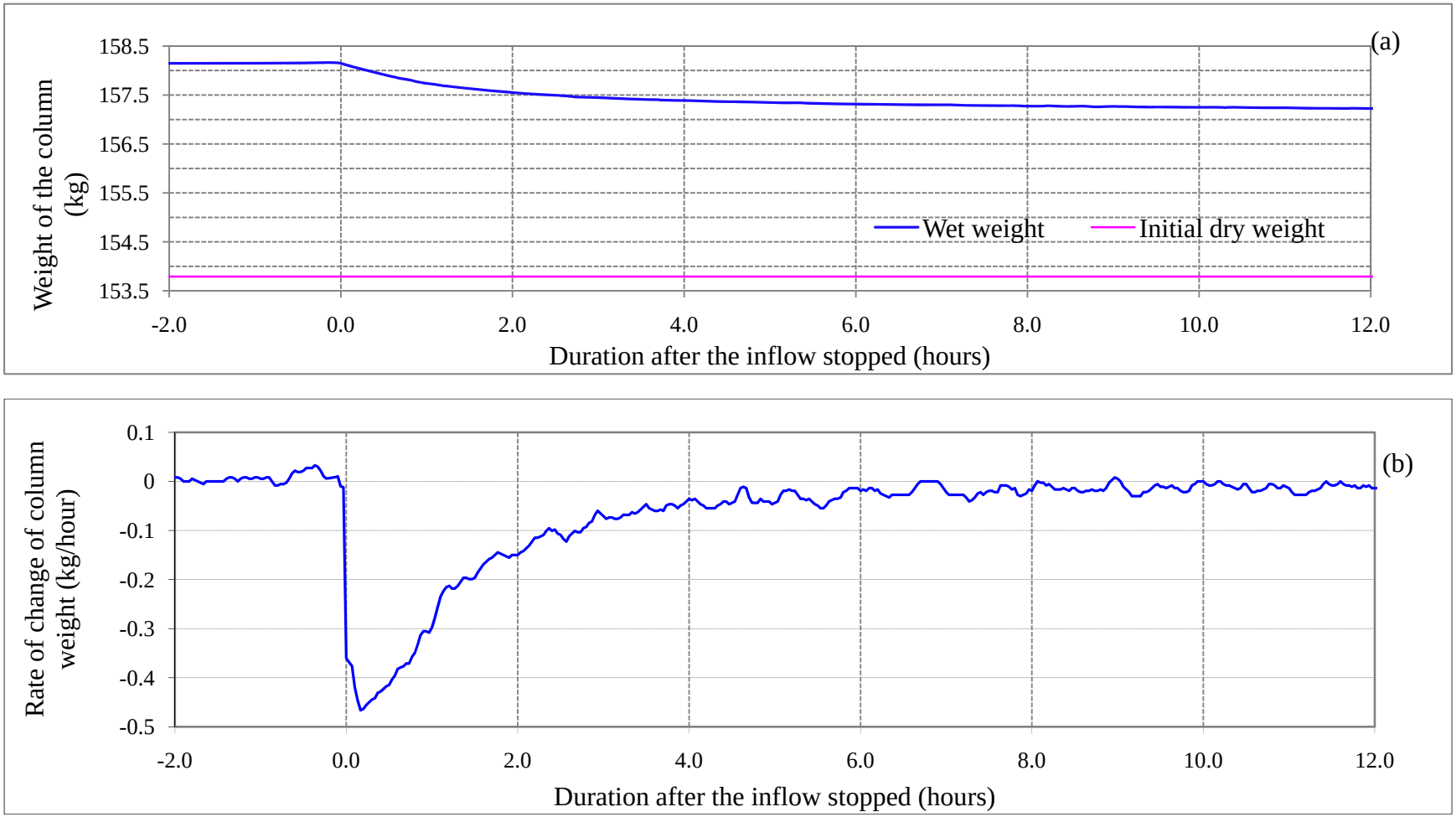

Figure 4.6 Change in weight of the column (a), and rate the change (b) after the inflow stopped at the end of experiment #1 (inflow was stopped at time zero on the X-axis)

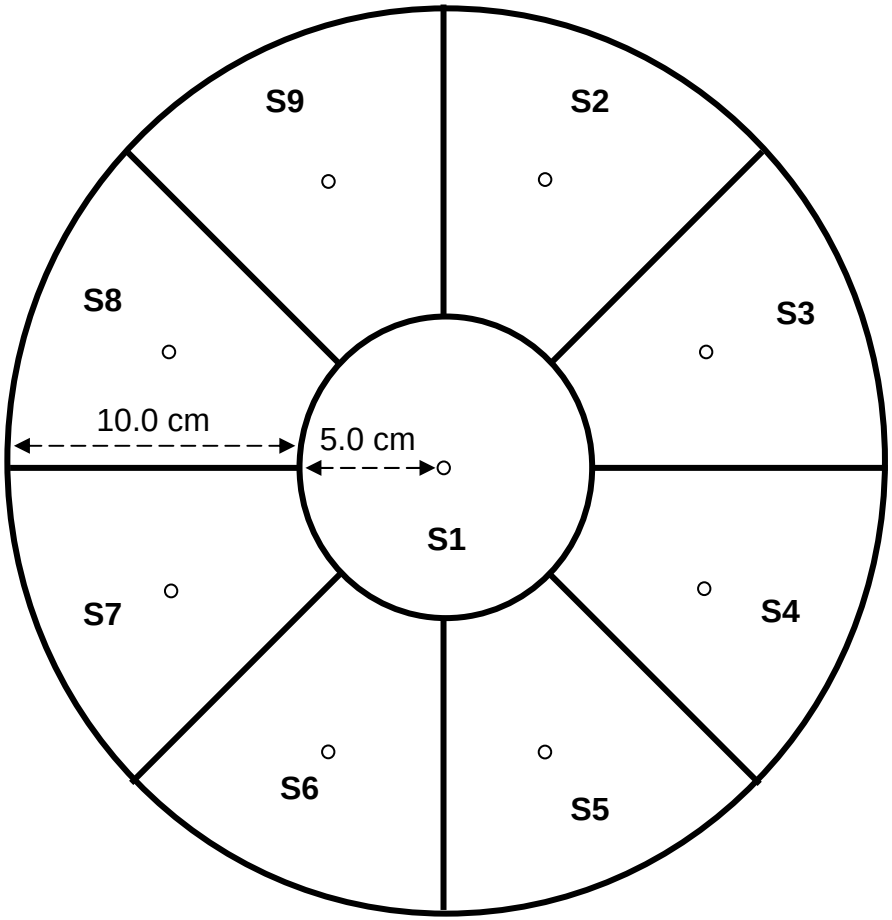

Figure 4.7 Numbering of the nine equal-area sections at the bottom of the test column

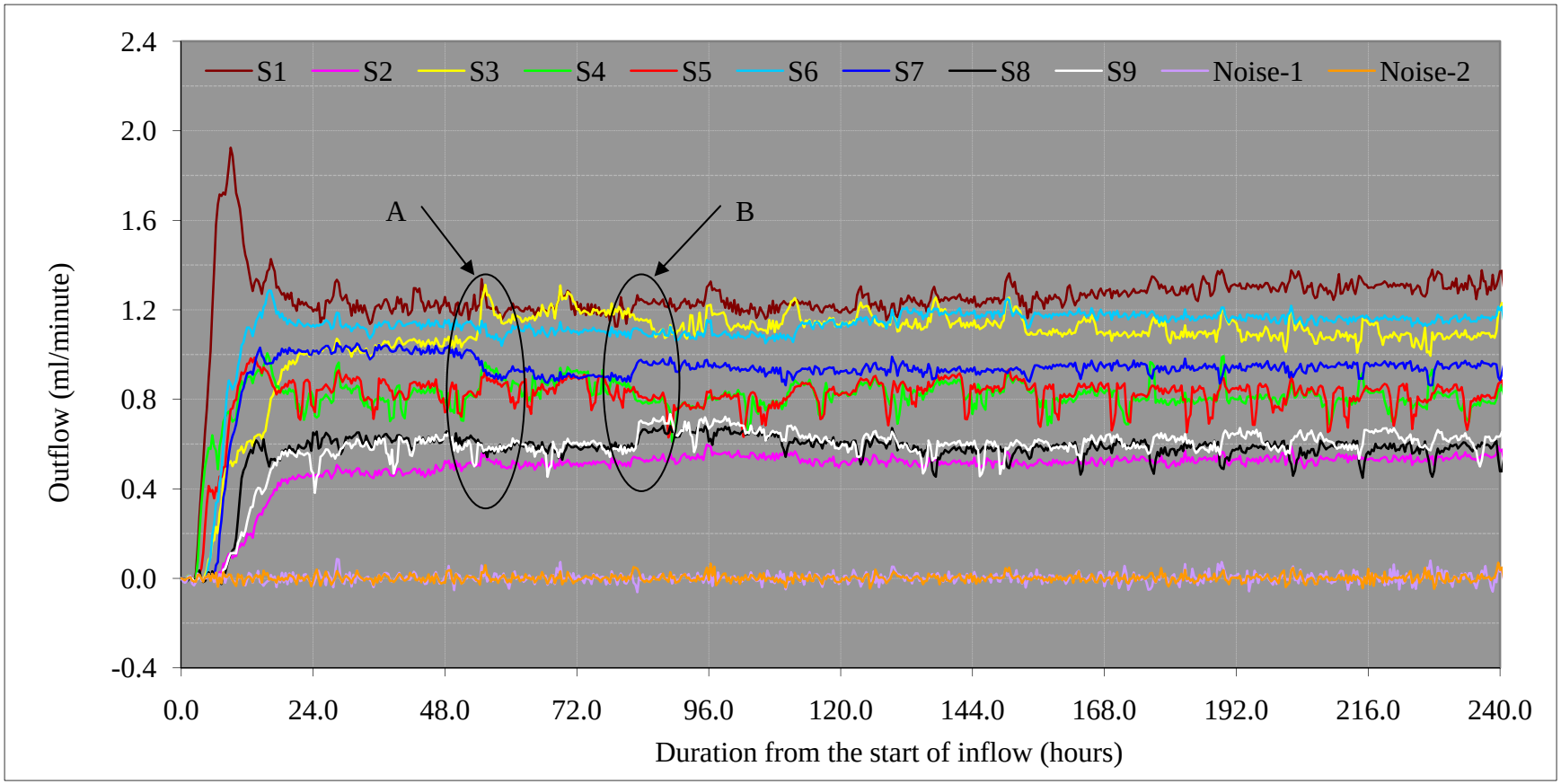

Figure 4.8 Outflow from all nine sections and background noise during the 10-day run of experiment #1

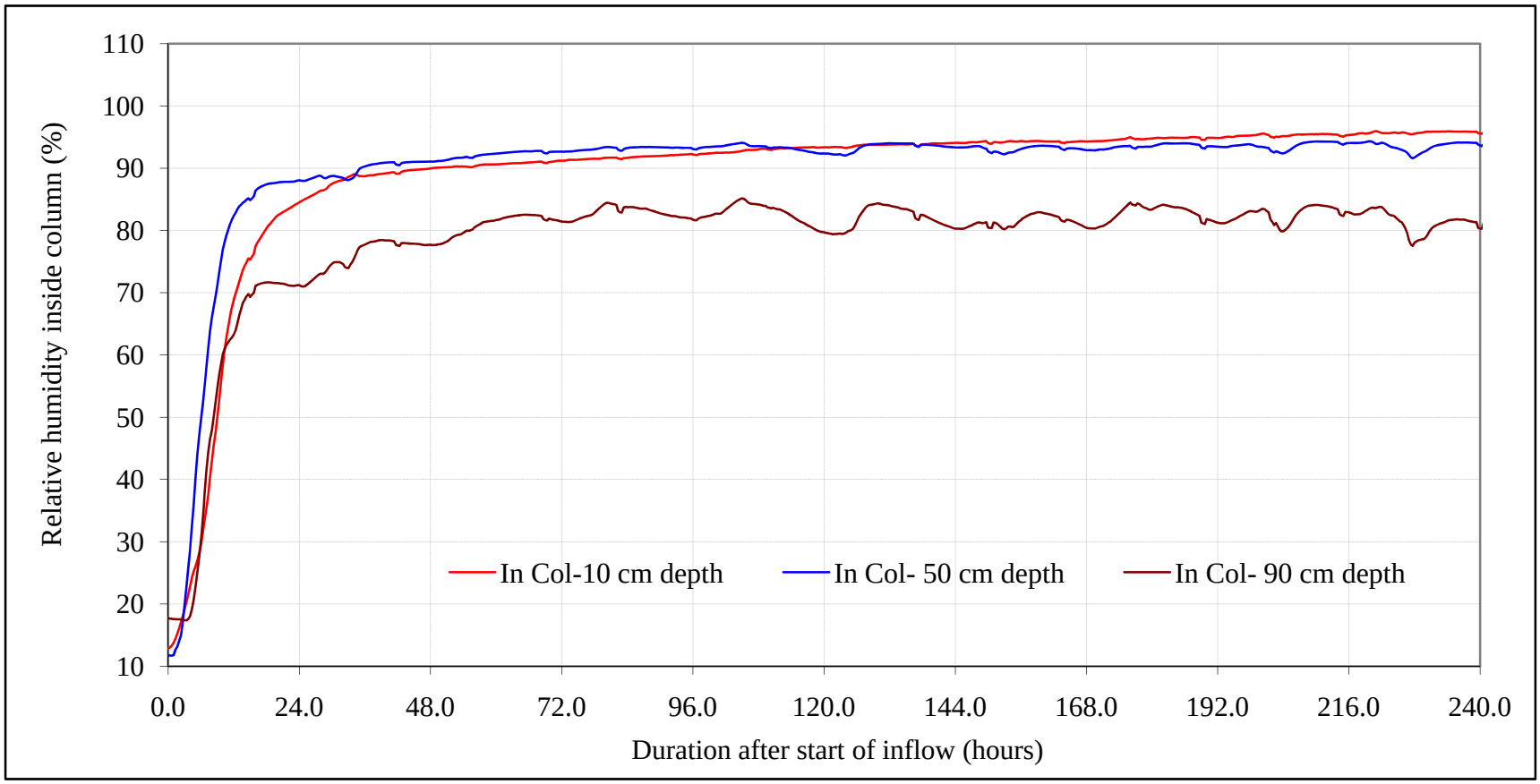

Figure 4.9 Variation of relative humidity inside the column during experiment #1

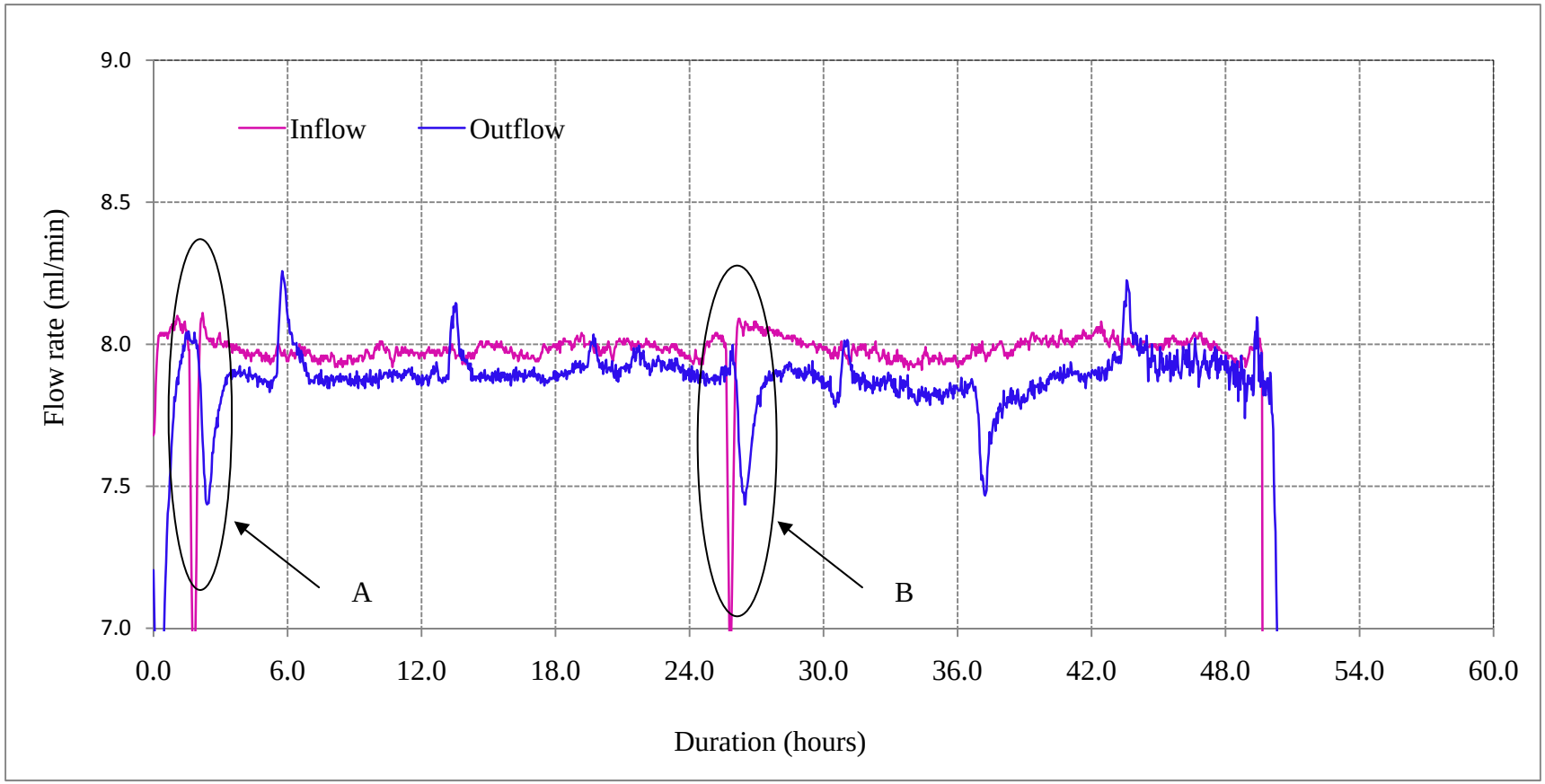

Figure 4.10 Variation of the inflow and the total outflow measured using an electronic balance at the end of experiment #1

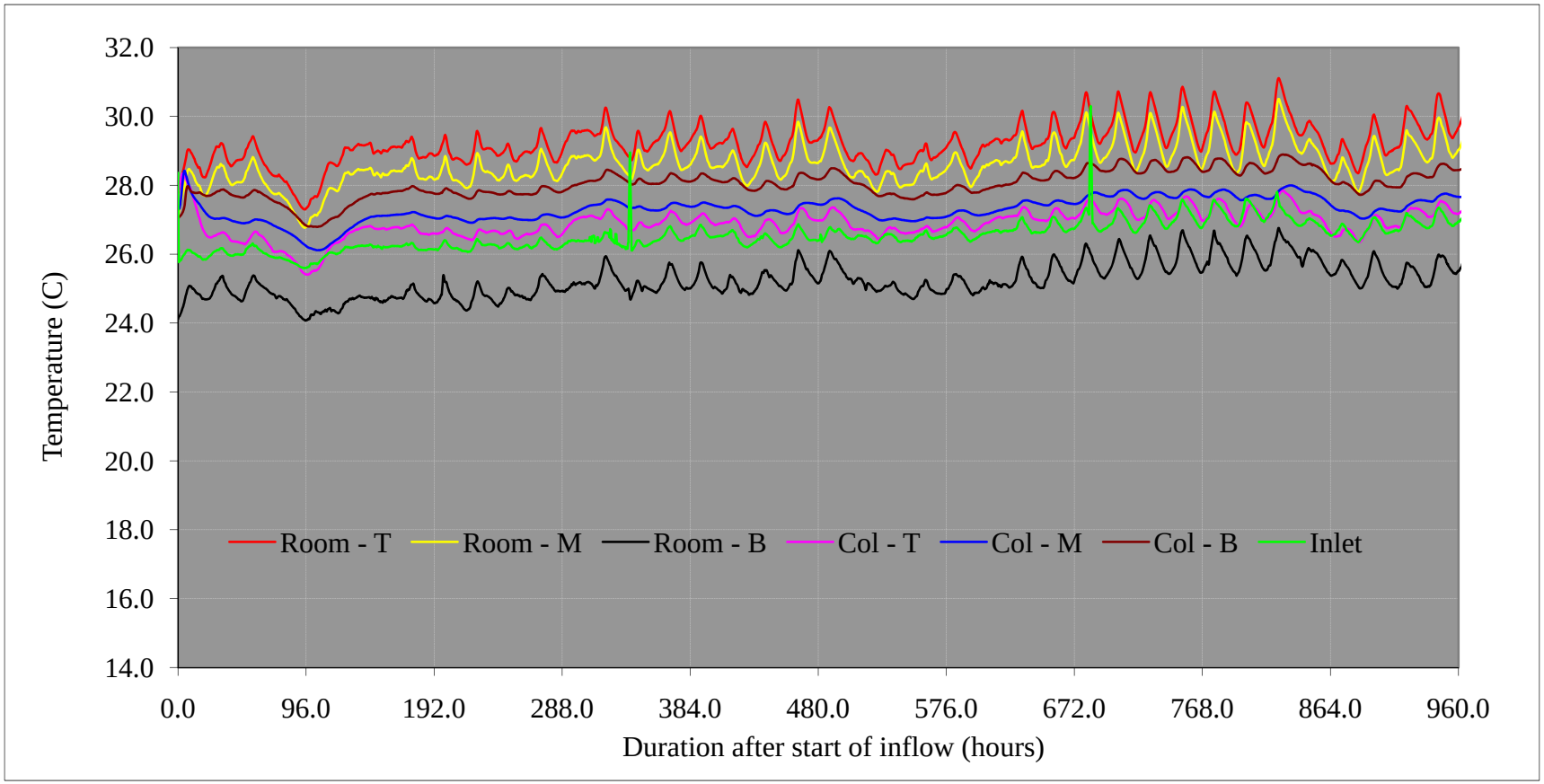

Figure 4.11 Variation of temperature in the room, inside the column and the inflow in experiment #2

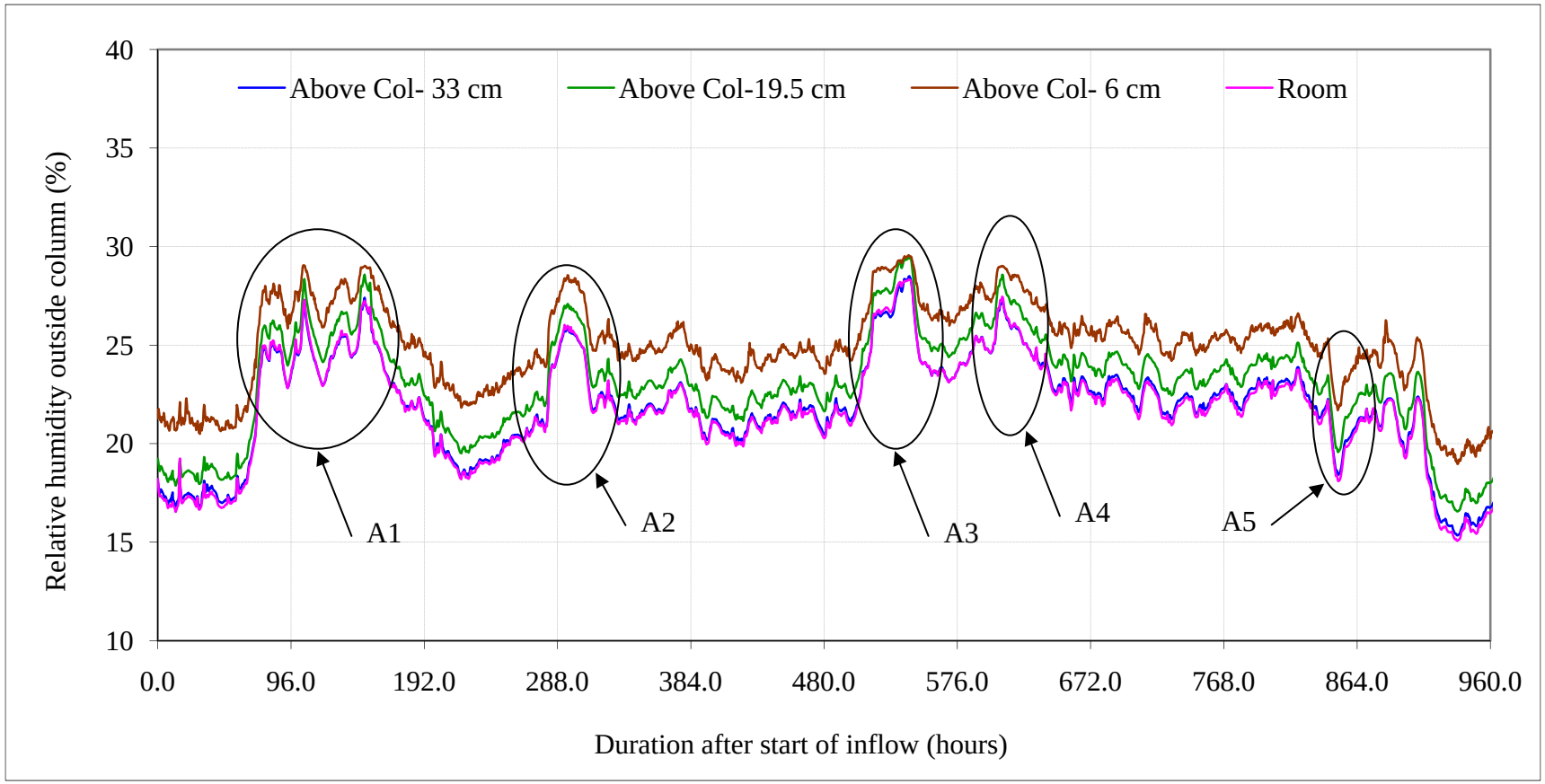

Figure 4.12 Variation of relative humidity in the ambient environment (room) and above the test column in experiment #2

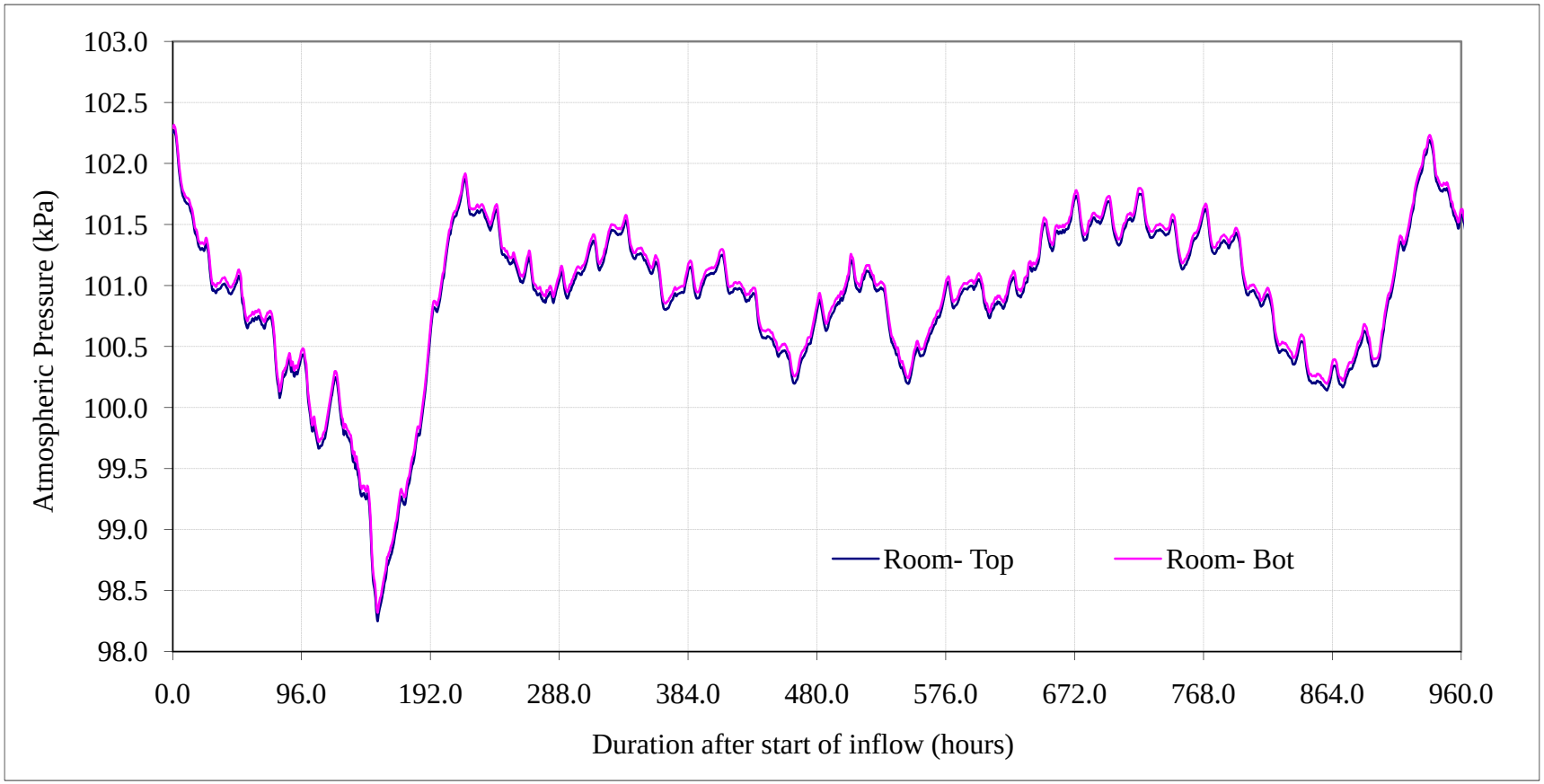

Figure 4.13 Variation of the atmospheric pressure during experiment #2

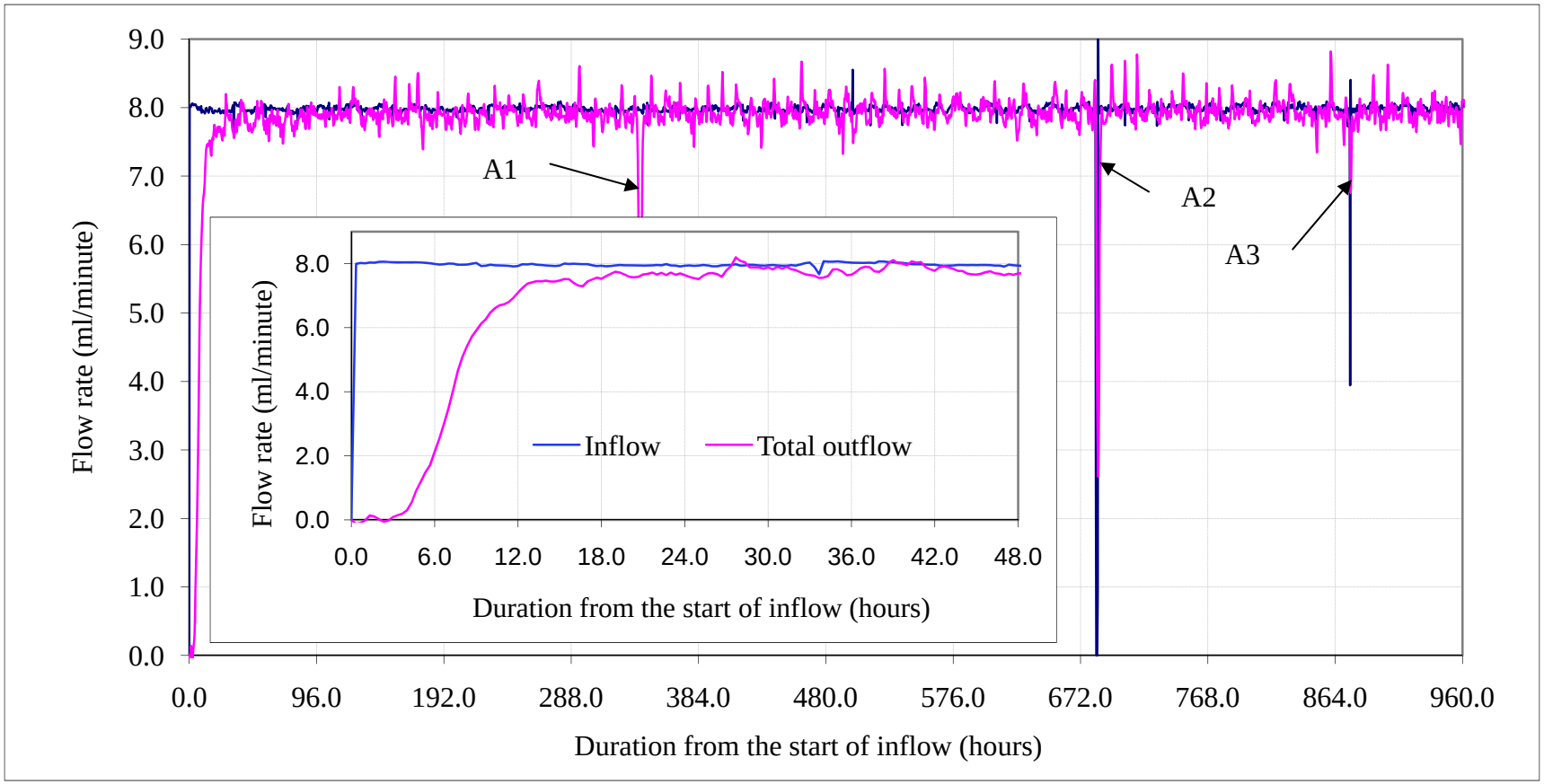

Figure 4.14 Variation of inflow and the total outflow during experiment #2 (A1, A2 and A3 are inflow interruptions). The inset graph shows the inflow and total outflow during the first 48 hours at a large scale.

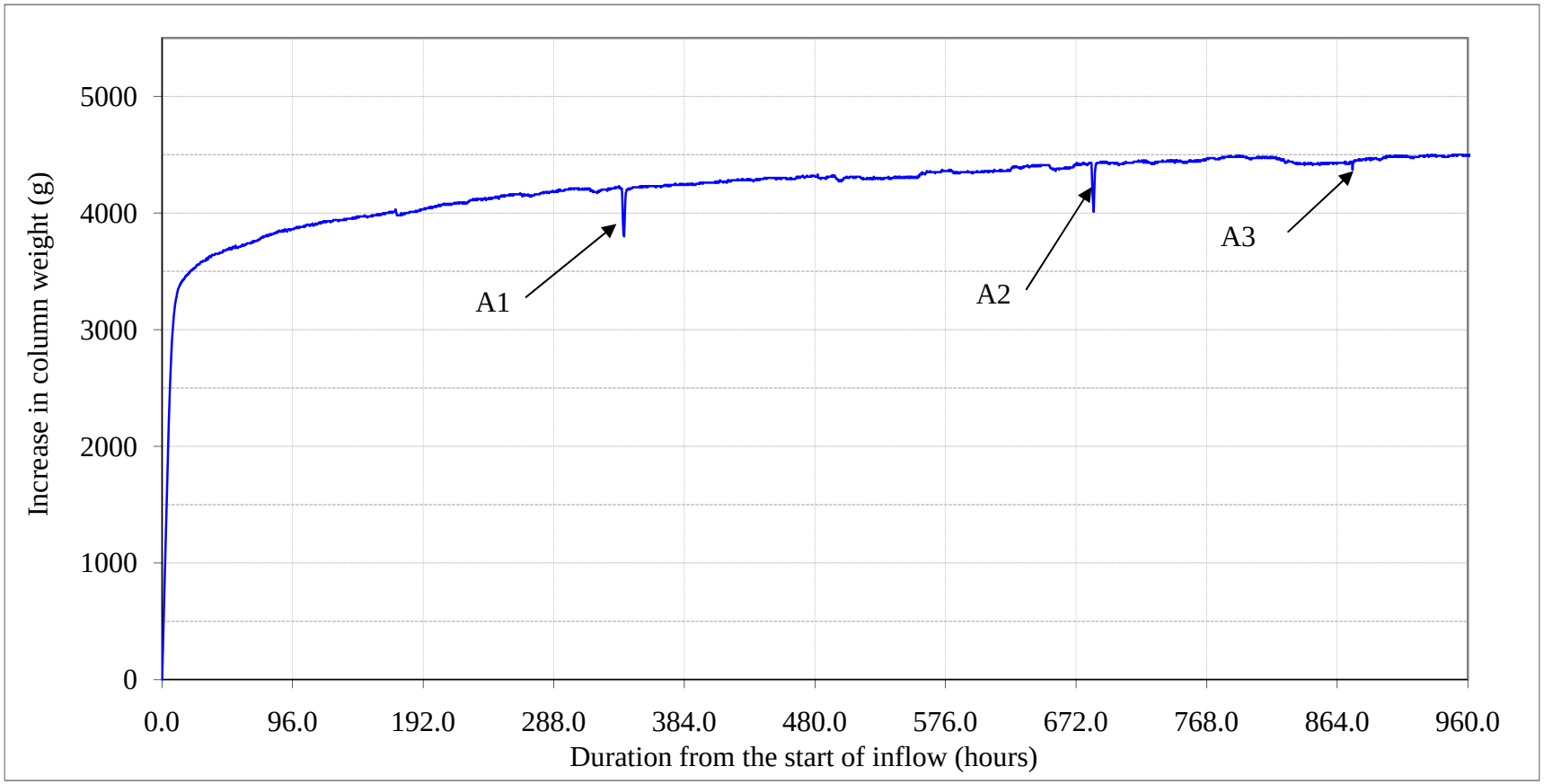

Figure 4.15 Increase of the weight of the test column due to the increase of saturation during experiment #2 (A1, A2 and A3 are inflow interruptions)

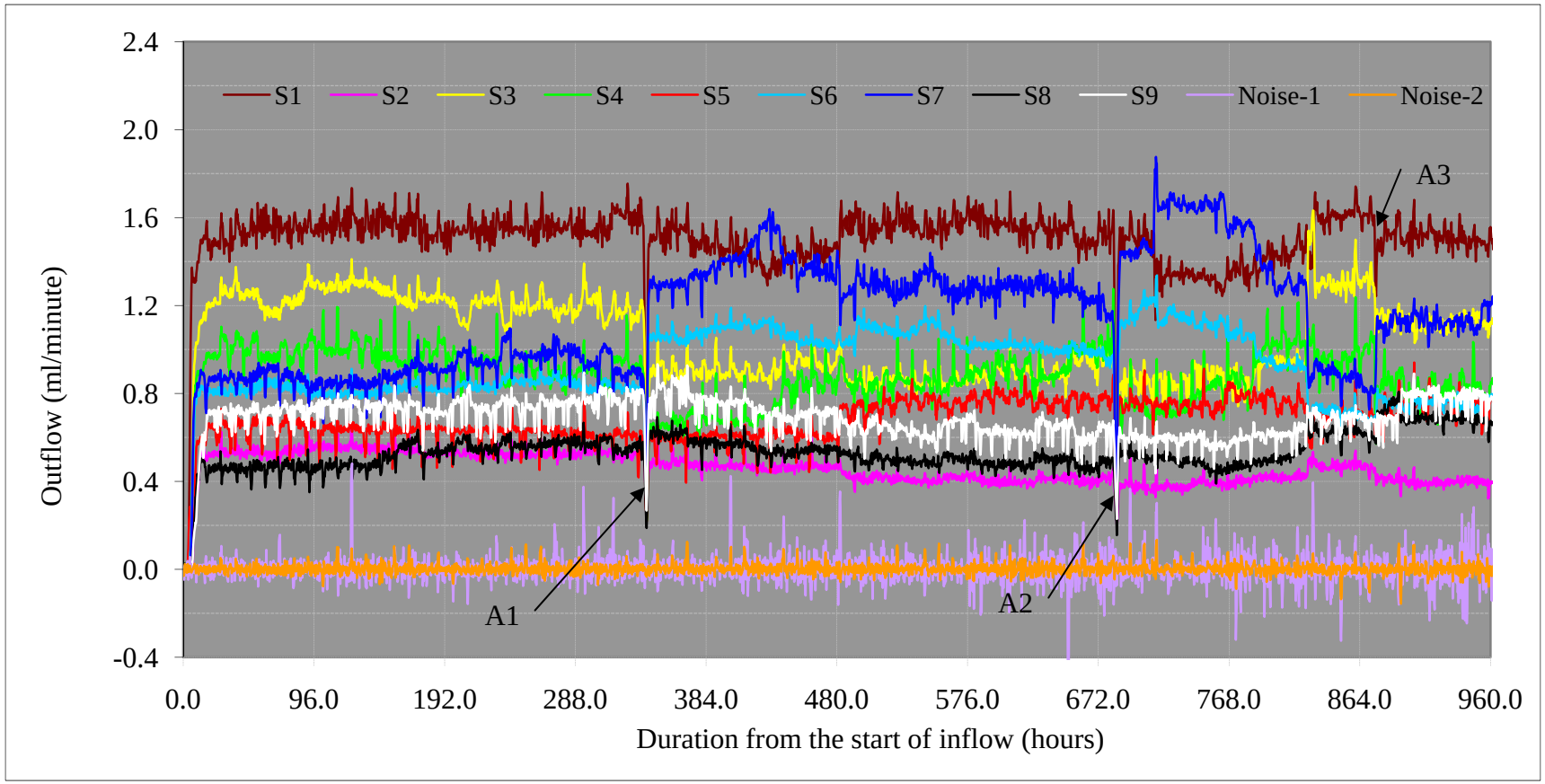

Figure 4.16 Outflow from all nine sections and the background noise during the 40-day run of experiment #2 (A1, A2 and A3 are inflow interruptions)

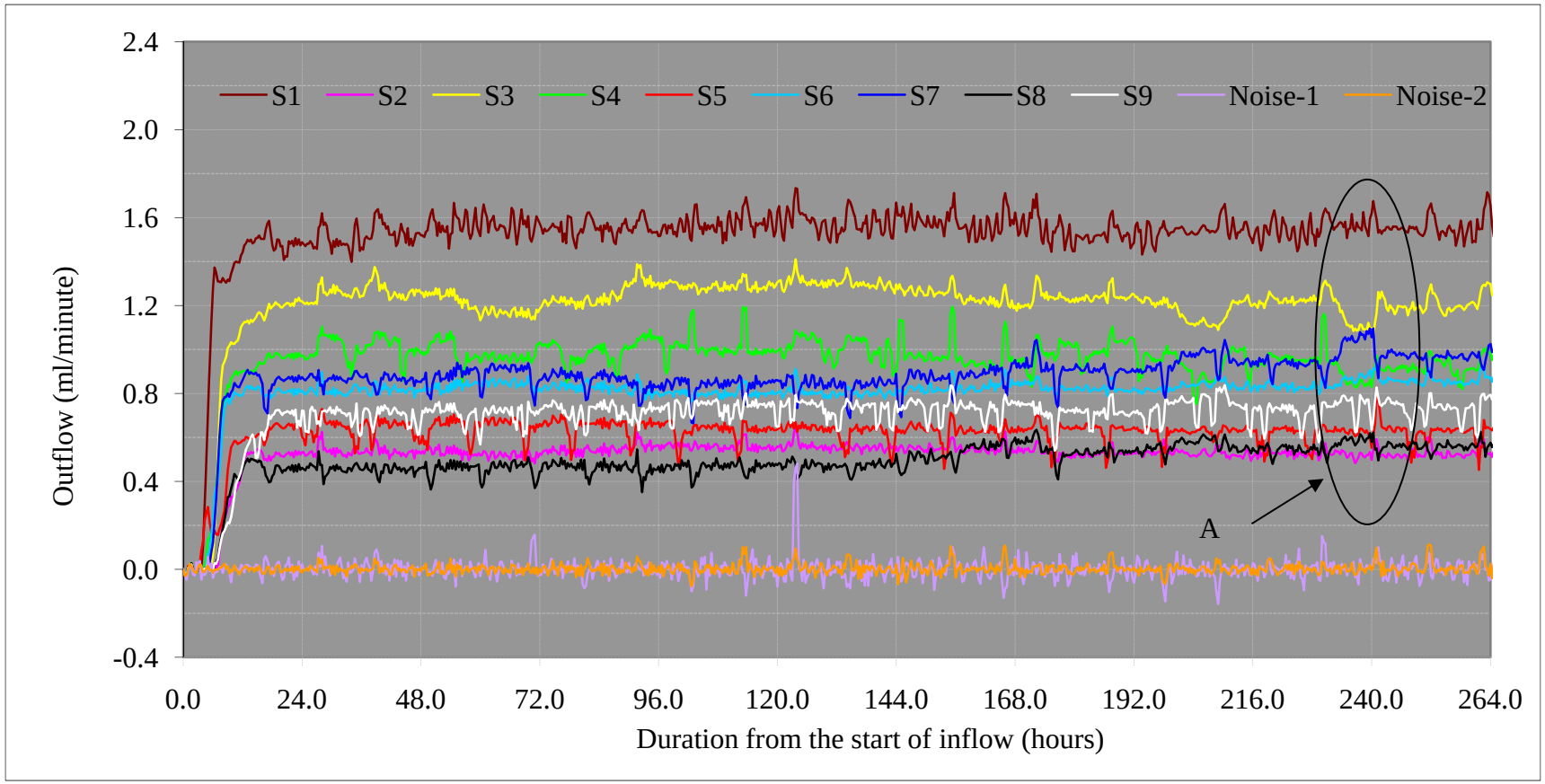

Figure 4.17 Outflow from nine sections during the first 11 days of experiment #2

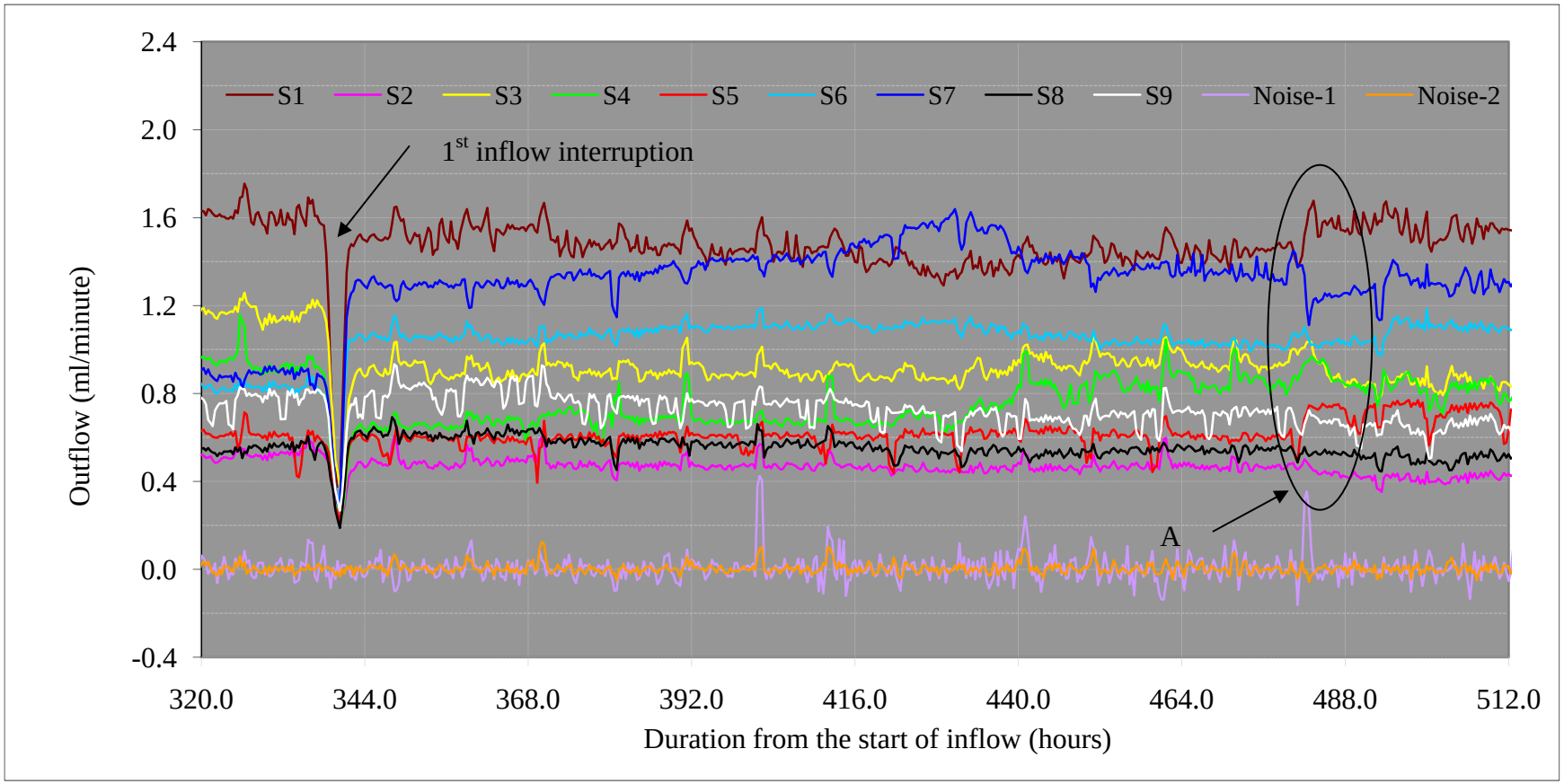

Figure 4.18 Outflow from nine sections before and after the first inflow interruption in experiment #2

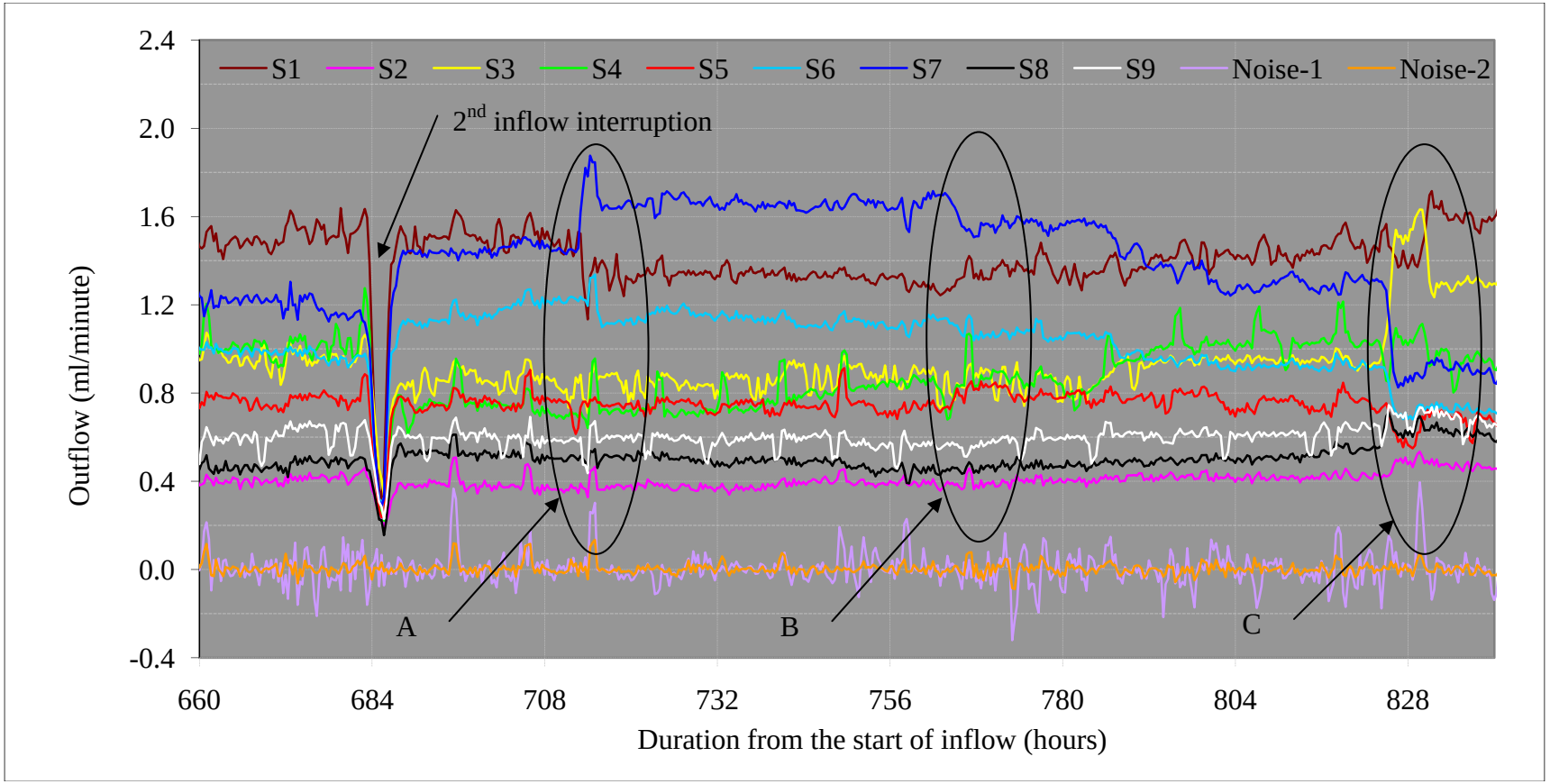

Figure 4.19 Outflow from nine sections before and after the second inflow interruption in experiment #2

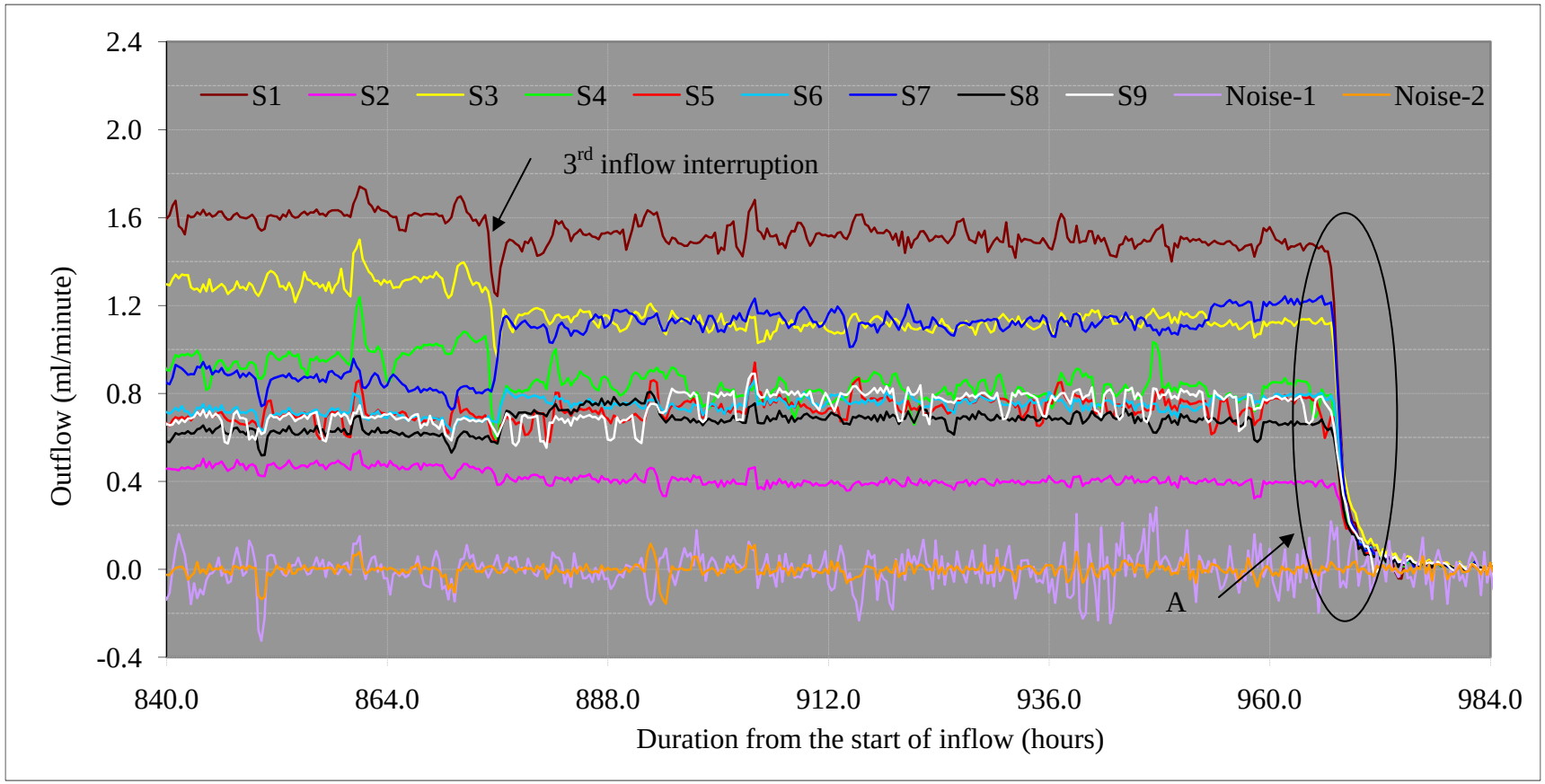

Figure 4.20 Outflow from nine sections before and after the third inflow interruption in experiment #2

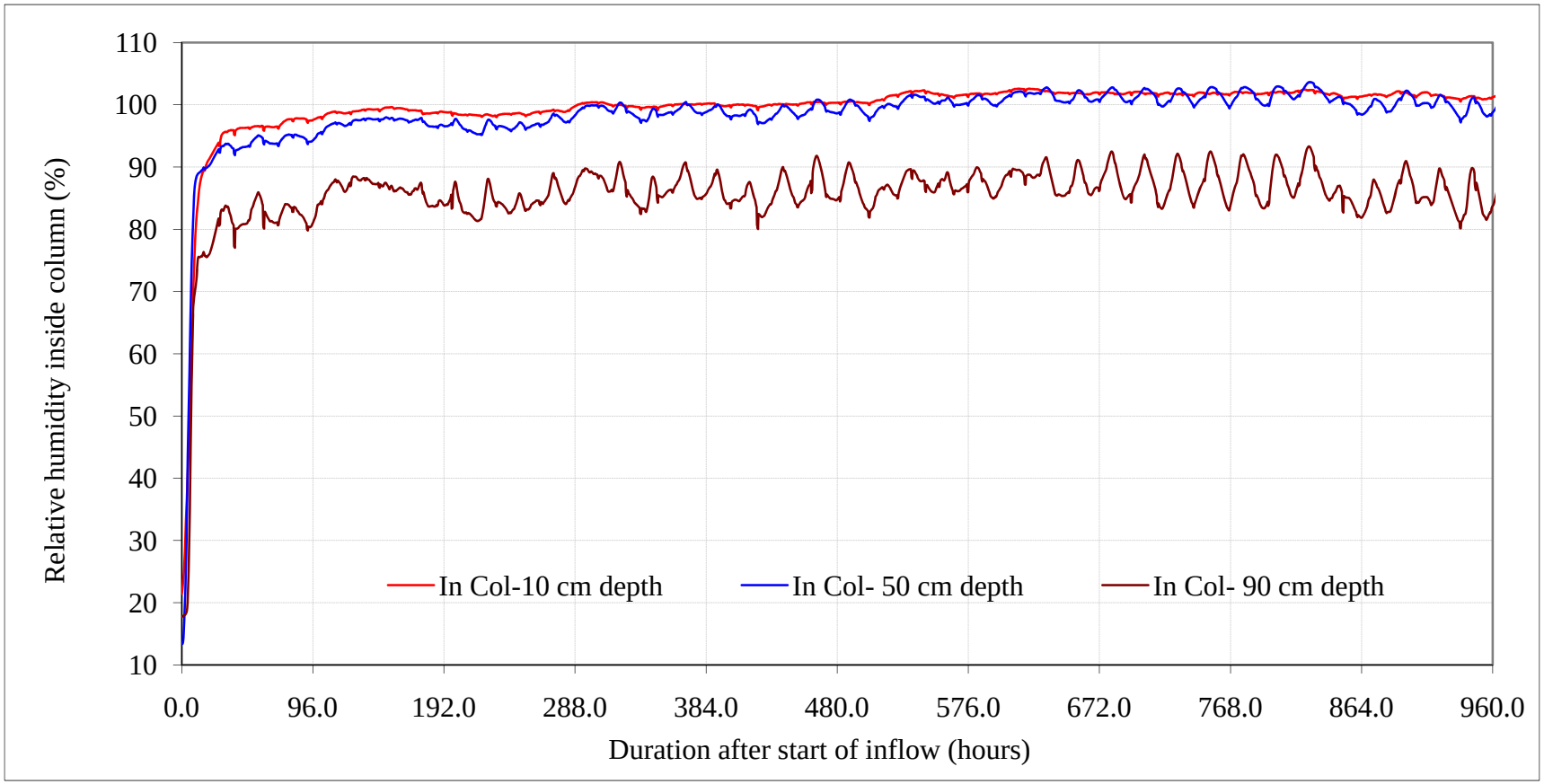

Figure 4.21 Variation of relative humidity inside the column during experiment #2 (Relative humidity over 100% is not physically realistic. Humidity sensors do not properly function at the vicinity of 100% relative humidity, thus provide erroneous data)

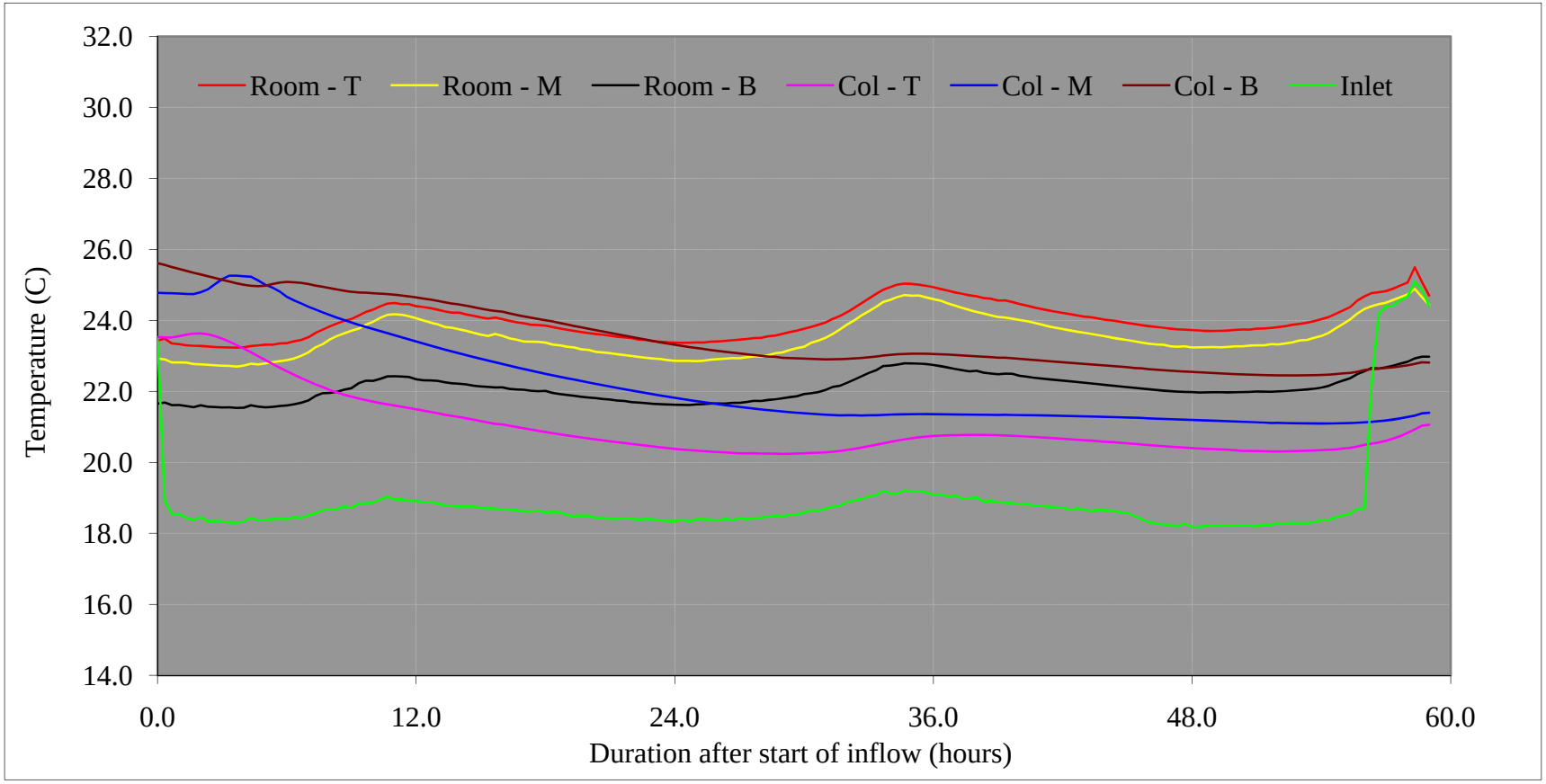

Figure 4.22 Variation of temperature in the room, inside the column and the inflow during experiment #3

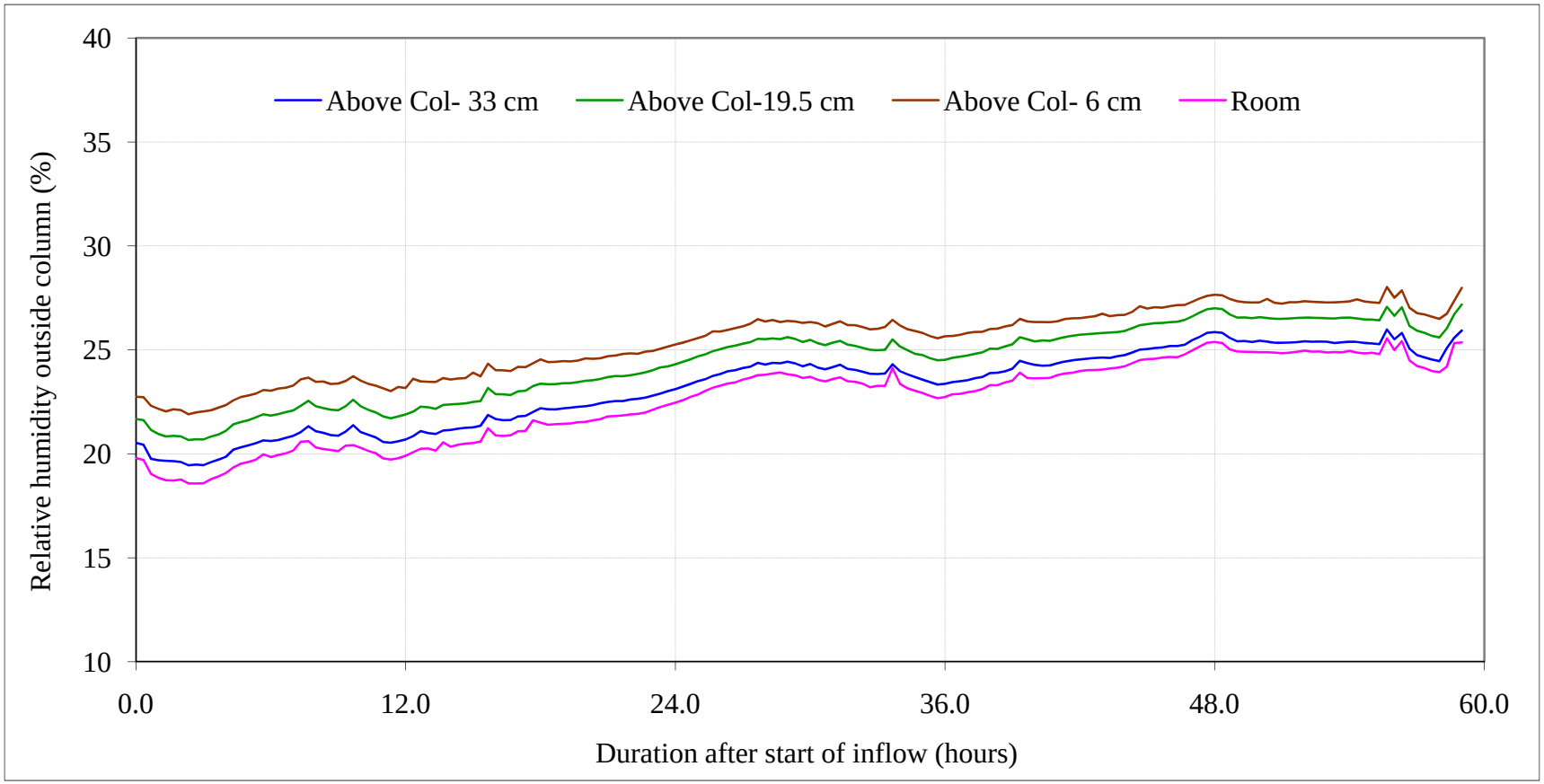

Figure 4.23 Variation of relative humidity in the ambient environment (room) and above the test column during experiment #3

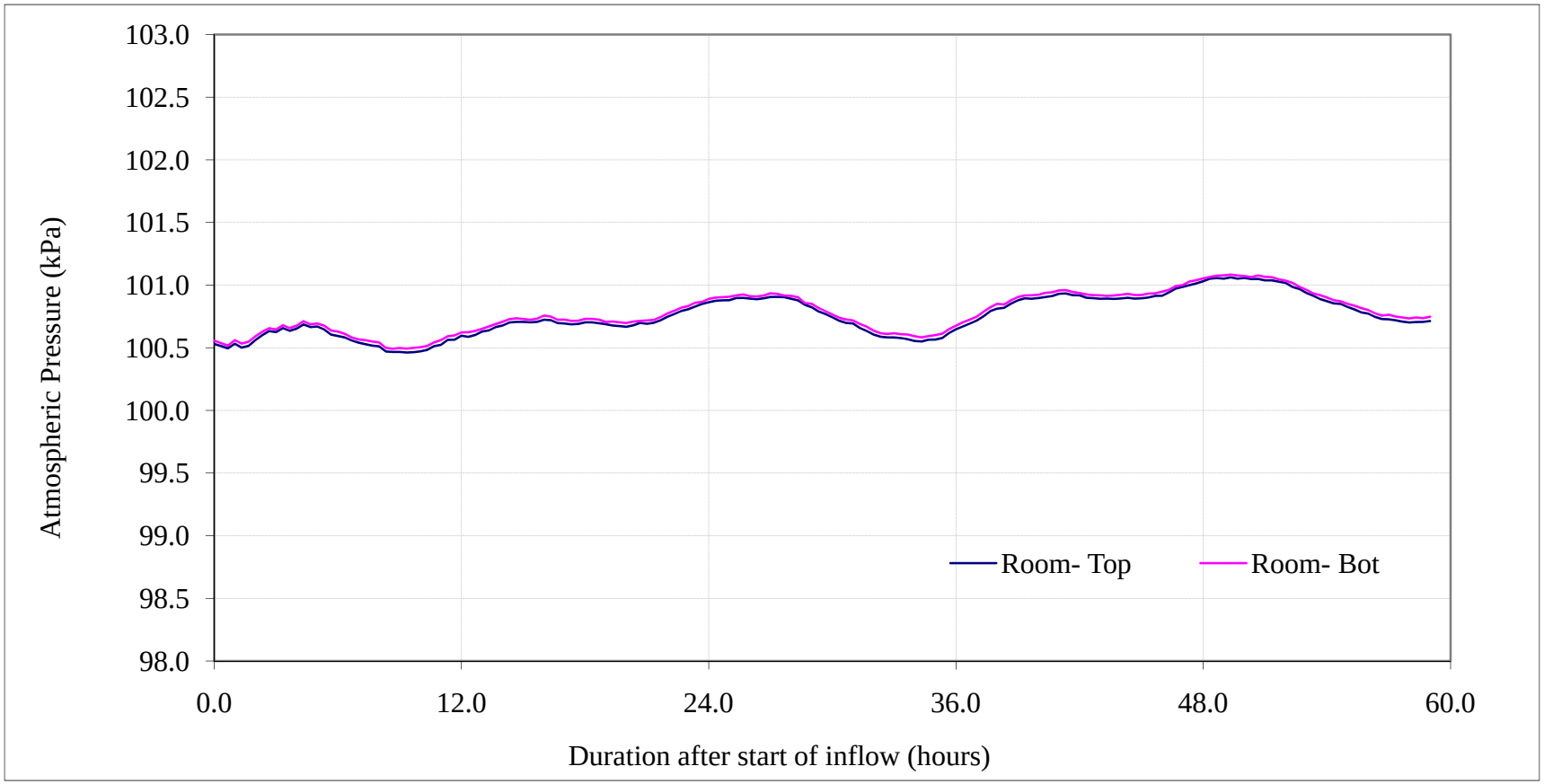

Figure 4.24 Variation of the atmospheric pressure during experiment #3

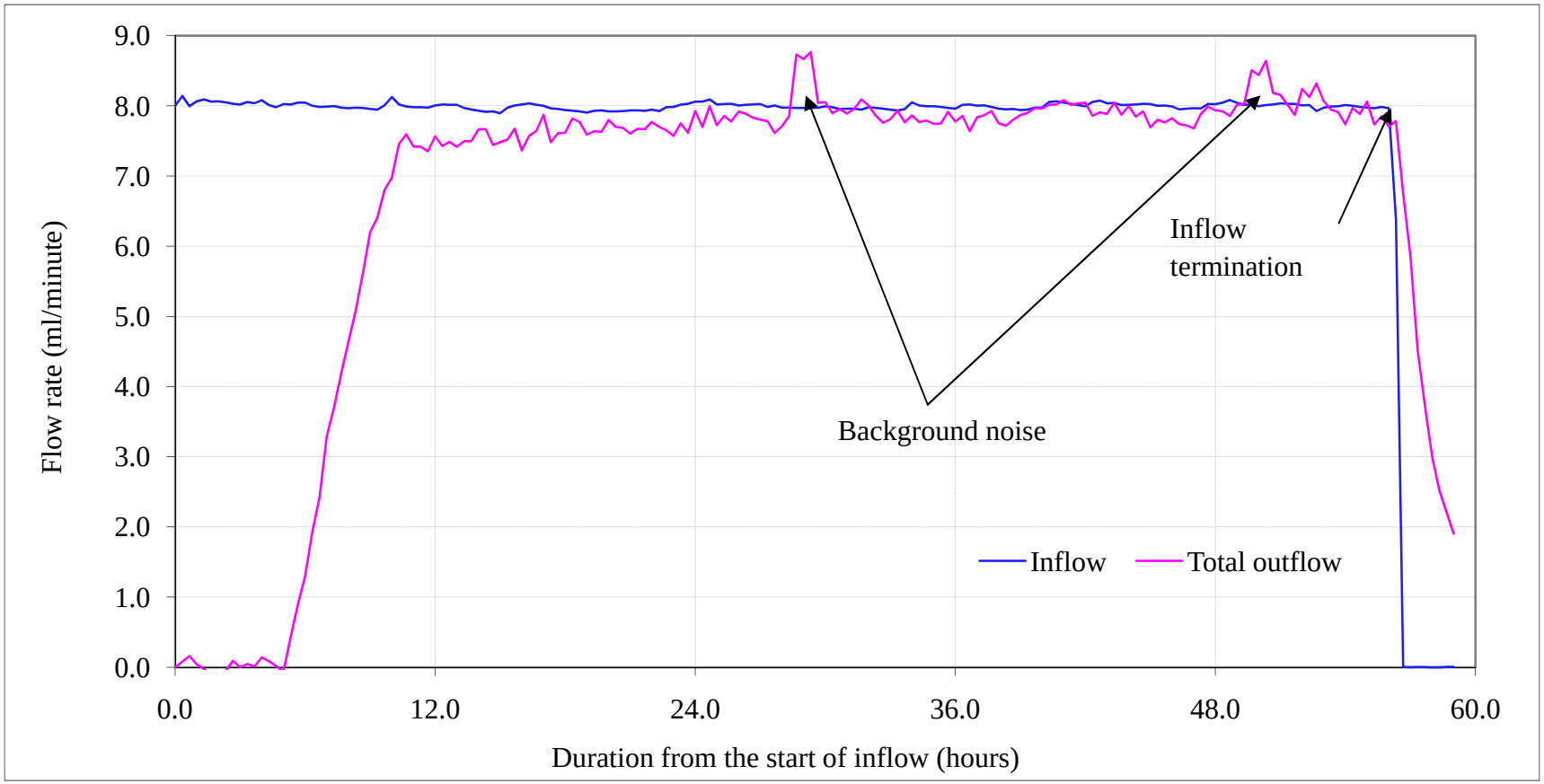

Figure 4.25 Variation of the inflow and total outflow during experiment #3

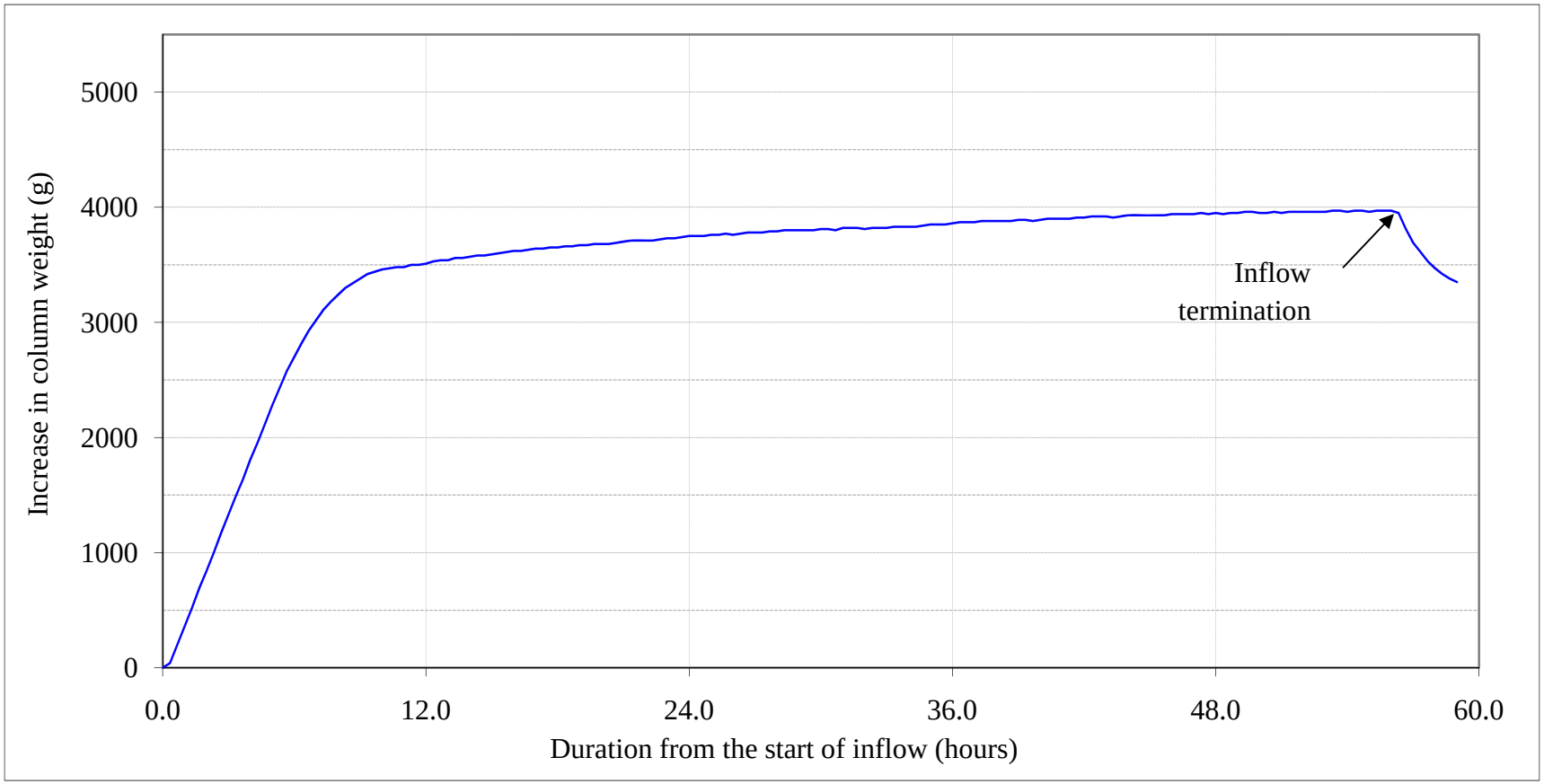

Figure 4.26 Increase of the weight of the test column due to the increase of saturation of during experiment #3

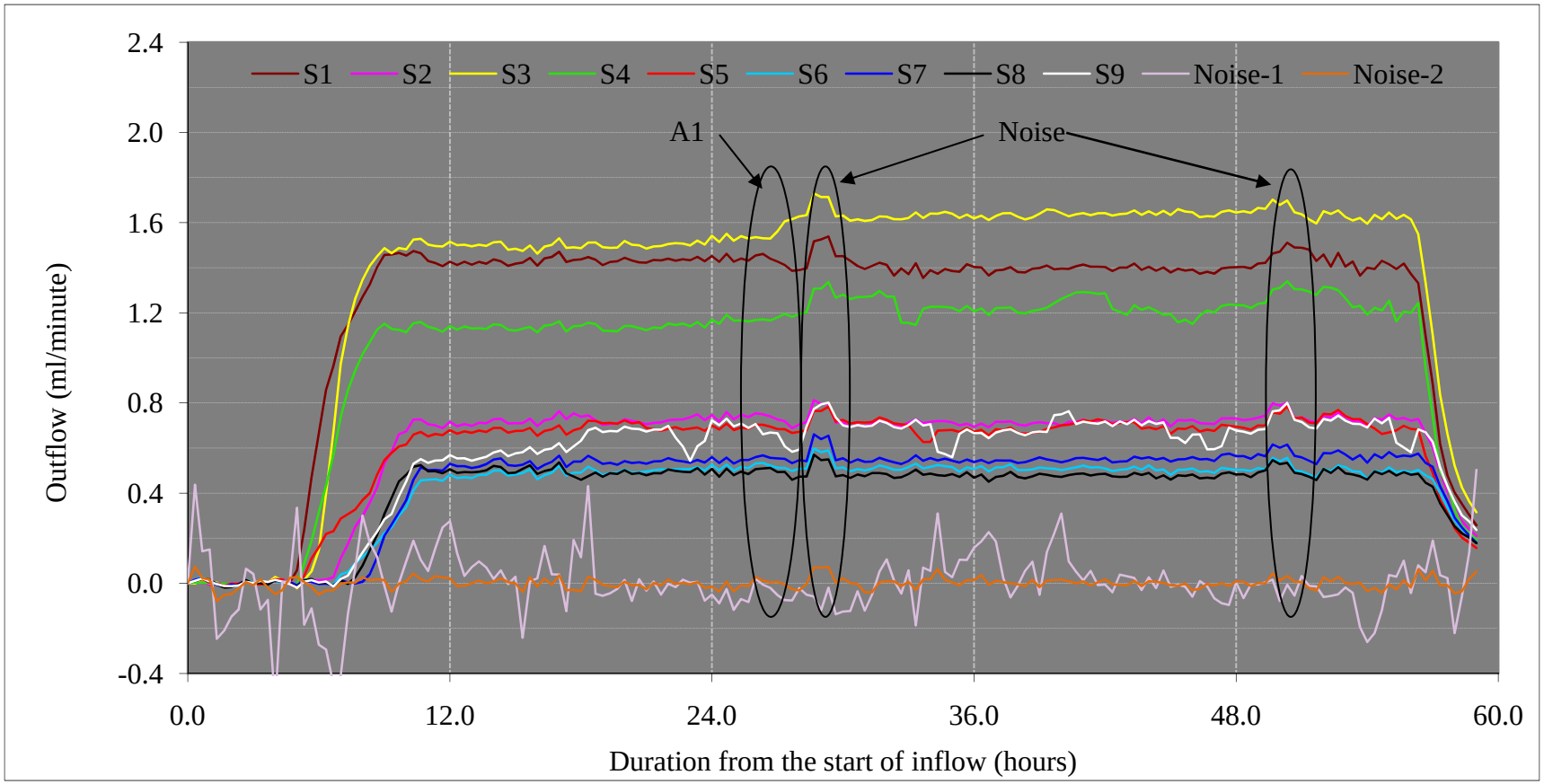

Figure 4.27 Outflow from all nine sections and background noise during the 56 hour run of the experiment #3

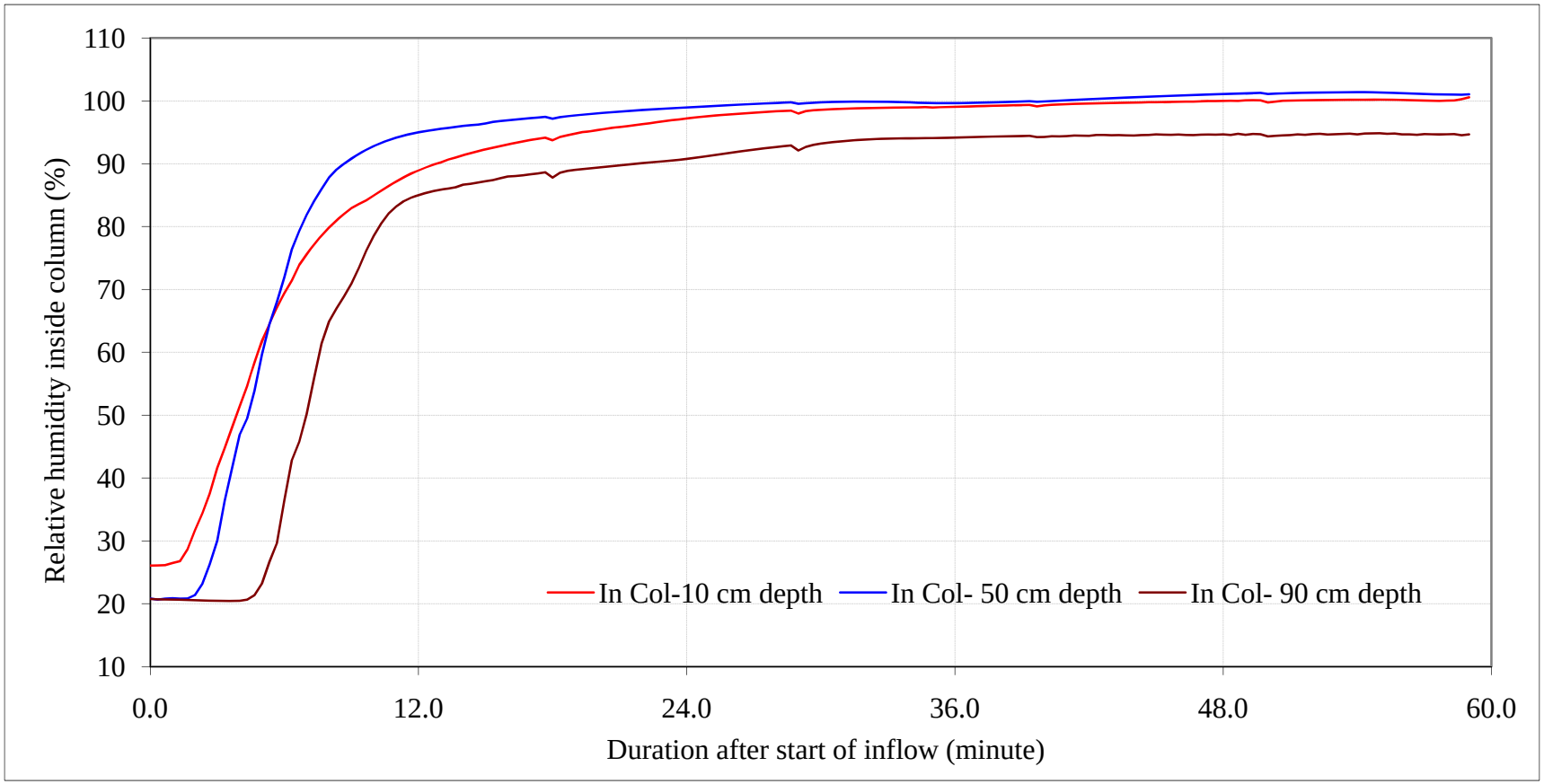

Figure 4.28 Variation of relative humidity inside the column during experiment #3

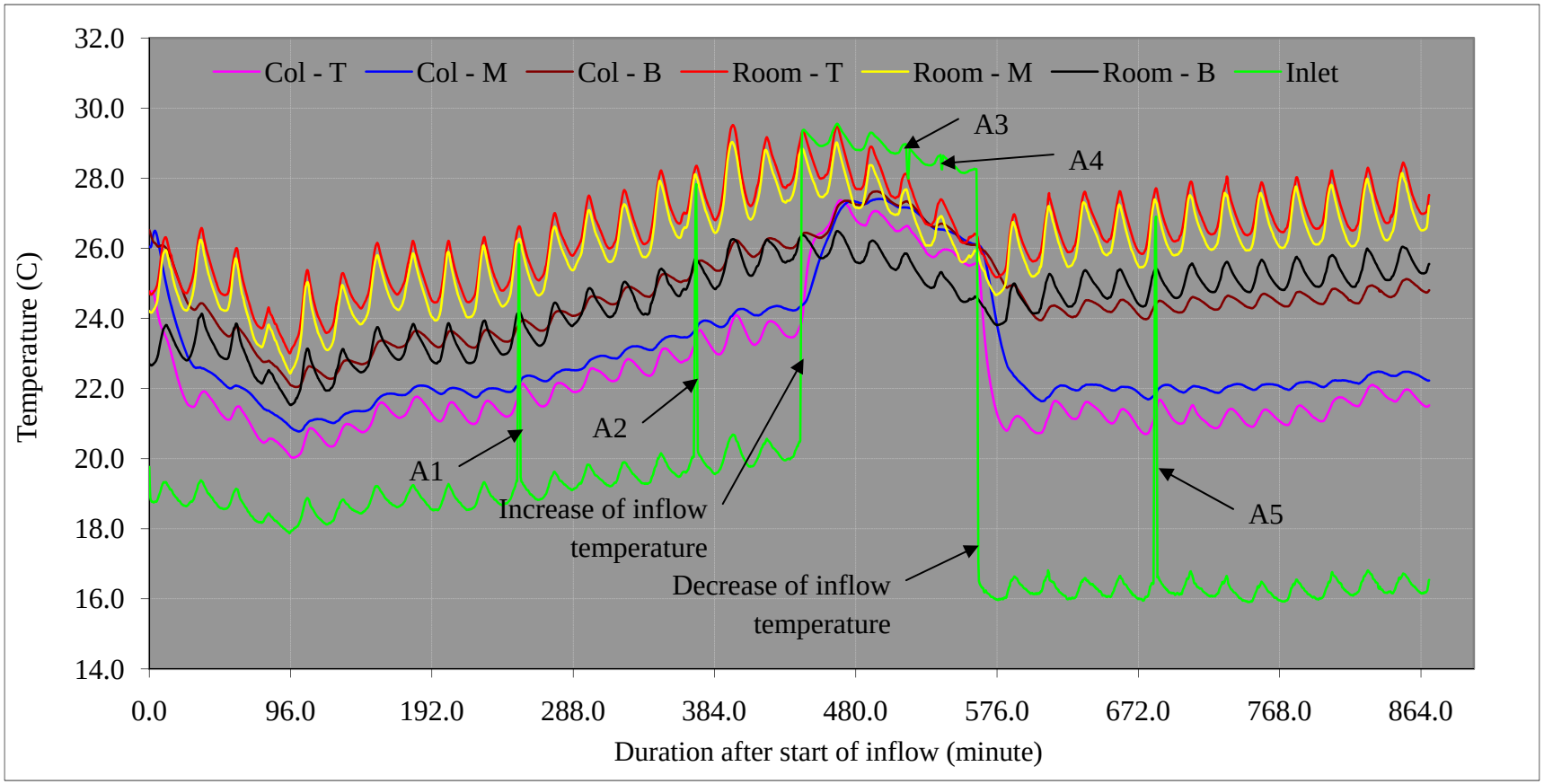

Figure 4.29 Variation of temperature in the room, inside the column and the inflow during experiment #4 (A1, A2, A3, A4 and A5 are inflow interruptions)

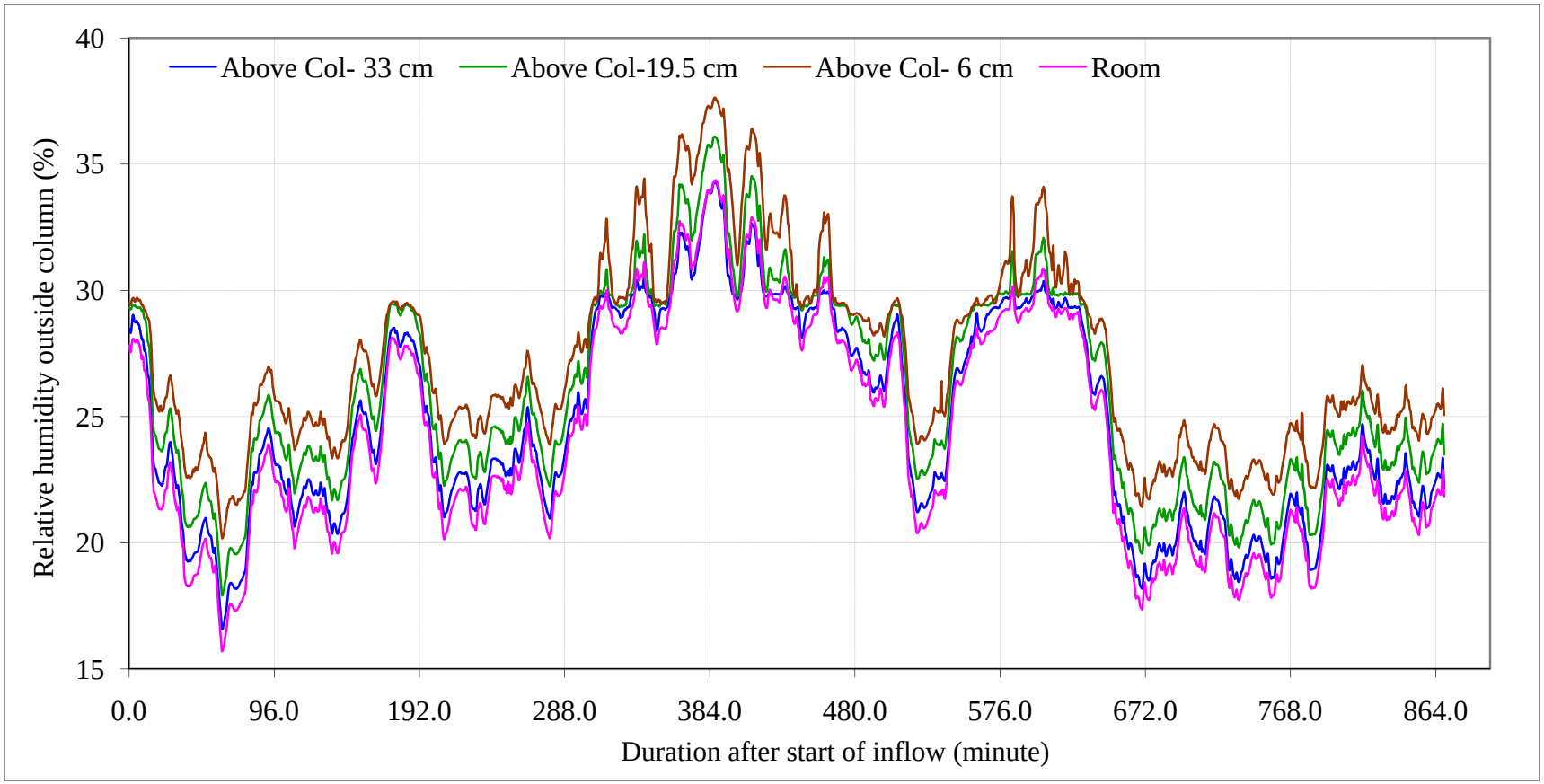

Figure 4.30 Variation of relative humidity in the ambient environment (room) and above the test column during experiment #4

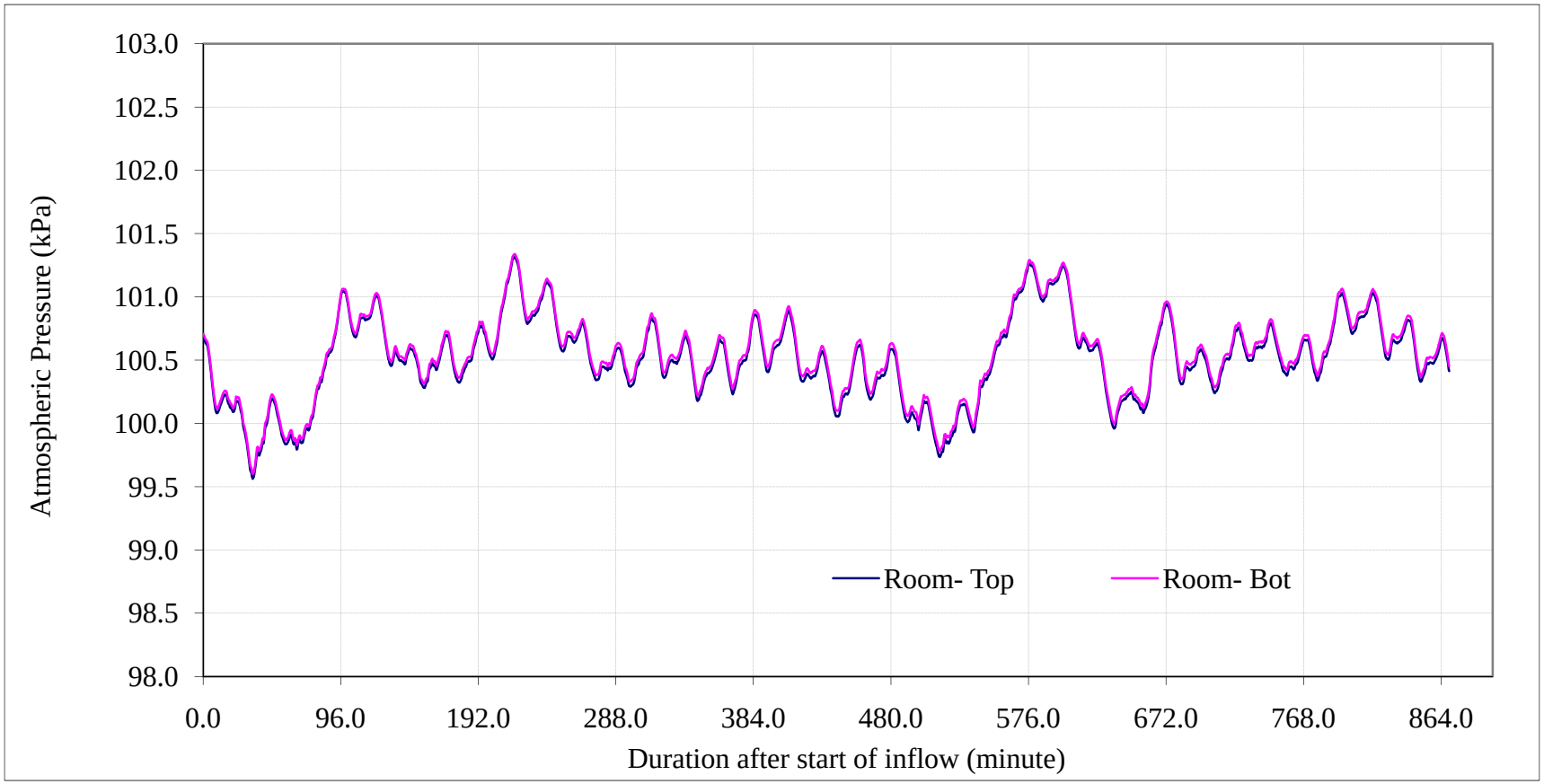

Figure 4.31 Variation of the atmospheric pressure during experiment #4

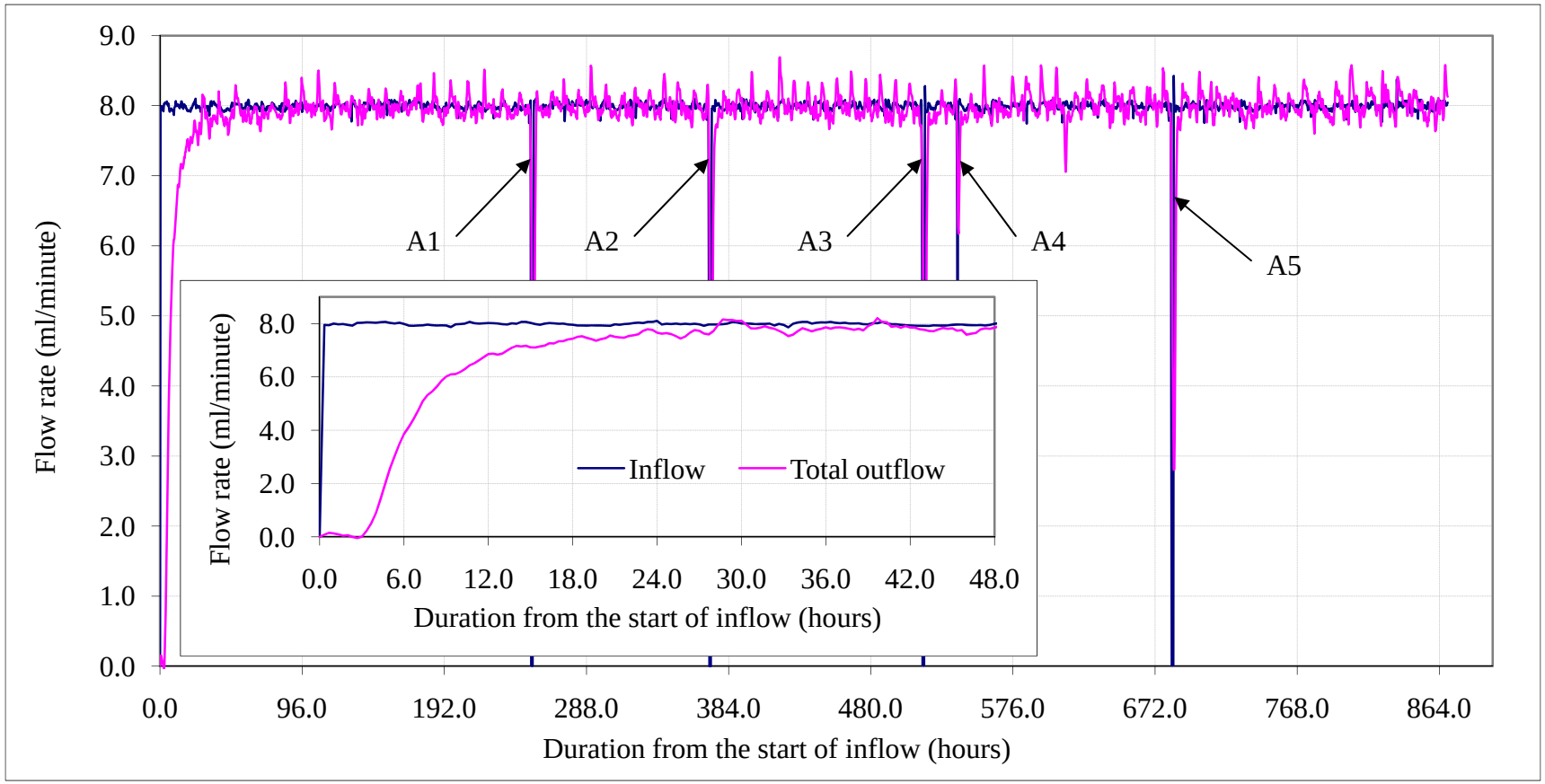

Figure 4.32 Variation of the inflow and the total outflow during experiment #4 (A1-A5 are inflow interruptions). The inset graph shows the inflow and total outflow during the first 48 hours at a large scale.

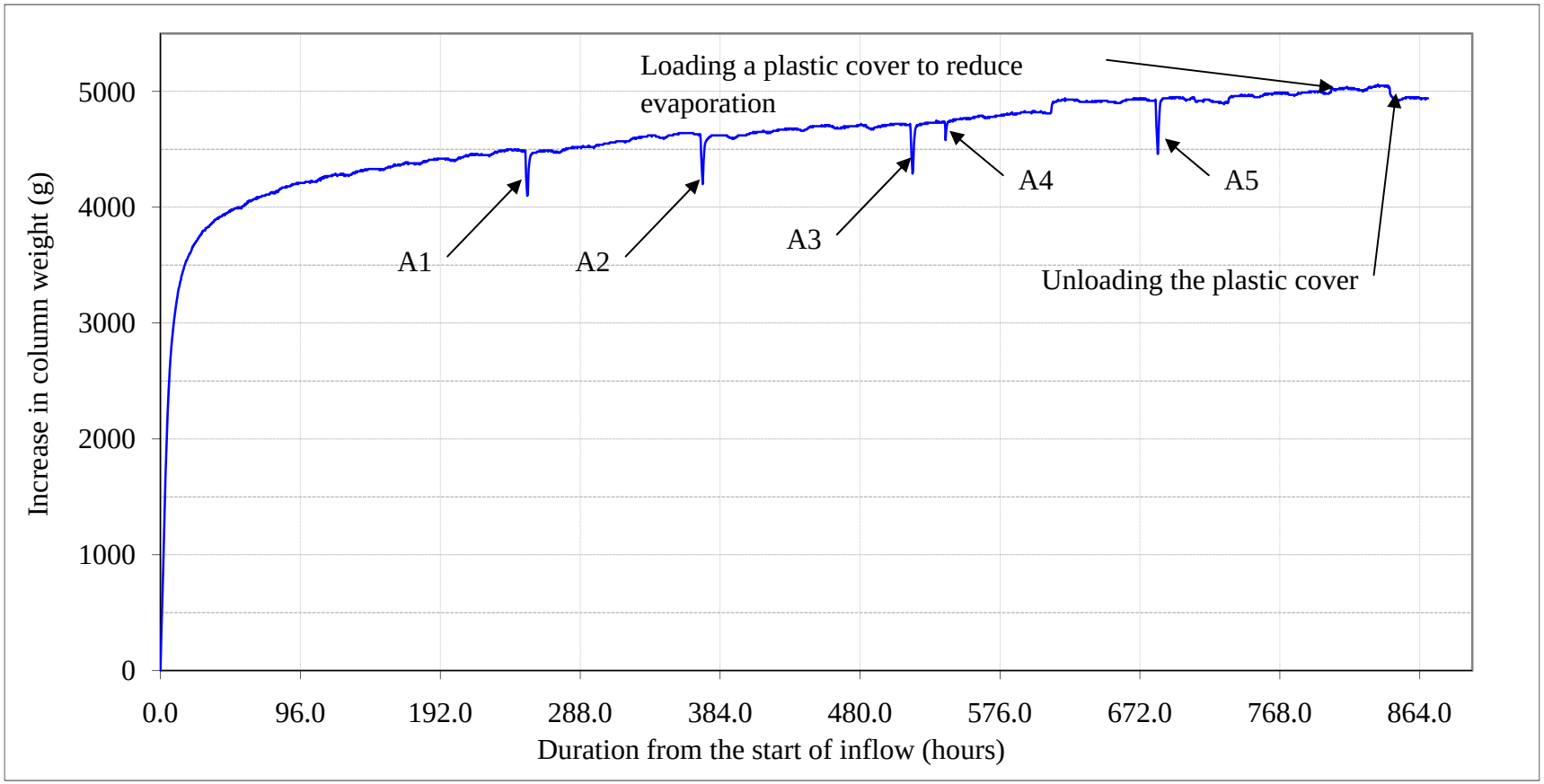

Figure 4.33 Increase of the weight of the test column during experiment #4 (A1-A5 are inflow interruptions)

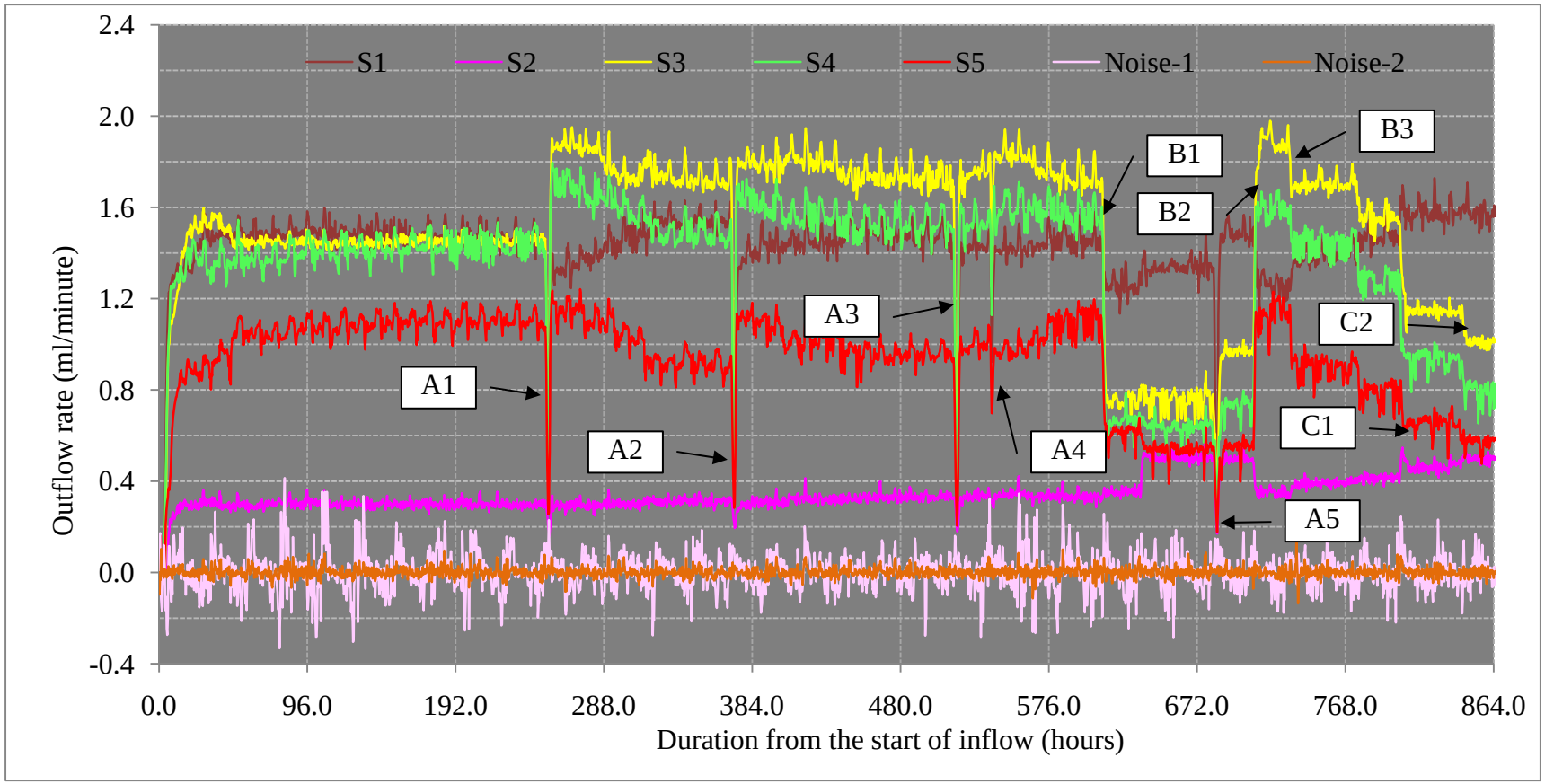

Figure 4.34 Variation of outflow from S1, S2, S3, S4, S5and the background noise during the total duration of the experiment #4 (A1-A5 are inflow interruptions; B1-B3 are inlet relocations; C1 is covering the top of the column and C2 is opening the top of the column).

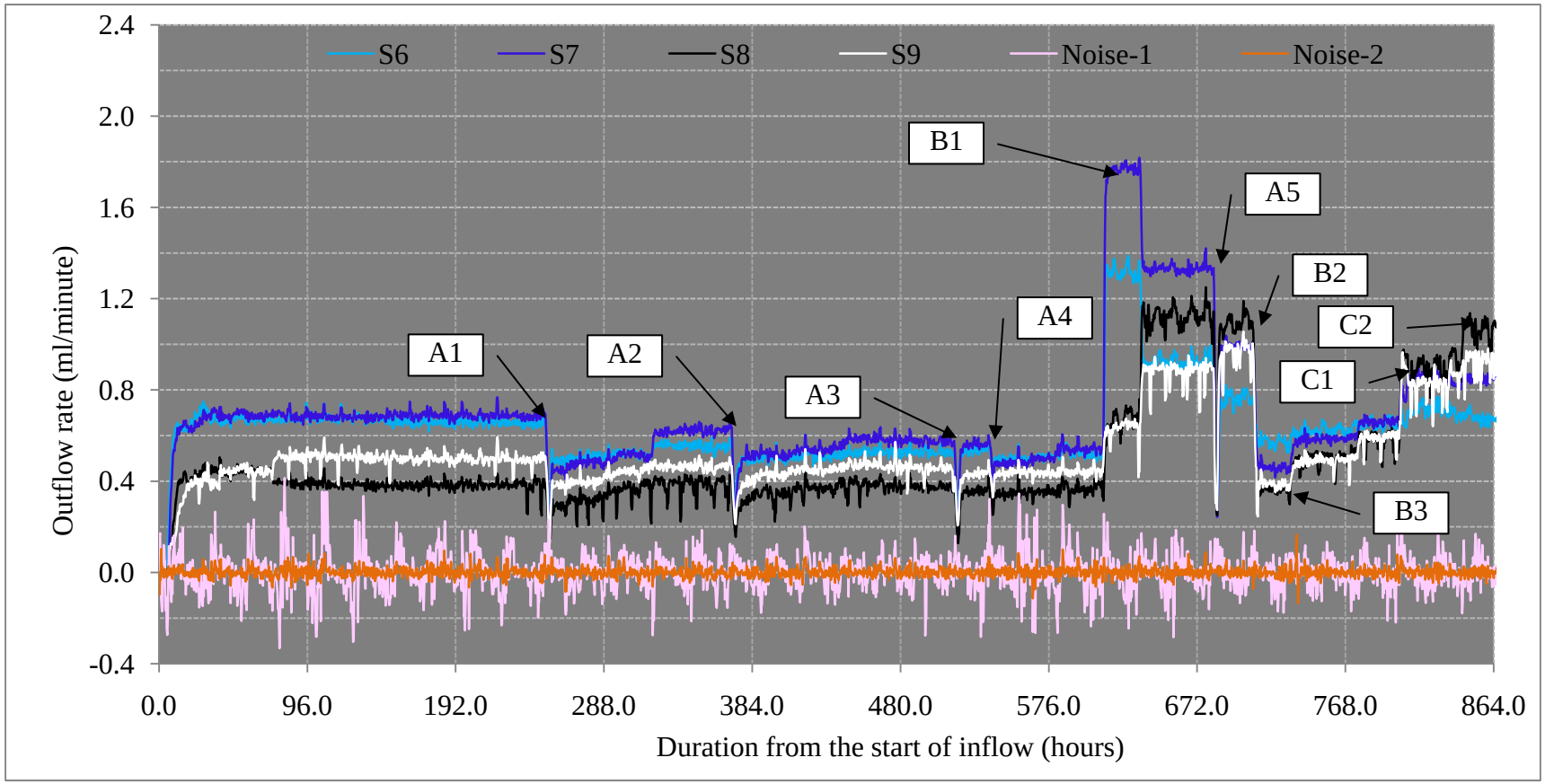

4.35 Variation of outflow from S6, S7, S8, S9 and the background noise during the total duration of the experiment #4

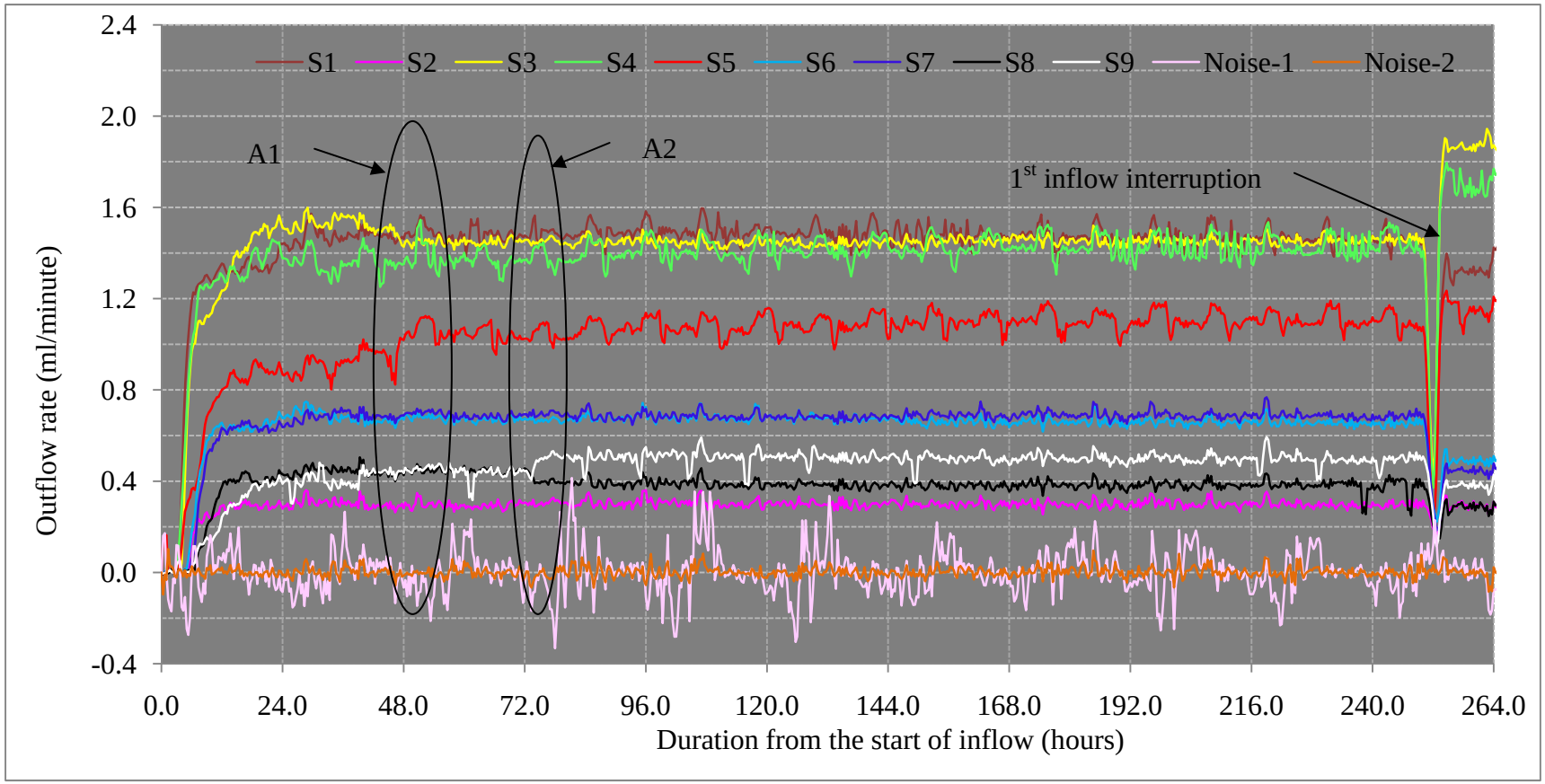

Figure 4.36 Changes of outflow at nine sections and the background noise during the first 11 days of experiment #4

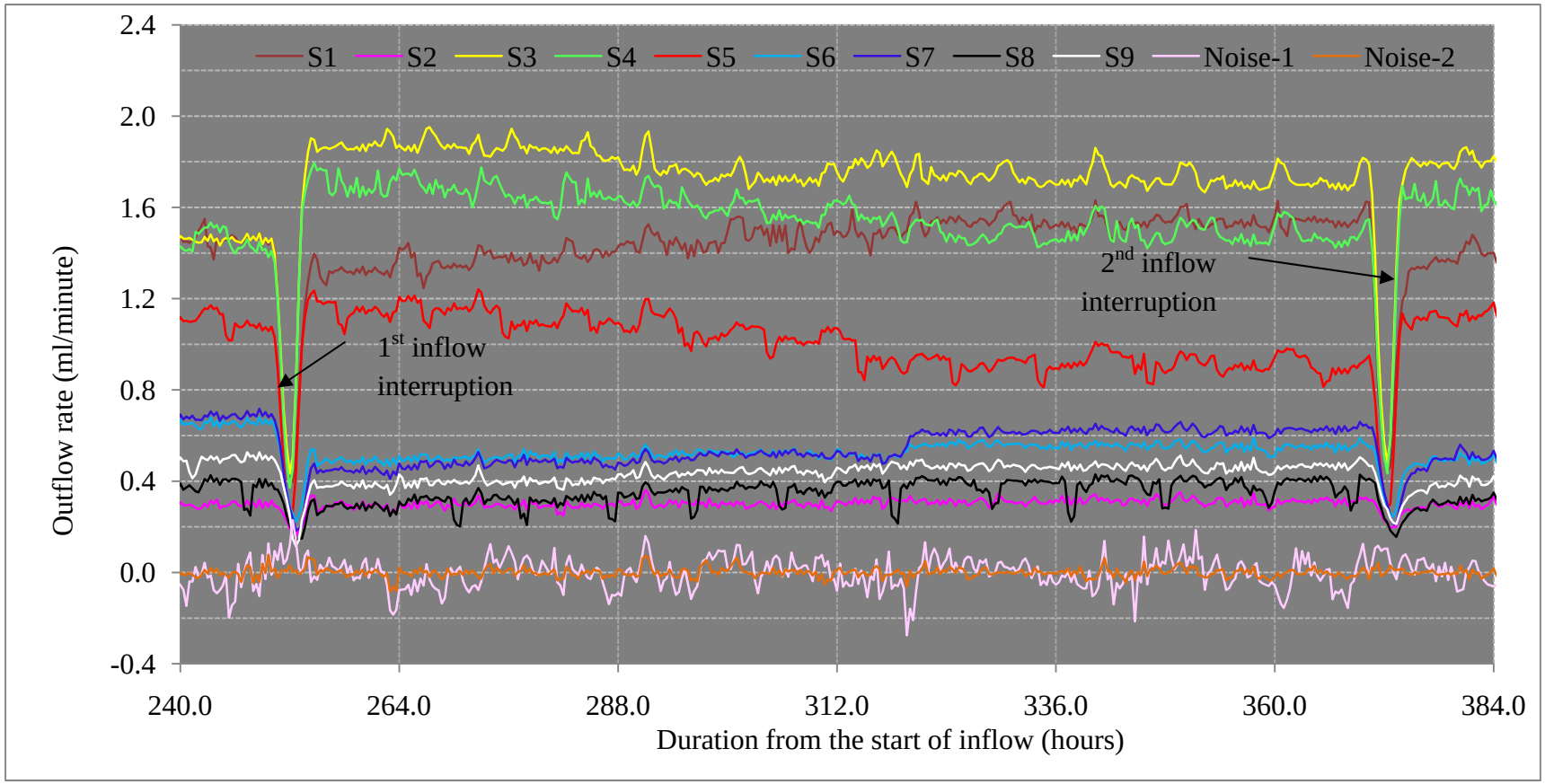

Figure 4.37 Variation of outflow at nine sections and the background noise before and after the first inflow interruption in experiment #4

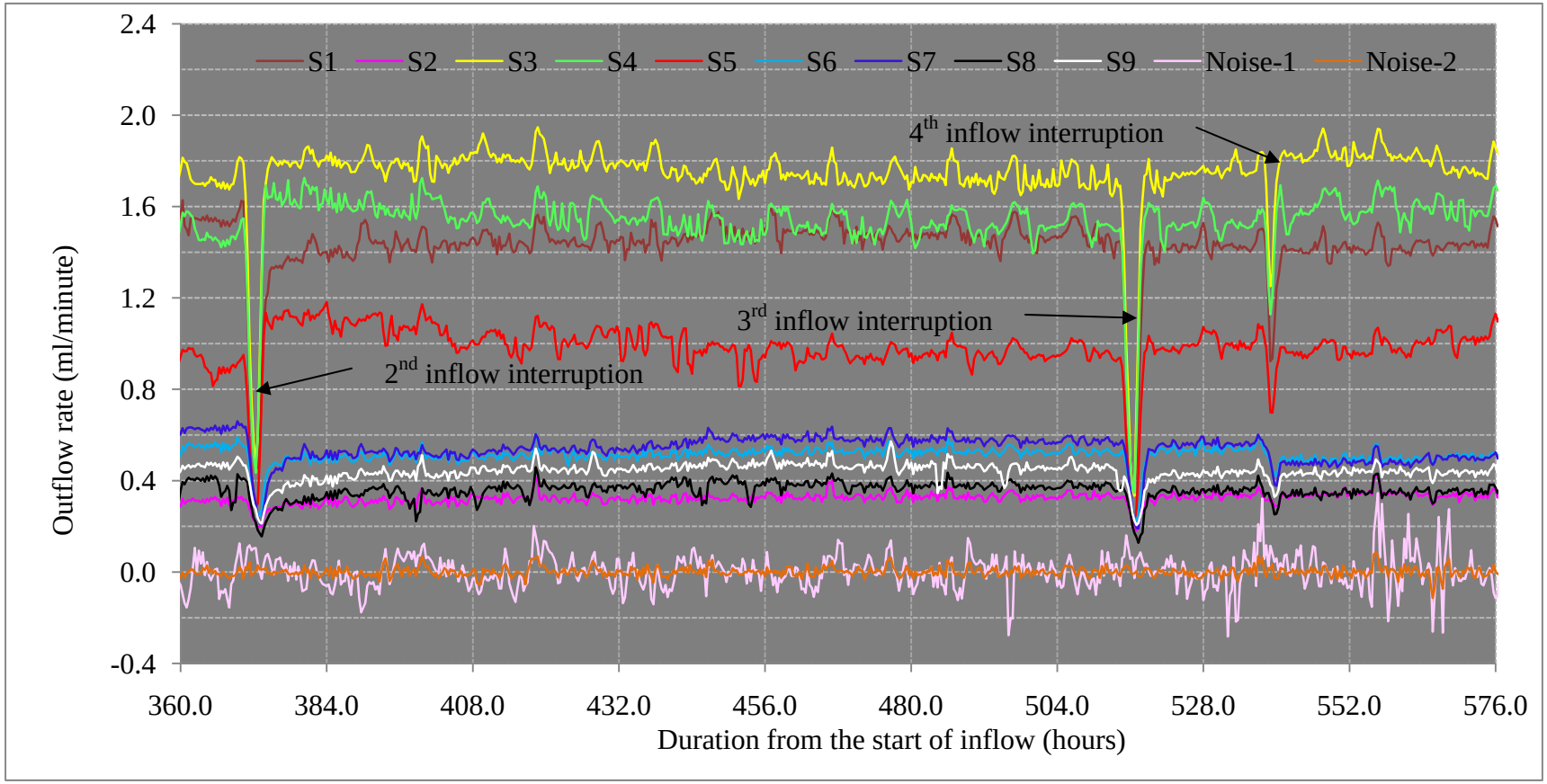

Figure 4.38 Variation of outflow from nine sections and the background noise from the 15th day to the 24th day in experiment #4

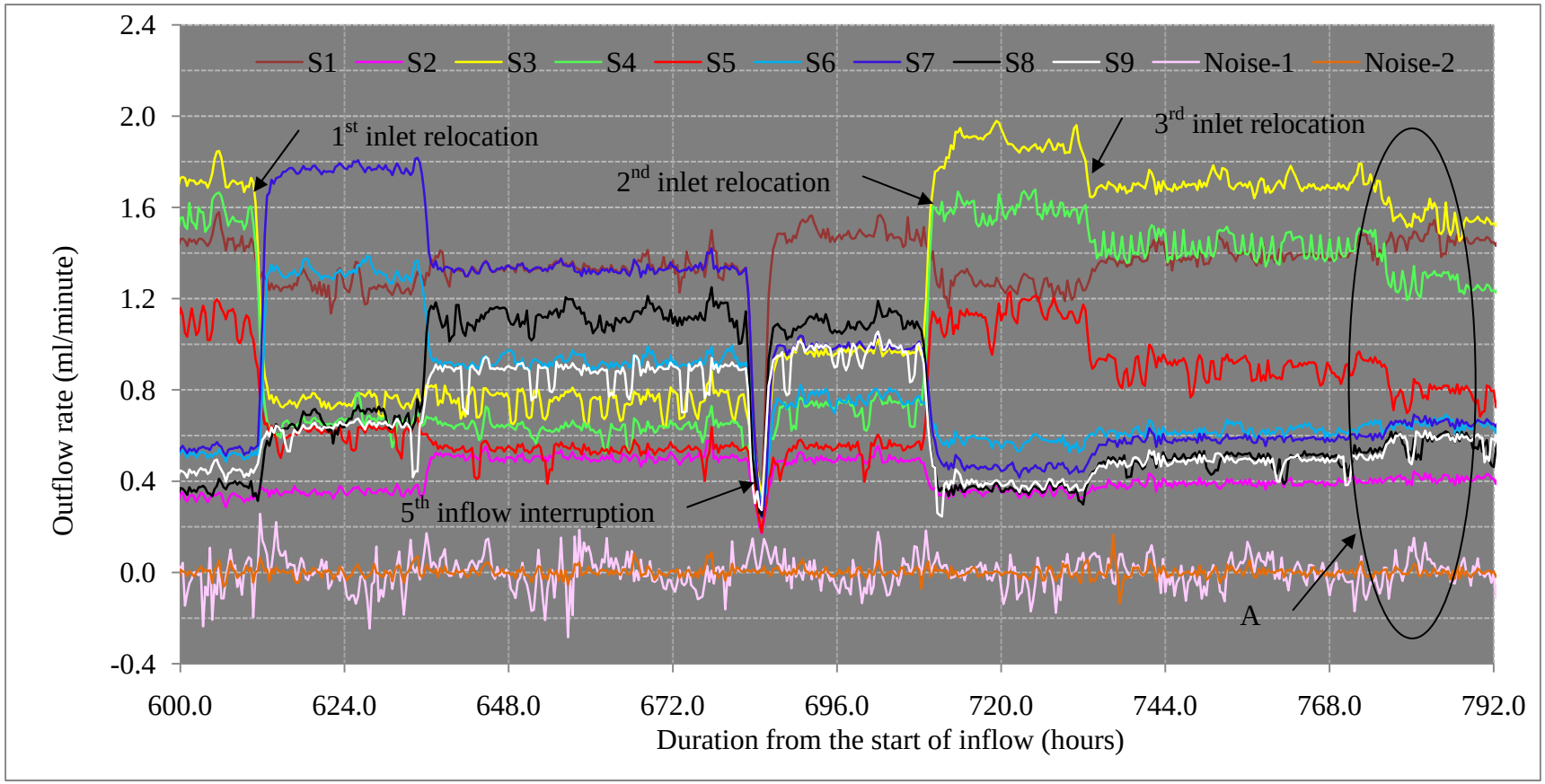

Figure 4.39 Variation of outflow at nine sections and the background noise from the 25th day to the 33rd day in experiment #4

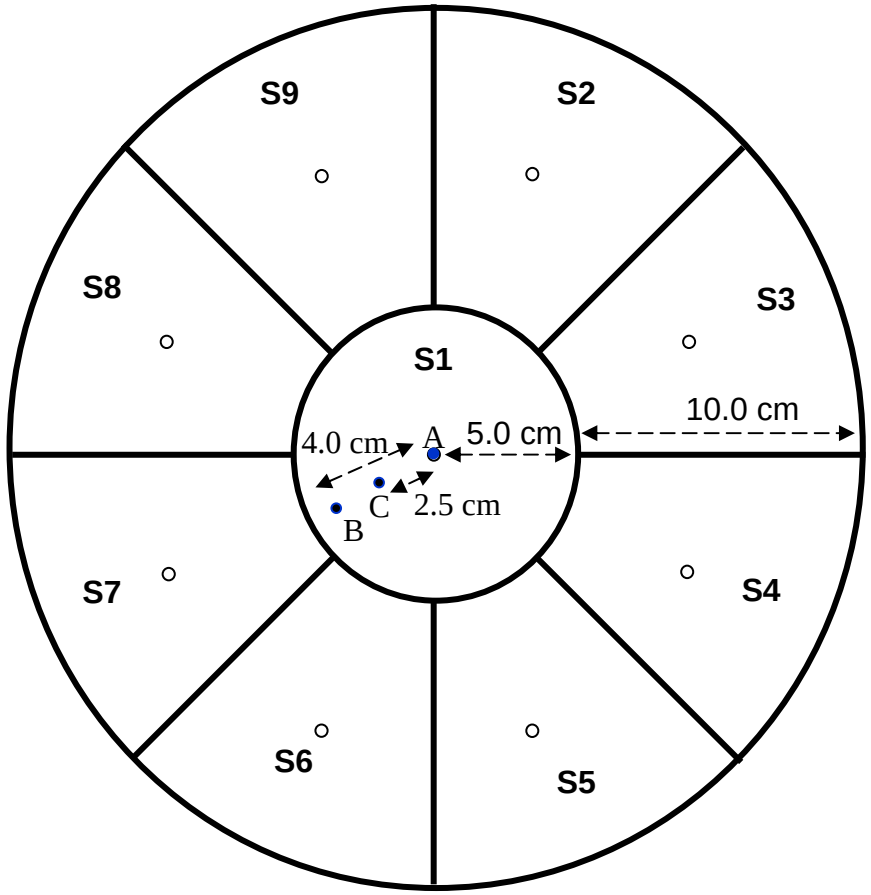

Figure 4.40 Locations of the inlet with respect to nine basins at the bottom of the test column. Dots at point A, B and C represent the inlet locations.

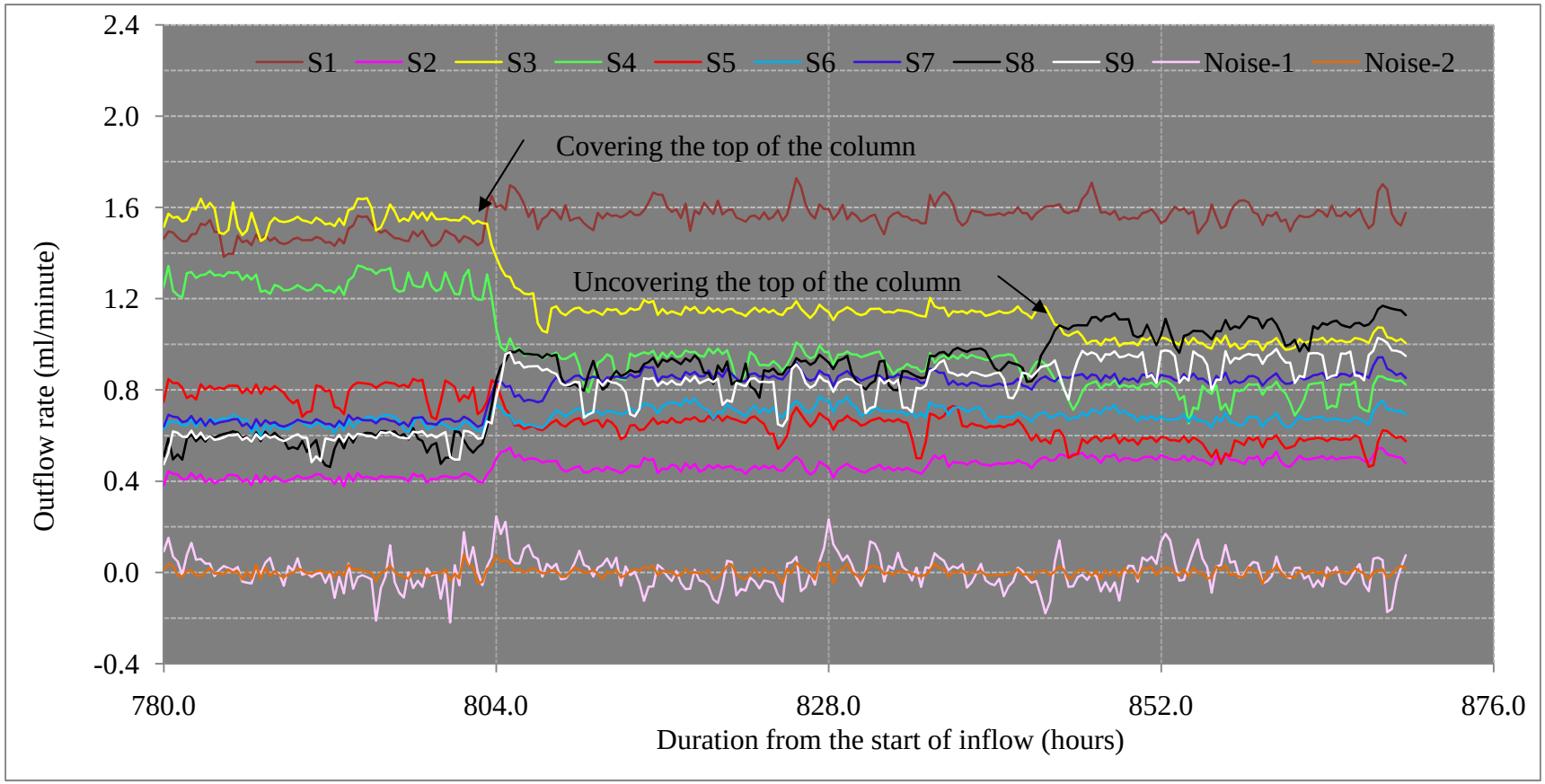

Figure 4.41 Variation of outflow from nine sections and the background noise from the 32nd day to the 36th day in experiment #4

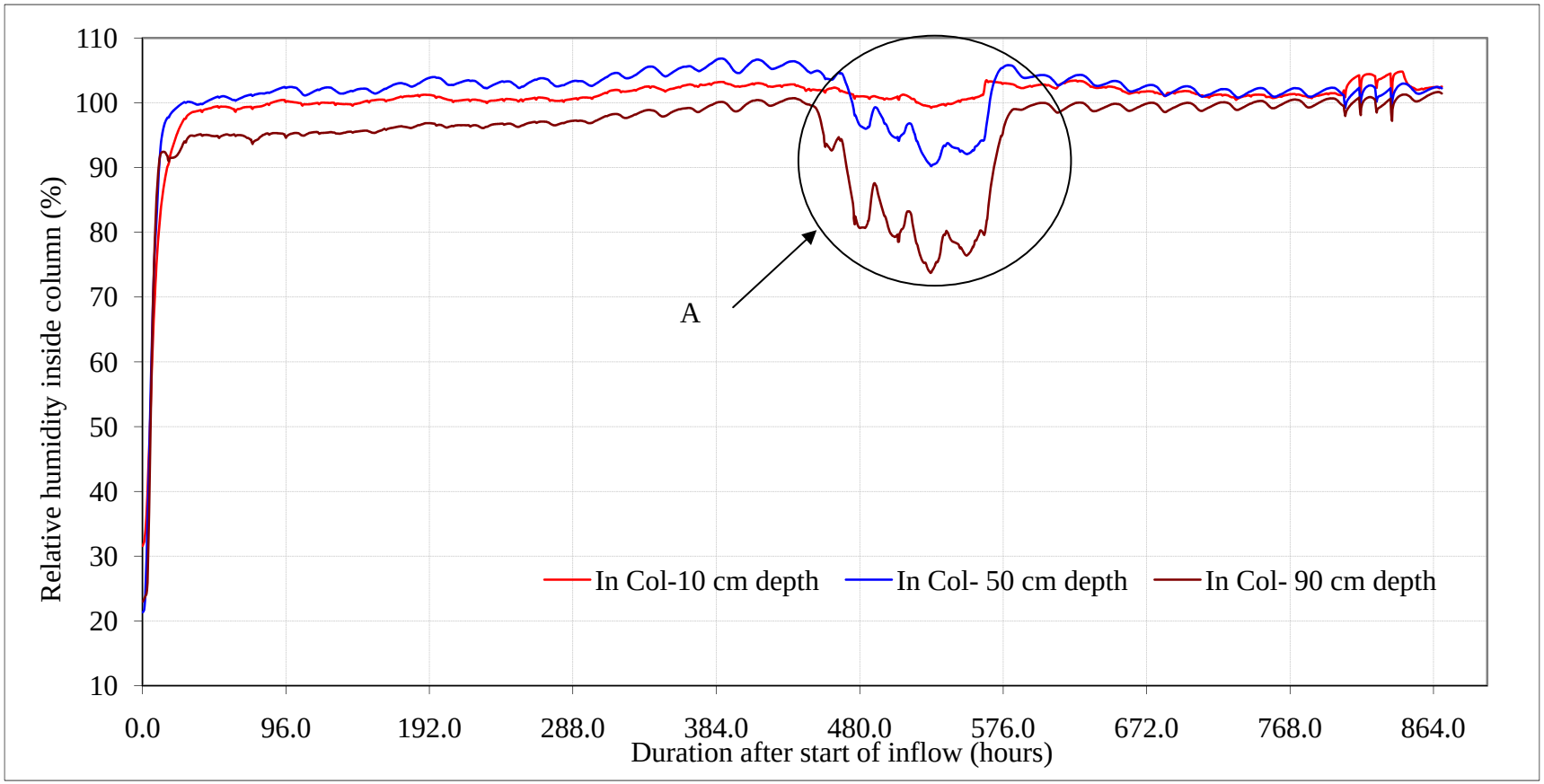

Figure 4.42 Variation of relative humidity inside the column during the experiment #4 (Relative humidity over 100% is not physically realistic. Humidity sensors do not properly function at the vicinity of 100% relative humidity, thus provide erroneous data)

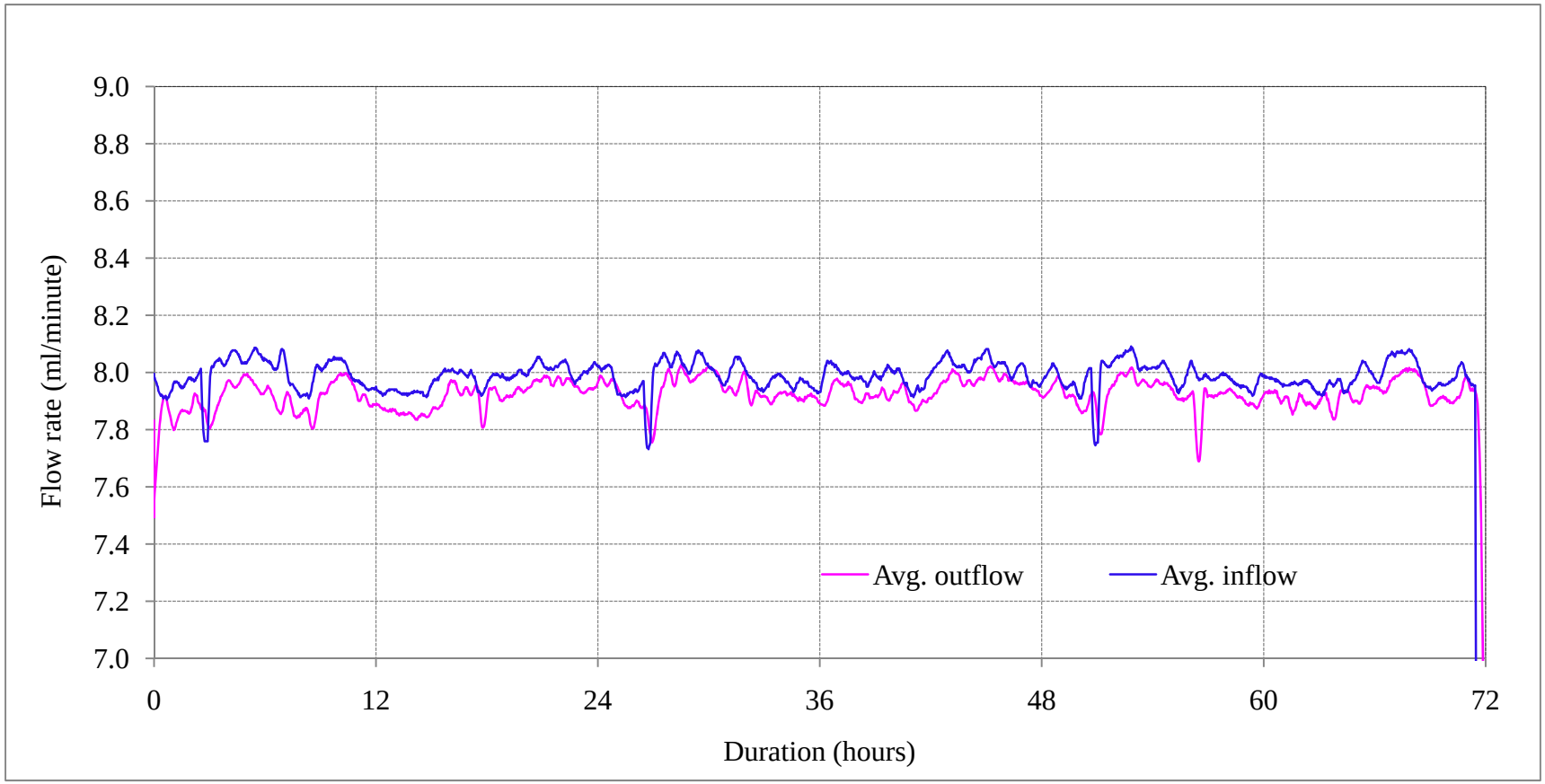

4.43 Variation of the inflow and the total outflow measured using an electronic balance at the end of experiment #4

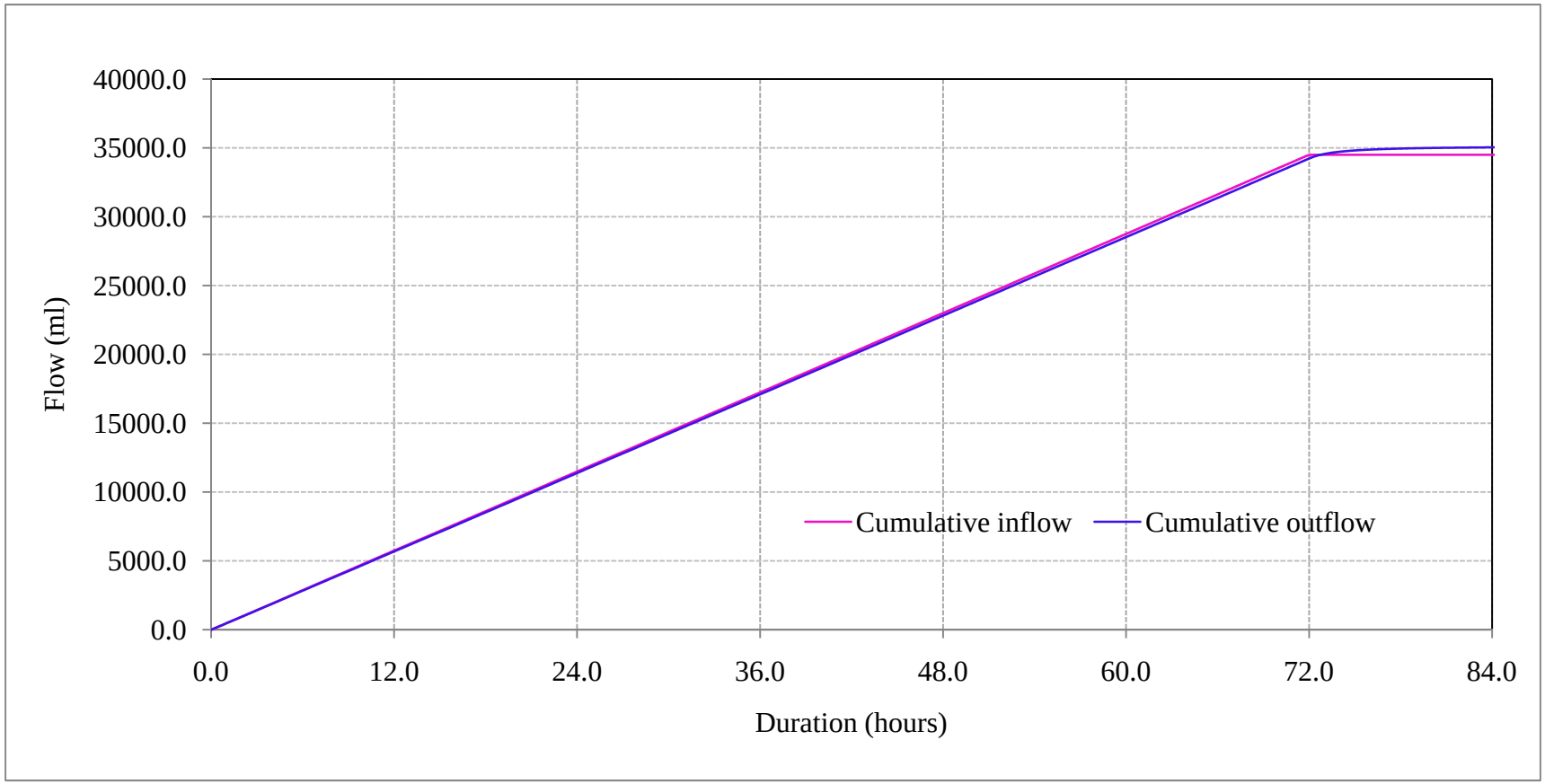

Figure 4.44 Cumulative inflow and cumulative outflow (measured using an electronic balance) at the end of experiment #4

CHAPTER 5

DISCUSSION

Results of the four experimental trials presented in chapter 4 are discussed here. In all four experiments, we monitored outflow from nine equal-area sections at the bottom of a test column filled with crushed sandstone (dual-porosity granular media). Our objective was to study the spatial and temporal structure of unsaturated flow in this type of media in response to steady inflow applied to the top of the column. It is assumed that a non-uniform spatial distribution of outflow from the bottom of the column indicates that macroscopic flow structure within the test column is also non-uniform. Likewise, we assume that temporal variations in the outflow result from changes to the flow structure within the column.

The discussion of experimental observations presented in this chapter is subdivided into five topics. First (section 5.1), integrated behavior of the system as a whole (i.e., inflow, beginning of outflow, saturation, variability of the total outflow, etc.) is discussed. Next (section 5.2), the spatial structure of the outflow during the initial development of the flow field (i.e., the first 48 hours of the experiments) is discussed. Subsequent spontaneous changes to the flow structure are discussed in section 5.3. Changes to the flow structure in response to imposed perturbations are discussed in sections 5.4 (inflow interruptions) and 5.5 (relocation of the inlet). Section 5.6 describes the influence of changes of evaporation from the column on the macroscopic flow structure. The last section of the chapter (5.7) presents statistics of inflow and outflow, as well as discusses the statistical significance of outflow changes at the bottom of the column.

5.1 General Behavior of the Flow System

In all four experiments, water was supplied to the test column through a single point source using a computer controlled pump. The inflow rate remained steady at 8.0 ± 0.1 ml/min most of the time; however, fluctuations were observed during every experiment. In addition to the interruptions described in chapter 4, the inflow showed apparently random short-term fluctuations that were likely the combined result of temperature fluctuations, tubing wear, and changes in building line voltage. Speed of the pump was not infinitely variable, thus the correction of the inflow rate was not always smooth. There was also a daily fluctuation on the order of 0.1 ml/min that lasted for ~3 hours as the system adjusted to the change in hydraulic head associated with refilling the supply container. All of these fluctuations were recorded, and their influence on the outflow was assessed.

5.1.1 The Start of Outflow

In three of the experiments (#1, 2 and 4), outflow from the bottom of the test column began ~3 hours after the inflow started and then increased rapidly over the next ~10 hours before it began to level off (figure 5.1). Experiment #3 was slightly different, as outflow began a little bit later (~4.5 hours after inflow started) and leveled off sooner (~6 hours after it started). The time lag to the beginning of outflow is much shorter than that would be suggested based on purely matrix flow (> 400 days at unit hydraulic gradient), but longer than would be expected for film flow alone (~20 minutes; estimated in chapter 4). The observed behavior suggests that flow within the system began with a combination of matrix imbibition and film flow.

The above result suggests that when water is first applied to the dry rocks in the column, some of it moves into the rock fragments, while the rest forms films on the fragment surfaces. The initially dry rock fragments exert strong capillary forces, thus a large portion of the initial inflow moves into the fragments. However, if the supply rate exceeds the local sorption capacity, the remaining water will form films on fragment surfaces and pendular rings at contacts between fragments. This process is likely to be time variant. Sorption capacity of a dry fragment will be initially high, and then gradually decreases as it wets, thus more water is progressively transferred into surface films. Note that the specifics of this behavior will be dependent on the number, size, shape, and saturation of rocks in contact with the wetting front, and will change in time. For example, in experiment #3, the delayed beginning of outflow could be due to domination of matrix filling over formation of films, while subsequent rapid increase of outflow could result from formation of a small number of flow paths with thick (highly conductive) water films.

5.1.2 Matrix Saturation

Saturation of the rock fragments is strongly correlated to weight of the test column. The amount of water contributing to film flow is a smaller portion of the total water mass in the column. Matrix saturation rapidly increased after initiation of inflow, because of the high sorptivity of the dry rock fragments. Overall, water uptake by the rock fragments gradually decreased as the matrix saturation increased, eventually reaching a steady rate. The increase in column weight (figure 5.2) was very similar for all experiments; however, the total increase for experiment #2 was lower than that for

other experiments. This difference could be attributed to different spatial flow structures that could largely control the saturation in the column, but the exact cause in not known.

It is expected that initial rapid increase of matrix saturation was limited to fragments that were in direct contact with active flow paths. Development of new flow paths over time can increase the number of fragments that are in direct contact with water. However, saturation of fragments that are not located in the vicinity of active flow paths mainly increases due to matrix diffusion. Diffusion of water between adjacent fragments is largely controlled by the contacts between them. A small number of such contacts and/or low surface area at contacts could largely limit matrix diffusion, thus the saturation in the medium. Because of this diffusive flow, the maximum matrix saturations in experiment #2 was only ~38% (~3.6 liters), while that in experiment #4 was ~43% (~4.1 liters), even after supplying ~460 liters of water over 40 days. As described in section 5.2.1, this difference in matrix saturation may be caused by differences in spatial flow structures between the two experiments. Matrix saturation in experiments #1 and #3 were considerably lower due to their short durations.

The observation of low and non-uniform saturation suggests the presence of spatially non-uniform narrowly focused flow paths in the column. If the concept of uniform flow was valid for this medium, the matrices of all fragments would have reached close to complete saturation over the 40-day period. Visual observations at the top surface and bottom (through the transparent bottom plate) of the column, suggest that rock fragments located away from the inlet at the top remained dry (or at low saturation), while all fragments at the bottom were wet. We expect that the lateral distribution of wet fragments increased with the depth because of branching of narrowly focused flow paths.

However, the spatial distribution (lateral and vertical) of matrix saturation within the column could not be measured with our experimental design.

5.1.3 Fluctuations in Total Outflow

In all four experiments, the total outflow rate leveled off ~48 hours after the start of inflow, and on average, remained slightly below the inflow rate to the end of the experiment (figure 5.1b). Note that the 48-hour time frame is an estimate that was selected after graphical analysis of the outflow data and does not represent an abrupt change in behavior. Even though the outflow had "leveled-off", fluctuations were noted about the mean behavior, and the outflow data appeared to be noisier than the inflow (figure 4.4, 4.14, 4.25 and 4.32). A source of this noise is likely in the outflow measurement methodology itself. If electrical noise affected all nine of the pressure transducers simultaneously, then they would each show local spikes in output that would be translated into spikes in the total outflow.

Fluctuations in the total outflow in response to inflow variability were also examined. At the end of experiment #4, total outflow was measured for a period of ~72 hours using an electronic balance to integrate all nine outlets and eliminate the effects of electrical noise in the individual collection vessels. This test indicated that fluctuations in the total outflow rate strongly correlate to inflow fluctuations (figure 4.43). Any detectable change (increase or decrease) in the inflow rate was followed by a similar directional change in the total outflow with a lag of 20-30 minutes. The highest coefficient of correlation (r) between inflow and total outflow rates, 0.73, was observed at a lag of 20 minutes. This suggests an effective flow velocity of ~3.0 m/hour (0.9 ml/min), which is much faster than expected for matrix flow (0.01 cm/hour). After the inflow was stopped in this

experiment, outflow remained relatively constant for ~20 minutes, then started to decrease rapidly, supporting the estimate of ~3.0 m/hour for the velocity of film flow (figure 4.6).

5.2 Outflow Distribution: Initial Development of the Flow Field

In all four experiments, water began to emerge from the bottom of the column ~3 - 4.5 hours after inflow started. In experiment #1 and 3, outflow began at the center outlet (S1 in figure 4.7), and there was a delay of 20-30 minutes before any of the other sections showed any measurable outflow. In experiment #2 and 4, the first outflow from section S1 coincided with outflow from one other section (S5 and S4, respectively). Measurable outflows started from all nine sections ~3 hours after the first observation of outflow. Outflow rate at each section rapidly increased for ~12 hours and then started to level off. Observed behavior suggests that flow structure within the column begins out as a narrow pathway, and then spreads laterally as film flow becomes dominant over matrix imbibition. In experiment #1 only, the outflow rate at the central section peaked, then gradually decreased, and leveled off as the flow at other sections increased (figure 4.8). This observation implies the initial development of a highly conductive narrow flow field that subsequently lost flow through lateral diversion into other pathways.

As reported in section 5.1, total outflow from the system stabilized roughly 48 hours after inflow started. The rapid changes in outflow from the individual sections of the column also leveled off in the same time frame. It is important to note that the choice of 48 hours is a judgment call, as the flow rates at individual sections showed fluctuations throughout all experiments. Looking at the outflow distribution at the end of the 48th

hour (figure 5.3), it is clear that flow at the bottom of the column was not uniform, as the flow from each section varied between 5% and 20% of the total outflow (figure 5.4).

The bottom of the column can be divided into three equal-area contiguous regions based on the flux at the 48th hour. The first region (S1, S3, S4), which included the central section, consistently showed high outflows in all experiments (~40% - 55% of the total flow). These three individual sections had the highest three outflows in all experiments, except for #1, where S4 ranked near the middle. The second region (S2, S8, S9) consistently showed lower than average outflows (~15% - 25% of the total flow), while the third region (S5, S6, S7) showed highly variable outflows between experiments (~20% - 40% of the total flow).

The flow distribution described above implies that the spatial arrangement of rock fragments in some regions preferentially creates high- or low-conductive flow fields, while the arrangement of fragments in other regions does not preferentially influence flow field development. Gravity-dominated vertical flow likely produces a high flux through the central section located vertically below the inlet. Preferential branching of flow paths from the centrally-developed flow field, due to arrangement of the fragments (thus inter-granular contacts), apparently results in consistently high flux through the first region described above. Consistently low flux through the second region may result from its lack of hydraulic connectivity to the central flow field, or diversion of flux away from that region before water reaches the bottom outlets. In the third region, the variability of flow may result from sensitivity of the flow elements (water films and pendular rings) to small changes in flow and/or saturation.

In addition to looking at regions of the column where outflow was generally higher, lower, or variable, the distribution of outflow around the expected value also can be considered. By definition, the expected value (mean) for the fractional outflow for each of the nine sections in a uniform flow field would be 11.1% (i.e., 100%/9). The variability about this expectation is described by the standard deviation, as shown in figure 5.5. The outflow distributions in experiments #1 and #2 were narrower around the mean in comparison to the distributions in #3 and #4. Furthermore, individual sections that exhibited high outflows were located non-adjacently in experiments #1 and #2, but adjacently (forming a large highly conductive region) in #3 and #4. Inflow temperature was the only significant factor that was different between the two sets of experiments; ~26 ^{o}C in experiments #1 and #2, while ~19 ^{o}C in #3 and #4. The lower inflow temperature increased the dynamic viscosity of water (by ~32%). It could reduce the branching of flow paths, as well as increase the thickness of water films on fragment surfaces and pendular rings. As a result, the spatial flow structure was limited to some highly conductive pathways constrained in a narrow region, and less conductive pathways in the rest of the domain.

5.3 Spontaneous Changes in the Outflow Distribution

After the initial 48-hour period, the distribution of outflow experienced substantial fluctuations that occurred despite the best attempts to isolate the system from external perturbations. Characteristics of these fluctuations such as: the magnitude of changes at different sections, number of sections that showed simultaneous changes, rate of change in flow, and the stability of the new flow distribution were largely different between

events. Small and short duration changes in measured outflow at individual sections were common in all experiments, and are not discussed further here. Of more interest are abrupt changes that occurred within a few hours, and progressive changes in outflow that occurred over several days.

5.3.1 Abrupt Changes in Outflow Distribution

In general, it was observed that an abrupt increase in outflow from one or more sections coincided with a decrease elsewhere (i.e., negligible change in total outflow). The magnitudes of the abrupt outflow changes at some sections were as large as 40% of their mean flow rate. The new flow distribution remained steady for some time (several hours to more than a day), and in many events it changed back to the previous distribution (e.g., A and B in figure 4.8; A in 4.17). In many instances, regions (i.e., sets of individual adjacent sections) that showed simultaneous increases and decreases were located at opposite sides of the column, but the central section that separated them showed only very small or undetectable changes in its flow. This implies a substantial change in flow structure, as outflow was diverted by at least 10 cm (the closest distance between two active sections).

The observed diversion of flow suggests the hydraulic connection between non-adjacent flow fields through narrowly focused pathways. Such flow paths would likely be composed of networks of water films on fragment surfaces and pendular rings at contacts between adjacent fragments. Sudden collapse or shrinkage in one or more water film(s) or pendular ring(s) can largely decrease the conductivity of an existing flow path. Also, the rapid development of such flow elements can produce new flow paths. Both of these processes would create large changes in the flow distribution and the effect of these

changes may be limited only to some regions in the flow domain. Stability of the new flow structure will be determined by the stability of individual flow elements; thus, it can be highly variable from event to event (from less than an hour to several days). Instability of flow elements will lead the flow structure to another configuration, or to the previous configuration.

Transfer of water between spatially non-adjacent flow fields without affecting the flow fields located between them implies that spontaneous changes are not limited to changing of flow paths between two adjacent regions. Furthermore, it supports the concept of discrete and narrowly focused flow paths in dual-porosity granular media. Such flow paths can have very complex spatial structures, and adjacently located flow paths within a small spatial unit may belong to different flow fields. Therefore, interactions between such flow paths in the scale of individual flow elements can largely influence the macroscopic flow structure in the medium.

5.3.2 Progressive Changes in Outflow Distribution

Progressive changes in outflow at individual sections that continued for more than two days were also observed. Such changes implied transfer of flow between two small flow fields at some instances (e.g., changes were limited to two individual sections; S1 and S7, figure 4.18), as well as between two large flow fields (e.g., flow rate fluctuations at many individual sections between 250 and 320 hours in figure 4.37). Most progressive changes of flow were observed between adjacent regions of the test column. It suggests progressive development of new flow paths and/or shrinking of some existing paths that hydraulically connect adjacent flow fields. Progressive changes will continue for long

durations because they occur gradually, thus the existing flow structure will not destabilize rapidly.

5.3.3 Possible Causes for Changes in Outflow Distribution

It is expected that microscopic and macroscopic changes of structure in pendular rings, as well as in water films on fragment surfaces alter the spatial structure of flow paths in dual-porosity granular media. However, any change in external experimental conditions (inflow, temperature, humidity or barometric pressure) that coincided with spontaneous changes in flow structure was not identified. Therefore, it is expected that micro-scale processes that changed the configuration of water films and pendular rings caused these changes. Similarities between spontaneous changes imply that the spatial arrangement of the rock fragments has a substantial influence on such micro-scale processes. Also, it is noted that the characteristics of spontaneous changes of flow fields (i.e., time, magnitude, frequency, rate of change, regions affected by a change etc.) were not predictable.

5.4 Variation of the Flow Structure in Response to Inflow Interruptions

Inflow to the test column was interrupted three times during experiment #2 (two pauses of 90 minutes and one pause of 10 minutes). For experiment #4, inflow was interrupted five times (four 90-minute pauses and one 20-minute pause). Large changes in the outflow distribution were observed for all of the interruptions during experiment #2. However, in experiment #4, one 90-minute interruption and the 20-minute interruption that followed it created only slight changes in the outflow distribution; the other three redistributions led to substantial redistributions of outflow.

5.4.1 Sections that Responded to Inflow Interruptions

Outflow at some regions (more than one adjacent sections) at the bottom of the column showed large changes, while that at some other regions consistently showed very small changes after inflow interruptions (figure 5.6, 5.7, 5.8 and 5.9). In contrast, other regions showed a range of flow rate changes after inflow interruptions. The regions that exhibited substantial spontaneous fluctuations of outflow showed a high sensitivity to inflow interruptions. The directionality of change in flow rates (i.e., increase or decrease) at each individual section was consistent between inflow interruptions in a single experiment, but was not consistent between the interruptions in two experiments (figure 4.16, 4.34, 4.35). This difference can be resulted from replacement of some rock fragments; thus, change in arrangement of fragments in the column between experiments #2 and #4. New flow rates at most sections showed progressive reversals to previous rates, which indicated the instability of the new flow structure. However, complete reversal was not achieved.

5.4.2 Possible Causes for Changes in Outflow Distribution

The most common characteristic of the change in flow distribution was a large increase in one region and simultaneously large decrease in another region; the central section (between the two active regions) showed a relatively small change in the central section of the column. This observation supports the concept of discrete flow fields and hydraulic connectivity between such flow fields through narrowly focused pathways.

We can expect that after inflow is stopped, water films on fragment surfaces and pendular rings that bridge individual water films become thin or discontinuous. As inflow is restarted, these features may develop in a new configuration, which results in a

different flow distribution. The spatial structure of flow paths that develops after an inflow interruption (i.e., in wet medium with residual matrix water, water films and pendular rings) differs from that develops at the initiation of the experiment (i.e., in a dry medium). However, the high consistency in the direction of flow rate changes within a given section (increase or decrease) after inflow interruptions in a single experiment implies that development of the flow structure under wet conditions is consistent. The arrangement of individual fragments (i.e., orientation of fragment surfaces and contacts between fragments etc.) can influence gravity-driven drainage of water films and pendular rings. Therefore, we expect that the residual flow structure remains mostly similar between interruptions, and leads to consistent flow structures after resumption of the inflow.

The magnitude of flow rate change consistently remained very small in regions where the original flow rate was very low. The original low flux results from either the small number of flow paths and/or presence of very thin water films in these regions. Gravity-driven drainage does not substantially change the spatial structure of such flow elements during inflow interruptions, thus the changes of flow rate are very small. Consistent increase or decrease of flow rates at some sections in one experiment, but opposite directional changes at the same sections between two experiments may attribute to the change of configuration of rock fragments.

Such physical changes can substantially alter the configurations of the flow paths that develop close to the inlet. The importance of the physical configuration of the fragments is supported by the high flow rate changes observed at section (S5) following interruption in experiment #. This section consistently showed extremely small or undetectable

changes in experiment #2. However, it was noted that outflow changes at another individual section (S2) consistently remained very low in both experiments despite the replacement of rock fragments.

5.4.3 Possible Causes for Observed Lack of Change in Outflow Distribution

Two consecutive inflow interruptions in experiment (90-minute and 20-minute) made only very small changes in comparison to changes associated with the other three interruptions in the same experiment. The only condition that was noticeably different between the two sets of interruptions was the inflow temperature. It was low (16-20 ^{o}C) during the three interruptions that led to significant outflow redistribution, but was high (~28 ^{o}C) during the two that had little effect. However, a similar inflow temperature (26.5 and 27.5 ^{o}C) was recorded during all three interruptions in the second experiment that led to significant redistribution of the outflow.

Characteristics of changes in flow structure observed after inflow interruptions imply that all regions in the flow domain do not necessarily respond to an individual inflow interruption. Also, the same region does not necessarily respond in a similar manner for inflow interruptions of similar duration. Some flow fields are highly sensitive even to short (10 minutes) inflow interruptions, but some are extremely low sensitive to even to long (90 minutes) interruptions. Furthermore, changes in the flux at different regions caused by inflow interruptions can be extremely low, moderate or very high. The expected direction of change of flux (i.e., increase or decrease) at a particular region can be predicted with a low uncertainty based on previous observations, provided that the material properties remain unchanged between inflow interruptions.

5.5 Variation of the Flow Structure in Response to Relocation of the Source

Changing the location of the single-point source led to larger changes in the outflow distribution than either spontaneous changes or interruptions to inflow. Initially, the inlet was located at the center of the column. At first, it was moved away from the center (figure 5.10 and 5.11, Move-1A and 1B), and then moved back to the center (Move-2). Lastly, it was again moved away from the center in the same direction, but by a shorter distance (Move-3; refer to figure 4.40 for relative locations of the inlet).

Flow rate at six sections at the bottom of the column consistently increased when the inlet was moved close to their projections at the top of the column, and the reverse happened when it was moved away (figure 5.12). Conversely, one region at the bottom of the column (consisted of S2 and S9) exhibited the highest flow when the inlet was located farthest away from it, and gradually lower flow when the inlet was moved closer to it.

All flow changes were reversible to a large extent; i.e., increased flow at a particular region due to change of the inlet location decreased when the inlet was moved back to its previous location. For instance, flow distributions between the nine sections were mostly similar when the inlet was located at the center of column before any relocation and after the second relocation, but actual flow rates were slightly different (figure 5.13).

The influence of gravity-driven vertical flow can increase and decrease the flow at a particular section when the source is moved close to and away from it respectively. However, increase in the vertical flow as the lateral distance to the source increases and the reverse as the distance to the source decreases cannot be explained with the concepts of uniform flow. We can expect that narrowly focused flow paths in dual-porosity

granular media have complex spatial structures, thus they can create spatially uneven flow distributions, which do not confirm with uniform flow.

In general, vertical flow due to the gravity creates a high flux below the source, but the lateral distribution of the flow around the source depends on the spatial configuration of pendular rings and water films. However, relocation of the source to a certain point does not necessarily increase the fluid flux though the vertical profile below it. Such a relocation may increase, decrease or may not change the flux through the zone vertically below the new location of the source.

5.6. Effect of Evaporation Changes on the Flow Structure

Immediately after covering the top of the column in order to minimize evaporation, outflow at all sections at the bottom of the column showed substantial changes (figure 5.14 and 5.15; refer to figure 4.41 for changes at individual sections), but the total outflow did not show any detectable change. After uncovering the top of the column, changes of flow distribution were observed again, but at a smaller number of sections and with smaller magnitudes. Any section that showed a flow rate increase or decrease after uncovering the column had showed the similar directional change after covering the column.

Formation of thicker water films and pendular rings at some flow paths likely resulted in increased flow after reducing the evaporation. Increased flow along these paths resulted in decreased flow in other paths. The subsequent increase in evaporation caused flow elements to shrink, but relatively thin elements were impacted the most. As a result,

the conductivity of less-conductive flow paths further decreased, and the conductivity of highly conductive flow paths further increased.

Outflow changes were identified very quickly (~20 minutes) after covering the column, but a longer duration (~1 hour) was required to create detectable flow changes after uncovering the column. This implies that the effects of condensation of water vapor within the flow system were more rapid than the effects of increased evaporation from the system.

5.7 Statistical Analysis of Results

The experiments described in this thesis present a complicated problem for statistical analysis. First, all four of the experiments differed from one another in one or more aspects (e.g., duration, inflow boundary, ambient environment, and configuration of the media). Second, the mechanisms controlling behavior changed over the course of an individual experiment; matrix imbibition was dominant at the beginning of each experiment, and film flow became the dominant flow mechanism subsequently. Third, the two long-term experiments (#2 and #4) were subjected to external perturbations that temporarily altered boundary conditions and created apparent changes within the experiments. Finally, the outflow from individual sections showed a high degree of spatial variability, some, but not all, of which was apparently correlated to the external perturbations. For these reasons, the nature of the outflow measurements does not fit well with statistical methods that assume a stationary mean.

In order to address the above issues, this analysis is focused on experiment #2, which had relatively large data sequences between the external perturbations. In contrast, the

other long-term experiment (#4) was subjected to a large number of external perturbations, thus greatly complicating analysis. Experiments #1 and #3 were of shorter duration (10 and 2 days respectively), and not subjected to external perturbations; thus they are not desirable for analysis. To evaluate experiment #2, we removed the first 48 hours where matrix imbibition was strong and outflow was rapidly changing. After that, we eliminated data for those time periods impacted by inflow interruptions. This produced four discrete data segments as follows: period between the 48th hour and the first inflow interruption (segment #1), between the first and second interruptions (segment #2), between the second and third interruptions (segment #3), and between the third interruption and termination of inflow (segment #4). The analysis below looks first at the mean behaviors and then at temporal changes in outflow from individual sections.

5.7.1 Variability of Inflow and Outflow

The combined mean inflow rate for all four data segments was 7.98 ml/min with a standard deviation (σ) of 0.04 ml/min (table 5.1). The mean inflow rate for each of the individual segments was within one σ of the mean, and the values of σ for the individual segments were very similar to the combined value. This result suggests that the inflow was stable and nearly constant throughout all four segments. Similarly, the total outflow rate for all four individual segments was within one σ of the mean for the combined value (mean = 7.93 ml/min, σ = 0.38 ml/min). In addition, values of σ for the total outflow for the individual segments were very similar to one another, again suggesting that the total outflow behaved similarly between the four segments. However, σ for the total outflow was larger than that for the inflow by an order of magnitude. This may be at least partially an artifact of the experimental methodology. The total outflow is the sum of nine

measurements from individual collectors, whereas inflow is measured by a single device. Furthermore, the outflow measurements are made using much less expensive devices than the inflow (pressure transducers vs. electronic balance), and the outflow drips into the collection vessels creating an inherently noisier measurement environment than the pumped withdrawal from the source bucket.

The mean outflow from the individual sections at the bottom of the column can be evaluated in a variety of ways. The sum of the individual means is equal to the mean total outflow; however, the sum of the standard deviations for the individual sections is greater than that for the total outflow. Looking first at σ across all four segments, the sum of σ for the individual sections is roughly three times greater than that for the total outflow (1.17 vs. 0.38 ml/min). For each of the individual segments, the sum of σ for the individual sections exceeds that for the total outflow by a factor of ~1.5 to 3.4. This result confirms that changes in outflow from a particular section were at least partially offset by an opposite change from one or more of the other sections. It also suggests that outflow variability for individual sections was different between the various segments.

The distribution of outflow between the nine sections was significantly non-uniform (at a significance of 0.05). In all four segments, outflow from the central section (S1) was consistently higher than the other eight. Outflow from S1 was significantly higher than that from any other individual section in segments #1 and #4 (at significance of 0.05). However, in segments #2 and #3, flow from S1 was not significantly different from that from S7, but was significantly higher than flow from any other section. Mean flow rates of five individual sections (S2, S3, S6, S7 and S8) were significantly different at least between two segments. Standard deviations for all individual sections in segment #1 and

#4 were on the order of 10^{-2} ml/min, which indicated relatively low fluctuations in outflow. However, standard deviation for five sections (S1, S3, S4, S6 and S7) were on the order of 10^{-1} ml/min in segment #2 and #3. This resulted from progressive and abrupt changes in flow rates at individual sections occurring after stabilizing the total outflow after inflow interruptions.

5.7.2 Statistical Significance of Outflow Changes at Individual Sections

Evaluating the statistical significance of outflow changes at individual sections requires comparison of the changes with the standard deviation for a substantially long representative period. The standard deviation for flows at several individual sections was different by an order of magnitude between different time segments (table 5.1). Therefore, a value that represents the normal variability of flow in the system cannot be determined using outflow at individual sections. Other reasonable alternatives are using the standard deviations of the total outflow or inflow. Since the standard deviation of total outflow can be influenced by that of individual sections, we decided to use the standard deviation of inflow rate as the parameter that best represents the natural variability of the flow. Any outflow change at an individual section that was larger than three times the standard deviation of the inflow rate was defined as a statistically significant change (i.e., ~0.01 significance). When the change was not significant, we considered that flow rate remained unchanged for statistical analysis. Outflow data filtered using this criterion were plotted as a function of time (figure 5.16). This approach allowed us to identify significant changes in outflow, that were not created due to fluctuations of the inflow. It was found that all three inflow interruptions created

statistically significant outflow changes. Also, there were several spontaneous changes that were statistically significant.

This procedure can be repeated to determine the statistical significance of changes observed in experiment #4. Intervals between some individual external perturbations in experiment #4 were much shorter than that in experiment #2; therefore, analysis will be more complex. However, comparison of magnitude of statistically significant outflow changes in experiment #2 with outflow changes occurring in experiment #4 after external perturbations (except inflow interruption 3 and 4) indicates that latter changes are also statistically significant. Therefore, it can be concluded that relocation of the source and imposed evaporation changes from the column resulted in statistically significant (at significance of 0.01) changes in outflow distribution.

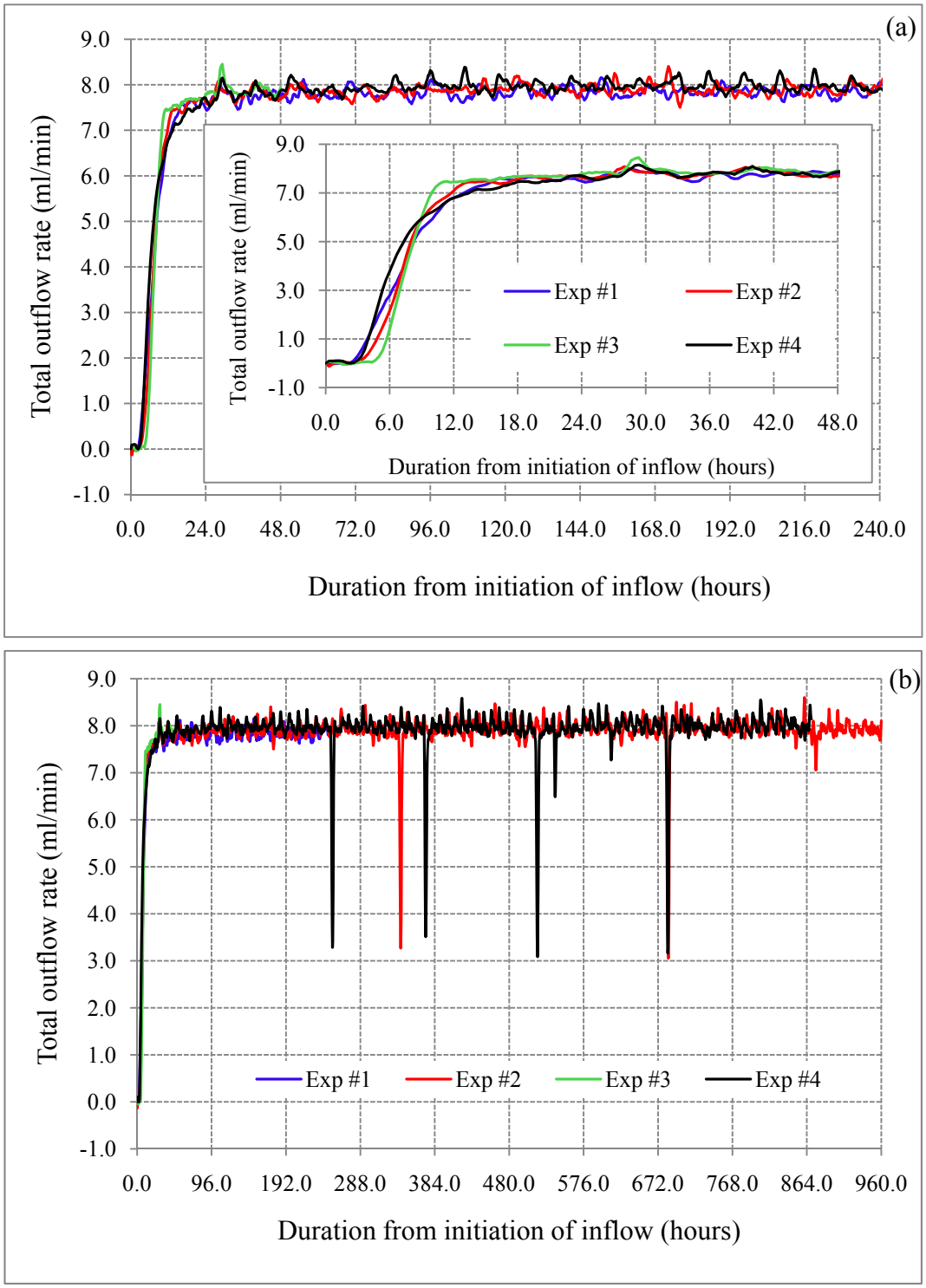

Figure 5.1 Variation of the total outflow during the first 10 days (a), and 40 days (b) in four experiments (note that experiment #1 and #3 ran only for 240 and 56 hours, respectively). Inset graph shows the outflow variation in the first 2 days. Sharp dips in figure b correspond to inflow interruptions.

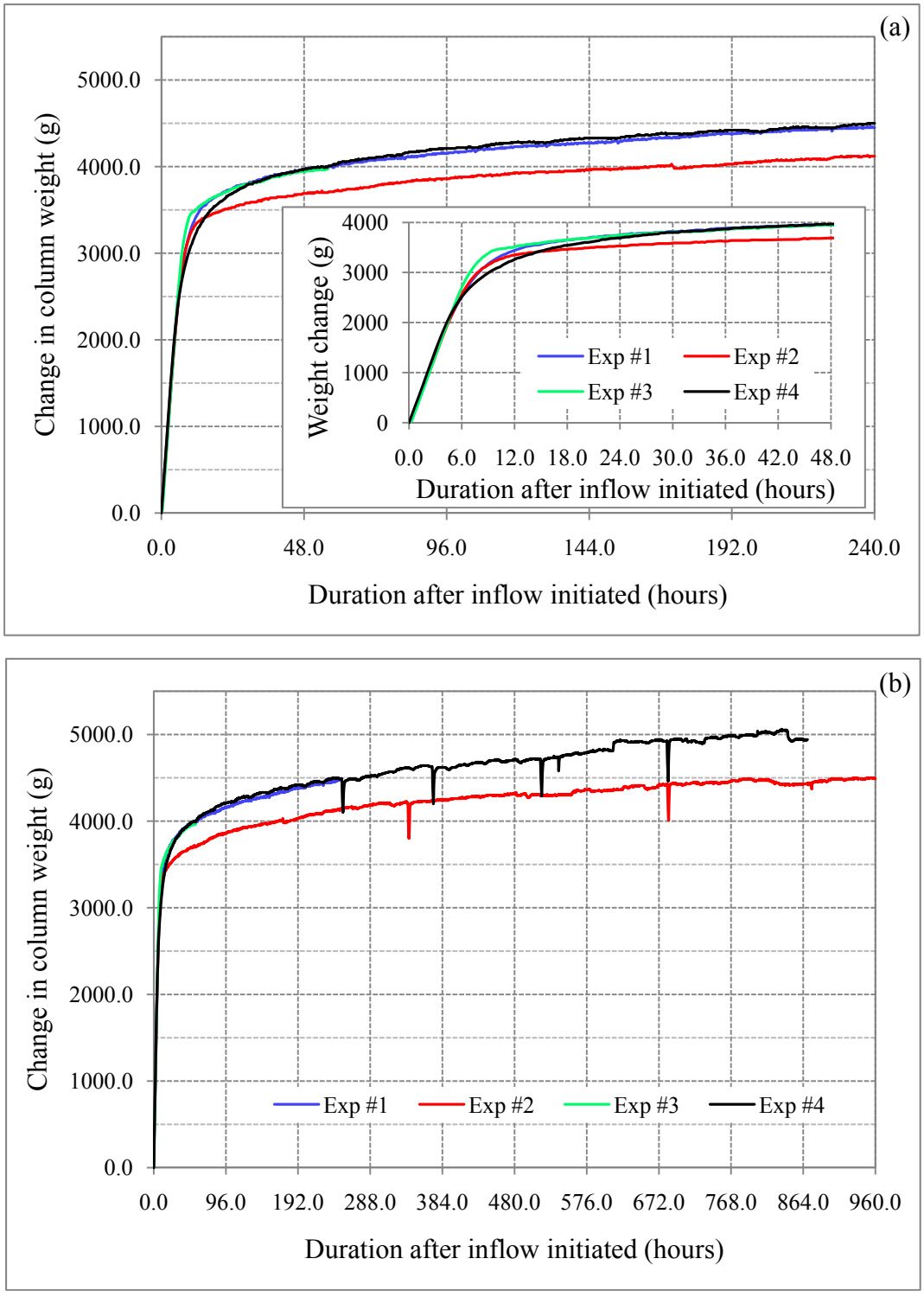

Figure 5.2 Increase of the column weight due to saturation during the first 10 days (a), and 40 days (b) in four experiments (note that experiment #1 and #3 ran only for 240 and 56 hours, respectively). Inset graph shows the weight increase in the first 2 days. Sharp dips in figure b correspond to inflow interruptions.

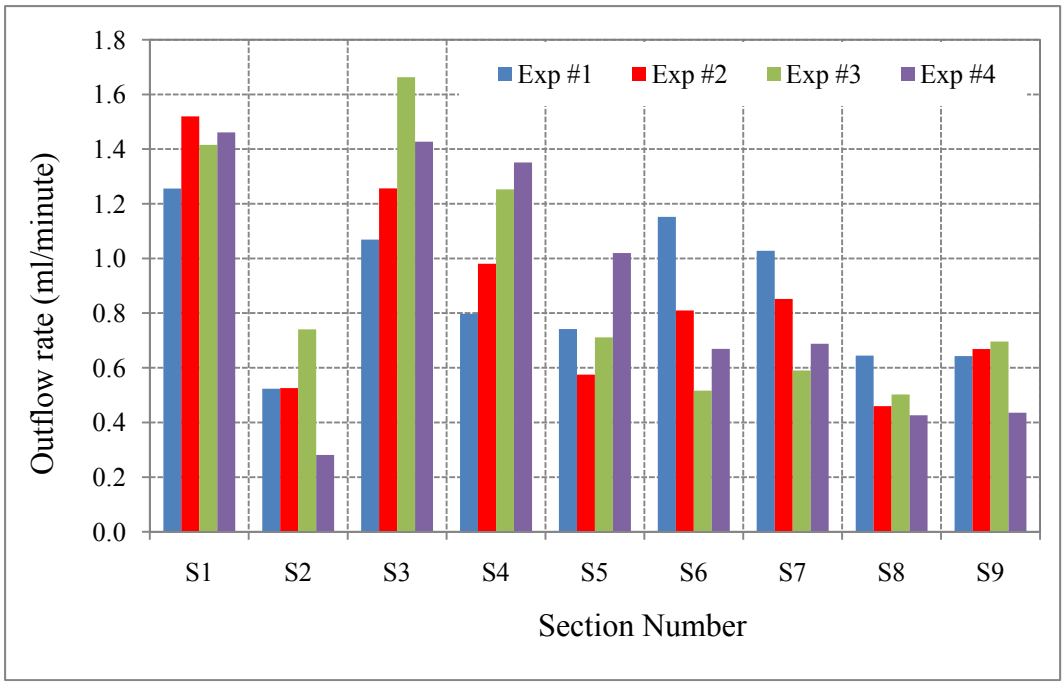

Figure 5.3 Mean outflow rate of each of the nine sections, 48 hours after initiation of inflow in each experiment

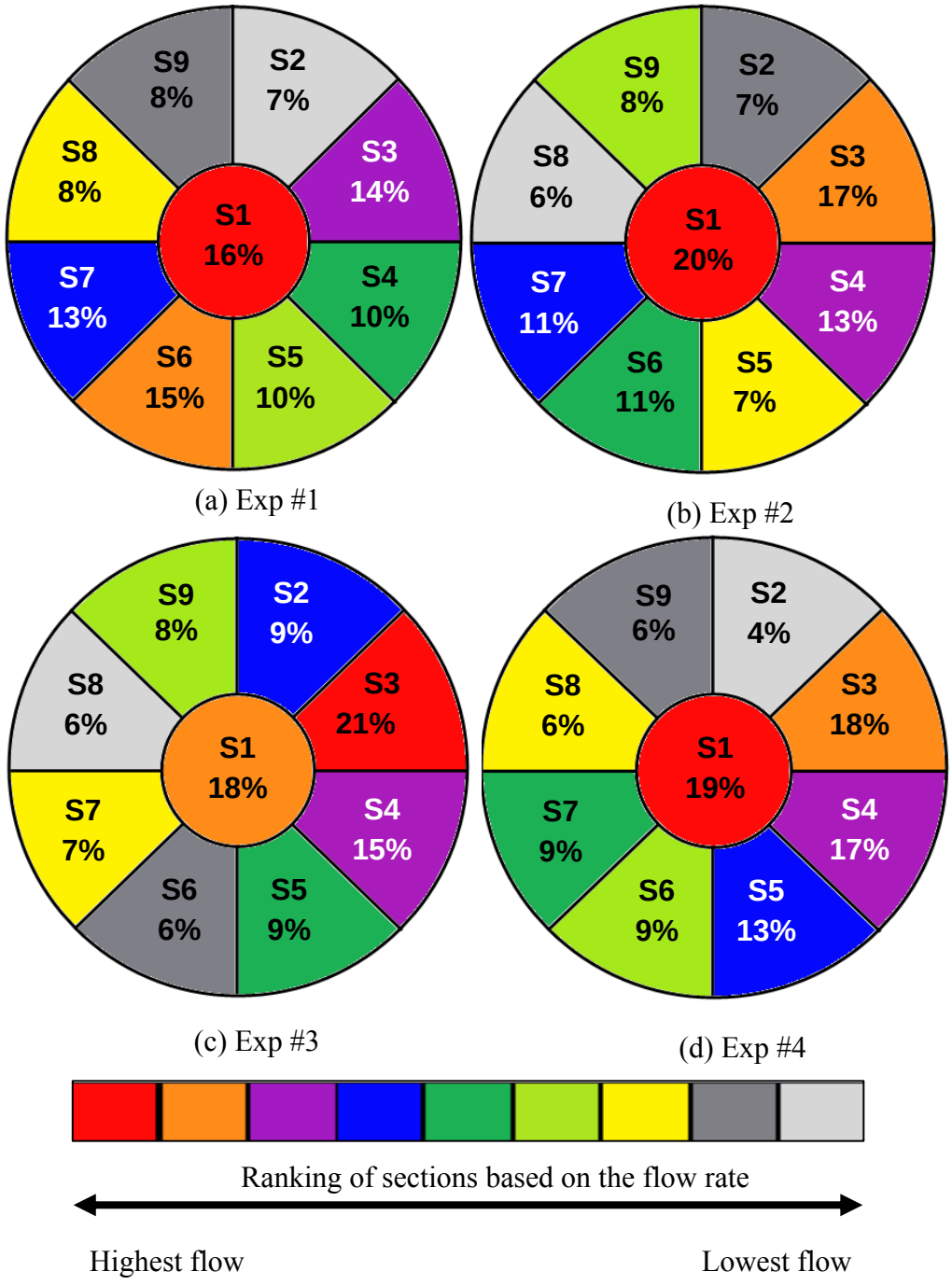

Figure 5.4 Proportionality of the mean outflow rates at nine sections 48 hours after the beginning of each experiment. Each section of a pie chart represents the percentage contribution of each section to the total outflow.

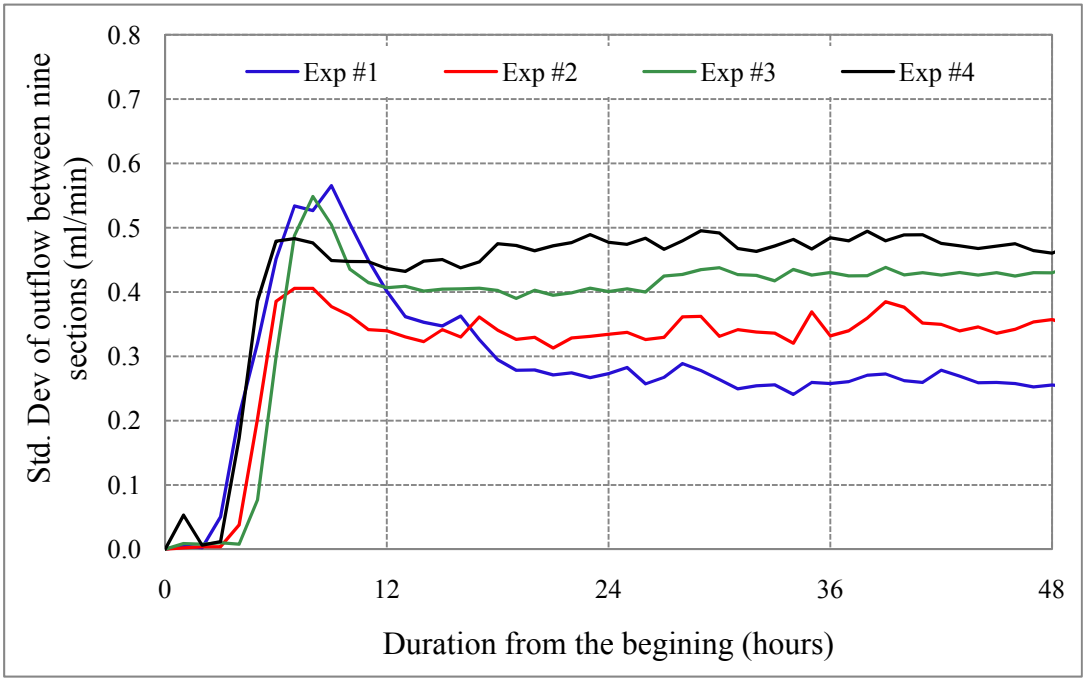

Figure 5.5 Standard deviations of the outflow rates between nine sections in four experiments

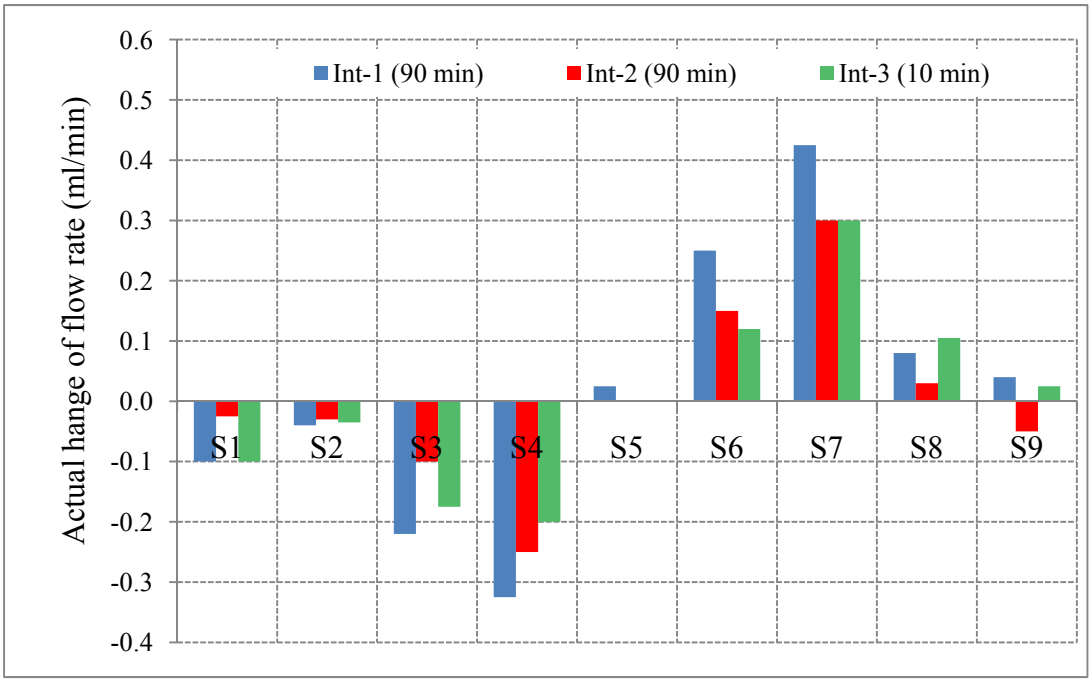

Figure 5.6 Actual change of outflow rate at each section after three inflow interruptions during the experiment #2

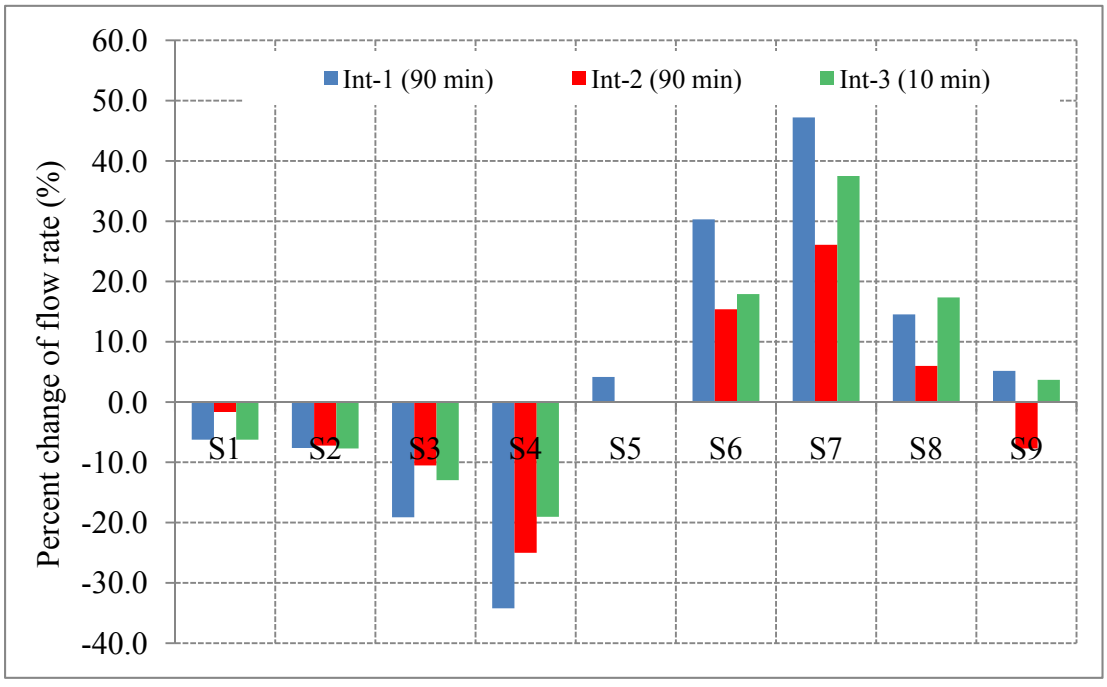

Figure 5.7 Percentage change of outflow at each section after three inflow interruptions during the experiment #2

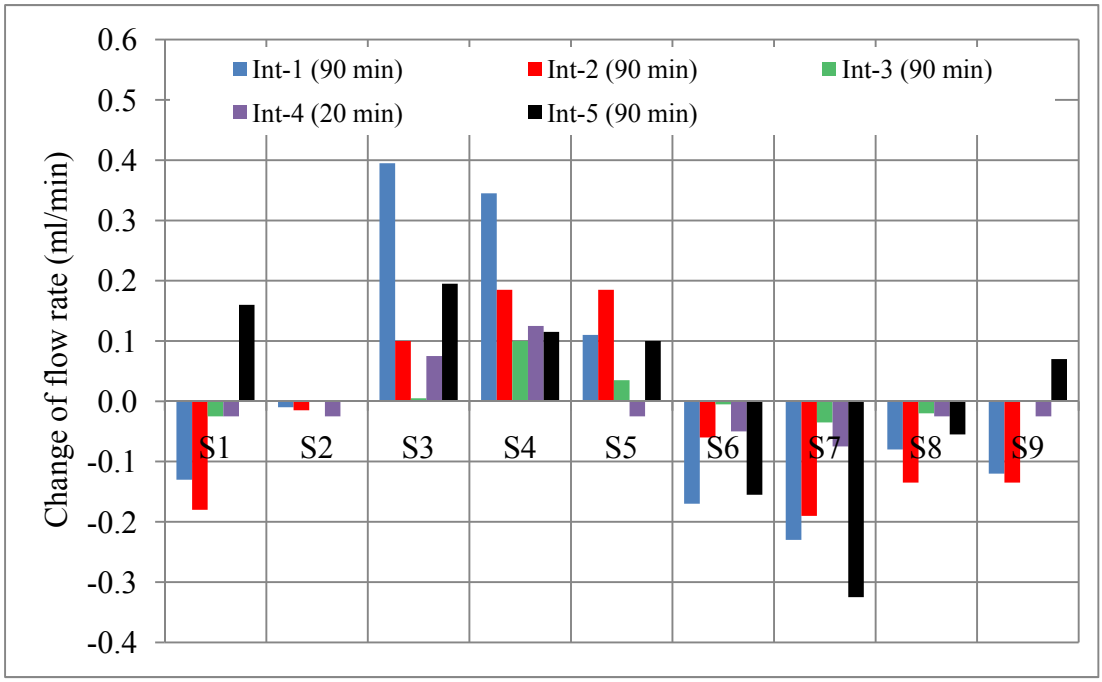

Figure 5.8 Actual change of outflow rate at each section after five inflow interruptions during the experiment #4

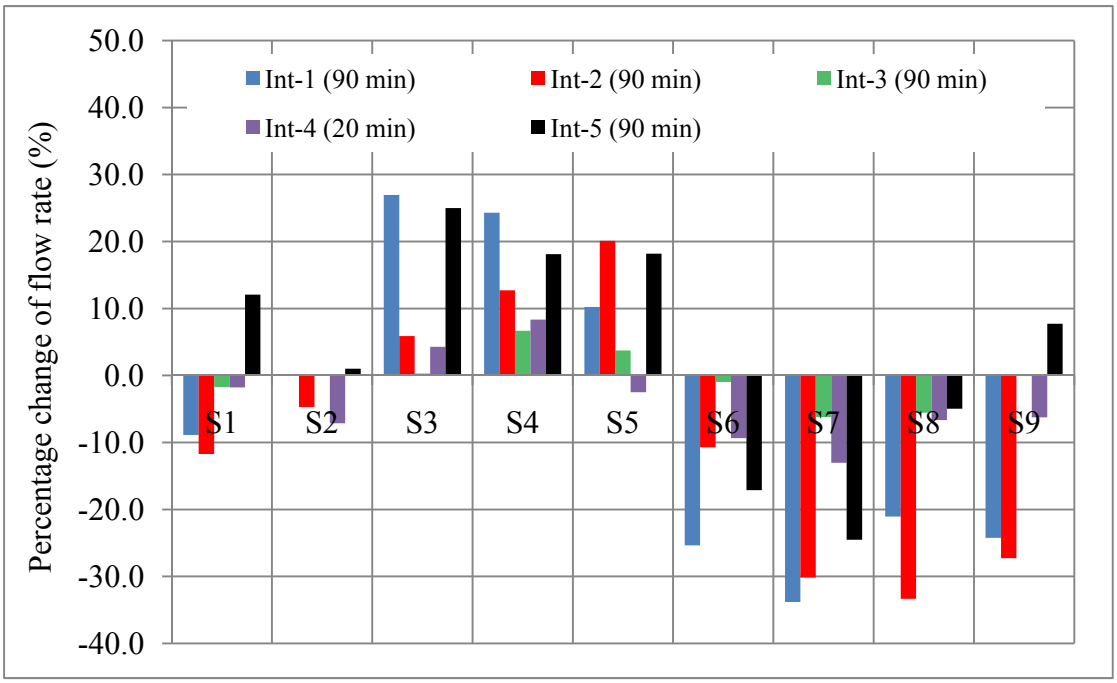

Figure 5.9 Percentage change of outflow at each section after five inflow interruptions during the experiment #4

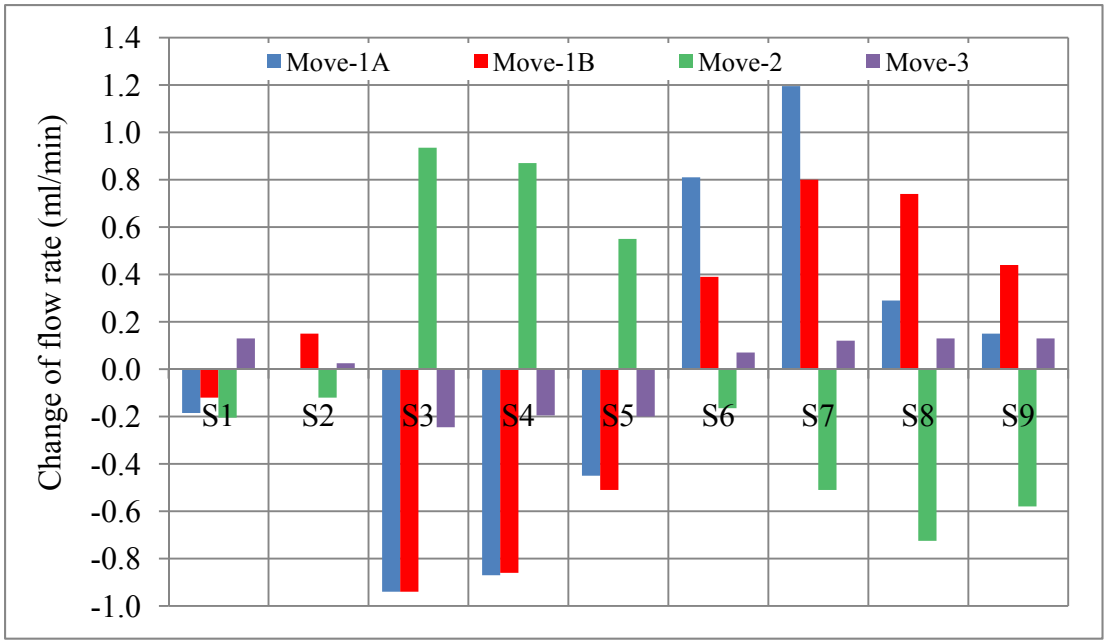

Figure 5.10 Actual changes of outflow rates at each section after changing the location of the inlet in the experiment #4 (1A shows the immediate changes and 1B shows the final result of all changes occurred over 25-hour period after the first change of the inlet location)

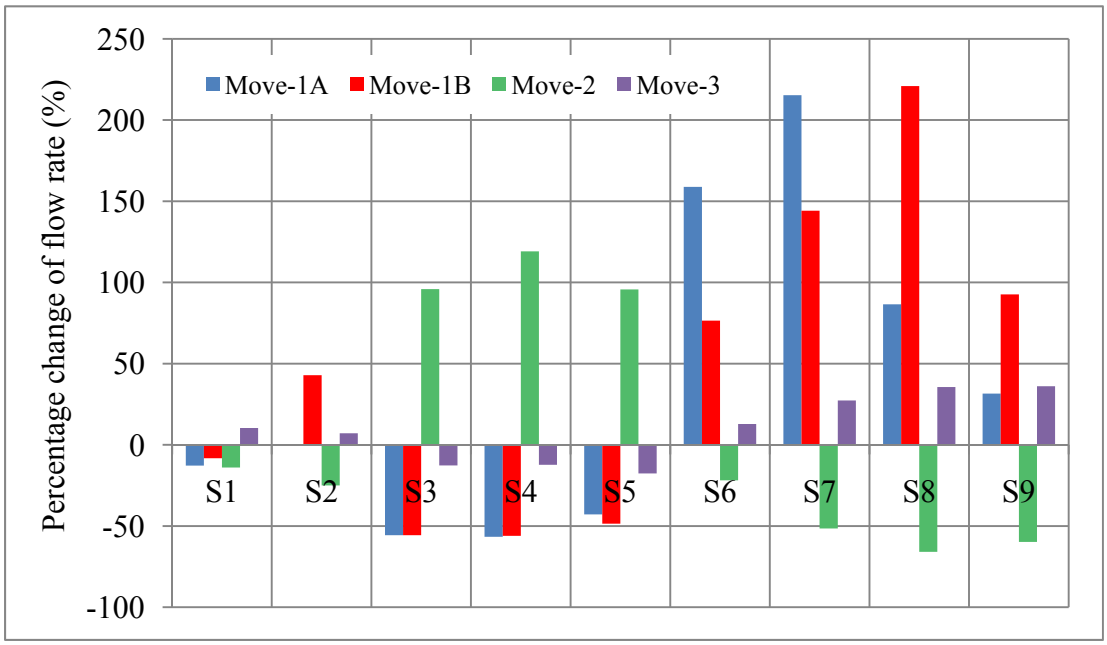

Figure 5.11 Percentage changes of outflow rates at each section after changing the location of the inlet in the experiment #4 (1A shows the immediate changes and 1B shows the final result of all changes occurred over 25-hour period after the first change of the inlet location)

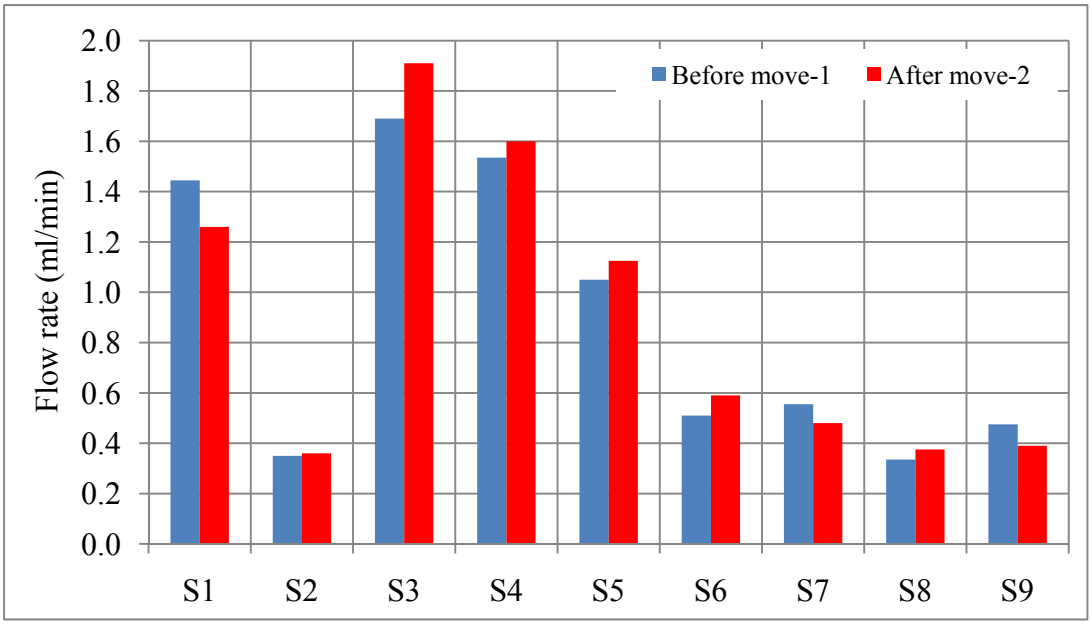

Figure 5.12 Outflow rates at each section when the inlet was located at the center of S1 before the first location change and after the second location change in the experiment #4

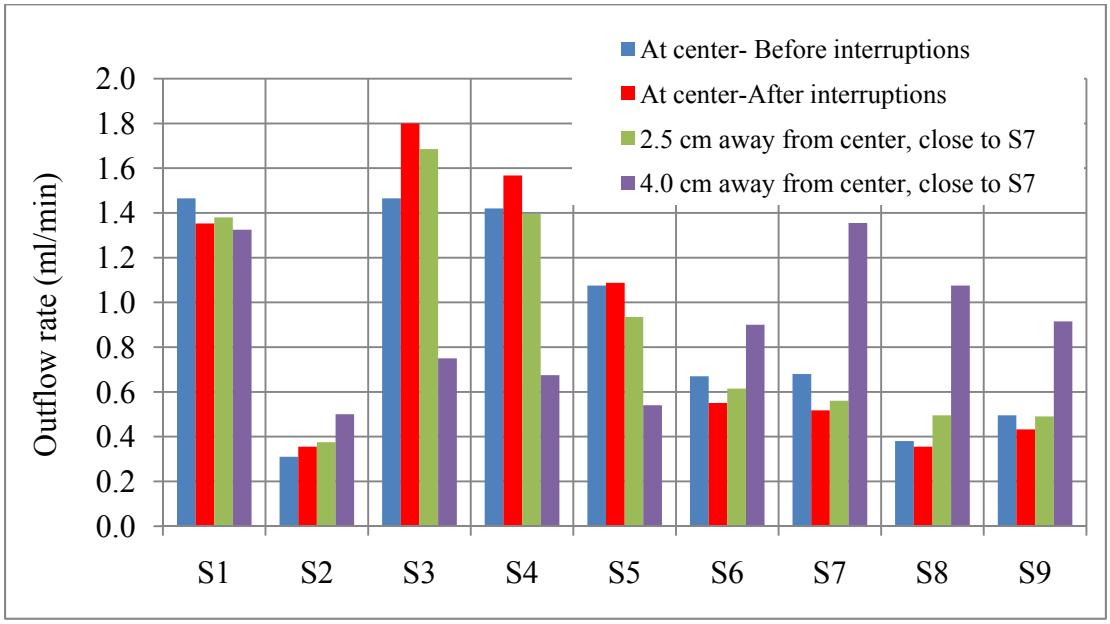

Figure 5.13 Mean Outflow rate of each section for different inlet locations. The first series represents the flow 240 hours after the beginning and before any perturbation; the second series represents the mean flow before the first and after the second inlet relocation. The third and fourth series represent flow after the second and third inlet relocations

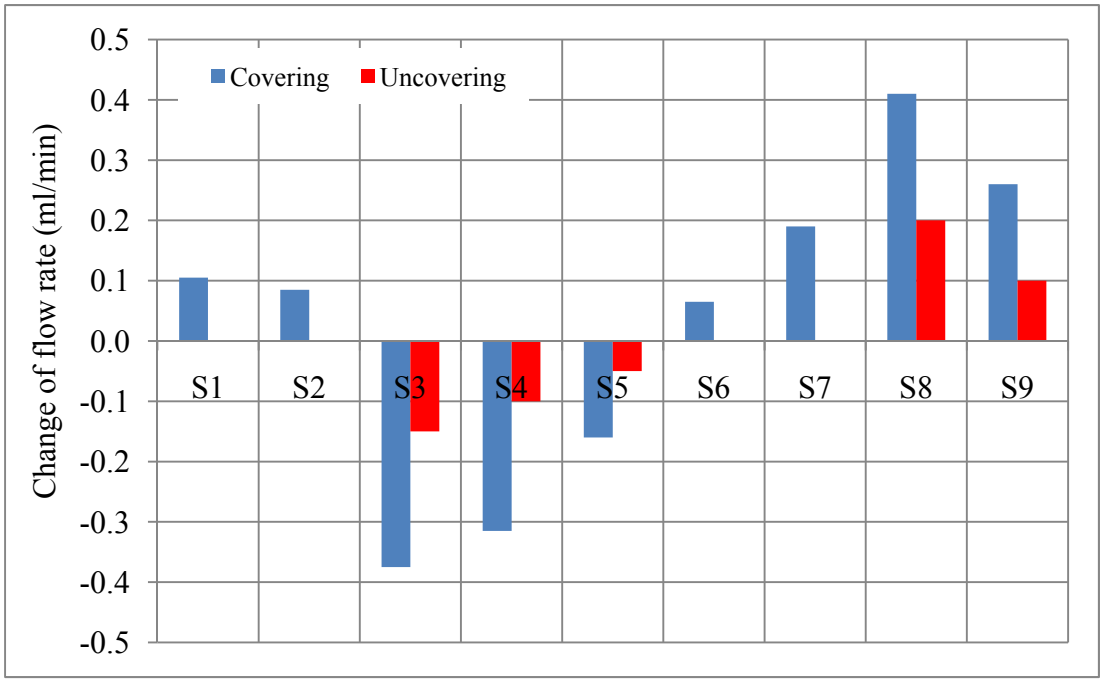

Figure 5.14 Actual change of outflow rate at each section after covering and uncovering the top of the column in the experiment #4

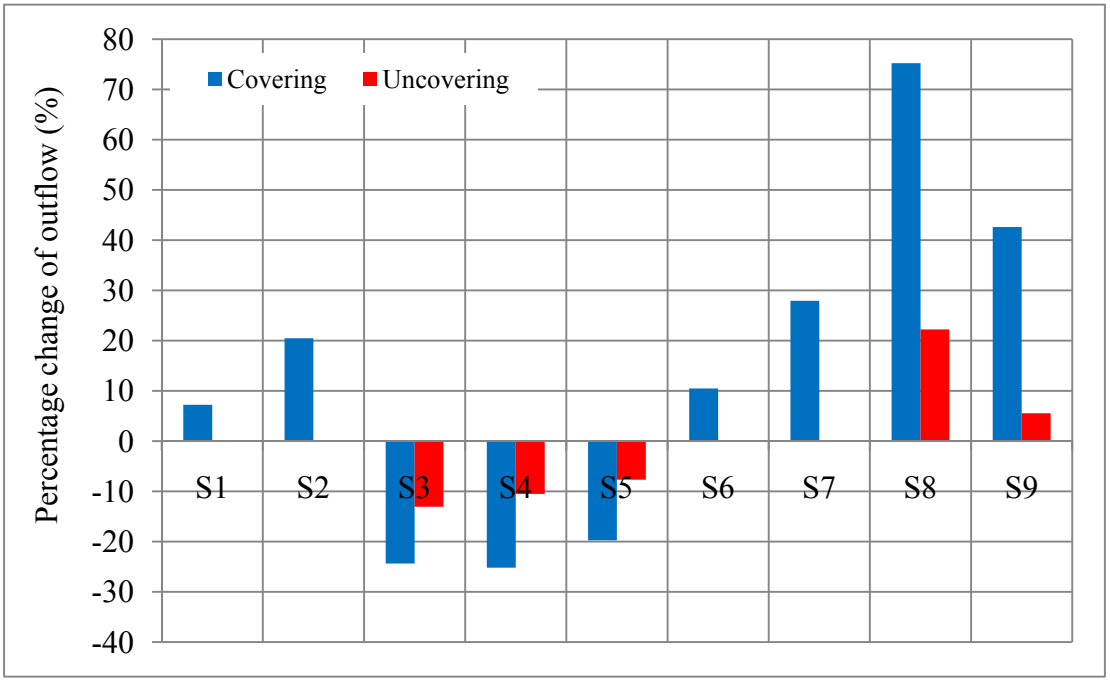

Figure 5.15 Percentage change of outflow rate at each section after covering and uncovering the top of the column in the experiment #4

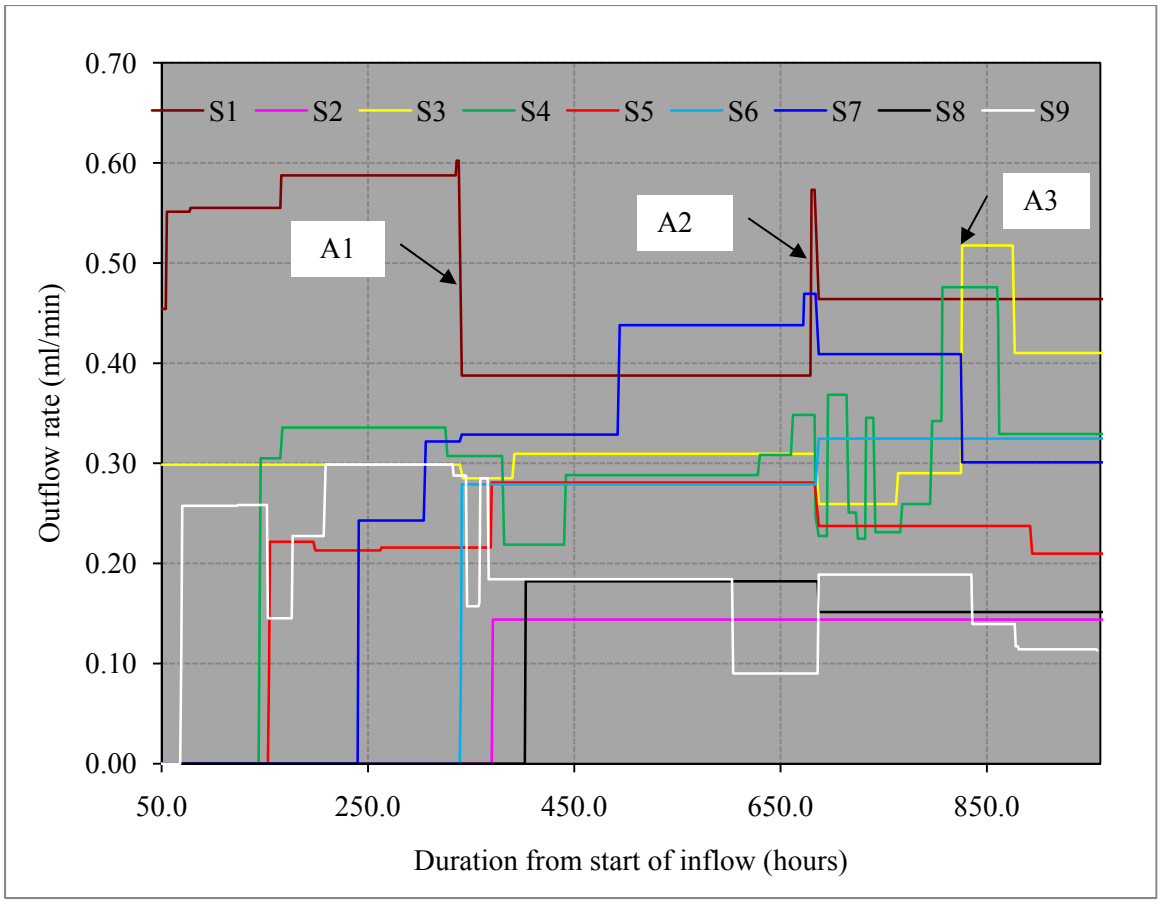

Figure 5.16 Statistically significant changes of outflow at individual sections (A1, A2 and A3 are inflow interruptions. Note that Y-axis does not show the actual flow rate because statistically non-significant changes were excluded in the analysis)

Table 5.1 Statistics of inflow, total outflow, outflow from nine sections (S1 through S9), and background noise (N1 and N2) in experiment #2 (flow rates are in ml/minute, n is the number of measurements recorded at 20-minute intervals, μ is the mean, σ is the standard deviation and cv is the coefficient of variance).

	Segment #1 (48 hour to interruption 1) n = 872			Segment #2 (between interruption 1 and 2) n = 1022			Segment #3 (between interruption 2 and 3) n = 563			Segment #4 (between interruption 3 to end) n = 271			Combination of four segments n = 2728		
	μ	σ	cv	μ	σ	cv	μ	σ	cv	μ	σ	cv	μ	σ	cv
Inflow	7.98	0.04	0.01	7.98	0.05	0.01	7.99	0.05	0.01	8.00	0.04	0.01	7.98	0.05	0.01
Total outflow	7.90	0.37	0.05	7.94	0.38	0.05	7.96	0.38	0.05	7.94	0.38	0.05	7.93	0.38	0.05
S1	1.56	0.09	0.06	1.52	0.13	0.08	1.45	0.13	0.09	1.51	0.08	0.05	1.52	0.11	0.07
S2	0.54	0.04	0.08	0.44	0.05	0.11	0.42	0.06	0.13	0.40	0.04	0.10	0.46	0.07	0.16
S3	1.22	0.07	0.06	0.90	0.09	0.10	1.00	0.22	0.22	1.13	0.05	0.05	1.05	0.18	0.17
S4	0.95	0.09	0.09	0.83	0.11	0.13	0.89	0.14	0.16	0.82	0.08	0.09	0.88	0.13	0.15
S5	0.62	0.07	0.11	0.69	0.07	0.11	0.74	0.07	0.10	0.74	0.08	0.11	0.69	0.10	0.14
S6	0.83	0.05	0.06	1.05	0.06	0.06	0.98	0.19	0.19	0.76	0.04	0.06	0.94	0.15	0.16
S7	0.91	0.09	0.10	1.32	0.10	0.07	1.34	0.31	0.23	1.14	0.06	0.05	1.17	0.25	0.22
S8	0.53	0.07	0.13	0.52	0.07	0.14	0.53	0.07	0.14	0.69	0.05	0.07	0.54	0.08	0.15
S9	0.73	0.08	0.11	0.67	0.09	0.13	0.61	0.08	0.13	0.75	0.10	0.13	0.69	0.10	0.15
N1	0.00	0.13	34	0.00	0.13	67	0.00	0.17	58	0.00	0.22	-274	0.00	0.17	68
N2	0.00	0.06	28	0.00	0.06	15	0.00	0.06	28	0.00	0.07	-83	0.00	0.06	24

CHAPTER 6

CONCLUSIONS AND SUGGESTIONS FOR FURTHER INVESTIGATIONS

The experiments described in this thesis were conducted to investigate the spatial structure of unsaturated water flow in dual-porosity granular media and any associated temporal variability. The first section (6.1) of this chapter presents the conclusions of this research, while the second section (6.2) presents suggestions for further investigations on unsaturated flow in dual-porosity granular media.

6.1 Conclusions

Observations made in a series of experiments led to several conclusions about unsaturated flow in dual-porosity granular media that are inconsistent with traditional unsaturated flow concepts as found in soil physics and geophysics literature (e.g., Hillel, 1998).

The spatial distribution of flow paths in dual-porosity granular media is largely non-uniform, even though the material and its hydrological properties are mostly uniform. Water flow in this type of media likely occurs through narrowly focused, discrete flow paths developed along networks of interconnected fragments. Both matrix flow and film flow contribute to the flow in dual-porosity granular media. However, film flow will start to dominate the flow when the influx exceeds the sorption capacity of fragments (at a matrix-saturation much smaller than 100%) at local scale.

The spatial structure of water-filled contacts between fragments, and films on fragment surfaces largely control the spatial distribution of flow paths. Because of the uneven spatial distribution of such flow elements, flux through the medium is likely to be

spatially non-uniform. Since the distribution of flow paths in the media is spatially uneven, saturation of matrices of fragments will be spatially non-uniform. Matrix-saturation of fragments located in the vicinity of active flow paths will be highly saturated (close to 100%), but that of fragments that do not get direct contact with water will be very low (close to 0%). When the entire flow domain is considered, saturation of the fragments will be much smaller than 100% even with a substantial influx.

Networks of flow paths developed along interconnected fragments will form discrete macroscopic flow fields within the medium. Flux (i.e., volumetric flow and effective flow velocity) will be measurably different through such flow fields. Spontaneous changes in the spatial structure of water films and pendular rings along an individual flow path will lead to interaction between adjacent flow paths, creating substantial changes in macroscopic flow distribution. As indicated by simultaneous and opposite directional changes in outflow at non-adjacent sections in our experiment, temporal changes in discrete flow paths will be able to divert flow between non-adjacent flow fields in the medium.

Inflow and boundary conditions have a significant impact on the spatial structure of unsaturated flow in dual porosity granular media. The location of the fluid source significantly (at 0.01 of significance) affects the flow distribution within the system. Gravity-driven vertical flow creates a high flux below the source, but the region located vertically below the source does not always show the highest fluid flux. Relocation of the source creates large changes in the flow structure. Lateral relocation of the source will change the flux in some regions of the flow domain, but will not affect the flow in other regions. In contrary to conventional flow concepts, moving the source away from some

regions will substantially increase the flux through them and vice versa. The directional change in the flux through a region due to relocation of the source in a particular direction will remain mostly consistent if the other conditions remain unchanged. Furthermore, macroscopic changes in the flow structure associated with relocation of the inlet will be reversible to a large extent.

Discontinuities of the inflow (even ~10 minutes) create significant changes (at 0.01 of significance) in the macroscopic structure of flow fields. Directional changes of the flow structure (i.e., increase or decrease of flux at different flow fields) in response to inflow interruptions will be mostly consistent under unchanged conditions. Changes in evaporation from the flow system will also significantly alter the spatial flow structure by changing dimensions and spatial distribution of pendular rings and water films to equilibrate to new conditions. Decreases in evaporation, which enhances the condensation, have larger influences on the flow structure in comparison to the increases of evaporation. Macroscopic changes of the flow structure associated with the evaporation changes are not reversible.

Viscosity of water, as controlled by temperature, showed a noticeable influence on the initial development of the flow structure. Relatively low inflow temperatures (<20 ^{o}C) are likely reduce the lateral distribution of flow and apparently create highly-conductive and very low conductive flow fields. Increasing temperature (>25 ^{o}C) will enhance lateral distribution and make the flow distribution more uniform. However, the existence of an optimal temperature that provides the most uniform flux distribution in the medium still needs to be determined. Fluctuations of the inflow temperature between ~15 and 30 ^{o}C did not noticeably affect spatial structure of flow paths after they were established.

Progressive changes of ambient temperature in the range of 20 and 30 ^{o}C, relative humidity in the range of 15% and 35% and atmospheric pressure in the range of 98.0 to 103.0 kPa do not create any noticeable change in the flow structure.

6.2 Suggestions for Further Investigations

In a series of experiments, it was found that unsaturated flow in dual-porosity granular media is not spatially uniform, and the spatial flow structure spontaneously changes over time. Furthermore, it was found that the viscosity of the fluid, continuity of the inflow, location of the fluid source, and evaporation from the system affect the spatial flow structure.

However, macro- and micro-scales investigations are further necessary to better understand flow processes in dual-porosity granular media. Following are some of the areas that should be explored in future investigations.

It was found that the temperature of the inflow, thus the dynamic viscosity of water, substantially affects the initial development of the flow fields. However, existing macroscopic flow structure did not change in response to changes of inflow temperature within the range of ~ 15-30 ^{o}C. This apparent contradictory behavior should be further investigated.

Changes in outflow distribution created by two out of the eight inflow interruptions were very small in comparison to the changes observed after the other interruptions. The reason for this difference was not identified; therefore, further investigations are necessary to characterize the variability of the flow in response to inflow interruptions.

We characterized the unsaturated flow structure in dual-porosity granular media using a single-point source to supply water to the flow system. Findings of this research is readily applicable for scenarios such as heap leach piles and rock drains, where liquid flow initiates from point sources, as well as migration of contaminants from point sources (e.g., leak though a hole in a waste storage tank) to natural gravel deposits. However, the flow structure under a multiple-point source or a uniformly distributed source may be different from the structure we observed. In our experiment, the distribution of flow is narrow at the top and laterally spreads with the depth. Distributed source will create a relatively uniform distribution at the top and potentially develop different flow fields. Interaction between such flow fields and macroscopic behavior of the flow should be investigated through experiments.

Variation of the interfacial tension of water during our experiments was extremely low. Changes of interfacial tension can substantially change the magnitude of capillary force on water, thus potentially changing the spatial structure of flow fields. Experiments that use surfactants to change the interfacial tension of water could lead to a better understanding of the influence of interfacial tension on the macroscopic flow structure.

Spatial structure of the unsaturated flow changed in response to imposed evaporation changes, but it did not show any variation in response to natural variations of evaporation due to the change of ambient temperature (between ~24 and 30 ^{o}C) and relative humidity (between ~15% and 35%). Therefore, studies should be conducted to investigate if the changes in ambient temperature and humidity outside this range can change the flow structure.

We monitored the inflow from the top and the outflow from the bottom of the test column, but did not monitor the distribution of individual flow paths in the dual-porosity granular space. An experiment that uses a tracer dye would enable us the ability to visualize the spatial structure of individual flow paths. Furthermore, it could also be used to confirm the existence of discrete flow paths in dual-porosity granular media. Identifying the spatial distribution of flow paths will also provide information about the distribution of matrix saturation in the media.

Micro-scale experiments are necessary to understand the development of pendular rings, water films, flow between two rock fragments and flow in networks of interconnected stones. Such experiments would provide greater information on the micro-scale physical processes related to the development of pendular rings and water films, as well as spatial and temporal variability of flow paths in dual porosity granular media.

APPENDIX A

INTRA-GRANULAR, INTER-GRANULAR AND TOTAL POROSITY

The size and partially unsealed boundaries of the experimental column preclude direct measurement of the total porosity. Instead, total porosity was estimated by assuming that the solid material in the rock fragments used to fill the column has a density equivalent to that of pure quartz. This same assumption was used in measuring the intra-granular porosity on a subset of the rock fragments. The intra-granular porosity is then used to estimate the volume of rock fragments inside the column, which leads to the inter-granular porosity.

A-1 Intra-granular Porosity of the Crushed Rock Fragments

Approximately 1 kg of rock fragments (about 50 - 60 individual pieces) was selected randomly from our stockpile. Ambient air in the pore spaces was replaced with CO_2 gas by storing the fragments in sealed plastic bags filled with CO_2 for about one week. The CO_2 gas is assumed to have replaced most of the ambient air in the pores through diffusion and density-driven displacement. After that, the rock fragments were vacuum saturated with distilled water for about a week. Since $CO_2$is highly soluble in water, it was expected that this procedure would cause all connected pores to become fully water saturated. Surface drips were removed from the wet rock fragments before weighing them to an accuracy of ± 0.1 g. The rock fragments were then oven-dried for 24 hours at ~105 ^{o}C and re-weighed. Assuming that water has a density of 1 gcm^{-3}, pore volume in the rock fragments was calculated from the difference between saturated and dry weights. The volume of the solid materials in the rock fragments is also required to calculate

porosity. The solid volume is obtained through an assumption that the fragments are mostly made up of pure silica, which has a density of 2.65 g/cm^3. Calculation of intra-granular porosity proceeds as follows:

Weight of dry rock fragments (W_D) = 1,030.5 g

Weight of saturated rock fragments (W_S) = 1,131.6 g

The solid volume of rock fragments (V_S) $= \frac{W_D}{\text{Density of silica}}$

$= \frac{1{,}030.5 \text{ g}}{2.65 \text{ gcm}^{-3}}$

$= 388.9 \text{ cm}^3$

Intra-granular pore volume (V_{Intra}) = Volume of water in fragments at 100% saturation

$= \frac{(1{,}131.6\text{-}1{,}030.5)\text{g}}{1.0 \text{ gcm}^{-3}}$

$= 101.1 \text{ cm}^3$

Intra-granular porosity (P_{Intra}) $= \frac{V_{Intra}}{V_S + V_{Intra}}$

$= \frac{101.1 \text{ cm}^3}{(388.9+101.1)\text{cm}^3}$

$= \underline{\underline{0.21}}$

A-2 Total Porosity of the Test Column

The volume of the test column was calculated from the internal dimensions. The weight of the rock fragments packed in the column was also measured after packing. The solid volume of rock fragments was calculated using the weight of the rock fragments and the density of silica. Calculation of the total porosity and bulk density are as follows:

Volume of the test column (V_{Col}) $= \pi \times (15.0\ cm)^2 \times 100.0\ cm$

$= 70{,}686\ cm^3$

The solid volume of rock fragments (V_S) $= \dfrac{\text{Weight of dry fragments}}{\text{density of silica}}$

$= \dfrac{95{,}350\ g}{2.65\ gcm^{-3}}$

$= 35{,}981\ cm^3$

Total porosity of the test column (P_T) $= \dfrac{V_{Col} - V_S}{V_{Col}}$

$= \dfrac{(70{,}686 - 35{,}981)cm^3}{70{,}686 cm^3}$

$= \underline{0.49}$

Bulk density of rocks in the column (ρ_b) $= \dfrac{\text{Weight of rock fragments}}{V_{Col}}$

$= \dfrac{95{,}350\ g}{70{,}686\ cm^3}$

$= \underline{1.35\ gcm^{-3}}$

A-3 Inter-granular Porosity of the Test Column

Calculating the inter-granular porosity requires the volume of pore space between the rock fragments, which is defined as that space within the column that is not occupied by either the solid mass or the intra-granular pore space. Calculation of the inter-granular porosity is as follows:

Intra-granular pore volume $= \frac{V_S x\ P_{Intra}}{1\text{-}P_{Intra}}$

$= \frac{(35{,}981\ cm^3 x\ 0.21)}{(1\text{-}0.21)}$

$= 9{,}564\ cm^3$

Total volume of rock fragments (V_F) $= V_S + V_{Intra}$

$= (35{,}981 + 9{,}564)\ cm^3$

$= 45{,}545\ cm^3$

Inter-granular porosity (P_{Intra}) $= \frac{V_{Col} - V_F}{V_{Col}}$

$= \frac{(70{,}686 - 45{,}545)cm^3}{70{,}686\ cm^3}$

$= \underline{0.36}$

APPENDIX B

SATURATED HYDRAULIC CONDUCTIVITY OF THE SANDSTONE AND THE TEST COLUMN

Saturated hydraulic conductivity of the sandstone was measured in the laboratory using the falling head method. Measuring the saturated hydraulic conductivity of the test column was practically impossible because of the large size and high permeability of the column. Therefore, saturated hydraulic conductivity of the column was estimated using the modified Kozeny-Carman equation proposed by Hansen (2004).

Appendix B-1 Saturated Hydraulic Conductivity of the Sandstone

Several larger pieces of crushed rock were obtained from the same locale for the purpose of hydraulic testing. One of these larger pieces was put through the same preparation as the rock fragments used in the column testing (See section 3.2) then cut to a size of 3.0 x 3.2 x 8.5 cm. The cut sandstone block was oven-dried for 24 hours at ~105 ^{o}C. The four long faces of the block were then sealed with epoxy (EasyCast®); the two short faces were left uncoated to allow flow along the long axis of the block (we selected the long axis parallel to bedding planes of the sample to get the highest saturated hydraulic conductivity). The coated block was then placed into a 9 cm long piece of 5.1 cm inside diameter schedule 40 PVC pipe and surrounded with more epoxy (EasyCast®) in order to form an impermeable seal around the sample. After that the PVC pipe was capped on each end with Schedule 40 cleanout plugs that were drilled and tapped to allow the attachment of 0.95 cm inner diameter flexible vinyl tubing (figure B.1).

Saturation of the sample was begun by displacing air from the pore space by flowing CO_2 gas from bottom to top for ~20 minutes at ~1 psi pressure. The sample was then placed in a tank of purified water for ~24 hours under a ~25 kPa vacuum to assure full saturation. Final assembly of the test apparatus (i.e., connection of hoses and fittings) was done under water to maintain saturation.

Based on the estimated saturated hydraulic conductivity of the sample (using the Kozeny-Carman equation; Carrier, 2003) it was decided to conduct a falling head test to measure the saturated hydraulic conductivity. The inflow side of the apparatus consisted of a ~180 cm tall column of 0.95 cm inner diameter flexible vinyl tubing, and was connected to the bottom end of the sample assembly. In order to compensate for the slight variations in cross-sectional area of the flexible tubing we decided to use a much longer inflow tube than normal to facilitate averaging. The drain tube was connected to the top of the sample assembly, with the open end of the tubing kept 4.4 cm above the sample to maintain a positive backpressure. Height of the water column was recorded nine times over a period of ~2 days.

The saturated hydraulic conductivity (K_{sat}) was calculated using the following equation:

$$K_{sat} = \left(\frac{aL}{At}\right) \text{ x } \ln\left(\frac{h_0}{h_1}\right) \qquad \text{Eq. (B1)}$$

where a is the cross-sectional area of the water column, L is the length of the sample, A is the cross-sectional are of the sample, t is the elapsed time, h_o is the hydraulic head at the beginning (when t=0), and h_t is the hydraulic head when time is t.

Cross-sectional area of the sample (A) = 3.0 cm x 3.2 cm = 9.6 cm^2

Length of the sample (L) = 8.5 cm

Cross-sectional area of the water column (a) = π x (0.47 cm)^2 = 0.7 cm^2

Table B.1 – Elapsed time, hydraulic head and calculated saturated hydraulic conductivity of the sample

Duration (t; minute)	Hydraulic head (h;cm)	K_{sat}(cm/min)	K_{sat} (cm/hr)
0	181.5		
48	180.6	6.4×10^{-5}	0.004
88	179.7	7.0×10^{-5}	0.004
763	168.4	6.0×10^{-5}	0.004
1005	165.1	5.8×10^{-5}	0.003
1142	163.5	5.6×10^{-5}	0.003
1386	161.2	5.3×10^{-5}	0.003
2325	151.7	4.7×10^{-5}	0.003
2815	147.9	4.5×10^{-5}	0.003

Mean saturated hydraulic conductivity of the sample = 0.003 cm/hour

Equation B1 can be rearranged in such a way that relation between the elapsed time to and height of water column can be tested for accuracy.

$$\ln\left(\frac{h_0}{h_1}\right)=\left(\frac{AK_{sat}}{aL}\right) t \qquad \text{Eq. (B2)}$$

Equation B2 implies that natural logarithm of (h_0/h_1) is linearly related to elapsed time. Our data also show a strong linear correlation between those two variables (figure B.2), thus prove the accuracy.

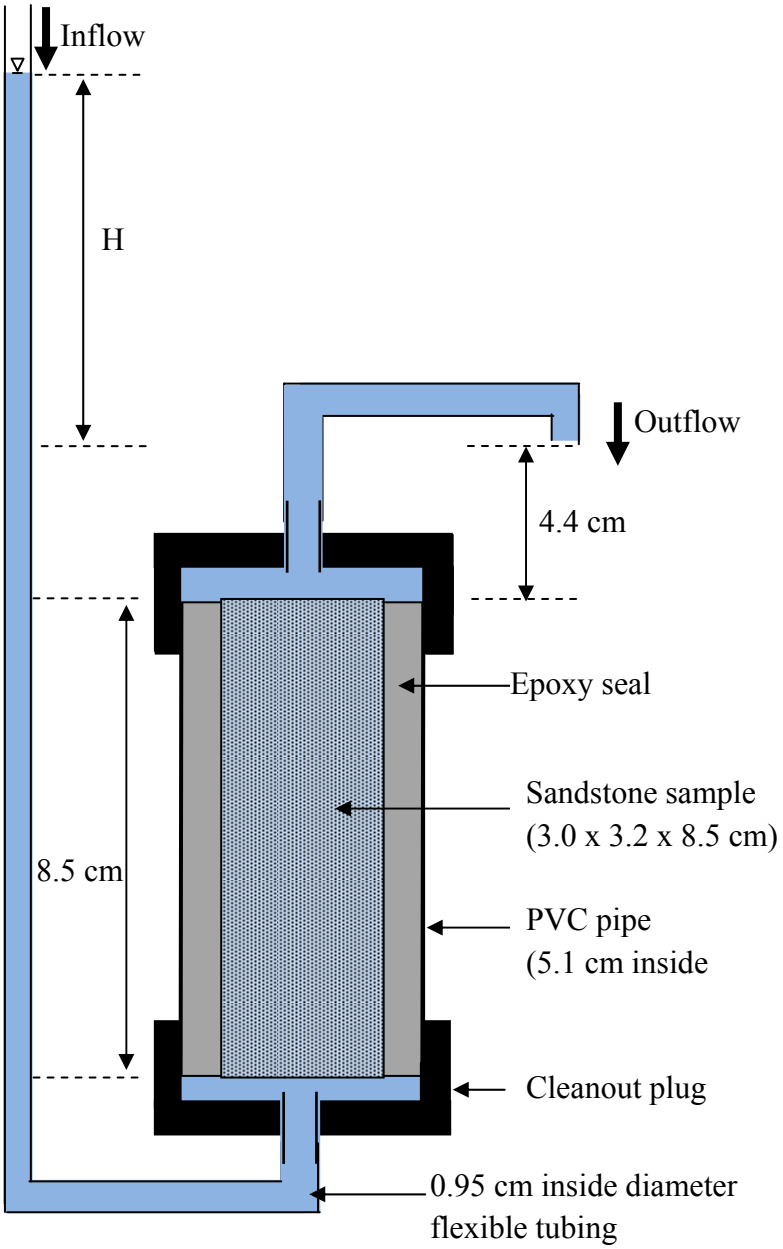

Figure B.1 – Schematic illustration of the setup of the falling head test for measuring the saturated hydraulic conductivity of the sandstone (not drawn to scale)

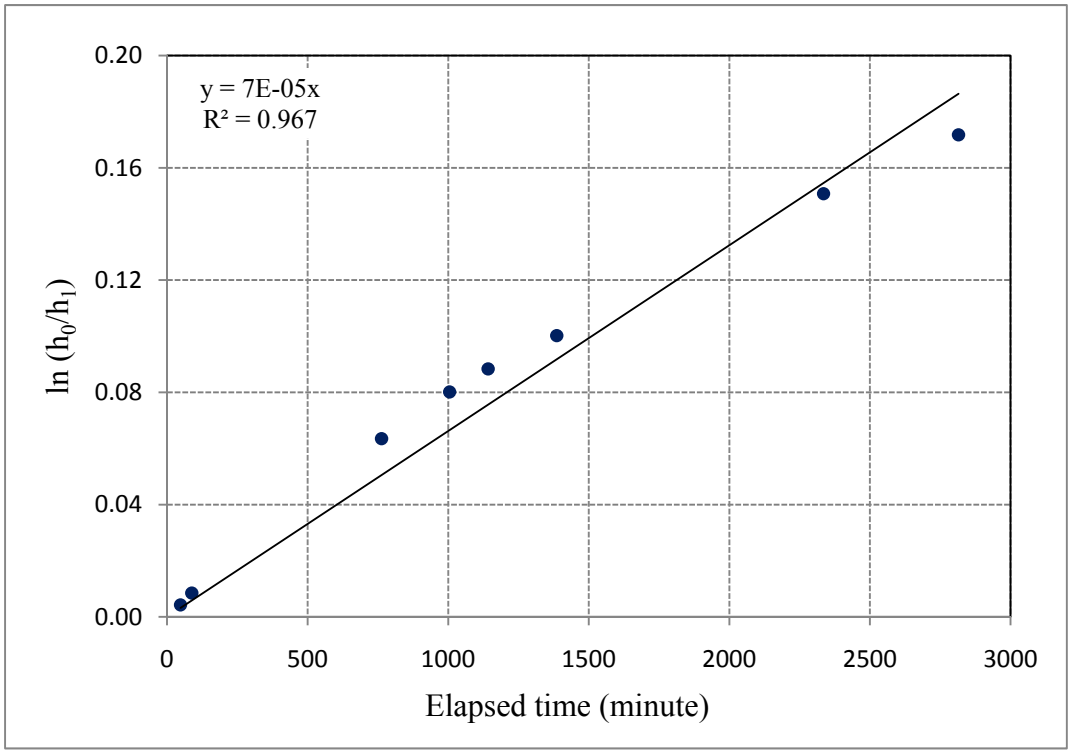

Figure B.2 The graph of $\ln(h_0/h_1)$ vs. time

Appendix B-2 Saturated Hydraulic Conductivity of the Test Column

The test column was filled with crushed sandstone fragments of 1-3 cm in diameter, and hence the medium was highly permeable. Considering that and the large size of the column (100 cm tall and ~30 cm diameter), it was decided to estimate the saturated hydraulic conductivity of the column using a semi-empirical equation (modified Kozeny-Carman equation) proposed by Hansen (2004) for estimating saturated hydraulic conductivity of mine tailings. Also, this approach to estimate the saturated hydraulic conductivity of the column assumed that: (a) saturated hydraulic conductivity of the sandstone matrix was extremely small in comparison to that of the column, and (b) Darcy's law was valid for saturated flow in the column.

Measured saturated hydraulic conductivity of a medium made up of coarse rock fragments can be related to Kozeny-Carman equation predicted saturated hydraulic conductivity by;

$$K_m = 100(K_p)^{1.5} \qquad \text{Eq. (B3)}$$

where K_m is the measured saturated hydraulic conductivity, K_p is the predicted saturated hydraulic conductivity using the Kozeny-Carman equation (Hansen, 2004). For water flow at 20 ^oC, K_p can be estimated from;

$$K_p = 552\ D^2 \frac{e^3}{(1+e)} \qquad \text{Eq. (B4)}$$

where D is the diameter of uniform spheres that make the porous medium (in centimeter), and e is the void ratio (Carrier, 2003). A large portion of crushed sandstone fragments used in the experiment exhibits 1-3 cm in diameter along long direction, but close to or less than 1 cm in short direction. Therefore, it was assumed that D = 1.0 cm for calculation purpose. Furthermore, assuming that the inter-granular flow is several orders of magnitude larger than the intra-granular flow under saturated conditions of the test column;

Void ratio (e) $= \frac{\text{inter\_granular porosity}}{(1-\text{inter\_granular porosity})} = \frac{0.36}{(1-0.36)} = 0.56$

From equation B4,

$K_p = 552 \times (1.0)^2 \frac{0.56^3}{(1+0.56)} = 62$ cm/S

From equation B3,

$K_m = 100 \times (62)^{1.5} =$ <u>4.9×10^{-4} cm/S</u>

Saturated hydraulic conductivity of the test column = <u>4.9×10^{-4} cm/S</u>

The above calculated saturated hydraulic conductivity of the test column is an approximate estimation. The actual saturated hydraulic conductivity of the column may be lower than that because the large pore size can potentially create turbulent flow.

APPENDIX C

CONSTRUCTION OF THE BOTTOM PLATE

A pattern was created by drawing the boundaries of the nine equal-area sections (drainage basins) on a sheet of white paper at 1:1 scale. A 30 cm diameter circle was drawn to mark the inner wall of the test column. This circular area (706.9 cm^2) was divided into nine 78.5 cm^2 basins, one at the center of the column and the other eight around the first. The circular central basin was 10 cm in diameter, while the eight surrounding basins were truncated 45^o wedges.

The basin pattern was glued onto a 36 cm x 36 cm plate of 4 cm thick acrylic (Plexiglass®). Pilot holes were drilled through the plate at the basin centers using a 4 mm diameter (5/32 inch) drill bit to mark locations for the drains (figure C.1a). Next, the shape of each basin was roughed out by carving benches to depths of first 3 mm and then 6 mm using a 6 mm (1/4 inch) diameter end-mill that was mounted in a Bosch® palm router model PR20EVS (figure C.1b). Then, the areas around the pilot holes were deepened to 9 mm with a 25 mm (1 inch) counter sink mounted in a drill press. The slopes of each basin were then shaped using an air-driven belt sander (Dynabrade® mini Dynafile II 15026) with a medium-grit belt (figure C.1c). Final polishing of the basin slopes was done by hand sanding with grits from 60 to 1000 (figure C.1d).

In order to create basin drains, the bottom plate was flipped over to the unmachined side, then each of the previously drilled pilot holes was enlarged using a 12 mm (29/64 inch) drill bit and tapped for 18 NPT threads. The actual drains were fabricated from 10 cm long pieces of 8 mm internal diameter, 13 mm outer diameter cross-linked polyethylene pipes (ZURN® PEX) by threading one end with a 18 NPT die. Each of the

drains was then threaded into the acrylic plate from the side opposite the basin, and then smoothly mated to the basin slope by drilling into the opening of the drain with a 25 mm (1 inch) counter sink. Finally, a polymer (Rust-Oleum® American Accents® Clear top coat) was sprayed onto the basin surfaces to form a micro-smooth and hydrophobic surface coating.

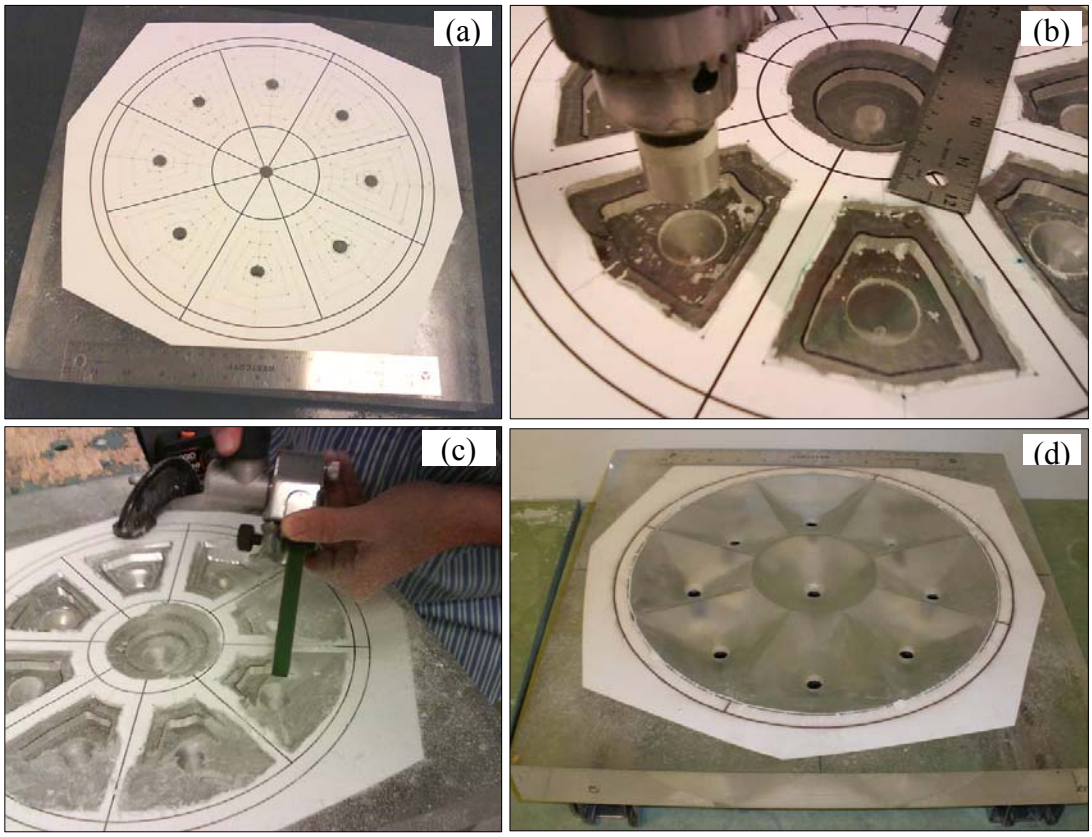

Figure C.1 – Construction of the bottom plate with nine equal-area basins.

APPENDIX D

CALIBRATION OF SENSORS AND INFLOW PUMP

Calibration of thermocouples, 1 psi pressure transducers and the inflow pump were done after the experimental set-up was completely assembled.

D-1 Thermocouples

The thermocouples were calibrated using a single-point technique after all of the wiring was installed and routed. All of the thermocouple tips were removed from their mounting points and gathered into a single bundle. The bundle was then immersed in a vacuum bottle filled with approximately 60% ice and 40% water (both were deionized). Temperature readings were collected from all thermocouples for about four hours at one minute intervals. This procedure was repeated twice and the average offset from 0 ^{o}C was calculated for each thermocouple. The calculated offset of each thermocouple was used to correct data measured during the experiment (table D.1).

Table D.1 Offset of thermocouples

Thermocouple number	1	2	3	4	5	6	7	8	9
Average offset (^{o}C)	0.3	0.4	0.3	0.2	0.3	0.5	0.3	0.5	0.4

D-2 1psi Pressure Transducers

The 1 psi pressure transducers connected to the collection vessels were individually calibrated in place, with the matching vessel. To begin, all of the collection vessels were filled up to their maximum levels with reverse osmosis water. A data acquisition program

was started to monitor pressure transducer voltages at 30 second intervals. Baseline data was collected for about five minutes, then ~100-130 g of water was removed from each collection vessel using an 60 ml capacity syringe. The exact weight of water removed from each vessel was measured using an electronic scale (Ohaus® Explorer Pro EP4101) of 4.1 kg capacity (± 0.1 g accuracy) and recorded. The system was allowed to stabilize for about five minutes while pressure data were collected. This step was repeated five more times, removing a total of 700-800 g of water from each vessel. The process was then reversed to add a measured amount of water to each vessel in discrete steps, with five minute pauses for data collection.

The average change in voltage was plotted against the total change in mass of water for each step (figure D.1); data for water removal and addition were plotted separately. In all instances, the relationship between voltage change and water mass change was very close to linear and could be fit to a straight line ($y = mx + c$). The gradient of the straight line provided the change of mass of water per unit change of output voltage. Calibration was done twice and the average change of mass of water per unit output voltage change for each pressure transducer was calculated (table D.2).

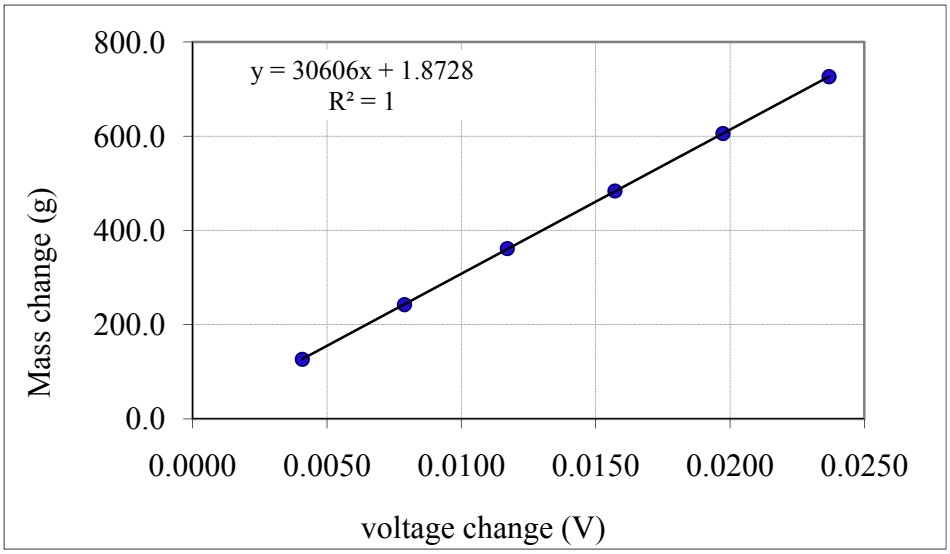

Figure D.1 – An example plot of water mass change in the collection vessel-1 and vs. output voltage change of the pressure transducer during calibration.

Table D.2 Calibration constants for 1 psi pressure transducers

Pressure Transducer Number	Calibration 1				Calibration 2				Average gradient (g/V)
	Gradient (g/V) – Removal of water	R^2	Gradient (g/V) – Addition of water	R^2	Gradient (g/V) - Removal of water	R^2	Gradient (g/V) - Addition of water	R^2	
1	30606	1.000	30645	1.000	30782	1.000	30627	1.000	30665
2	31591	1.000	31654	1.000	31733	1.000	31718	1.000	31674
3	34011	1.000	33504	1.000	33741	1.000	33631	1.000	33722
4	31872	0.999	31465	1.000	31555	1.000	31599	1.000	31623
5	30654	0.999	30327	1.000	30466	1.000	30403	1.000	30463
6	33975	1.000	33964	1.000	34090	1.000	34198	1.000	34057
7	31515	1.000	31301	0.999	31612	1.000	31290	0.999	31430
8	32276	1.000	32251	1.000	32434	1.000	32350	1.000	32328
9	33221	1.000	33243	1.000	33339	1.000	33336	1.000	33285
10	33885	1.000	33710	1.000	34038	1.000	33794	0.999	33857
11	34117	0.999	34511	0.999	33971	1.000	34194	1.000	34198

D-3 Inflow Pump

To begin, the inflow line was set-up so that water was diverted away from the column, but at the same head difference as would occur during the experiment. Next, the pump was run through a series of steps, beginning with a 5.0 mA control current, and increasing by 0.5 mA at each step until a current of 8.0 mA was attained. The change in mass for the source water container and the current sent to the pump were recorded at 30 second intervals during each step. The discharge rate from the source container was plotted against the direct current sent to the pump (figure D.2). A best fit linear trend line to the data provides an estimate of the relationship between control current and flow rate in ml/minute. We note that this calculation in only valid for the selected head difference, inflow line configuration and the tubing used in the pump head. Also, drawdown at the source water container was very small during the period of calibration, but may be significant during the experiment.

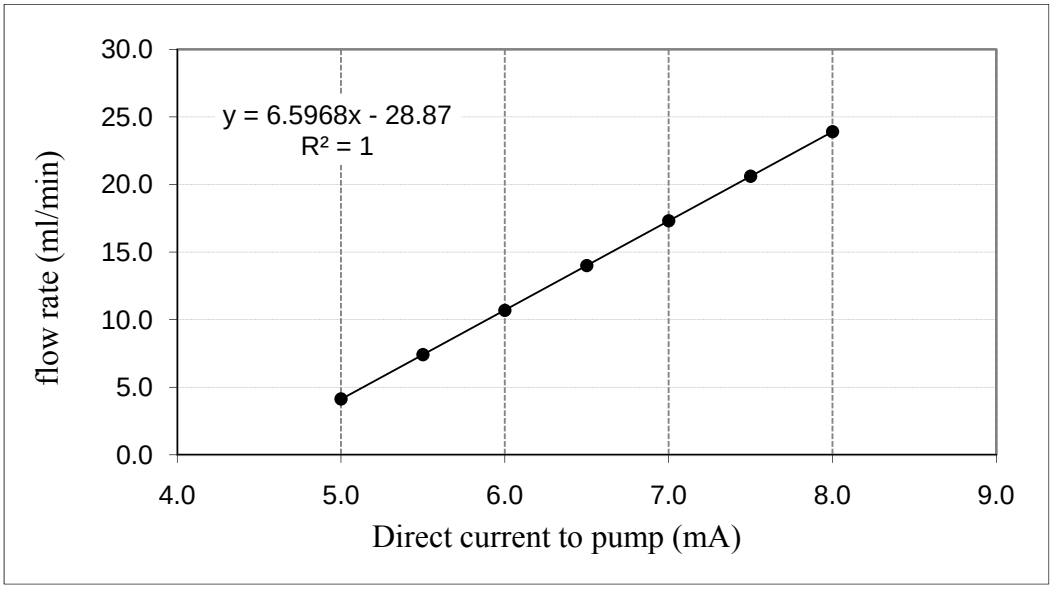

Figure D.2 Inflow rate to the column vs. control current sent to the inflow pump

APPENDIX E

EXPERIMENT LOG

Experiment # 1		
Date	No. of the Day	Notes/Comments
12/26/2009	1	Configuration of the set-up: Single-point inlet at the center of the column Temperature of the water-bath set at 25 ^{o}C Nominal inflow - 8.0 ml/min DAQ program was started at 07:23 Inflow to the column was started at 07:53 Dry weight of the column was 153.79 kg
12/29/2009	4	Air-bubbles formed in the inflow tubings on the upstream side of the supply pump and moved along the plumbing.
1/5/2010	11	Inflow was turned off at ~15:00 The total outflow was diverted to a bucket that sat on an electronic balance and then the inflow was started (~15:10). Deaired water was used in the experiment, so no air-bubbles in the inflow plumbing.
1/7/2010	13	Inflow was turned off at ~17:15, but data were collected continuously.
1/8/2010	14	The experiment was shutdown and the test column was dried.

Experiment # 2		
Date	No. of the day	Notes/comments
1/15/2010	1	Configuration of the set-up: Single-point inlet at the center Nominal inflow - 8.0 ml/min Temperature of the water-bath set at 25 ^{o}C Used deaired water DAQ program was started at 7:43 Water flow in to column was started at 8:09 Dry weight of the column 154.56 kg No air bubbles in inflow plumbing
1/16/2010	2	Few bubbles formed in inflow plumbing after refilling, but all were removed within ~ 4 minutes.
1/29/2010	15	Inflow tubing between the pump and heat exchanger ruptured close to the heat exchanger. It was noticed ~ 11:39, then fixed within ~ 10 minutes.
2/4/2010	21	A small rupture was found in the inflow plumbing at previously cracked location, but water did not leak. It was repaired at ~ 10:07-10:15
2/5/2010	22	After the reading at 4:07:45, next data were collected at 4:08:32 - i.e., 47 S, not 2 min after the last one. High inflow rate to column due to this error

2/9/2010	26	Early refill of source water container ~ 16:32
2/12/2010	29	90-minute long inflow interruption Inflow turned off at 19:34 and turned on at 21:05
2/18/2010	35	Slightly ruptured inflow tubing close to heat exchanger was repaired at 17:16 - 17:28. Inflow was interrupted for ~ 2 minutes
2/20/2010	37	10-minute long inflow interruption from 19:12 to 19:22.
2/24/2010	41	Inflow was turned off at 15:00
2/25/2010	42	DAQ was turned off at 21:13

Experiment # 3		
Date	No. of the day	Notes/comments
5/11/2010	1	Configuration of the set-up: Single-point inlet at the center Nominal inflow - 8.0 ml/min Temperature of the water-bath set at 15 ^{o}C Used deaired water DAQ program was started at 7:25 Water flow in to column was started at 7:53 Dry weight of the column 153.94 kg 4 pieces of rock fragments (including the one right below the inlet) were removed from the top of the column because of a black precipitate on surfaces. Remaining rock fragments around the inlet were rearranged.
5/13/2010	3	Inflow was turned off at 15:55. A black precipitate was formed on rock fragments around the inlet. Heat exchanger and inflow plumbing were removed from the experiment for inspection at 17:55. Corrosion in the heat exchanger in source water channel, but not in the water bath channel. Drying of the column was started at 19:20.

Experiment #4		
Date	No. of the day	Notes/comments
5/20/2010	1	Configuration of the set-up: Single-point inlet at the center Nominal inflow - 8.0 ml/min Temperature of the water-bath set at 15 ^{o}C Used deaired water DAQ program was started at 7:25 Water flow in to column was started at 8:09 Dry weight of the column 154.08 kg Brass fittings of the heat exchanger were replaced with stainless steel fittings to prevent corrosion. About 930 g of contaminated rock fragments (due to black precipitate came from heat exchanger) were replaced with fresh rock fragments. Heat exchanger was insulated with fiberglass thermal blanket.
5/30/2010	11	90-minute inflow interruption Inflow was turned off from 18:33 to 20:03.
6/2/2010	14	Light Grey color precipitate on the 1st rock fragment below the inlet.
6/4/2010	16	90-minute inflow interruption Inflow was turned off between 18:45 and 20:15.
6/7/2010	19	Temperature of water-bath was increased to 30C at 19:00.

6/10/2010	22	90-minute inflow interruption Inflow was turned off from 18:45 to 20:21.
6/11/2010	23	20-minute inflow interruption Inflow was turned off from 18:29 to 18:49.
6/12/2010	24	Temperature of water-bath was decreased to 10^{o}C at 18:40.
6/14/2010	26	Inlet was moved ~ 4 cm away from the center of S1 towards the center of S7 at 19:00-19:13.
6/17/2010	29	90-minute inflow interruption from 19:01 - 20:33.
6/18/2010	30	Inlet was moved back to the center of S1 at 20:41-20:45.
6/19/2010	31	Inlet was moved ~ 2.5cm away from the center of S1 towards the center of S7 at 20:27-20:33.
6/22/2010	34	The top of the column was covered with a plastic sheet to minimize evaporation at 19:10-19:28. Added weight to the column ~ 24.7 g.
6/24/2010	36	Top cover of the column was removed at 11:47
6/25/2010	37	Total outflow was collected to a single vessel placed on a 6kg balance at 14:00. Modification of set-up was completed at 14:26. Inflow continued during modification.
6/28/2010	40	Inflow was turned off at 14:26.
6/29/2010	41	Total outflow reading was stopped at 15:49.

REFERENCES

Arya, M.L., Leij, F.J., Shouse, P.J., and van Genuchten, M. T., 1999, Relationship between the hydraulic conductivity function and the particle-size distribution, Soil Science Society of America Journal, v.63, p.1063–1070

Azam, S., Wilson, W., Herasymuik, G., Nichol, C., and Barbour, L., 2007, Hydrogeological behaviour of an unsaturated waste rock pile: a case study at the Golden Sunlight Mine, Montana, USA, Bulletin of Engineering Geology and the Environment, v.66, p.259–268

Barr, D.W., 2001, Turbulent flow through porous media, Ground Water, v.39, no.5, p.646-650

Bartley, J.T., and Ruth, D.W., 1999, Relative permeability analysis of tube bundle models, Transport in Porous Media, v.36, p.161–187.

Bolt, G.H., Iwata, S., Peck, A.J., Raats, P.A.C., Rode, A.A., Vachaud, G., and Voronin, A.D., 1976, Soil physics terminology, Bulletin of the international society of soil science, no.49, p.26-36

Bouma, J., and Dekker, L.W., 1978, A case study on infiltration into dry clay soil, I. Morphological observations, Geoderma, v.20, p.27-40

Brouyere, S., Dassargues, A., and Hallet, V., 2004, Migration of contaminants through the unsaturated zone overlying the Hesbaye chalky aquifer in Belgium: a field investigation, Journal of Contaminant Hydrology, v.72, p.135-164

Carminati, A., Kaestner, A., Fluhler, H., Lehmann, P., Or, D., Lehmann, E., and Stampanoni, M., 2007, Hydraulic contacts controlling water flow across porous grains, Physical Review, e.76, 026311

Carminati, A., Kaestner, A., Lehmann, P., and Fluhler, H., 2008, Unsaturated water flow across soil aggregate contacts, Advances in Water Resources, v.31, p.1221–1232

Carrier, W.D., 2003, Goodbye, Hanzen; Hello, Kozeny-Carman, Journal of Geotechnical and Geoenvironmental Engineering, p.1054-1056

Chahar, B.R., 2004, Determination of length of a horizontal drain in homogeneous earth dams, Journal of Irrigation and Drainage Engineering, v.130, no.6, p.530-536

Cho, W.J., Lee, J.O., and Chun, K.S., 1999, The temperature effects on hydraulic conductivity of compacted bentonite, Applied Clay Science, v.14, p.47-58

Conca, J.L., and Wright, J., 1992, Diffusion and flow in gravel, soil and whole rock, Applied Hydrogeology, v.1, no.1, p.5-24

Conca, J.L., Apted, M.J., Zhou, W., Arthur, R.C., and Kessler, J.H., 1998, Flow barrier system for long-term high-level-waste isolation: experimental results, Nuclear Technology, v.124, p.88-100

Constantz, J., 1982, Temperature dependence of unsaturated hydraulic conductivity of two soils, Soil Science Society of America Journal, v.46, no.3, p.466-470

Corey, A. T., and Klute, A., 1985, Application of the potential concept to soil water equilibrium and transport, Soil Science Society of America Journal, v.49, p.3-11

Crist, J.T., McCarthy, J.F., Zevi, Y., Baveye, P., Throop, J.A., and Steenhuis, T.S., 2004, Pore-scale visualization of colloid transport and retention in partly saturated porous media, Vadose Zone Journal, v.3, p.444–450

Dong, M., Dullien, F.A.L., Dai, L., and Li, D., 2005, Immiscible displacement in the interacting capillary bundle model part I. Development of interacting capillary bundle model, Transport in Porous Media, v.59, p.1-18
Dragila, M.I., and Weisbrod, N., 2003, Parameters affecting maximum fluid transport in large aperture fractures, Advances in Water Resources, v.26, p.1219-1228
Dubinin, M.M., 1980, Water vapor adsorption and the microporous of carbonaceous adsorbents, Carbon, v.18, p.355-364
Elberling, B., Larsen, F., Christensen, S., and Postma, D., 1998, Gas transport in a confined unsaturated zone during atmospheric pressure cycles, Water Resources Research, v.34, no.11, p.2855-2862
Eriksson, N., Gupta, A., and Destouni, G., 1997, Comparative analysis of laboratory and field tracer tests for investigating preferential flow and transport in mining waste rock, Journal of Hydrology, v.194, p.143-163
Gerke, H.H., and van Genuchten, M.T., 1993, A dual-porosity model for simulating the preferential movement of water and solutes in structured porous media, Water Resources Research, v.29, no.2, p.305-319
Glass, R.J., Nicholl, M.J., Pringle, S.E., and Wood, T.R., 2002, Unsaturated flow through a fracture-matrix network: Dynamic preferential pathways in mesoscale laboratory experiments, Water Resources Research, v.38, no.12, p.1281-1298
Green, W.H., and Ampt, G.A., 1911, Studies on soil physics Part-I, The flow of air and water through soils, The Journal of Agricultural Science, v.4, p.1-24
Guebert, M.D., and Gardner, T.W., 2001, Macropore flow on a reclaimed surface mine: infiltration and hillslope hydrology, Geomorphology, v.39, p.151-169
Gvirtzman, H., Magaritz, M., Kanfi, Y., and Carmi, I., 1988, Matrix and fissure water movement through unsaturated calcareous sandstone, Transport in Porous Media, v.3, p.343-356
Hansen, D., 2004, Discussion of "On the use of the Kozeny-Carman equation to predict the hydraulic conductivity of soils", Canadian Geotechnical Journal, v.41, p.990-993
Hewett, D.F., 1931, Geology and ore deposits of the Goodsprings quadrangle, Nevada: U.S. Geological Survey Professional Paper, 162
Hillel, D., 1998, Environmental soil physics, Academic Press, San Diego, CA, USA
Hu, Q., Kneafsey, T.J., Roberts, J.J., Tomutsa, L., and Wang, J.S.Y., 2004, Characterizing unsaturated diffusion in porous tuff gravel, Vadose Zone Journal, v.3, p.1425-1438
Huang, T.T., Taylor, D.G., Lim, K.S., Sedlak, M., Bashir, R., Mosier, N.S., and Ladisch, M.R., 2006, Surface-direct boundary flow in microfluidic channels, Langmuir, v.22, p.6429-6437
Jarvis, N.J., 2007, A review of non-equilibrium water flow and solute transport in soil macropores: principles, controlling factors and consequences for water quality, European Journal of Soil Science, v.58, p.523-546
Kappes, D. W., 2002, Precious metal heap leach design and practice, Proceedings of the Mineral Processing Plant Design, Practice, and Control, Littleton, CO, Society for Mining, Metallurgy, and Exploration, p.1606–1630.
Kellner, E., Price, J.S., and Waddington, J.M., 2004, Pressure variation in peat as a result of gas bubble dynamics, Hydrological Processes, v.18, p.2599-2605

King, J.R., Ockendon, J.R., and Ockendon, H., 1999, The Laplace-Young equation near a corner, Quarterly Journal of Mechanics and Applied Mathematics, v.52, no.1, p.73-97
Kutilek, M., 2004, Soil hydraulic properties as related to soil structure, Soil and Tillage Research, v.79, p.175-184
Lin, C., Greenwald, D., and Banin, A., 2003, Temperature dependence of infiltration rate during large scale water recharge into soils, Soil Science Society of America Journal, v.67, p.487-493
Luxemoore, R.J., 1981, Micro-, meso-, and macroporosity of soil, Science Society of America Journal, v.45, p.671-672
Mali, N., Urbane, J., and Leis, S., 2007, Tracing of water movement through the unsaturated zone of a coarse gravel aquifer by means of dye and deuterated water, Environmental Geology, v.51, p.1401-1412
Milczarek, J.J., Fijal-Kirejczyk, I., Zoladek, J., Chojnowski, M., and Kowalczyc, G., 2008, Effect of gravitation on water migration in granular media, Acta Physica Polonica A, v113, no.4, p.1245-1254
Moldrup, P., Olesen, T., Komatsu, T., Schjonning, P., and Rolston, D.E., 2001, Tortuosity, diffusivity, and permeability in the soil liquid and gaseous phases, Soil Science Society of America Journal, v.65, p.613-623
Mualem, Y., 1976, A new model for predicting the hydraulic conductivity of unsaturated porous media, Water Resources Research, v.12, no.3, p.513-522
Nichol, C., Smith, L., and Beckie, R., 2005, Field-scale experiments of unsaturated flow and solute transport in a heterogeneous porous medium, Water Resources Research, v.41, W05018, doi:10.1029/2004WR003035
Nitao, J.J., and Bear, J., 1996, Potentials and their role in transport in porous media, Water Resources Research, v.32, no.2, p.225-250
Palmer, A.N., 1991, Origin and morphology of limestone caves, Geological Society of America Bulletin, v.103, p.1-21
Philip, J.R., 1977, Unitary approach to capillary condensation and adsorption, The Journal of Chemical Physics, v.66, no.11, p.5069-5075
Philip, J.R., 1970, Flow in porous media, Annual Review of Fluid Mechanics, v.2, p.177-204
Price, M., Low, R.G., and McCann, C., 2000, Mechanisms of water storage and flow in the unsaturated zone of the chalk aquifer, Journal of Hydrology, v.233, p.54-71
Reinson, J.R., Fredlund, D.G., and Wilson, G.W., 2005, Unsaturated flow in coarse porous media, Canadian geotechnical Journal, v.42, p.252-262
Richards, L.A., 1931, Capillary conduction of liquids through porous mediums, Physics, v.1, p.318-333
Schaap, M.G., and Leij, F.J., 2000, Improved prediction of unsaturated hydraulic conductivity with the Mualem-van Genuchten model, Soil Science Society of America Journal, v.68, p.843-851
Sutera, S.P., and Skalak, R., 1993, The history of Poiseulle's law, Annual Review of Fluid Mechanics, v.25, p.1-20
Tidwell V.C., Glass R.J., Chocas, C., Barker, G., and Orear, L., 2003, Visualization experiment to investigate capillary barrier performance in the context of a Yucca

Mountain emplacement drift, Journal of Contaminant Hydrology, v.62-63, p.287-301
Tippkotter, R., 1983, Morphology, spatial arrangement and origin of macropores in some hapludalfs, West Germany, Geoderma, v.29, p.355-371
Tokunaga, T.K., and Wan, J., 1997, Water film flow along fracture surfaces of porous rock, Water Resources Research, v.33, no.6, p.1287-1295
Tokunaga, T.K., Wan, J., and Sutton, S.R., 2000, Transient film flow on rough fracture surfaces, Water Resources Research, v.36, no.7, p.1737-1746
Tokunaga, T.K., Olson, K.R., and Wan, J., 2003, Moisture characteristics of Hanford Gravels: Bulk, grain-surface, and intragranular components, Vadose Zone Journal, v.2, p.322-329
Touma, J., and Vauclin, M., 1986, Experimental and numerical analysis of two-phase infiltration in a partially saturated soil, Transport in porous media, v.1, p.27-55
Tschapek, M., 1984, Criteria for determining the hydrophilicity-hydrophobicity of soils, Journal of Plant Nutrition and Soil Science (Zeitschrift für Pflanzenernährung und Bodenkunde), v.147, no.2, p.137-149
Tuller, M., Or, D., and Dudley, M., 1999, Adsorption and capillary condensation in porous media: Liquid retention and interfacial configurations in angular pores, Water Resources Research, v.35, no.7, p.1949-1964
van Genuchten, M.Th., 1980, A closed-formed equation for predicting the hydraulic conductivity of unsaturated soils, Soil Science Society of America Journal, v. 44, p.892-898
Vogel, T., and Cislerova, M., 1988, On the reliability of unsaturated hydraulic conductivity calculated from the moisture retention curve, Transport in porous media, v.3, p.1-15
Wang, J.S.Y., and Narasimhan, T.N., 1985, Hydrologic mechanisms governing fluid flow in a partially saturated, fractured, porous medium, Water Resources Research, v.21, no.12, p.1861-1874
Webb, G., Tyler, S.W., Collord, J., Zyl, D.V., Halihan, T., Turrentine, J., and Fenstemaker, T., 2008, Vadose Zone Journal, v.7, p.899-908
Wildenschild, D., Hopmans, J.W., and Simunek, J., 2001, Flow rate dependence of soil hydraulic characteristics, Soil Science Society of America Journal, v.44, p.892-898
Wu, A., Yin, S., yang, B., Wang, J., and Qiu, G., 2007, Study on preferential flow in dump leaching of low-grade ores, Hydrometallurgy, v.87, p.124-132
Yanful, E.K., Riley, M.D., Woyshner, M.R., and Duncan, J., 1993, Construction and monitoring of a composite soil cover on an experimental waste-rock pile near Newcastle, New Brunswick, Canada, Canadian Geotechnical Journal, v.30, p.588-599
Zhang, Y., Liu, H., Zhou, Q., and Finsterle, S., 2006, Effects of diffusive property heterogeneity on effective matrix diffusion coefficient for fractured rock, Water Resources Research, v.42, W04405, doi:10.1029/2005WR004513

VITA

Graduate College
University of Nevada, Las Vegas

Jeevan Anuradha Jayakody Rathmalsinghe Rajakaruna Jayakodilage

Degrees:

Bachelor of Science, Geology, 2005
University of Peradeniya, Sri Lanka

Thesis Title: Characterization of Unsaturated Flow in Dual-porosity Granular Media

Thesis Examination Committee:

Chairperson, Michael Nicholl, Ph.D.
Committee Member, Adam Simon, Ph.D.
Committee Member, Michael Young, Ph.D.
Graduate Faculty Representative, Dale Devitt, Ph.D.